Fall 2022

Durability Enhancement of Anion Exchange Membrane Based Fuel Cells (AEMFCS) And Water Electrolyzers (AEMELs) By Understanding Degradation Mechanisms

Noor Ul Hassan

DURABILITY ENHANCEMENT OF ANION EXCHANGE MEMBRANE BASED FUEL CELLS (AEMFCS) AND WATER ELECTROLYZERS (AEMELS) BY UNDERSTANDING DEGRADATION MECHANISMS

by

Noor Ul Hassan

Master of Science
Istanbul Sehir University Turkey, 2015

Bachelor of Science
University of Engineering and Technology Lahore Pakistan, 2006

Submitted in Partial Fulfillment of the Requirements

For the Degree of Doctor of Philosophy in

Chemical Engineering

College of Engineering & Computing

University of South Carolina

2022

Accepted by:

William E Mustain, Major Professor

Paul A. Kohl, Committee Member

Monirosadat (Sanaz) Sadati, Committee Member

Chang Liu, Committee Member

Melissa Moss, Committee Member

Cheryl L. Addy, Interim Vice Provost and Dean of the Graduate School

DEDICATION

To my beautiful wife, Samina Zafar, lovely kids Abdul Quyum and Zainab Noor Ul Hassan who constantly supported me in the ups and downs of my PhD journey. Their patience and love made me strong during the challenges of this graduate program.

ACKNOWLEDGEMENTS

I express my utmost gratitude to Dr. William E. Mustain for his supervision, guidance, and feedback throughout this journey. Special Thanks to Professor Paul A. Kohl, for giving me an opportunity to work on his state-of-the-art polymer materials. I am thankful to Fulbright, United States Educational Foundation in Pakistan (USEFP) and Institute of International Education (IIE) for proving me financial support to complete my study program. Moreover, I highly appreciate the U.S. Department of Energy (DOE) for funding and giving me an opportunity to work on projects related to hydrogen energy conversion and hydrogen production technology.

ABSTRACT

The past several years have seen remarkable progress in renewable energy sources such as solar and wind, showing excellent efficiency and significant cost reduction. The intermittent nature of renewable resources requires them to be integrated with energy storage systems that can hold or convert this excess energy into other forms. Though batteries have been the most popular, it is also possible to store the energy as chemicals and fuels, such as hydrogen (H_2). Hydrogen generation from water electrolysis has been receiving significant attention in recent years. Among the existing water electrolysis technologies, anion exchange membrane electrolyzers (AEMELs) are the most immature and have thus been receiving a high level of interest in the research community. Anion exchange membrane fuel cells (AEMFCs), which operate in the reverse direction to produce energy from hydrogen and oxygen, are also a nascent technology that suffers from lower efficiency and poor durability.

For both AEMELs and AEMFCs, there is a growing body of literature pushing for the design of new materials to concomitantly increase performance and durability. This thesis describes an effort to address the limitations of AEMELs and AEMFCs. First, the effect of electrode design and cell operation on the performance and stability of AEMELS will be discussed, elaborating the current challenges in this technology and how to approach them in a scientific manner. It will be shown that the detailed understanding of device operation is essential before new materials can be fairly evaluated and their impact on the performance and durability elucidated. Specifically, highly durable AEMELs were

created and operated over 500 hours at 1.0 A/cm^2 with no significant degradation, both on dilute alkaline feed as well as pure water. The pros and cons of alkaline feed are also discussed. Secondly, device designs were conceived that increased the durability of AEMFCs. This thesis reports an optimized high performing AEMFC that was stably operated continuously for 3600 hours (150 days) with a very low degradation rate. Moreover, at the end of life, the cell was disassembled and subjected to a number of experiments probing the physical and chemical degradation that occurred during normal operation – including high resolution STEM imaging and chemical mapping. Well-described physical and electrochemical evolution of the fuel cell operation, degradation mechanisms and pathways leading to both reversible and irreversible performance loss were identified. Finally, advances in both AEMELs and AEMFCs were used to improve the efficiency and cycling durability of AEM unitized regenerative fuel cells (AEM-URFCs).

Considering all of the work in this thesis, the main contribution of the work was the unveiling of the variables that limit both the performance and lifetime of anion-exchange membrane-based devices. In particular, new designs for electrodes were conceived and insights into the behavior of operating cells (particularly related to water) were attained. It is expected that the new learning in this document will allow future researchers to take active steps towards improving performance, durability, and commercial viability.

TABLE OF CONTENTS

LIST OF TABLES

LIST OF FIGURES

LIST OF ABBREVIATIONS

AC ..... Alternating Current

AEMEL ..... Anion Exchange Membrane Electrolyzer

AEMFC ..... Anion Exchange Membrane Fuel Cell

ASR ..... Area Specific Resistance

AST ..... Accelerated Stress Testing

AWE ..... Alkaline Water Electrolyzer

BBNB ..... Bromobutyl Norbornene

BOE ..... Bifunctional Oxygen Electrode

BOL ..... Beginning of Life

BP ..... Bipolar Plate

BP ..... Bipolar Plate

BPNB ..... Bromopropyl Norbornene

CCM ..... Catalyst Coated Membrane

CCS ..... Catalyst Coated Substrate

CE ..... Constant Electrode

CG ..... Constant Gas

CL ..... Catalyst Layer

DI ..... Di-Ionized

DMA ..... Dynamic Mechanical Analysis

DOE ..... Department of Energy

DoE ..... Design of Experiments

EDS ..... Energy Dispersive X-ray Spectroscopy

EIS ..... Electrochemical Impedance Spectroscopy

EL ..... Electrolyzer

EOL ..... End of Life

ETFE ..... Ethylene-Tetrafluoroethylene

FC ..... Fuel Cell

GDE ..... Gas Diffusion Electrode

GDL ..... Gas Diffusion Layer

HAADF ..... High-Angle Annular Dark-Field

hBN ..... Hexagonal Boron Nitride

HDPE ..... High density Polyethylene

HER ..... Hydrogen Evolution Reaction

HFR ..... High Frequency Resistance

HOR ..... Hydrogen Oxidation Reaction

HX ..... Hastelloy

IEC ..... Ion Exchange Capacity

IPA 2-Propanol

KOH ..... Potassium Hydroxide

LDPE ..... Low Density Polyethylene

MEA ..... Membrane Electrode Assembly

OCV ..... Open Circuit Voltage

OER ..... Oxygen Evolution Reaction

ORR ..... Oxygen Reduction Reaction

PEMEL ..... Proton Exchange Membrane Electrolyzer

PEMFC ..... Proton Exchange Membrane Fuel Cell

PGM ..... Platinum Group Metals

PNB ..... Poly(norbornene)

PPD ..... Peak Power Density

Pt-Ir ..... Platinum Iridium

PTL ..... Porous Transport Layer

RDE ..... Rotating Disc Electrode

RTE ..... Round Trip Efficiency

SMR ..... Steam Methane Reforming

SS ..... Stainless Steel

STEM ..... Scanning Transmission Electron Microscopy

THF ..... Tetrahydrofuran

URFC ..... Unitized Regenerative Fuel Cell

WU ..... Water Uptake

CHAPTER 1

INTRODUCTION

Renewable energy sources such as solar, wind and tidal are gaining much attention worldwide due to their ability to generate clean energy, to help with the ambitious aim to reduce global CO_2 emissions. However, due to the intermittent nature of these energy sources, direct dependance on them for prolonged, stable power generation is impractical. Excess energy storage using battery systems is expensive and likely preferred for short-duration (hours to days) storage. Hydrogen generation (by water electrolysis) using excess energy from the renewables is gaining popularity and is becoming hot topic in research, industry and at government levels. Hydrogen is a high energy density carrier (especially in pressurized gas or liquified form) that can be stored underground, transported over long distances and have several applications including energy conversion back to electricity using fuel cells or combustion engines. Moreover, a single compact device may also be used to reversibly store (electrolyzer mode) and generate (fuel cell mode) electricity.

In low temperature water electrolysis, there are two main technologies being used commercially today for hydrogen production. One is the traditional alkaline water electrolyzer (AWE), which is very mature (in use for over 100 years) and being used for large scale hydrogen production. However, these systems have limitations of low current density, low hydrogen discharge pressure and safety issues due to use of highly concentrated KOH. The second electrolyzer technology deployed today is the proton

exchange membrane electrolyzer (PEMEL), which is also quite mature for small scale deployment with a compact design offering advantages of high current density operation and pressurized hydrogen discharge. However, due to its highly corrosive acidic operating environment, PEMELs require the use of expensive platinum group metal (PGM) catalysts and specialized component materials and coatings that add to the overall stack cost. A third technology, the anion exchange membrane water electrolyzer (AEMEL), although quite early in its development, may potentially combine benefits from both AWEs and PEMELs while reducing overall cost of the system. However, there are several challenges and open questions to make this technology commercially viable.

This chapter provides motivation for conducting research on hydrogen technology starting with importance of renewables and their integration with energy storage options. Then there is an overview of existing hydrogen production technologies, a literature review highlighting the limitations, gaps in knowledge and related fundamentals. Then, discussion is progressed to include energy conversion technology (fuel cells) and how the knowledge gained from discrete water electrolyzer and fuel cell systems can be used to develop reversible unitized regenerative fuel cell (URFC) systems. The chapters that follow this one provide in-depth details for research done related to AEMELs, AEMFCs and AEM-URFCs with each chapter focusing on a specific aspect of the underlying system.

1. Significance and recent progress of renewable energy sources

Renewable energy sources such as solar, wind and tidal etc. are gaining much interest in the public and business communities due to their potential role of addressing the issues of fossil fuel depletion and global climate change **[1]**. These renewables are environmentally friendly, clean and critically important for the economic development of

nations **[2], [3]**. These sources are expected to potentially provide net zero carbon and greenhouse gas emissions while fulfilling domestic and global energy requirements **[4], [5]**. Reducing dependance on fossil fuels and widespread use of renewables may require decentralization in the energy sector. Significant growth has been reported in the deployment of photovoltaics (27%) and wind energy (13%), accompanied by a drastic reduction in cost in recent years **[6], [7], [8]**.

The renewable energy sources listed above differ in many ways compared to conventional energy generators, including the need to build small individual modules that are interconnected into systems. They are also non-synchronous with demand and have unpredictable availability and output **[9], [10]**. These variable features may introduce challenges to existing power systems, such as (i) power system performance characteristics can be affected due to the capacity for transmission lines, loss or inadequate generation, (ii) the inability to balance the supply of power to the needs/demand at any given time **[11], [12], [13]**. To achieve decarbonization targets, integration of these renewable energy sources connected to power systems requires technological solutions. Four main factors may cause complications when deciding to implement a technology including, (i) the implicit or explicit costs, (ii) the maturity and technological preferences of policymakers as well as companies, (iii) regulation and control of several actors in deciding new technology implementation, such as utilities, system operators and regulators, and (iv) region or geographic location of the renewable desired powerplant **[14], [15], [16], [17]**. Reliable technologies are essential that convert the output power from renewables to a nonelectrified form that allows for supply and demand to be balanced over all timescales

[18]. One of the promising technologies is to convert excess renewable energy into hydrogen gas (H_2).

1.2 Why use hydrogen for energy storage?

Historically, hydrogen has been a valuable commodity gas and chemical feedstock, and it has potential to become an important fuel and energy storage vector for the energy transition from fossil fuels **[19]**. Hydrogen can be transported to long distances through pipelines, stored underground for long duration and can be used as fuel in transportation or heat generation **[20], [21], [22]**. An overwhelming majority of the hydrogen produced today comes from the steam reforming of fossil fuels, which is emits a significant amount of CO_2 into the atmosphere. However, this is not the only way. Hydrogen can also be produced electrolysis, which can compete with reforming by using cheap energy from renewable energy **[22]**. Figure 1.1 shows an illustration of power from renewable energy sources, including short-term and long-term storage solutions, including the use of electrolyzers and hydrogen storage.

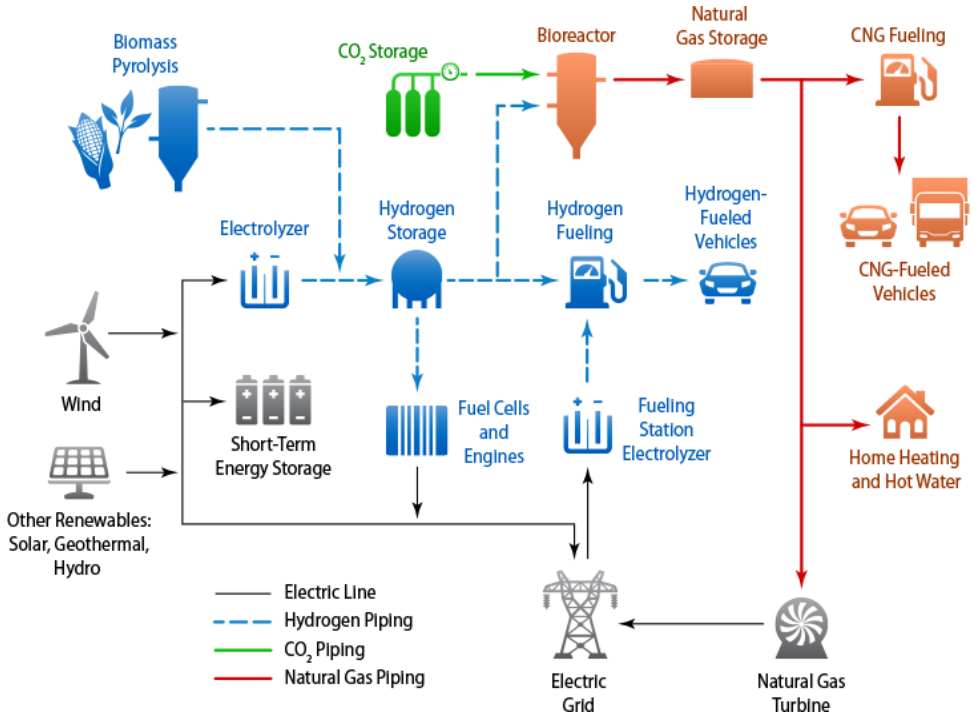

Figure 1.1: Diagram depicting various scenarios for producing renewable hydrogen and electricity. With permission from **[23]**.

It is noteworthy in Figure 1.1 that batteries are specifically illustrated as a short-term solution. This has to do with the mass and volume required for storage as well as cost and the self-discharge rate. Long-term stored hydrogen has a very low self-discharge rate that is linked to its leakage and/or permeation. Long-term hydrogen storage also allows for the decoupling of energy rating from the power rating **[24]**. Hydrogen as an energy carrier may potentially contribute to energy system security and reliability. Moreover, solutions such as power-to-gas and refueling stations for hydrogen-driven vehicles are being proposed for decarbonizing the heating and transport sector, respectively **[25]**. Looking at the exceptional recent growth in renewables and significant cost reductions, low-cost electricity may be advantageous for hydrogen production at times of low electricity demand, the electrolyzer must be capable of flexible, low-capacity factor operation **[7], [18], [22]**.

Present hydrogen production technologies

About 95% of hydrogen today is produced by steam methane reforming (SMR), where water and natural gas are fed into a reactor at high temperature and pressure. Because SMR is endothermic, energy input is required for this reaction to proceed, which is provided by the burning of methane – meaning that CO_2 is not only produced from the reforming, but also reactor heating. This makes SMR one of the largest contributors to man-made CO_2 emissions. The other 5% of commercially produced hydrogen is mostly derived from large AWEs. AWEs apply a voltage to the cell (as opposed to a thermal load) to drive electrochemical water splitting, producing H_2 at the device cathode and O_2 at the anode. A small, but rising, percentage of non-SMR H_2 comes from PEMELs. Though AWEs and PEMELs are both electrochemical technologies, their operating principles are different, as shown in Figure 1.2. They also have distinct pros and cons which are bulleted below.

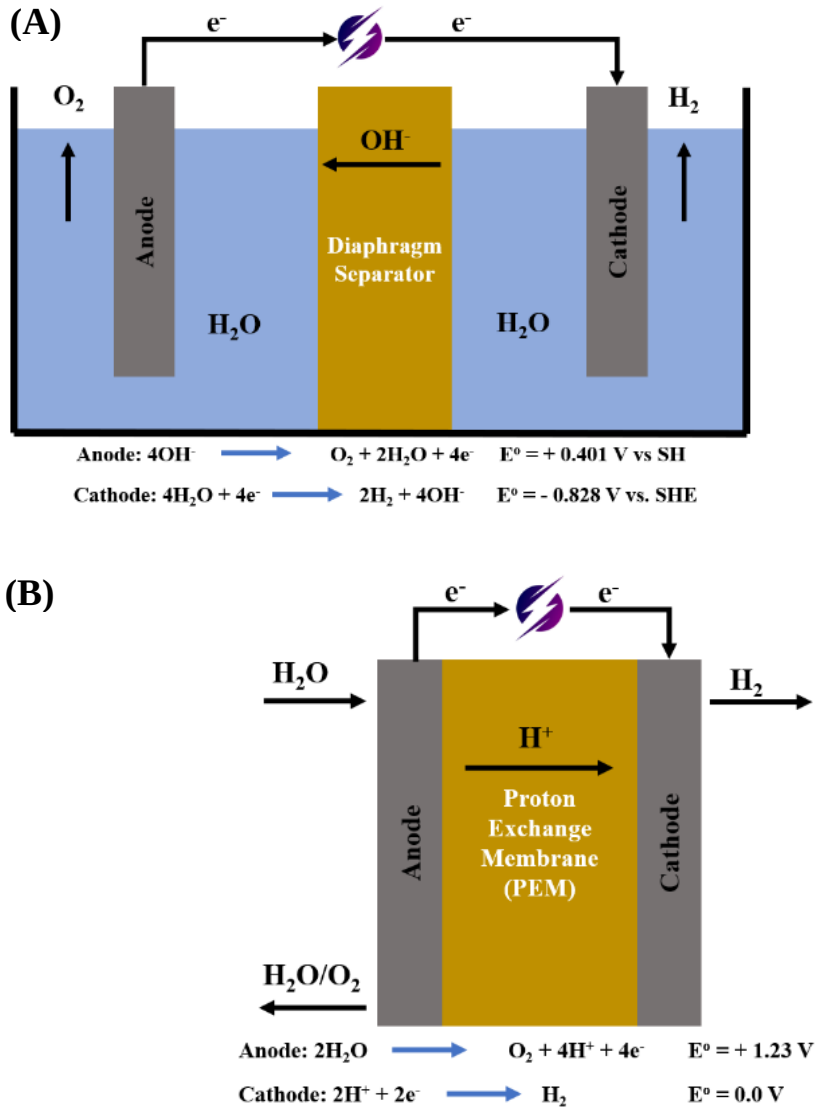

Figure 1.2: Schemtic showing (A). Alkaline water electrolyzer, (B). Proton Exchange Membrane water electrolyzer

Alkaline Water Electrolyzers

Advantages

- Mature technology capable of producing high purity hydrogen
- Wide range of capacities (10 – 1500 Kg H_2 day^{-1}) **[26]**
- Very durable with proven system lifetime of 30–40 years **[26]**

- Low-cost due to use of platinum group metal (PGM) free electrocatalysts and component materials **[27]**
- Large scale hydrogen production **[27]**

Disadvantages

- Low voltage efficiency due to high ohmic losses caused by the use to thick diaphragm separator and bubble formation **[26], [28]**
- Low current density operation in the range of 250-450 mA/cm^2 **[29]**
- Slow response to transient power load
- Material handling due to highly concentrated corrosive liquid electrolyte
- Inability to apply differential pressure to get compressed hydrogen
- Requirement of additional H_2 compressors add extra balance of plant cost

Proton exchange membrane water electrolyzers

Advantages

- Mature technology for small scale hydrogen production systems
- High current density operation offering high voltage efficiency **[30], [31]**
- Fast dynamic response to any change in the power input due to the use of solid polymer electrolyte membrane **[30], [32]**
- High pressure H_2 discharge to end user reducing additional compression requirements **[31]**

Disadvantages

- Highly corrosive acidic operating environment requires specialized electrocatalyst (PGM-based) and component materials with protective coatings

- Generally, titanium based stack components with precious metals coating are used that are more expensive than stainless steel (used in AEWs) **[33]**
- Expensive Nafion-based membranes and ionomers which are also not environmentally friendly as their manufacture requires HF and perfluorinated compounds can be released into the environment over time.

Compared to the AWE and the PEMEL, the anion exchange membrane water electrolyzer (AEMELs) is relatively a new technology that was first introduced in 2012 **[34]**. A simple schematic showing working principle of the AEMEL is shown in Figure 1.3. The AEMEL has gained traction in recent years because it potentially can combine benefits from both AWEs and PEMELs – leading to an economically viable and scalable solution **[35], [36], [37], [38]**. In an AEMEL, the electrode compartments are separated by a thin, dense, polymer membrane, similar to the PEMEL. This anion exchange membrane (AEM) transports hydroxide ions (OH^-) from the cathode to the anode during operation, similar to AWEs, but the system is much more compact. The operating pH of the system reduces corrosion of the component materials, allowing the platinized titanium in the PTLs and bipolar plates to be replaced by cheap stainless steel (SS) or nickel alloys. It is also possible for platinum group metal (PGM) catalysts to be substituted by cheap and abundant materials like iron, nickel, etc. **[37]**, and extensive research is being done to explore PGM-free or lower PGM content materials for efficient water electrolysis.

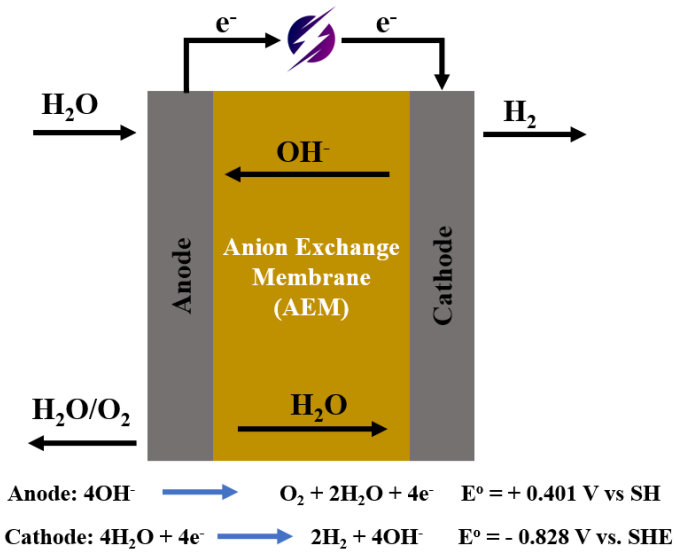

Figure 1.3: Schemtic showing Proton Exchange Membrane water electrolyzer

2. Fundamentals of AEM water electrolysis

In AEMELs, water is reduced at the cathode to form H_2 and OH^- anions through the hydrogen evolution reaction (HER), Equation 1.

$$4H_2O + 4e^- \rightarrow 2H_2 + 4OH^- \qquad E^o = -0.828 \text{ V vs. SHE} \qquad (1)$$

The OH^- ions migrate through the anion exchange membrane (AEM) to the anode where they are oxidized to O_2 and H_2O, Equation 2. Water is involved in both half reactions, though the overall reaction, Equation 3, is identical to PEMELs. At standard temperature and pressure, water electrolysis has a thermodynamic voltage of 1.23 V (V^o, based on ΔG) and a thermoneutral voltage of 1.48 V (V_{TN}, based on ΔH).

$$4OH^- \rightarrow O_2 + 2H_2O + 4e^- \qquad E^o = 0.401 \text{ V vs SHE} \qquad (2)$$

$$2H_2O \rightarrow 2H_2 + O_2 \qquad V^o = 1.23 \text{ V} \qquad (3)$$

If the cell voltage is lower than V^o, no electrolysis occurs and if the cell voltage is greater than V^o but lower than V_{TN}, additional heat energy must be supplied to start the reaction.

In real applications, an activation barrier exists in both electrodes that limits the reaction rate. Therefore, an overpotential (η) is required at both electrodes to drive those reactions, meaning that the operating cell voltage will always be different than the thermodynamic voltage. For electrolyzers, the applied voltage will always be higher than V^o and for fuel cells the operating voltage will always be less than V^o. Additionally, there are resistances from ion transport through the polymer membrane, the electrical circuit and reactant/product mass transport. Hence, the total cell voltage can be expressed as:

$$V_{cell} = V^o - |\eta^a| - |\eta^c| - \eta_\Omega - \eta_{mt} \quad (4)$$

Where η^a is the anode overpotential, η^c is the cathode overpotential, η_Ω is caused by the ionic resistance of the membrane, the electrical resistance of catalyst layers, PTLs, BPs and interfacial resistances between the components, η_{mt} is caused by resistance to fluid transport across the catalyst layer and PTL plus ionic transport in the catalyst layers. Understanding of these individual losses is essential for development and exploration of cutting-edge materials and processes achieving high voltage efficiency.

It should be noted that the actual voltage is always below the thermodynamic voltage. For a galvanic cell, that means that the operating voltage is still positive, but lower in magnitude. For an electrolytic cell, the voltage is lower than the thermodynamic voltage (more negative), but its absolute magnitude is greater. From these values, it is also possible to calculate the thermal efficiency of the cell. Assuming that the energy consumed in the auxiliary equipment is neglected, then the thermal efficiency (ε_{cell}) can be expressed as:

$$\varepsilon_{cell} = V_{cell} / V^o \text{ for a galvanic cell} \quad (5a)$$

$$\varepsilon_{cell} = V^o / V_{cell} \text{ for an electrolytic cell} \quad (5b)$$

There are multiple ways to operate an AEMEL. One possibility is to feed water or an alkaline salt solution (e.g., KOH or carbonates) to the cathode where water is required as a reactant. In this case, the electrochemically active surface area would be lower than desired at the AEMEL anode **[39]**. Also, the wet hydrogen produced would have to be separated from the liquid water, which limits the option for electrochemical compression. A second option is to feed liquid to both electrodes, which has emerged as the most common method in the literature **[40]**. However, the problem of separating the wet hydrogen from the liquid water followed by drying and pressurizing remains. Therefore, the most scalable operation of an AEMEL is to supply the aqueous feed to the anode electrode, as shown in **Figure 1.3**. The presence of water or KOH in the anode does not interfere with the OER; in fact, it can help it. The water diffuses from the anode to the cathode where it is reacted. In this way, facile collection, separation, and pressurization of hydrogen from the cell is possible.

Current state-of-the-art for AEMELs

One of the main AEMEL challenges to achieving high performance at low cost is the development of highly active PGM-free catalysts for both the OER and HER. More work has been done with the OER catalyst, where several classes of materials have been conceived to replace expensive IrOx **[43], [44], [45], [46], [47]**. Hiao and Lu et al., **[56]** used PGM-free catalysts (NiMo in the cathode and NiFeOx in the anode) and a self-made membrane and ionomer to achieve a current density of 300 mA cm^{-2} at 1.8 V. However, the cell was able to operate effectively for only 8 hr. An additional issue with AEMELs is the need for durable, low-cost cell components including porous transport layers (PTL) to make the three-dimensional electrodes. It was recently shown that the PTL with a small

fiber size and smooth surface results in enhanced performance likely due to its large contact area, higher catalyst utilization, and decreased lateral catalyst-layer electrical resistance **[48], [57]**. Similar studies have also been reported on graded-pore structures to improve mass transport in PEMELs **[58]**.

In addition to the catalyst, it is also important to understand how membrane and ionomer properties affect performance **[41], [42]** as well as how electrode design and optimization can be used to increase performance and durability. To help in the design of AEMEL electrodes, Sung et al., **[50]** showed that electrolyzer performance can be improved by optimizing the anode catalyst loading. Additionally, choosing the correct porous transport layer (PTL) is important **[40], [48]** as the PTL geometry, and thermal and electrical properties **[49]** can affect the electrode-level heat, mass, and ion transport **[40], [48]** and hence cell performance and durability. Moreover, additives have been introduced into the catalyst layers **[50], [51]**. Continued improvement of AEMELs requires the development of efficient new materials as well as the systematic design and operation of the anode and cathode electrodes.

Another important aspect of AEMEL operation is the nature of the feed: either pure water or alkaline solution to the system. To simplify the balance-of-plant, and reduce maintenance, it is preferable to operate membrane-based electrolyzers with deionized water (DI) feed. This is already done in PEMELs; however, most of the reported AEMELs in the literature feed carbonate or hydroxide-based electrolytes (although typically at a much lower concentration than in an AWE). The electrolyte feed is used to increase the electrochemically active surface area of the anode electrode where the OER occurs **[39]**. Moreover, the adsorption of metal cations like K^+ can stabilize the transition state of the

water dissociation step in the HER **[59]**. K^+ may also enhance the OER by enabling a lattice oxygen-mediated mechanism **[60]**. When DI water is fed to the cell, the performance typically is lower, with the operating voltage at 1.0 A/cm^2 increasing by 300 mV or more. Some recent studies have reported good AEMEL performance with DI water, achieving 1.0 A/cm^2 below 2.0 V **[53], [54], [61]**. However, DI water feed tests are typically performed by first breaking-in (break-in is used here to describe a startup procedure meant to activate an MEA for stable operation before collecting polarization scans and steady-state performance evaluation) the cell with an aqueous KOH feed, then replacing the KOH with **[54], [61], [62]**. There are also many studies where the protocol to transition from KOH to DI water operation is either poorly described or not described at all. Because residual alkaline electrolyte in the cell can enhance transient activity, it has been previously noted by Lindquist et al., **[63]** that it is very important that all excess salt from feeding KOH is flushed from the cell before claiming DI water operation.

Regarding performance, Wang et al. **[52]** reported a current density of 400 mA/cm^2 at 1.8 V and 50^o C using Pt black as the hydrogen evolution reaction (HER) cathode electrocatalyst and IrOx as the oxygen evolution reaction (OER) anode) electrocatalyst. However, the durability was poor in pure DI water. Li et al., **[53]** utilized a high ion-exchange capacity (IEC) ionomer (3.3 meq g^{-1}) to achieve an operating current of 906 mA/cm^2 at 1.8 V. However, due to high water uptake and solubility of their high IEC ionomer the catalyst was washed away resulting in quite high degradation rates in short term testing, and poor durability in long term testing. Most recently, Yan and coworkers **[54]** reported 1020 mA/cm^2 at 1.8 V in pure water. However, the degradation rate was high at both low current density (0.56 mV/h at 200 mA/cm^2) and intermediate current density

(1.81 mV/h at 500 mA/cm^2). In fact, the degradation rates for AEMELs are presently much higher than PEMELs, ranging from 0.1-2 mV/h **[53]** while PEMELs have degradation rates that typically range from 2-10 µV/h **[55]**. Therefore, the AEMEL remains a relatively new technology and a significant improvement is needed to achieve high performance and durability.

AEM water electrolysis - limitations and gaps in knowledge

Despite the remarkable recent progress that has been made in AEMELs, there are still many challenges and a lack of knowledge to realize the true potential of this technology. AEMELs still have lower-than-desired thermal efficiencies and durability, which limits their ability to displace incumbent AWEs and PEMELs. Most of the reported AEMELs make use of PGM based materials, concentrated alkaline KOH feed and have limitations in polymers materials employed. There are several aspects related to the design and operation of AEMELs that need to be further studied to overcome these issues. Some are addressed later in this thesis and others are being investigated by other researchers around the world. They are:

<u>Electrocatalysis</u>

The anode electrode typically uses Ir based catalysts while Pt-based catalysts are used for making the cathode. Although several types of PGM-free electrocatalysts have been tried, they show relatively lower performance and durability – particularly at the cathode. Alternate efficient PGM-free catalyst materials are needed with proven durability in the system.

Anion exchange membranes and ionomers

Currently, the polymer membranes being used in AEMELs have lower conductivity than desired and also suffer from H_2 crossover. Their anion conductivity along with mechanical properties need to be improved for higher voltage efficiency and durability. Moreover, the ionomeric binders should be designed for efficient water and ion transport while maintaining mechanical strength of catalyst layer.

Porous transport layers (PTLs)

Due to higher cell potential at high pH, carbon based PTLs cannot be used in the anode. Alternate materials with better electrical, thermal, and physical properties PTLs need to be explored for efficient water, electron and gas transport.

Flow field/bipolar plates

Cost effective alternate materials are required for fabrication of bipolar plates with efficient flowfield designs. Surface passivation over time increases Ohmic losses and increases the voltage degradation rate. Materials resistant to alkaline environment with protective coatings are needed for large scale commercial deployment of AEMELs.

Operating conditions

Further studies are needed to evaluate the advantages and disadvantages of alkaline feed vs pure water and weigh economical aspects for long-term operations. Moreover, electrolyzers are operated at lower temperature due to limitations in polymer membranes and ionomers. Additional studies are needed to explore the effects of higher temperature operation highlighting pros and cons with control strategies. Lastly, in-depth studies are needed to demonstrate pressurized cell operation.

3. Energy conversion - AEM fuel cells

A fuel cell is an energy conversion device that can directly convert the chemical energy of hydrogen or other fuels into electricity. With pure hydrogen as an input fuel, the only products are electricity, water, and heat. Fuel cells can be used in a variety of applications including stationary power generation, transportation, and small electronics. A polymer electrolyte membrane fuel cell has a very similar construction to polymer electrolyte membrane electrolyzer, but is operated in reverse. Oxygen and hydrogen are consumed and water is created. A fuel cells works like a battery that will never stop as long as H_2 and O_2 are supplied.

A polymer electrolyte membrane fuel cell consists of a polymer membrane, an anode and a cathode, all sandwiched between two flowfield plates. There are two types of polymer electrolyte fuel cells, the proton exchange membrane fuel cells (PEMFC) and the anion exchange membrane (AEMFC). Though their overall reactions are identical, they differ in their medium of operation and operating priniples. Figure 1.4 shows the working principles for both PEMFCs and AEMFCs. The operating environment in PEMFCs is acidic due to generation of protons (H^+) on the anode side which travel through the Nafion^{TM} cation exchange membrane to the cathode side where they react with O_2 (and electrons) to produce water. In AEMFCs, oxygen is reduced with water at the cathode to yield OH^-. These hydroxide ions travel through the AEM to the anode where they react with H_2, releasing water.

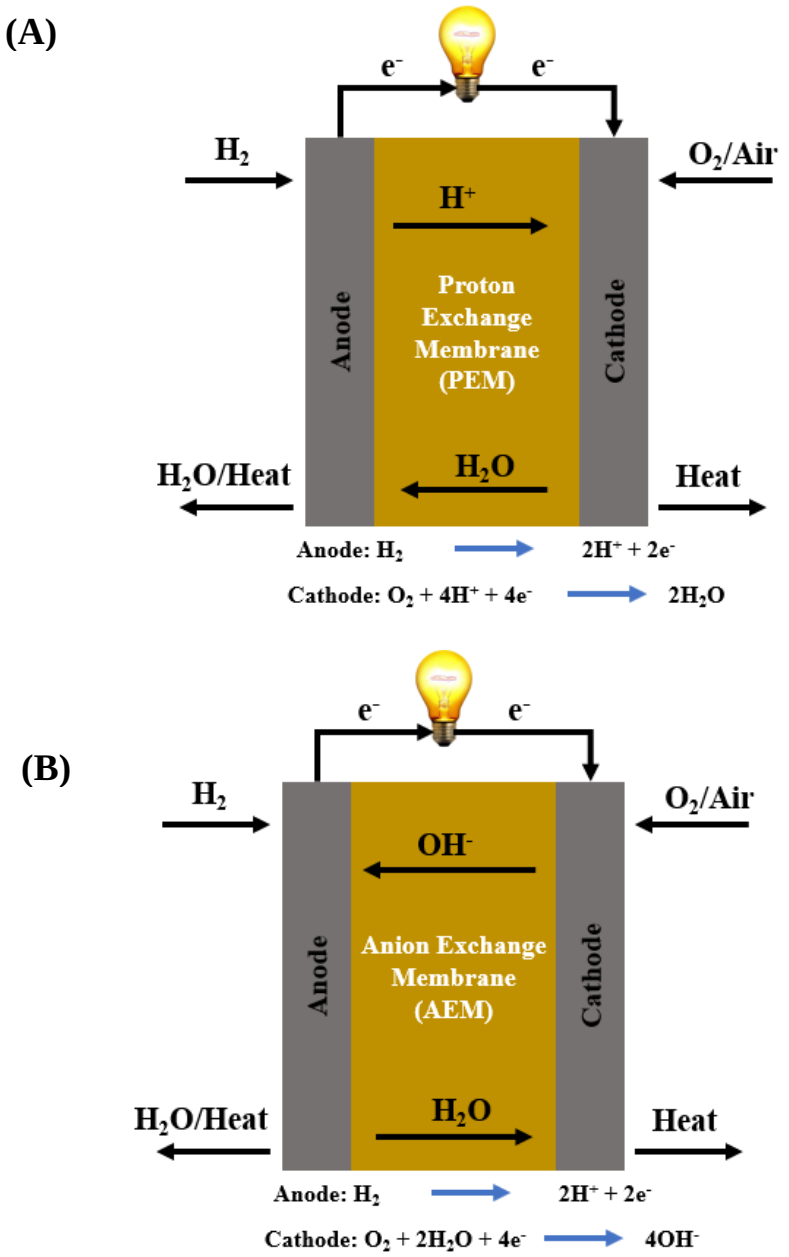

Figure 1.4: Schemtic showing the operating principles of, (A). Proton Exchange Membrane fuel cell, (B). Anion Exchange Membrane fuel cell

In PEMFCs, almost 50% of the system cost comprise of stack cost as shown in Figure 1.5. Due to highly corrosive acidic working media, PEM fuel cells require the use of PGM based electrocatalysts, graphite-based bipolar plates (BPs) and stack components with protective coatings to avoid corrosion / stack degradation. These are all expensive,

making it very challenging (if not impossible) for PEMFCs to meet DOE stack-level and system-level cost targets for widespread commercialization.

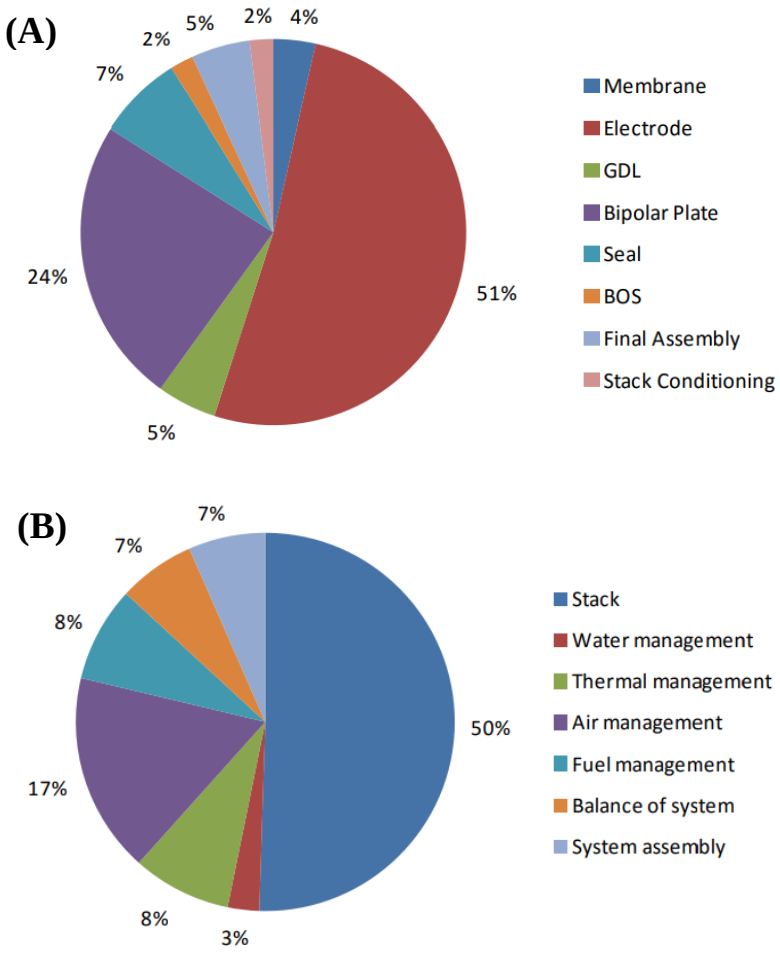

Figure 1.5: Costs of an 80-kW net PEM fuel cell stack system (A) Stack costs; (B) stack system costs **[47]**.

To alleviate these costs, anion exchange membrane fuel cells (AEMFCs) have recently emerged as an alternative to PEMFCs. The higher pH operating environment offers several advantages such as lower material and manufacturing costs. For example, AEMFCs can use platinum group metal (PGM) free cathodes, have more facile oxygen reduction kinetics **[66], [67]** and may enable a wider range of fuels (e.g. methanol,

hydrazine). However, there are several challenges yet to be overcome to advance this new technology.

Current state-of-the-art AEMFCs

Early AEMFC development suffered from very low overall performance and durability **[68], [69]**. From a durability perspective, cells were mostly believed to be limited by chemical degradation of the anion exchange membrane (AEM) and ionomer at high pH. Because of this, there was a significant financial investment targeting the design and manufacturing of stable AEMs and ionomers. As a result, several AEMs have been shown to be stable both at elevated temperature ($\geq 80^{o}$C) and pH for hundreds or even thousands of hours during ex-situ testing **[70], [71], [72]**.

Another issue that has started to be addressed in the AEMFC literature is water management. As mentioned above, water is formed at the AEMFC hydrogen anode and consumed at the oxygen cathode. As water is produced at the anode, it must be removed to avoid flooding – either through the anode gas stream or, preferably, through the AEM to the cathode (via back-diffusion) where it is needed to react **[73]**. If too little water is supplied to the cathode by diffusion it can dry out; if more water arrives to the cathode than can be reacted, it is also possible for the cathode to flood. Therefore, there is a need for both the anode and cathode catalyst layers to be able to passively transport water. The ability of the ionomer in the catalyst layer to facilitate such ion transport is related to the overall hydrophilicity of the monomers used in the polymer membranes and ionomer. One example where ionomer water uptake has been limiting is the well-known ethylene-tetrafluoroethylene copolymer (ETFE) based powder ionomer **[74]**. Though the ion exchange capacity (IEC) of that material is modest (only 1.24 meq/g), recent work has

found that its water uptake was very large, and the high water content of the AEMFC anode resulted in excessive electrode swelling, **[75]**, which blocked the catalyst sites and hindered gas transport, resulting to lower cell performance in fully humidified cells **[76]**. One of the ways that the amount of water in the electrodes can be reduced and avoid swelling is to lower the relative humidity of the feed gases during AEMFC operation and rely on convective evaporation to remove excess anode water **[77]**. Another method to mitigate electrode swelling is to reconfigure the electrode composition and architecture. For example, Yang et al., **[78]** showed that ionomer content plays a significant role in activation, ohmic and mass transport losses within the cell. Later, Omasta et al., **[79]** optimized the ionomer:carbon:catalyst ratio of an AEMFC anode catalyst layer, finding that having increased void space in the catalyst layer can improve performance and operational stability, likely by being able to accommodate swelling. Recently, Truong et al., **[80]** and Peng et al., **[75]** have shown that adding a hydrophobic agent (PTFE) into the catalyst layers can improve both performance and stability.

Wang et al. **[111], [112]** reported radiation-grafted low-density polyethylene (LDPE) as well as high density polyethylene (HDPE) anion exchange membranes in fuel cell assembly comparing their performance on H_2/O_2 fuel. They achieved 2.01 W/cm^2 peak power density (PPD) at 80 C using LDPE membranes and demonstrated 27% increase in peak power density (2.55 W/cm^2) using HDPE membranes with enhanced water transport. Cha et al. **Error! Reference source not found.** reported poly(carbazole)-based anion e xchange membranes performance, in fuel cell assembly and compared with commercially available FAA-3-50 membranes. They observed high peak power density of 1.61 W/cm^2 at 60 °C using PtRu/C and Pt/C as anode and cathode catalysts, respectively while only

0.738 W/cm^2 was achieved when poly(carbazole)-based membrane was replaced by FAA-3-50 membrane, tested with same conditions. Recently, record high fuel cell peak power density on H_2/O_2 was reported by Peng et al. **Error! Reference source not found.**, using P oly(norbornene) based membranes and ionomers in AEM fuel cells achieving PPD of 3.4 W/cm^2. Despite of these impressive PPD demonstrations, very few studies have shown up to 1000 hours of durability and still had higher degradation rates.

Limitations and perspective

To advance AEM fuel cell technology, further performance and life-time enhancement is necessary. Very few studies have been conducted to understand degradation mechanisms, however, new performance loss mechanisms may be present in AEMFCs that are not yet documented or understood. To move AEMFC technology forward, it is important to identify the relevant degradation mechanisms and understand the extent to which the corresponding performance losses are reversible (e.g., driven by sub-optimal operating conditions) or irreversible (e.g., from material or interface degradation). Such information may enable appropriate methods for minimizing their effects to be developed. Moreover, Department of Energy (DOE) has outlined performance targets for AEM fuel cells which provide a pathway for development of this technology **[81]**. Following areas need immediate attention to address the challenges to advance AEMFC technology.

Electrocatalysis

AEMFC anode typically employs Pt or bimetallic PtRu supported on carbon catalysts while Pt-based catalysts are used for making the cathode. Due to complex water management and sluggish HOR, very few PGM-free electrocatalysts have been reported

for anode electrode, and yet show very poor activity and durability in MEA evaluation. On cathode side, several PGM-free options have been tried, however, they show relatively lower performance and durability. Alternate efficient PGM-free catalyst or low loading PGM electrode development strategies are needed with proven durability in the system.

Anion exchange membranes and ionomers

Several types of polymer membranes are being used in AEMFCs, however, AEMs are thicker with high HFR, lower conductivity than desired and suffer from H_2 crossover. Thinner membranes offering higher anionic conductivity along with improved mechanical properties need to be explored for higher voltage efficiency and durability. Moreover, the ionomeric binders should be designed manipulating their characteristic properties suitable for efficient water and ion transport while maintaining mechanical strength of catalyst layer.

Flow field/bipolar plates

AEMFCs typically use graphite-based BPs, however, they are costly. Cost effective alternate materials are required for fabrication of bipolar plates with efficient flowfield designs. Use of metal-based BPs in alkaline media, will introduce surface passivation issues over time increasing Ohmic losses and increase the voltage degradation rate. Less expensive, earth abundant, easy to manufacture materials which are resistant to alkaline environment with protective coatings are needed for large scale commercial deployment of AEMELs.

Operating conditions

Several contributions have been reported to address water management through operating conditions, such as gas dew points, flow rates and backpressure etc. Very precise controls have been suggested for optimal performance and long-term durability which may add extra balance-of-plant cost. Moreover, membrane / electrode dry-out events introduce accelerated degradation rates at higher operating temperatures. Further studies are needed to evaluate the advantages and disadvantages of higher temperature operation with flexible operating conditions.

4. AEM – Regenerative reversible fuel cells

A unitized regenerative fuel cell (URFC) can combine the functionalities of both electrolyzer and fuel cell into a single device, enabling lower weight, volume, and capital cost. A URFC can serve as an energy storage device (via water electrolysis) to store excess electricity in the form of hydrogen during peak production times. This is particularly attractive from intermittent renewable energy resources like solar, wind, tidal, etc. **[83], [84]**, where a large amount of storage may be needed and traditional batteries would require a very large footprint. URFCs can also function as an energy conversion device (fuel cell mode) that generates electricity from the stored hydrogen and oxygen (either co-stored from electrolysis or from air). URFCs can be a high energy storage capacity, low cost, simple, compact, and environmentally friendly technology with advantages over conventional energy storage technologies **[85], [86], [87]**. Because of this, URFCs have received an increased amount of research attention in recent years.

There are two configurations for a URFC to operate. The first configuration is constant-gas (CG) where hydrogen and oxygen are always fed/collected to/from the same electrode. The second configuration is a constant electrode (CE) configuration where the positive and a negative electrode are held constant (meaning that the H_2 electrode in the fuel cell mode is the O_2 electrode in electrolyzer mode). These two configurations are illustrated in Figure 1.6.

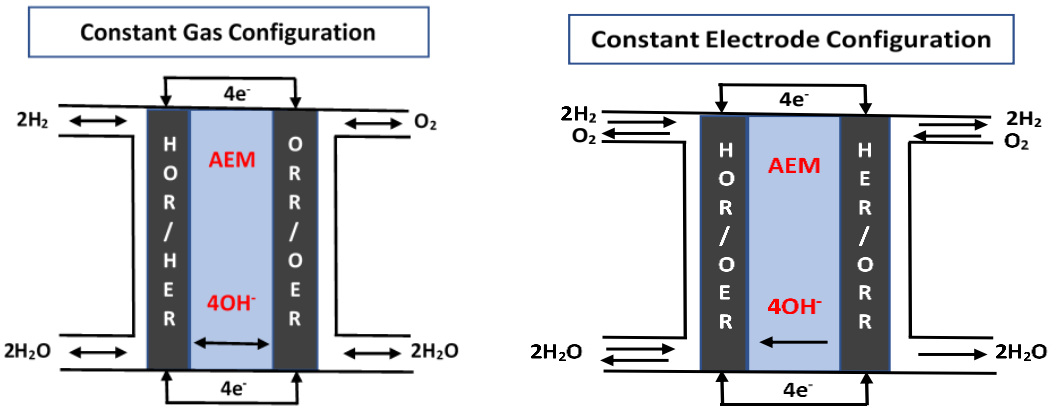

Figure 1.6: Schematic showing two configurations for a URFC operation. Adapted from Error! Reference source not found.

Both CG and CE modes have their distinct advantages and disadvantages. The CE configuration operation allows the separation of ORR and OER to different electrodes, providing enhanced electrode design for gas/liquid diffusion layers to achieve better cell efficiency. The disadvantages arise from a wider range of operating potentials for both electrodes, which might lead to faster materials degradation, and the potential risk of mixing H_2 and O_2 in flammable stoichiometries when switching between fuel cell and electrolyzer modes. CG mode avoids the risk of mixing of H_2 and O_2 /air, favorable to quick switching between charge/discharge sequence. However, liquid water purging between charge and discharge would still be required. On the negative side, since we

combine two limiting reactions (ORR and OER) on the same electrode of the cell, the design suffers from cell inefficiencies. In either configuration, bifunctional electrodes are essential for AEM-URFC operation, which would introduce complex electrode design compared to traditional discrete fuel cell and electrolyzer devices.

Current state-of-the-art AEM-URFCs

PEM based URFCs have been extensively studied covering range of bifunctional catalysts, component materials and operating conditions. Table 1.1 provides an overview of the state-of-the-art PEM based URFCs which would help to compare works related to AEM-based URFCs, highlighting knowledge gaps and opportunities for development of this technology.

Table 1.1: Recent developments in PEM based URFCs reported in literature

OER/ORR	**HOR / HER**	**Electrolyte**	**Temperature**	**Round-trip-efficiency**	**Reference**
Pt-IrO2 (1:1 wt ratio)	Pt	Nafion 115	80 °C	40.9% at 400 mA/cm^2	Shao et al. **[92]**
Pt-IrO2 (10-30 mol% IrOx)	Pt	Nafion 115	80 °C	42% at 500 mA/cm^2	Ioroi et al. **[93]**
Pt-IrO2 (20 at% IrOx)	Pt	Nafion 115	80 °C	44% at 500 mA/cm^2	Ioroi et al. **[94]**
Pt-IrO2 (10 at% IrOx)	Pt	Nafion 115	80 °C	50% at 200 mA/cm^2	Ioroi et al. **[95]**
Pt-Ir (1:1 wt ratio)	Pt	Nafion 1135	80 °C	46% at 500 mA/cm^2	Yim et al. **[96]**
Pt-Ir (99:1 wt ratio)	Pt	Nafion 1135	80 °C	47% at 500 mA/cm^2	Yim et al. **[97]**
Pt-IrOx (1:1 wt ratio)	Pt	Nafion 115	Room Temp	30% at 200 mA/cm^2	Cruz et al. **[98]**
Pt-IrOx	Pt/C	Nafion 1135	80 °C	44.2% at 500 mA/cm^2	Chen et al. **[99]**
Pt-IrOx	Pt/C	Nafion 1035	80 °C	42.1% at 800 mA/cm^2	Chen et al. **[100]**
Pt-Ir	Pt	Nafion 1135	Room Temp	35% at 100 mA/cm^2	Patterson et al. **[101]**
Pt-Ir (85:15 at. Ratio)	Pt	Nafion 115	80 °C	46.5% at 500 mA/cm^2	Ioroi et al. **[102]**

Pt-Ir (85:15 wt % ratio)	Pt	Nafion 115	80 °C	49% at 500 mA/cm^2	Jung et al. **[103]**
Pt-Ir mixture	Pt	Nafion 115	80 °C	53% at 1000 mA/cm^2	Peng et al. **[104]**

It should be noted that, PGM-based catalyst materials are essentially required for PEM-based URFCs to operate the system. Moreover, stack components such as BPs and PTLs require protective coatings (usually PGM based metals) to prevent corrosion and degradation of the cell components adding huge overall stack cost. Moreover, these systems still show lower efficiencies and higher degradation than desired.

AEM-based URFCs can potentially employ PGM-free electrocatalysts, cheap earth abundant stack component materials reducing overall system cost. To provide a quick overview of recent work on AEM-based URFCs, Table 1.2 summarizes state of the art AEM-URFCs.

Table 1.2: Recent works on AEM-based URFCs reported in literature

H_2 Electrode	**O_2 Electrode**	**Membrane**	**Op. Temp.**	**Round-trip efficiency**	**Stability / Durability**	**Ref.**
Pt / C	$Cu_{0.6}Mn_{0.3}Co_{2.1}O_4$	Customized	40 °C	31.9% at 100 mA/cm^2		Wu et al **[105]**
Pt / C	$Cu_{0.6}Mn_{0.3}Co_{2.1}O_4$	Porous PTFE filled with qPDTB-OH^-	20 °C, 45 °C	34% at 100 mA/cm (22 °C)	Degradation rate of 0.0379 mV/h at 100 A/cm^2 in EC mode for the first 120 h (22 °C)	Wu et al **[106]**
Ni / C	NiC + MnOx	FAA-3, Fumatech	65 °C	40% at 10 mA/cm^2	RT-efficiency dropped	Ng et al **[107]**

					from 40–34% after 8 cycles (160 mins)	
Pt / C	MnOx	FAA-3, Fumatech	55 °C	42–45% at 20 mA/cm^2	Quite stable for 10 cycles, with Rtefficiency dropped from 45–42%.	Ng et al **[108]**
Pt / C	$LaSr_3Fe_3O_{10}$	A201, Tokuyama	60 °C			Takeguchi et al. **[109]**
$LaNi_5$	$La_{0.6}Ca0.4CoO_3/C$	Tokuyama, A3PE		52% at 0.1 mA/cm^2	Very stable in WE mode at 1 mA/cm^2 and in FC mode at 0.5–2 mA/cm^2	Bretthauer et al. **[110]**

It can be noted that PGM-based as well as several PGM-free bifunctional electrocatalysts have been tried for both electrodes. However, AEM-URFCs still suffer from low round trip efficiencies, even at very low current densities. They also show poor cyclic durability. Therefore, there is an essential need to demonstrate higher efficiencies with lower cyclic degradation comparable to PEM-based URFCs using standard PGM-based materials. Also, to realize the true promise of AEM-URFCs, PGM-free bifunctional catalysts and cheap component materials be explored demonstrating promising results to advance this technology.

AEM-URFCs – limitations and perspective

Looking at the available literature reports, it is appropriate to say that AEM-URFCs have shown lower operating current densities and higher degradation rates than its counterpart PEM-URFCs. This is true in the case of PGM-based catalysts that have been carried over from PEM-URFCs. At the oxygen electrode, the ORR and OER require different active sites since their rate determining steps (RDS) and the electrocatalyst surfaces are completely different under ORR and OER conditions **[88], [89]**. In PEM-URFCs, this has been mostly accommodated by mixing Pt and Ir, the most stable and mature catalysts for ORR and OER, together in one electrode. This allows them to be operated as a mixture of their base metals (in FC mode) and oxides (in electrolyzer mode) in traditional URFCs **[90], [91]**. These bimetallic composites of Pt-Ir have been shown to efficiently enable both OER and ORR on the same electrode **[31], [32]** in PEM-URFCs. This approach should be repeated for AEM-URFCs, then efforts should be transitioned to PGM-free catalysts.

5. Outlines for next chapters

In this chapter, a case was made for using H_2 as an energy carrier in the future. One possible family of electrochemical devices that can facilitate the use of H_2 in the future are anion exchange membrane based devices like the AEMEL, AEMFC and AEM-URFC. This thesis details progress that has been made at the University of South Carolina with each of these devices. Of particular note are advances in cell performance and durability through electrode component design and operating condition optimization.

Chapter 2 will discuss hydrogen generation using AEMELs. It will provide comprehensive electrode optimization for an efficient oxygen evolution reaction electrode.

Four electrode parameters are systematically studied and optimized: catalyst loading, catalyst chemistry, PTL type and inclusion of a conductive additive in the OER catalyst layer. The influence of each factor is elucidated through a design of experiments (DoE) approach with a full statistical analysis. The DOE factorial analysis allows rational design of future generations of the anode electrode, including predictions for output voltage response with response validation. Important insights about systems voltage response corresponding to the input parameters were achieved.

Chapter 3 primarily probes the transition of AEMEL initial operation with KOH to true DI water operation. This was achieved through a combination of experiments. During the transition, polarization curves were collected, and electrochemical impedance spectroscopy (EIS) was performed to understand the system behavior in different alkaline conditions. This study compares prospects of electrolyzer operation on pure water vs. different concentrations of alkaline solution (KOH) highlighting the performance losses. This leads to new guidelines for the field to use to ensure that they are operating on pure DI water in their experiments. This chapter also discusses the advantages and disadvantages of breaking-in cells using alkaline feed vs pure DI water with a focus on degradation issues during operation.

Chapter 4 is an in-depth investigation of PTLs, one of the AEMEL stack components contributing the most to voltage efficiency and overall cost. This chapter makes definitive links between the PTL material, porosity, structure, and fabrication process and performance. This study was intended to fill the gaps in the literature and to make the needed definitive links by investigating a series of anode PTLs that cover a

spectrum of materials, fabrication processes, physical structure, and electrical properties. The contents of this chapter provide new design guidelines for cell manufacturers.

Chapter 5 aims to improve the performance and durability of AEMFCs by investigating three poly(norbornene) based ionomers with different IEC, molecular weight, dispersity, and water uptake. These ionomers were integrated into operating AEMFCs with symmetric (same ionomer in both catalyst layers) and asymmetric (different ionomers in the anode and cathode catalyst layers) electrode configurations. The in-depth understanding of ionomer properties developed in this work resulted in highly efficient and durable AEM fuel cell system. This work highlights the balance between ionic conductivity, hydrophobicity and morphology (molecular weight) of ionomers which are essential for high-performance and long-term stability in AEM fuel cells and other electrochemical devices.

Chapter 6 investigates degradation phenomena occurring during 150-day (3600 hour) continuous AEMFC operation through a combination of electrochemical experiments and post-mortem membrane electrode assembly (MEA) assessment using high resolution imaging. The behavior of the beginning of life (BOL) and end of life (EOL) cells were investigated by electrochemical impedance spectroscopy (EIS), high resolution microscopic imaging and elemental analysis. This work provides interesting insights about catalyst layer structure, the behavior of ionomer and membrane, and the sources and solutions for reversible vs. irreversible voltage loss in operating cells.

Chapter 7 transitions moves to the development of AEM-URFCs. This chapter provides a detailed analysis of two electrode designs where one configuration resulted in outstanding efficiency with very low degradation using PGM-based catalysts (traditional

Ir and Pt metals). Subsequently, the optimal electrode design was used to demonstrate reasonably good performance and cyclic durability using PGM-free catalyst materials (cobalt-based), moving the technology towards its true promise of AEM-based URFC systems.

Chapter 8 summarizes the important findings of this work and suggests opportunities for future studies related to all three technologies.

CHAPTER 2

UNDERSTANDING AND IMPROVING ANODE PERFORMANCE IN AN ALKALINE MEMBRANE ELECTROLYZER USING STATISTICAL DESIGN OF EXPERIMENTS[1]

Abstract

The behavior of the oxygen-evolving positive electrode (i.e. anode) in the anion exchange membrane water electrolyzer (AEMEL) is complex and influenced by several factors. Very few studies have been performed to understand oxygen evolution reaction (OER) behavior by optimizing the individual factors that influence performance. This study highlights the effects of catalyst loading, catalyst selection, porous transport layer (PTL) type and conductive additive content. The influence of each factor is elucidated through a design of experiments (DoE) approach with a full statistical analysis. Electrochemical data, alongside Pareto charts, parametric trends and their mutual interactions are discussed. This DoE approach is also helpful in making useful predictions and discovering new combinations to be tested. The end result was a high-performance

---

[1]Hassan, N.U., Mandal, M., Zulevi, B., Kohl, P.A. and Mustain, W.E., Understanding and improving anode performance in an alkaline membrane electrolyzer using statistical design of experiments, *Electrochimica Acta,* **409,** 140001 (2022).

AEMEL able to operate at a current density of 1.0 A/cm^2 at 1.80 V with IrOx OER and PtNi hydrogen evolution reaction (HER) catalysts using 0.3 M KOH fed to the anode. Even lower operating voltage was observed with PbRuOx catalyst at the anode, 1.64 V @ 1.0 A/cm^2, though the cell decay rate was higher. Lastly, a IrOx/PtNi cell was stably operated continuously for 30 days (720 hours) at 1.0 A/cm^2. This study can serve as a guide for optimal electrode design with insights into component-performance compromises, which can aid in making design choices and performing techno-economic analyses.

1. Introduction

Significant progress has been made in reducing the cost of wind energy and solar photovoltaics, but their intermittent nature requires local energy storage to balance energy supply and demand **[115]**. Therefore, to maximize the benefits of renewable energy from the sun and wind, technologies are needed to transfer their output to non-electrified energy storage. Hydrogen can be produced from on-demand electricity, which can be stored underground for months **[116],** transported through pipelines **[117]**, and used as a chemical feedstock for combustion or transportation fuel **[118]**. Hydrogen has a variety of industrial applications including chemical production, refining, metallurgy, and glass and electronics manufacturing **[119]**. Today, hydrogen is primarily made from methane steam reforming (MSR), which contributes to carbon dioxide pollution and global warming. Low temperature electrolysis has the potential to drive future growth and eliminate greenhouse gas emissions **[118]**.

To compete with MSR, electrolyzers benefit from low-cost electricity, which is coming closer to reality **[118]** , **[120]**, and low capital cost. Because of this, the most common commercial solution today is the alkaline electrolyzer (AEL). In the AEL, nickel-

based electrodes are used at an intermediate operating temperature (e.g., 150-200 ^{o}C) with a liquid KOH electrolyte that is imbedded into a porous glassy diaphragm (e.g. Zirfon®). However, AELs have drawbacks including: (i) the need to pump highly corrosive KOH in a production facility, which is a safety, cost and corrosion concern; and (ii) the operating current density is typically relatively low (e.g., a few 100 mA/cm^2) making the stack and system relatively large per quantity of hydrogen produced. Proton exchange membrane electrolyzers (PEMELs) have been steadily advancing and have emerged as a promising alternative to AELs. PEMELs operate in a solid polymer acid environment and use a proton exchange membrane for gas separation and electrochemical compression of the hydrogen. Electrochemical compression is enabled in PEMELs by use of a robust membrane and requires less energy than mechanical compression at high pressures. Modern PEMEL systems have several desirable attributes compared to AELs, such as higher operating currents (~2 A/cm^2), more compact design and eliminating the need for concentrated KOH. However, PEMEL technology is expensive due to the need for platinum-based electrocatalysts, the high-cost of perfluorinated membranes, and the need to use component materials that are stable in a highly acidic operating environment **[118], [121], [122]**.

The anion exchange membrane electrolyzer (AEMEL) is a relatively new technology that seeks to combine the advantages of AEL and PEMEL technology to offer a low-cost option with compact design and high current density operation **[118], [121], [122]**. To produce H_2, water is reduced at the cathode to form H_2 and OH^- anions through the hydrogen evolution reaction (HER), **Equation 1**.

$$4H_2O + 4e^- \longrightarrow 2H_2 + 4OH^- \quad E^o = -0.828 \text{ V vs. SHE} \qquad (1)$$

The OH^- ions migrate through the anion exchange membrane (AEM) to the anode where they are oxidized to O_2 and H_2O, **Equation 2**. Water is involved in both half reactions to split water to into H_2 and O_2, **Equation 3,** with a standard potential (V^o, based on ΔG) as well as its thermoneutral voltage (V_{TN}, based on ΔH).

$$4OH^- \longrightarrow O_2 + 2H_2O + 4e^- \qquad E^o = 0.401 \text{ V vs SHE} \qquad (2)$$

$$2H_2O \longrightarrow 2H_2 + O_2 \qquad V^o = 1.23 \text{ V} \qquad (3)$$

Despite the straightforward overall operating principles of the cell, there are multiple ways to operate an AEMEL. One possibility is to feed water or an alkaline salt solution (e.g., KOH or carbonates) to the cathode where water is a reactant. However, doing so results in a lower than desired electrochemically active surface area at the AEMEL anode **[123]**, and having to separate the wet hydrogen produced from liquid water, which limits the option for electrochemical compression. A second option is to feed liquid to both electrodes **[124], [125]**. In fact, feeding the liquid electrolyte to both sides has emerged as the most common method in the literature **[124]**. However, the problem of separating the wet hydrogen from the liquid water followed by drying and pressurizing remain. Therefore, the most scalable operation of an AEMEL is to supply the aqueous feed to the anode side, as depicted in **Figure 2.1**. Doing so allows for facile collection, separation, and pressurization of hydrogen from the cell.

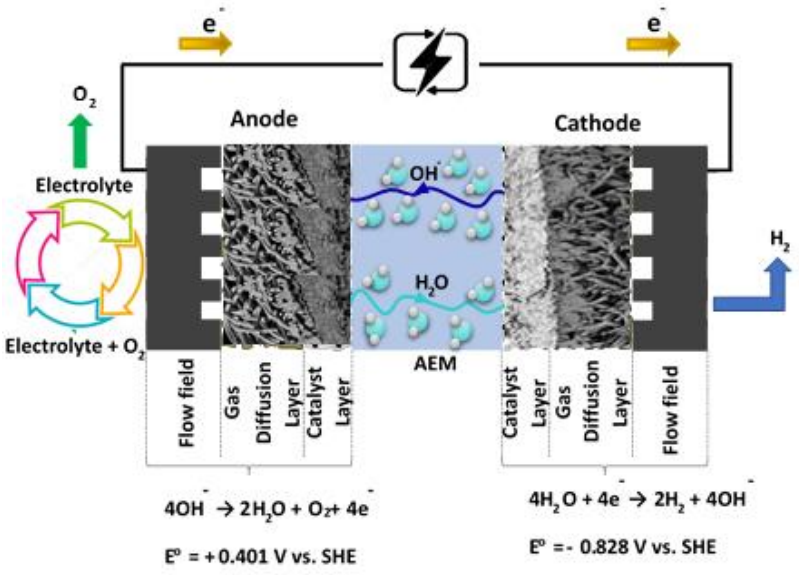

Figure 2.1: Schematic of an AEMEL operating with the liquid phase being fed only to the anode side. In the diagram, the transport of water and OH^- are particularly noted in order to highlight the need for water diffusion from the anode to the cathode, which is in the opposite direction of electro-osmotic drag (adapted from **[126]**.

Despite offering several possible advantages, AEMELs have many challenges to overcome. In fact, the first AEMEL was reported in the literature in 2012, less than a decade ago **[127]**. Significant progress has been made and a few of the recent impactful works are highlighted here to show the present state-of-the-art performance and remaining challenges. Kim et al., **[128]** demonstrated that high local pH is critical for efficient OER and HER. They were able to increase the effective pH of the electrodes by developing highly quaternized polystyrene ionomers with high IEC and increasing ionomer content. Using TMA-53 bonded MEAs, they were able to achieve an operating voltage of ~1.8 V and current density of 1.0 A cm^{-2} at 60 ^oC while circulating 0.1 M KOH electrolyte. Unfortunately, despite the promising transient performance, the durability of these cells was generally poor. Yan and coworkers **[129]** reported a high performing AEMEL operating on deionized water feed using a PGM-free OER electrode. Their AEMEL was able to achieve 1.0 A/cm^2 at 1.8 V and 80 ^oC. However, one issue was that the cell

degradation was high and increased with current density. The degradation rate of the cell was 1.81 mV/h at an operating current of 500 mA/cm^2. High degradation rates are not uncommon when operating modern AEMELs with DI water, making it important to study the design and performance of cells fed with dilute salt solutions so that long-term solutions can be found.

Although many of the efforts have advanced AEMEL performance, very few studies have focused directly on electrode design and optimization. This includes our previous studies **[140], [141]** where the focus was understanding how the ionomer characteristic properties (water uptake, conductivity, etc.) affected the AEMEL performance. Additionally, researchers have explored a variety of OER catalyst materials to replace expensive IrOx **[133], [134], [135], [136], [137]**. To help in the design of AEMEL electrodes, Sung et al., **[130]** showed that electrolyzer performance can be improved by optimizing the anode catalyst loading. Additionally, choosing the correct porous transport layer (PTL) is important **[124], [131]** as the PTL geometry, and thermal and electrical properties **[132]** can affect the electrode-level heat, mass, and ion transport **[124], [131]** and hence cell performance and durability. Moreover, additives have been introduced into the catalyst layers **[138], [139]**. Continued improvement of AEMELs requires the development of efficient new materials as well as the systematic design and operation of the anode and cathode electrodes.

In this study, the effect of catalyst loading, catalyst chemistry, PTL type and inclusion of a conductive additive in the OER catalyst layer are systematically studied and optimized. The influence of each factor is elucidated through a design of experiments (DoE) approach with a full statistical analysis. Such an analysis allowed for the rational

design of future generations of the anode electrode, including predictions for output voltage response, which were validated. The approach in this paper allows for electrochemical data to be analyzed alongside Pareto charts, parametric trends, and their mutual interactions to be discussed. From this, important insights about systems voltage response corresponding to the input parameters are gained.

2. Materials and Methods

2.1 Catalyst and Polymer Materials

Two HER cathode catalysts were used in this work, platinum supported on carbon black (Pt/C, Nel Hydrogen) and Platinum Nickel (PtNi, Pajarito Powder). These catalysts were deposited onto Toray-60 carbon paper with 5% wetproofing (Fuel cell store). At the anode, either PbRuOx (Pajarito Powder) or Iridium Oxide (IrOx, Nel Hydrogen) were used to catalyze the OER. The anode porous transport layer (PTL) was either platinized titanium (Pt-Ti, Nel Hydrogen), nickel foam (Ni-foam, EQ-bcnf-80um, MTI corporation) or Nickel fiber felt (Dioxide Materials Inc.). Characteristic properties of those three PTLs like thickness, porosity, fiber diameter, pore size etc. are summarized in **Table 2.1**.

Table 2.1: Characteristic properties of Porous Transport Layers (PTLs)

	Ni Foam	**Platinized Titanium**	**Ni Fiber Felt**
Thickness (mm)	0.3	~ 0.3	~ 0.3
Porosity (%)	≥ 95	~ 67	~ 68
Fiber / feature size (µm)	~60	~ 20	~ 10
Pore/hole size (µm)	>100	>10	>10

The AEM was a functionalized and quaternized poly(norbornene) sold as XION™ Composite-72-10CL-30μm (72% halogenated monomer, 10 mol% crosslinker and 30 μm thickness) by Xergy, Inc. The anode and cathode ionomers (synthesized at Georgia Tech) were also poly(norbornene)-based. At the anode, an ionomer with 32% halogenated monomer (GT32; IEC = 1.88) was used and at the cathode an ionomer with 73% halogenated monomer (GT73; IEC = 3.56) was used. The synthesis of the poly(norbornene) (PNB) tetrablock copolymers and homopolymers used as the ionomers and AEMs in this work were previously reported by Kohl and coworkers**[140], [141], [142], [143], [144], [145]**.

2.2 Design of Experiments (DoE) Approach

Minitab® factorial Design of Experiments (DoE) was used for creating an experimental matrix as well as performing a statistical analysis and response optimization. In this study, two factorial DoE matrices were used to optimize the anode electrode. The first was a 2^4 analysis (four factors with two levels), which was done with only one replication. The four factors in this analysis were: 1) catalyst loading (1.5 and 3.0 ± 0.1 mg/cm^2); 2) additive carbon in the catalyst layer (0 wt. % and 30 wt. %); 3) catalyst selection (IrOx and PbRuOx); and 4) PTL type (commercialized platinized titanium and nickel foam). This 2^4 factorial design resulted in 16 unique experimental conditions, **[146], [147], [148]**, which are shown in **Table 2.2**. The figure of merit that was used was the steady-state voltage at an operating current 1.0 A/cm^2. Additional details on the electrochemical experiments are provided in the next section. After the data collection, Minitab software was used to perform a robust statistical analysis with the goal of

understanding how the four input variables and their interactions effect the output response (voltage).

Table 2.2: Design layout and experimental results of full factorial design. Last column is the experimental data as a Voltage response while cell operated at a current density of 1.0 A/cm^2

Exp. #	Catalyst load. (mg/cm^2)	Catalyst type	PTL type	Additive carbon (wt % in electrode)	Voltage at 1.0 A/cm^2
1	1.5	PbRuOx	Ni Foam	0 %	2.243
2	3.0	PbRuOx	Pt-Ti	0 %	1.828
3	3.0	PbRuOx	Pt-Ti	30 %	1.794
4	3.0	IrOx	Ni Foam	0 %	2.187
5	1.5	PbRuOx	Pt-Ti	30 %	1.824
6	1.5	IrOx	Pt-Ti	30 %	1.869
7	1.5	PbRuOx	Ni Foam	30 %	2.115
8	3.0	PbRuOx	Ni Foam	30 %	2.086
9	1.5	IrOx	Ni Foam	0 %	2.214
10	3.0	IrOx	Pt-Ti	30 %	1.833
11	3.0	IrOx	Ni Foam	30 %	2.221
12	1.5	PbRuOx	Pt-Ti	0 %	1.863
13	1.5	IrOx	Ni Foam	30 %	2.268
14	1.5	IrOx	Pt-Ti	0 %	1.886
15	3.0	PbRuOx	Ni Foam	0 %	2.163
16	3.0	IrOx	Pt-Ti	0 %	1.865

As described above, the first 2^4 analysis contained four variables to study. Two of those variables were naturally binary: catalyst type and PTL type. This limited the number

of runs that could be done for the other two variables. Hence, the first DoE matrix can inform which of the binary variables is preferred. It also allows for understanding whether the catalyst loading or additive carbon have an influence on the operating voltage or not. However, it does not provide enough data points to optimize either of those non-binary variables. Therefore, further analysis was performed on those two non-binary variables (with four levels each) to visualize any nonlinear characteristics. Therefore, a second factorial DoE was executed. This time a general factorial design (two factors with four levels) matrix was executed. The two non-binary variables from the first DoE were elaborated as shown in **Table 2.3**. For this general factorial design, the anode catalyst was always PbRuOx and the PTL was always platinized titanium.

Table 2.3: Design layout and experimental results with 2 factors and 4 levels. Last column is the experimental data as a Voltage response while cell operated at a current density of 1.0 A/cm^2

Exp. #	**Anode Catalyst loading (mg/cm^2)**	**Additive carbon (wt % in electrode)**	**Voltage at 1.0 A/cm^2**
1	1.0	45	1.766
2	5.0	0	1.746
3	5.0	45	1.762
4	3.0	45	1.693
5	5.0	15	1.736
6	1.0	30	1.732
7	5.0	30	1.746
8	2.0	15	1.711
9	3.0	15	1.641
10	2.0	45	1.731

11	2.0	30	1.717
12	2.0	0	1.721
13	1.0	15	1.738
14	3.0	30	1.636
15	1.0	0	1.742
16	3.0	0	1.641

2.3 Electrode Fabrication

The anode and cathode electrodes were prepared by hand spraying a catalyst ink directly onto the PTLs. The ink preparation method was adapted from our previous work **Error! Reference source not found.**, **Error! Reference source not found.**, though the fo rmulation of the anode and cathode are different as detailed below. At the anode, a typical process began by soaking 62.5 mg of GT32 in DI water (1-2 mL) for 30 mins. Then, the swollen ionomer was ground with a mortar and pestle for 10 minutes to allow it to break up into its fine particles. Next, 250 mg of the catalyst and 20 mg PTFE powder (Ultraflon MP-25, Fuel Cell Store) was added, along with any additive carbon (130 mg = 30 %), and the materials were further ground for 10 minutes, forming a uniform paste. Then, 9-10 mL of 2-Propanol (IPA) were added to convert this slurry into uniformly dispersed ink. The ink was then transferred to a Teflon-lined vial and sonicated for 60 – 90 mins. Finally, the catalyst ink was hand sprayed using an Iwata spray gun onto a 25 cm^2 PTLs, which were later cut into 5 cm^2 electrodes for testing.

An identical procedure was applied for preparing the cathode ink. The catalyst to ionomer ratio in cathode was 4:1 while it was 3:1 in the anode. Typically, 30 mg of GT73 ionomer and 200 mg of catalyst were used. In addition, 16 mg of PTFE was added to

increase the hydrophobicity of the electrode. Toray TGP-H-060 with 5% wetproofing was used for the cathode PTLs.

2.4 AEM Electrolyzer Assembly and Testing

The AEMs and electrodes were ion exchanged in aqueous 1.0 M KOH solution for a total of 60 min (refreshing the solution every 20 minutes) prior to cell assembly. The poly(norbornene) AEM was sandwiched between the two electrodes and pressed together in the hardware with no prior hot pressing. The custom cell hardware had an active area of 5.0 cm^2 and was made from 316 stainless steel. The anode flowfield had parallel channels while the cathode flowfield had a single serpentine channel. Appropriate thickness gaskets were used to provide suitable MEA compression, with a target of 25%. The torque applied to the cell hardware was 40 in-lb. Once assembled, the lab-scale AEMELs were tested using a custom-built electrolysis test station powered by an Arbin Model BT-2000. All tests are performed at a cell temperature of 50 °C. All cells were fed a salt solution in DI water, either 1.0 wt% potassium carbonate or 0.3 M KOH. The solution was fed only to the anode at a rate of 0.2 L/min using a KNF IP65 NF 100 KT.18S liquid pump. The electrolyte was preheated to 50 ^oC in a N_2-purged tank with a KD Titanium Fully Submersible Portable Electric Immersion heater before feeding to the electrolyzer cell. The cathode inlet was closed while the outlet was fed to a bubbler to visualize hydrogen evolution before being sent to the building exhaust. The cell was equilibrated at the desired temperature for 30-60 min at zero current while feeding the preheated electrolyte. The cell was conditioned by applying a small current (100 mA/cm^2) and waiting for the voltage to equilibrate. This typically took 30 – 60 mins after which polarization curves were collected by scanning the voltage from 1.3 V to 2.4 V at a 20

mV/s scan rate. Steady state voltage measurements were done at a constant current density of 1.0 A/cm^2.

3. Results and Discussion

The first DoE factorial analysis studied the effect of four variables, at two levels each. The experimental matrix was described in the Experimental Section and summarized in **Table 2.2**. The purpose of this analysis was to develop a **s**ystematic understanding of how the selected four variables effect the transient and steady-state performance of the OER electrode in an AEMEC. For this first analysis, two of the variables, PTL type and catalyst type, were intrinsically binary and two of the variables could contain a wide range of possible values. In this first DoE set of experiments, the catalyst loading and amount of additive carbon in the electrode were selected to represent a broad range of possible values. For this data set, the primary performance metric was the operating voltage at a constant current density of 1.0 A/cm^2. The measured steady state voltage (at a current density of 1.0 A/cm^2 after stabilization and 60 min of operation) for each of the experiments is provided as the last column in **Table 2.2**.

After measuring the operating voltage at constant current for each permutation of the 2^4 DoE matrix, a statistical analysis was done in Minitab – which allowed the relative importance of each variable to be determined by the Pareto chart, main effects plots and interaction plots. The Pareto chart is a graphical representation of standardized effects of the individual factors and their interaction. The Pareto chart shows the absolute value of the standardized effects from the largest effect to the smallest effect, **Figure 2.2**. The reference line (red vertical line in **Figure 2.2**) is a standard outcome of the Pareto chart. A parameter with a standardized effects value greater than the reference line (2.36 here)

indicates a parameter that has a statistically significant effect. All of the variables had a statistically significant effect. The PTL type had the most significant influence over the output voltage. This lends a significant amount of support to recent studies by several groups **[124], [131], [132], [149], [150]** in this area. The PTL has a significant effect on several phenomena occurring in the cell, including water/gas transport, contact resistance, AEM-catalyst layer contact area, catalyst layer compression and adhesion. From **Figure 3.2A**, it can be seen that there was a negative shift in the electrolyzer voltage in the kinetic region of over 100 mV when the platinized titanium PTL was used. Also, the slope in the polarization curve in the Ohmic region was much larger when the Ni foam PTL was used. The Ni foam had much larger pores compared to platinized titanium (**Figure 2.4**), which is beneficial for O_2 bubble removal but decreases the contact area between AEM and catalyst layer and hence increases resistance – meaning that fewer active sites were available for reaction. This led to an increasing separation between the two curves over the current entire range, and by 1.0 A/cm^2 the operating voltage difference was around 400 mV. Moreover, the large feature size and large pore size of the Ni foam resulted in poorer adhesion. In fact, when using the Ni foam, black particles were observed in the circulated electrolyte. When the platinized titanium PTL was used, no particles were observed for the same period of AEMEL operation.

However, the result here does not imply that platinized Ti is intrinsically better than Ni. It is likely that this PTL – which is already used commercially in PEM electrolyzers and has already gone through a significant amount of engineering to optimize its behavior for that application – is superior overall to this specific Ni foam. In fact, later in this publication excellent performance and durability is demonstrated with a Ni-based PTL

(with similar physical properties to the platinized Ti PTL) at the anode later in this work. These results suggest that the PTL represents a significant opportunity for improvement in the operating cell voltage and will be our focus in upcoming experimental investigations to enhance electrolyzer performance and durability.

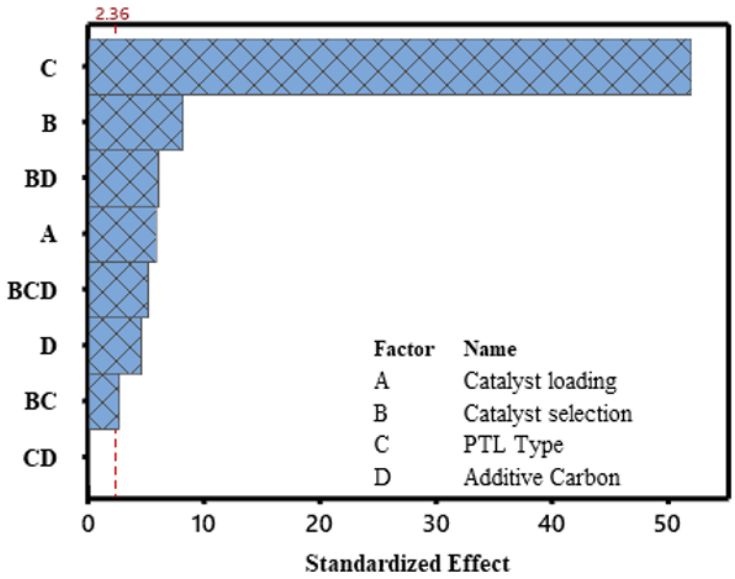

Figure 2.2: Pareto Chart of standardized effects. The values greater than the (Red) reference line (2.36) indicate a parameter that has a statistically significant effect

The second most important variable in deciding the operating voltage was the catalyst type. It was found that the PbRuOx OER catalyst was statistically better than IrOx, which is supported by RDE and cell studies elsewhere **[151], [152]** **Figure 2.3B** compares the polarization curves where the catalyst type is changed, but the PTL (platinized Ti), added C (30 %) and catalyst loading (3.0 %) were held constant. The lower operating voltage in the kinetic region of the polarization curve confirms that PbRuOx possesses superior intrinsic activity over IrOx, which is in agreement with previous studies **[151], [152]**. The slope in the polarization curve with PbRuOx was very similar to the slope with

IrOx, suggesting that the mass transport and Ohmic resistances were not significantly affected.

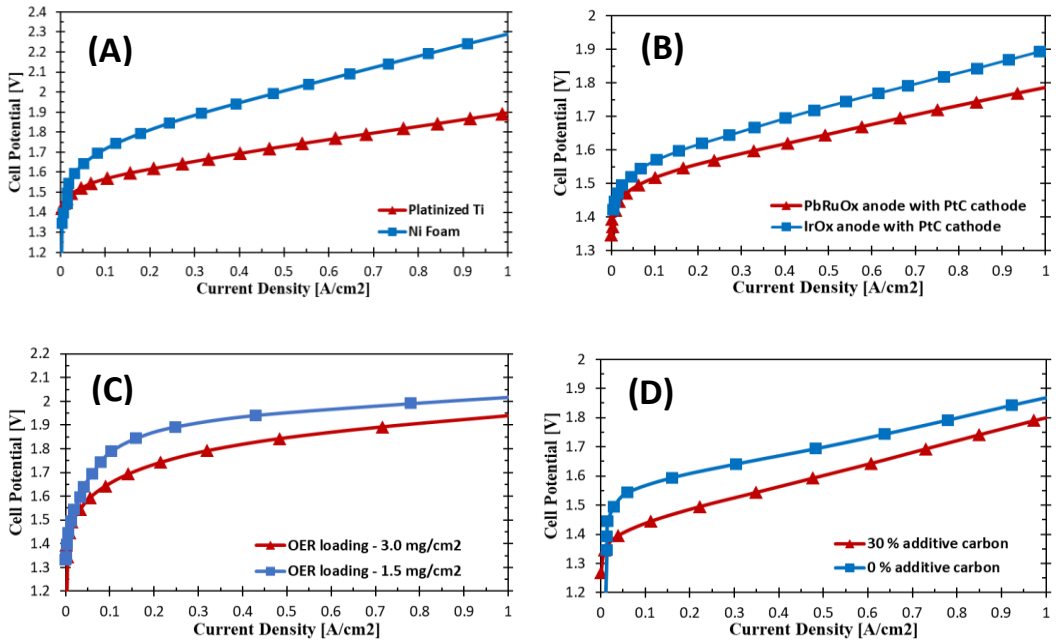

Figure 2.3: Polarization curves showing, A) Effect of OER electrode PTL type – Plat. Ti vs Ni foam, keeping IrOx as catalyst, 30% additive carbon and loading of 1.5 mg/cm2 constant, B) Effect of OER catalyst material - IrOx vs PbRuOx keeping Plat. Ti PTL, 30% addive carbon and loading of 3.0 mg/cm2 constant, C). Effect of catalyst loading – 1.5 mg/cm2 vs 3.0 mg/cm2, keeping PbRuOx catalyst, 30% additive carbon and Ni foam PTL constant, D) Effect of additive carbon – 0 % vs 30 %., keeping IrOx catalyst with loading of 3.0 mg/cm2 and Plat. Ti PTL constant. All tests were performed with GT72-10 (30 um) AEM at 50 C cell temperature, PtC as the HER electrocatalyst deposited on Toray 060 carbon paper and 1 w% K_2CO_3 in DI water fed to OER electrode only.

Polarization curves from the initial 2^4 analysis for the other two variables, catalyst loading and amount of additive carbon, are shown in **Figure 2.3C** and **Figure 2.3D**, though not extensively discussed as they were studied in greater detail in the second statistical analysis. Lastly, the interaction between variables on output response was obtained where

PTL type with additive carbon appeared to have the most significant interaction. The most likely underlying reason for that interaction is that both of those variables set the electrode porosity, which dictates the rates of water penetration into the electrode as well as bubble removal from the OER. They also can dictate the contact resistance between the PTL and the catalyst layer.

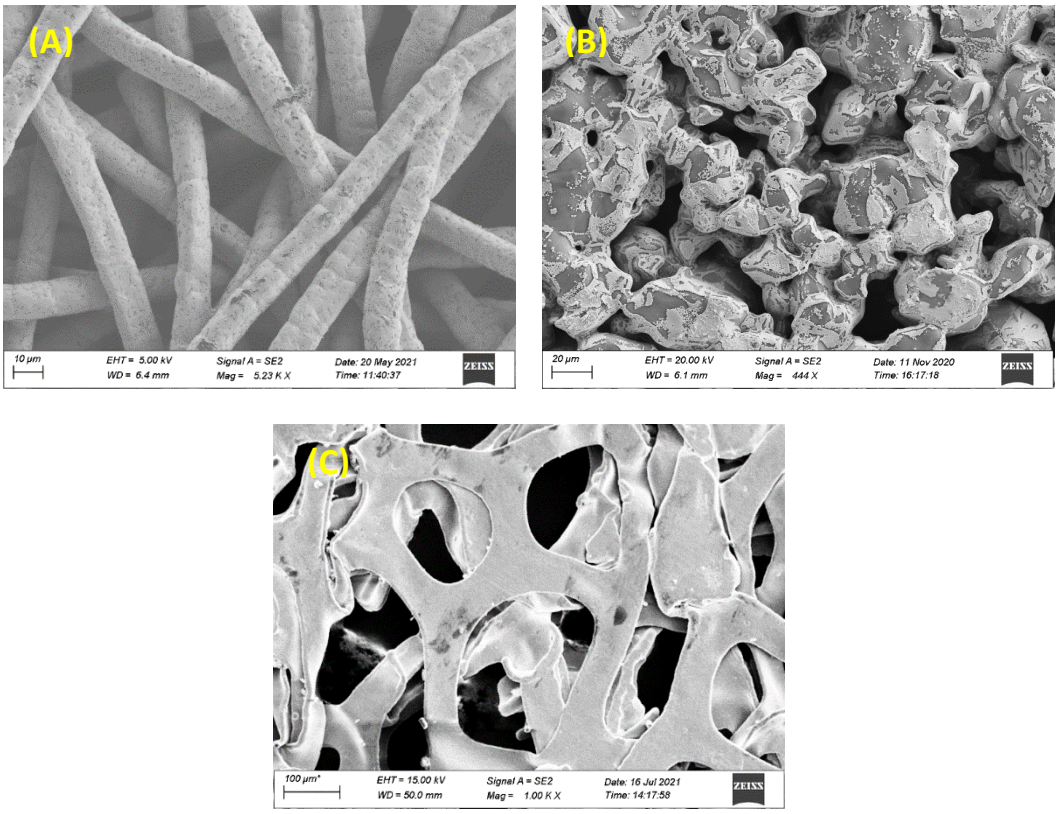

Figure 2.4: SEM images of, **(A)** Ni Fiber Felt Porous Transport Layer (PTL) purchased from Dioxide Materials Inc. **(B)** Platinized Titanium provided by Nel Hydrogen, **(C)** Nickel foam purchased from MTI corporation. Characteristic properties measured or provided by manufacturers are provided in Table 1 of main document.

The discussion above used the statistical analysis to understand whether each of the design variables influenced performance. However, a DoE response optimizer in the Minitab software allows the user to target a desired output response. This can lead to a more complete result where the software dictates to the user the appropriate parameter values to use. The model can also predict multiple responses showing a defined level of probability and confidence interval. In this case, the optimizer suggests a cell construction given a targeted output voltage. Here, an operating voltage at 1.0 A/cm^2 was selected that was well within the experimental space above, 1.85 V. To achieve this, the program

selected a catalyst loading of 1.5 mg/cm^2, an additive carbon loading of 10 wt%, a PbRuOx catalyst and Pt-Ti PTL. With a confidence interval of 95%, the predicted voltage was between 1.830 V and 1.868 V. This cell construction was assembled, and the cell operated at 50 ^{o}C with no back pressure. The result is shown in **Figure 2.5**. The output voltage response was 1.84 V, which is within the predicted range. This shows the possible power of statistical DoE approaches where other outputs may be desired. For instance, an economic target ($/cm^2) could be inserted into the model, which would provide useful insights for decision making, though such a target is outside of the focus of this work.

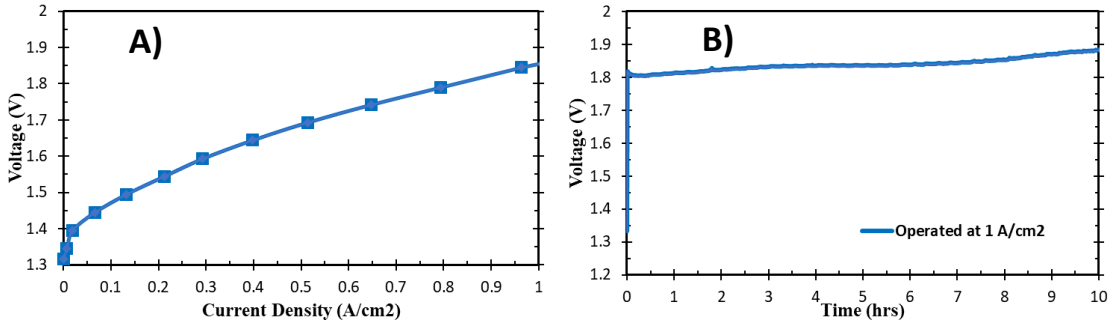

Figure 2.5: A). Polarization curve and B). steady-state response voltage with PbRuOx OER catalyst, loading of 1.5 mg/cm^2 and 10% additive carbon while using a platinized Ti PTL. The cathode electrode for the HER used a Pt/C catalyst with loading of 1.2 mg/cm^2. The cell temperature was 50^{o}C, and the electrolyte solution was 1 w% K_2CO_3 in DI water fed only to the OER electrode.

In the next step of the OER electrode optimization, catalyst loading, and additive carbon content were further analyzed. Since they are variables that can have a wide range of values, and possible non-linear response, electrode optimization required a finer assessment of the variables. Four levels of catalyst loading (1.0, 2.0, 3.0 and 5.0 mg/cm^2) and additive carbon (0, 15, 30 and 45 %) were selected for further analysis. For these variables, a 4^2 DoE experimental matrix (**Table 2.2**) was executed where the anode catalyst

was always PbRuOx and the PTL was platinized Ti (based on the output of the 2^4 DoE matrix). Steady state voltage at 1.0 A/cm^2 (final column in **Table 2.2**) and polarization curves were measured as before. The Pareto chart (**Figure 2.6A**) confirms no significant interaction between the two variables. For optimization, the main effects plots (**Figure 2.6B**) can be far more useful. It was found that as the catalyst loading increased, the voltage response initially decreased but increased at higher loadings. This makes sense practically as the initial increase in the loading likely improves the electrochemically active surface area while very high loadings lead to thicker catalyst layers and increased mass transport resistance. A similar trend was observed for the additive catalyst support where it has positive effect up to 30 % additional support and then a negative effect on the steady-state operating voltage as the amount was further increased.

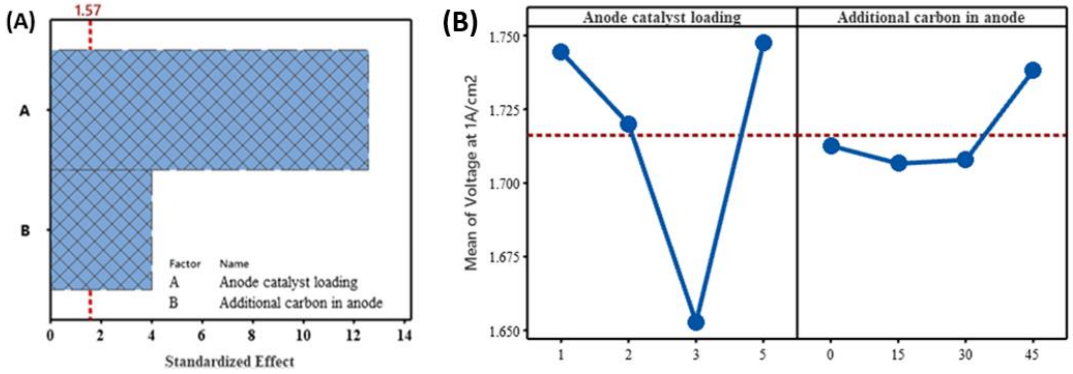

Figure 2.6: (A). Pareto chart, (B). Main effect plots for two parameters showing general trend

Polarization curves summarizing the dynamic response of these cells to changes in both variables is shown in **Figure 2.7.** Polarization curves comparing the four catalyst loadings (without any additive carbon) are shown in **Figure 2.7A**. In addition to the different voltage at 1.0 A/cm^2, there were interesting changes in the shape of the polarization curve. Generally, it appears that as the catalyst loading was increased that operating voltage was reduced in the low-current regime, indicating an improvement in the

cell kinetics. However, at low loadings there appears to be a faster transition to Ohmic and mass transport control from kinetic control. At 1.0 A/cm^2, the operating voltage decreased to 1.64 V as the loading was increased from 1.0 to 3.0 mg/cm^2. Further increase in loading, however, had negative effect increasing voltage to 1.75 V at 5.0 mg/cm^2, which was even slightly higher than the cell with a loading of only 1.0 mg/cm2. At the highest catalyst loading, there was also a clear upward trend in the polarization curve starting at around 400 mA/cm^2, suggesting that mass transport effects were also influencing the observed behavior.

The polarization curves demonstrating the influence of added carbon content in the electrodes on the cell performance is shown in **Figure 2.7B**. Additive carbon had a positive effect on the cell voltage response up to 30% but then had negative effect which also correlates with DoE factorial analysis. Carbon added in the electrode increases electronic conductivity and provides inactive void volume by making the electrode thicker at similar porosity, facilitating access to catalyst active sites and gas mass transport. This effect was indicated by the lower operating voltage in the polarization curves. In the lower current density region of the polarization curve (at around 100 mA/cm^2), the operating voltage was decreased by approximately 30 mV by the addition of 30% carbon, although there was no significant difference at higher current densities. However, excess carbon leads to thick catalyst layers, and a poor utilization of catalyst near the electrode/membrane interface, which increases the kinetic resistance of the cells, which manifested as a 70 mV increase in the operating voltage at 45% added carbon.

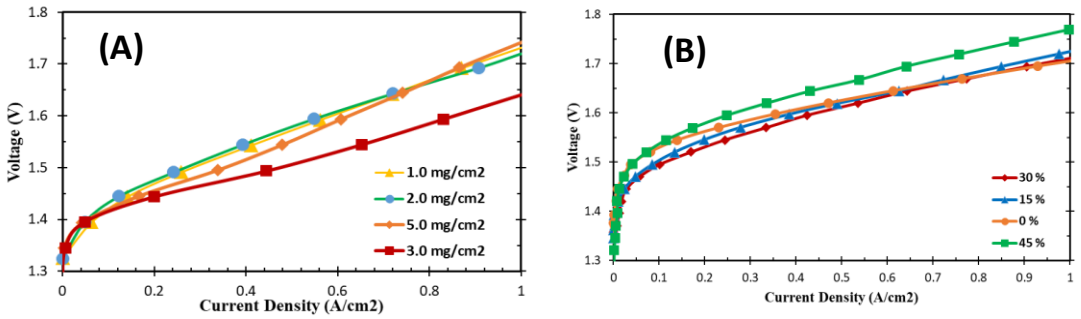

Figure 2.7: A) Polarization curves comparison with different catalyst loadings keeping 0 % additive carbon constant, B) Additive carbon support in anode electrode, keeping 2.0 mg/cm2 catalyst loading, with AEM: GT72-10 (30um), PbRuOx OER with PtC HER electrocatalyst, Plat. Ti PTL, GT-25 ionomer in anode and GT73 ionomer in cathode, cell temperature 50 C, feeding 0.3 M KOH to the anode.

Next, the Minitab DoE factorial response optimizer was used to predict the cell configuration that would yield the minimum operating voltage at 1.0 A/cm^2 within the parameter values in our data set. The Minitab response optimizer predicted operating voltage between 1.645 V and 1.654 V with a 95% confidence interval if OER electrodes were created with a catalyst loading of 2.8 mg/cm^2 and 18% added carbon. Such electrodes were fabricated with realized catalyst loading and additive carbon content of 2.86 mg/cm^2 and 19.8 % respectively. They electrodes were integrated into operating AEMELS and the results are shown in **Figure 2.8.** During polarization, the cell showed very good performance and the voltage at 1.0 A/cm^2 was 1.643 V. This compares very well with the value at steady-state (**Figure 2.8B**), which was 1.652 V (recorded after several of hours of operation). For both, the voltage response achieved experimentally was within the predicted range, validating the DoE model. However, **Figure 2.8B** also shows that the durability for this electrode, optimized for OER performance, was not particularly good, with a relatively high degradation rate of 44 mV/hr.

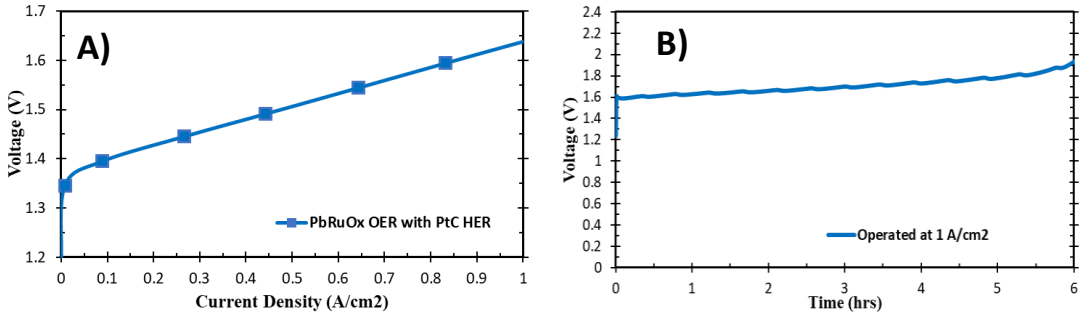

Figure 2.8: A). Polarization curve; B). Steady response voltage with PbRuOx OER catalyst, loading of 2.86 mg/cm^2 and 18% additive carbon while using a platinized titanium PTL, HER PtC catalyst with loading of around 1.34 mg/cm^2, cell temperature 50 ^{o}C, feeding 0.3 M KOH to the anode.

There are several possible explanations for the relatively high degradation rate in **Figure 2.8B**. First, carbon was added into the electrode to increase the electrode thickness with the idea that it would provide more void volume for mass transport. However, carbon is not thermodynamically stable at the OER operating potential. The fact that it provided a benefit suggests that other, more stable, conductive additives should be developed). Second, although the platinized titanium PTL performance was better than the Ni foam, it is possible for any titanium exposed to the electrolyte to passivate, increasing contact resistance. Titanium corrosion in harsh alkaline conditions has also been elsewhere for pH > 10, where crevice-type corrosion can occur over a wide range of temperatures **[153], [154]**. Finally, although the PbRuOx OER catalyst clearly shows better performance compared to IrOx, in agreement with reports elsewhere **[151], [152]**, there was evidence for slight dissolution of Pb and Ru during cell operation. **Table 2.4** shows the results of an elemental analysis of the electrolyte follow a 48 hour operation of an identical cell to the one in **Figure 2.8**. It was found that some bromide was present due to incomplete ion

exchange, giving the electrolyte a yellow coloring. Small amounts of Pb and Ru were also found in the electrolyte. This suggests that new materials are needed and compromises are going to need to be made to achieve significantly improved operational stability.

Table 2.4: Elemental analysis report of 0.3 M KOH electrolyte after 48-hour operation. The analysis was performed by Roberton Microlit Laboratories in Ledgewood, NJ on 7/1/2021.

Sr No.	**Element present**	**Concentration (µg/g)**
1	Na	355
2	K	> 1%
3	Mg	7
4	Sr	10
5	Ba	16
6	Zr	263
7	Cr	8
8	Mo	17
9	Ru	76
10	Ni	8
11	Cu	15
12	Pb	6
13	B	233
14	Al	96
15	Si	2980
16	Br	1936

To improve operational stability, our team made three changes to the optimized anode and one change to the cathode. First, a Ni-based PTL sold by Dioxide materials (SKU 68844) was employed. This PTL had a similar porosity and pore size to the platinized titanium (**Table 2.1**), though the feature size of the Ni fiber felt was smaller and (~10 vs. 20 μm). Another difference was that the platinized Ti was comprised of sintered, not fibrous materials. **Figure 2.4** shows images of the three PTLs used in this study with intrinsic difference in structural details. Given the thinness of the AEM, it is possible to have local areas of high stress, which could cause membrane mechanical failure and/or catalyst detachment. During long-term testing, we did observe some catalyst detachment when using the platinized titanium PTL. As highlighted earlier, Boettcher et al., **[131]**, analyzed commercial stainless-steel fibers with different pore and surface structure for the OER electrode. They found that the PTL with smallest fiber diameter and smoothness showed the best performance, presumably due to larger contact area, higher catalyst utilization, and decreased lateral catalyst-layer electrical resistance. The Dioxide Materials Ni fiber paper has a primary fiber diameter of ~10 μm (**Figure 2.4**).

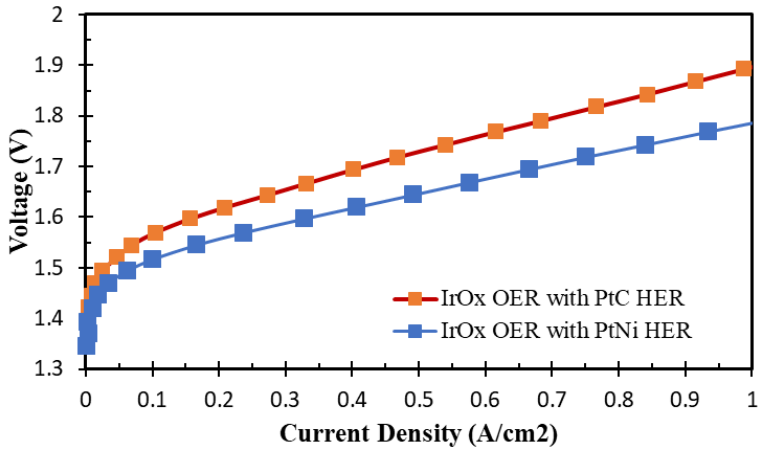

Figure 2.9: Comparison of PtNi vs PtC HER catalyst, tested with GT72-10 (30um) membrane, IrOx on Ni fiber felt + 25 w% GT32 ionomer as OER and PtNi or PtC on carbon paper + 15 w% GT69 ionomer as HER electrode in 0.3 M KOH feed to anode only with no backpressure.

The second change that was made to improve operational stability was the use of IrOx as the anode catalyst instead of PbRuOx. The final change that was made to the anode was to remove the added carbon from the anode catalyst layer. The last two changes obviously move somewhat far away from the optimized electrode discussed above, but that does not invalidate that analysis. It shows how durability and performance are often at odds and that important compromises need to be made to facilitate practical systems. From Minitab, we found that minimum operating voltage loss from the optimized cell to one with no conductive additive and IrOx catalyst is 1.786 V, a loss in the operating voltage of approximately 150 mV. This operating voltage loss is unacceptably high, and it needs to be mitigated. One way to do that is to change the cathode catalyst to one that shows better performance. Therefore, the one change that was made to the cathode was to replace the Pt/C catalyst with PtNi from Pajarito Powder (a comparison of Pt/C and PtNi in an AEMEC is shown in **Figure 2.9**).

Plots showing the effects of these changes are presented in **Figure 2.10**. **Figure 2.10A** implemented three of the changes to the cell: Pt-Ti was replaced with Ni fiber felt, the additive carbon was removed from the anode and the cathode catalyst was PtNi. This is shown as an intermediate state because it shows how the transition to PtNi and removal of the additive carbon (blue diamonds) essentially offset one another in terms of their effect, with the operating voltage at 1.0 A/cm^2 being 1.64 V. The durability (**Figure 2.10B**) was improved, with a much lower decay rate of 0.6 mV/hr being observed. This can be explained by the fact that with the Ni fiber PTL and no added carbon, no catalyst detachment from the anode was observed. The effect of the last change, replacing PbRuOx with IrOx, is shown in **Figures 2.10C-D**. Here, the polarization curves, are compared with and without additive carbon in OER catalyst layer. The cell with IrOx clearly had a higher operating voltage than the PbRuOx in the kinetic regime in the polarization curve, and the operating voltage at 1.0 A/cm^2 was 1.79V. However, positively, the cell with all of the changes showed better stability and was operated continuously for 30 days (720 h) with no significant degradation in the voltage. In fact, the degradation rate was very low, only 8.3 μV/hr during this, which to our knowledge is the lowest value reported in literature to date.

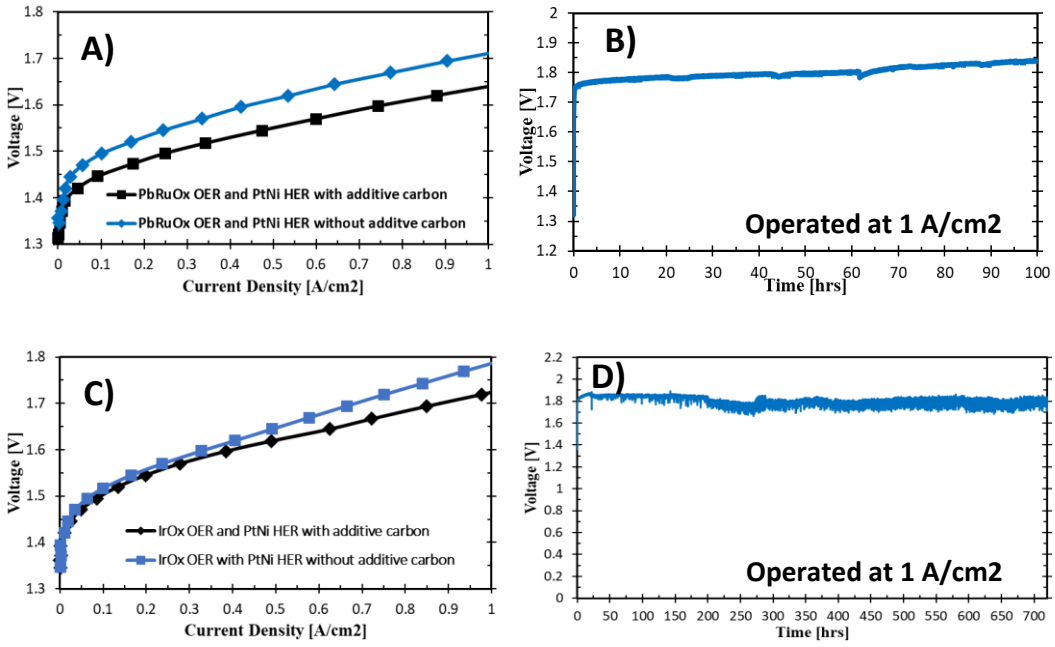

Figure 2.10: A). Polarization & B). Durability test with GT72-10 (30um) membrane, PbRuOx on Ni fiber felt + 25 w% GT32 ionomer as OER and PtNi on carbon paper + 15 w% GT69 ionomer as HER electrode in 0.3 M KOH feed to anode only. Current density = 1.0 A/cm^2, C). Polarization & D). Durability test with GT72-10 (30um) membrane, IrOx on Ni fiber felt + 25 w% GT32 ionomer as OER and PtNi on carbon paper + 15 w% GT69 ionomer as HER electrode in 0.3 M KOH feed to anode only. Current density = 1.0 A/cm^2

4. Conclusion

Low temperature anion exchange membrane electrolyzer OER electrode was studied using DoE factorial design approach. In first step four parameters with two levels were selected for designing DoE 2^4 factorial matrix. The four factors include catalyst loading, catalyst material selection, additive catalyst support and PTL type. Voltage at 1.0 A/cm^2 was recorded as the output response in experiment matrix. It was found that all four factors had statistically significant effect on voltage response, with the PTL type being the most influential. Catalyst loading and additive support were further analyzed using DOE

4^2 factorial analysis with 4 levels each. It was found that higher the catalyst loading, lowered the voltage response (positive) up to 3 mg/cm^2 after which increasing the catalyst loading had negative effect. Similarly, introduction of additive carbon in electrode had positive effect on voltage response up to 30 % addition after which it had negative impact. However, the performance-optimized electrode was not able to show sufficient stability to enable long-term performance. Because of this, compromises were made – and four aspects of the cell were changed to encouraged improved durability, albeit at a higher operating voltage. The outcome there was a well-performing electrolyzer that was able to run stably over 720 hr (30 days) without significant degradation.

CHAPTER 3

KOH VS. DEIONIZED WATER OPERATION IN ANION EXCHANGE MEMBRANE ELECTROLYZERS[2]

Abstract

Anion exchange membrane water electrolyzers (AEMELs) have recently received significant attention due to their potential advantages over proton exchange membrane electrolyzers (PEMELs). However, some AEMELs feed an aqueous salt solution to the cell where PEMELs typically feed deionized (DI) water. DI water is preferred to keep the system and maintenance costs low. Because of this, many AEMEL researchers report performance both in the salt solution (typically KOH) and DI water. However, the methodology for switching between KOH and DI water is often poorly defined, and it is unclear what impact the residual salt has on cell performance after switching from salt to DI water. Having a fully deionized environment is important because the presence of salts in the water feed increase the effective electrochemical surface area of the catalyst in the three-dimensional electrode and residual salt remaining after switching to DI water feed can have a misleading transient effect on cell performance. This paper focuses on

---

[2]Hassan, N.U., Zheng, Y., Kohl, P.A. and Mustain, W.E., KOH vs Deionized Water Operation in Anion Exchange Membrane Electrolyzers, *J. Electrochem. Soc*. **169,** 044526 (2022).

understanding the transition from KOH to DI water testing in AEMELs. It is shown that when switching from salt to DI water feed, a large volume of DI water must be fed over several hours to achieve true DI-water performance. It is also shown that starting AEMELs from the beginning with DI water feed (without any KOH ever being fed to the cell) results in better cell durability. Lastly, a cell is demonstrated having operated exclusively on DI water at 1.0 A/cm^2 for 500 hours at an operating voltage of ca. 2 V and a low degradation rate.

1. Introduction

Significant progress has been made in reducing the cost of energy systems that rely on renewable sources such as wind, tidal and solar **[155]**. However, the intermittent nature of each of these does not allow them to temporally balance their energy supply with the grid demand **[156]**. Electrical energy produced from these systems can be converted to chemical energy carriers such as hydrogen, especially during non-peak hours. By directly utilizing low-cost, off-peak electrical energy, the cost of hydrogen via electrolysis could be lower than conventional processes including steam reforming **[157]**. The resulting hydrogen can then be utilized for chemical reactions or used to generate power from an internal combustion engine or fuel cell. Hydrogen can also be stored or transported over long distances.

Water electrolysis is a well-established technique for converting water into molecular hydrogen and oxygen at relatively low temperatures. Among low-temperature electrolysis systems (< 100 ^{o}C), the alkaline water electrolyzer (AWE) using a liquid electrolyte is the most well-established technology, having already been commercialized for decades with low-cost catalysts and cell components **[158], [159]**. However, they do

have three important limitations **[160], [162]**. The first limitation is that the AWE operates at low current density, which leads to a large systems with relatively expensive balance of plant **[159], [163]**. The second limitation is that they are fed a concentrated alkaline (aqueous KOH) solution as the electrolyte, which provides both the water for electrolysis and cell-level ionic conductivity. The concentrated KOH is a plant-level safety hazard and it also leads to relatively high maintenance costs **[163]**. Finally, the AWE can only discharge low pressure hydrogen, which must be mechanically compressed, due to the fluidic nature of the liquid electrolyte **[164], [165]**. To overcome these issues, the proton exchange membrane electrolyzer (PEMEL) was developed. A PEMEL can operate at higher current density than an AWE, giving it a more compact design **[165], [166], [167]**. The solid polymer electrolyte in a PEMEL also enables the discharge of pressurized hydrogen (so-called electrochemical compression). However, the cost of PEMEL systems is still relatively high due to the use platinum group metal catalysts and perfluorinated membranes **[168]**. Therefore, there is an incentive to combine the high pH advantages of an AWE (i.e., low cost catalysts and membranes) with the solid-state advantages of a PEMEL to create the anion-exchange-membrane electrolyzer (AEMEL) **[167], [169], [170]**. The goal is to achieve high current density, low gas cross-over, pressurized discharge gas without the high-cost PEMEL components.

Over the past several years, AEMEL performance has significantly improved. Many of the reported cells operate with an aqueous salt feed solution (either dilute KOH or carbonate), although typically at a lower concentration than in an AWE. Regarding performance, Wang et al. **[171]** reported a current density of 400 mA/cm^2 at 1.8 V and 50^o C using Pt black as the hydrogen evolution reaction (HER) cathode electrocatalyst and

IrOx as the oxygen evolution reaction (OER) anode) electrocatalyst. However, the durability was poor in pure DI water. Li et al., **[172]** utilized a high IEC ionomer (3.3 meq g^{-1}) to achieve an operating current of 906 mA/cm^2 at 1.8 V. However, due to high water uptake and solubility of their high IEC ionomer the catalyst was washed away resulting in somewhat high degradation rates in short term testing, and poor durability in long term testing. Most recently, Yan and coworkers **[173]** reported 1020 mA/cm^2 at 1.8 V in pure water. However, the degradation rate was high at both low current density (0.56 mV/h at 200 mA/cm^2) and high current density (1.81 mV/h at 500 mA/cm^2). In fact, the degradation rates for AEMELs are presently much higher than PEMELs, ranging from 0.1 - 2 mV/h **[172]** while PEMELs have degradation rates that typically range from 2-10 μV/h **[174]**. Therefore, the AEMEL remains a relatively new technology and a significant improvement is needed to achieve high performance and durability.

One of the main AEMEL challenges to achieving low-cost performance is the development of highly active PGM-free catalysts for both the OER and HER. Hiao and Lu et al., **[175]** used PGM-free catalysts (Ni−Mo in the cathode and Ni−Fe in the anode) and a self-made membrane and ionomer to achieve a current density of 300 mA cm^{-2} at 1.8 V. However, the cell was able to operate effectively for only 8 hr. An additional issue with AEMELs is the need for durable, low-cost cell components including porous transport layers (PTL) to make the three-dimensional electrodes. It was recently shown that the PTL with a small fiber size and smooth surface results in enhanced performance likely due to its large contact area, higher catalyst utilization, and decreased lateral catalyst-layer electrical resistance **[176], [177]**. Similar studies have also been reported on graded-pore structures to improve mass transport during in PEMELs **[178], [179]**.

Lastly, to simplify the balance-of-plant, and reduce maintenance, it is preferable to operate membrane-based electrolyzers with deionized water (DI) feed. As discussed above, this is already done in PEMELs; however, most of the reported AEMELs in the literature use carbonate or hydroxide-based electrolytes. The electrolyte feed is used to increase the electrochemically active surface area of the anode electrode where the OER occurs **[180]**. Moreover, the adsorption of metal cations like K^+ can stabilize the transition state of the water dissociation step promoting HER **[181]**. K^+ may also enhance the OER by enabling a lattice oxygen-mediated mechanism **[182]**. When DI water is fed to the cell, typically the performance is lower, with the operating voltage at 1.0 A/cm^2 increasing by 300 mV or more. Some recent studies have reported good AEMEL performance with DI water, achieving 1.0 A/cm^2 below 2.0 V **[172], [183], [184]**. However, DI water feed tests are typically performed by first breaking-in (break-in is used here to describe a startup procedure meant to activate an MEA for stable operation before collecting polarization scans and steady-state performance evaluation) the cell with an aqueous KOH feed, then replacing the KOH feed in favor of a DI water feed **[183], [184], [185]**. Different protocols are used to transition from KOH to DI water feed in terms of the amount of DI water fed to the cell as well as the time that the cell is exposed to DI water before performing the electrolysis tests. There are also many studies where the protocol to transition from KOH to DI water operation is either poorly described or not described at all. Because residual alkaline electrolyte in the cell can enhance transient activity, it has been previously noted by Lindquist et al. that it is very important that all excess salt from feeding KOH is flushed from the cell before claiming DI water operation **[186]**. Because of the uncertainty in the procedures to transition from KOH to DI water feed in the literature, as well as some that

have very short flushing times, it is possible that some of the reported operating voltages may not be accurate representations of true DI water performance.

Therefore, the primary purpose of this communication is to probe the transition of AEMELs initially operated with KOH to true DI water operation. This was done through a combination of experiments. First, cells were operated at steady-state for several hours with aqueous KOH fed to the anode only. Then, the feed was shifted from KOH to DI water and the voltage response was observed over a 100 hr period. During the transition, polarization curves were collected and electrochemical impedance spectroscopy (EIS) was performed. In addition, exposure to any amount of KOH might lead to chemical or mechanical changes in the cell from degradation due to the high anode operating potential. Thus, cells were also broken-in on DI water without any aqueous KOH exposure and their performance and durability are discussed.

2. Materials and Methods

2.1 Catalyst and Polymer Materials

A platinum-nickel (PtNi, Pajarito Powder) catalyst was used at the cathode electrode for the HER. The catalyst was deposited onto a Toray-60 carbon paper porous transport layer (PTL) with 5% wetproofing (Fuel Cell Store). At the anode, iridium oxide (IrOx, Nel Hydrogen) was used as the OER catalyst and a nickel fiber felt (300 μm, Dioxide Materials) was used as the PTL. The AEM was a 30 μm-thick functionalized and quaternized poly(norbornene) polymer film, sold as XION^{TM} Composite-72-10CL-30μm (72% halogenated monomer and 10 mol % crosslinker) by Xergy, Inc. The anode and cathode ionomers were also poly(norbornene)-based. At the anode, an ionomer with 32% halogenated monomer (GT32; IEC = 1.88) was used and at the cathode an ionomer with

69% halogenated monomer (GT69; IEC = 3.46) was used. GT32 and GT69 were synthesized and characterized as reported previously **[187]- [192].**

2.2 Electrode Fabrication

The anode (OER) and cathode (HER) electrodes were prepared by hand spraying a catalyst ink directly onto the PTLs. The ink preparation method was adapted from our previous work **[191], [192]**. The formulation of the anode and cathode were different as detailed below. At the anode, a typical process began by soaking 50 mg of GT32 in DI water (1-2 mL) for 30 min. Then, the swollen ionomer was ground with a mortar and pestle for 10 minutes to allow it to break up into fine particles. Next, 250 mg of the catalyst was added to the mortar along with 20 mg of PTFE powder (Ultraflon MP-25, Fuel Cell Store – added to help with water transport as the bubbles are released from the catalyst layer **[191], [192]**, and the materials were further ground for 10 min, forming a uniform paste. Then, 9-10 mL of 2-propanol (IPA) were added to convert the slurry into a uniformly dispersed ink. The ink was then transferred into a vial and sonicated in an ice bath for 60 min. Simultaneously, a 10% ionomer (25 mg) solution in IPA was prepared and sonicated (ionomer/IPA solution). Half of the ionomer/IPA solution was sprayed onto a 25 cm^2 PTL as a base layer using an Iwata spray gun. Then, the catalyst layer was sprayed onto the base layer using an identical spray gun. Next, the other half of the ionomer/IPA solution was sprayed on top of the catalyst layer as a final coating layer. Finally, the catalyst-coated PTLs were cut into smaller electrodes for testing.

An identical procedure was applied for preparing the cathode ink. The catalyst:ionomer weight ratio in cathode was 4:1 while it was 3:1 in the anode. Typically, 30 mg of GT69 ionomer and 200 mg of catalyst were used. In addition, 16 mg of PTFE

powder (Ultraflon MP-25, Fuel Cell Store) was added to increase the hydrophobicity of the electrode. Toray TGP-H-060 with 5% wetproofing was used for the cathode PTLs.

2.3 AEM Electrolyzer Assembly and Testing

The AEMs and electrodes were ion exchanged in a 1.0 M KOH solution for a total of 60 min (refreshing the solution every 20 min) prior to cell assembly. Excess surface KOH was removed from the electrodes and AEM by rinsing with DI water, followed by lightly dabbing with Kimwipes prior to MEA assembly. The poly(norbornene) AEM was sandwiched between the two electrodes and pressed together in the hardware with no prior hot pressing. The custom cell hardware had an active area of 5.0 cm^2. The anode flowfield was made from 316 stainless steel while the cathode flow field was made from graphite. The anode and cathode flowfields both had single serpentine channels. Appropriate thickness gaskets were used to provide suitable MEA compression, with a target of 25%. The torque applied to the cell hardware was 40 in-lb. Once assembled, the lab-scale AEMELs were tested using a custom-built electrolysis test station powered by an Arbin Model BT-2000. All tests were performed at a cell temperature of 60 °C. All cells were fed either 0.3 M KOH solution in 18.2 MΩ·cm DI water or pure DI water to the anode side only at a rate of ~ 2 mL/min using a BT100S Basic Variable Speed Peristaltic Pump with Pump Head YT25. The feed solution was preheated to 60 ^oC before being fed to the electrolyzer cell. The cathode inlet was closed while the outlet was fed to a bubbler to visualize hydrogen evolution before being sent to the building exhaust. The cathode effluent was periodically fed to a Thermo Fisher Scientific GFM Pro Flowmeter in order to measure the volumetric flowrate of the evolved gas. This was then used to determine the faradaic efficiency of the operating cells.

To begin cell testing, each cell was equilibrated to the desired temperature for 30 to 60 min at zero current with the desired feed solution. The cell was conditioned by applying a small current (100 mA/cm^2) and waiting for the voltage to equilibrate, which typically took 30 to 60 min. After the cells equilibrated, polarization curves were collected from 1.3 V to 2.4 V at 20 mV/s scan rate. Then, steady state voltage measurements were collected at a constant current density of 1.0 A/cm^2.

2.4 Electrochemical Impedance Spectroscopy

Electrochemical impedance spectroscopy (EIS) was also used to investigate the behavior of the cells. EIS is a very common experimental technique where a small alternating current (AC) current or voltage signal is imposed on an electrochemical device and the amplitude and phase shift of the response are monitored. EIS experiments were carried out from 0.1 Hz to 10 kHz with an amplitude of 5% of the applied current. The resulting data was fit to an appropriate equivalent circuit model and important properties of the cell including Ohmic resistance, charge transfer resistance, double layer capacitance and diffusion behavior were extracted. EIS data was collected at three different current densities, 100 mA/cm^2, 500 mA/cm^2 and 1000 mA/cm^2 while cell operated on 0.3 M KOH and DI water feed.

3. Results and Discussion

3.1 Transition from KOH to DI water operation

As mentioned earlier, different protocols are used in the AEMEL research community for cell break-in before operating in DI water. This can lead to uncertainty with regards to the accuracy of reported data while flowing DI water due to the presence of residual base. Polarization curves are typically collected while the cell is operated with

solutions of various concentrations of alkaline solution, starting from salt solutions and ending in DI water. One of the main issues with this approach is that any residual KOH in the operating cell could erroneously boost the cell performance, showing high performance with DI water. Therefore, this work started from the opposite direction, where the cell was initially broken in at steady state with a DI water feed. Then, increasing concentrations of KOH were fed to the cell. The results are shown in **Figure 3.1** for an AEMEL operating at 1.0 A/cm^2 and 60 ^{o}C. For the first 12 hours, the cell was fed 18.2 MΩ DI water. Under this condition, the cell started at a voltage of 2.15 V, settling down to a steady-state value of 2.11 V. After this initial operation on DI water, the feed was replaced with 0.01 M KOH solution and the operating voltage dropped precipitously to just over 1.9 V. This >200 mV drop in the cell operating voltage with very dilute KOH shows how trace amounts of KOH in the cells can affect the operating voltage. Next, the electrolyte was progressively changed to feed solutions with higher KOH concentration. Every increase in KOH concentration improved the cell operating voltage. The final electrolyte fed to the cell was 0.3 M KOH, which had a stable operating voltage of ~1.75 V, which is 350 mV lower than true DI water operation.

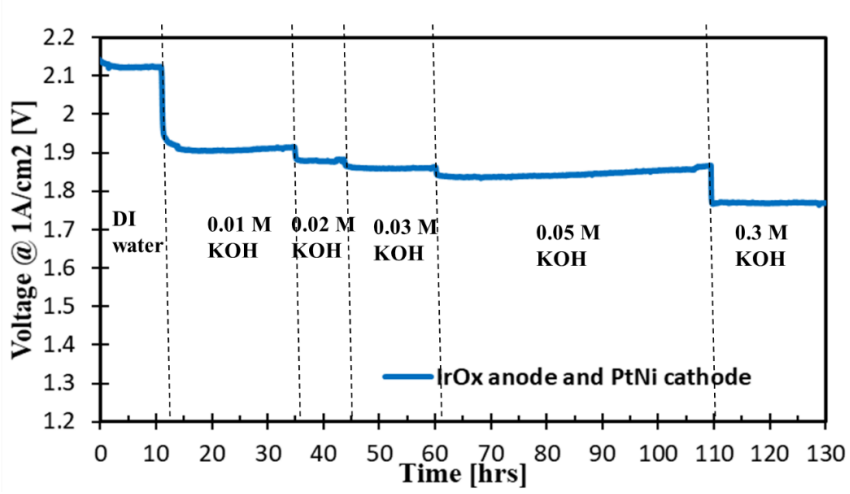

Figure 3.1: Operation of an AEMEL at 1.0 A/cm^2 and 60 ^{o}C with various concentrations of added KOH. The cells were first operated with DI water and no initial KOH feed. Anode: IrOx catalyst with GT69 ionomer. Cathode: PtNi catalyst with GT-32 ionomer; AEM: GT72-10 (30 µm).

The results in Figure 1 call into question any studies in the literature where polarization curves were collected relatively quickly after being operated initially with an alkaline solution (0.1 – 1 M KOH) and then switched to DI water. It is our contention that many of those cells did not purge the cell for a long enough time with a sufficient volume of DI water. Hence, they still contain significant KOH in the cell. This statement is supported by Lindquist et al. **[186]**, who showed that there is a significant difference in the performance of cells based on the amount of time that they were flushed with DI water after KOH operation. To show the role of trapped KOH on cell behavior, we started a cell operating on 0.3 M KOH. The polarization curve for the aqueous 0.3 M KOH feed is shown as red triangles in **Figure 3.2a**. At this condition, a cell voltage of 1.71 V was recorded at a current density of 1.0 A/cm^2. This voltage response is comparable to literature reports utilizing noble metal-based catalysts and similar operating conditions.

Next, the cell feed was switched to DI water. To initiate this, DI water was fed to the cell at open circuit at flowrate of ~ 50 mL/min for 5 minutes. Then, the DI water flowrate was reduced to the typical value of 2 mL/min. A polarization curve (Green diamonds) was collected at this point and the polarization curve nearly overlaps with the polarization curve taken with 0.3 M KOH. There was only a small deviation at higher currents where the operating voltage was increased to 1.74 V at 1.0 A/cm^2. Continuing with the same water flowrate, after 1 hour (where ~350 mL of DI water had been fed), another polarization curve was collected, shown as orange squares in **Figure 3.2a**. both polarization curves showed similar behavior in the kinetic region of the polarization curve, but there was a clear increase in the Ohmic resistance of the cell. At 1.0 A/cm^2, a voltage of 1.8 V was recorded, which is slightly higher than operation with 0.3 M KOH. However, a clearer picture of what is happening is shown in transient response experiment in **Figure 3.2b** where a cell was operated at a constant current density of 1.0 A/cm^2 for 100 hours. For the first ca. 5 hours, the cell was operated on 0.3 M KOH, where a steady-state voltage nearly identical to the polarization curve was observed. Then, the cell was switched to DI water. From that point, the voltage rose and it took the cell more than 3 hr to reach the new steady state voltage of just over 2.0 V, a 300 mV increase. After only 1 hr on DI water feed, the cell voltage was just over 1.8 V. Based on this, it is clear that after 1 hr of DI water feed (even in **Figure 3.2a** where 350 mL of water had been run through the cell), there is still residual KOH in the cell that is affecting the cell performance. To show the importance of adequately flushing the cell before taking DI water fed polarization curves, a polarization curve was taken after 13 hours of constant DI water flow and the resulting polarization curve (indicating true DI water operation) is shown as blue diamonds in

Figure 3.2a. The polarization curve collected after 13 hr (**Figure 3.2a**) shows a clear loss in performance. It also shows an operating voltage at 1.0 A/cm^2 that exactly corresponds to the steady state value in **Figure 3.2b**, suggesting that the true voltage response on DI water had been achieved. It is noteworthy that the total volume of DI water flowed through the cell during this time was ~2 L, which is larger than typical in the literature for switching from KOH to DI water feed. Based on **Figures 3.2a** and **3.2b**, it appears that an appropriate standard procedure would be to flush all AEMELs for at least 5 hr before taking a polarization curve meant to represent pure DI water conditions, and longer times are even better.

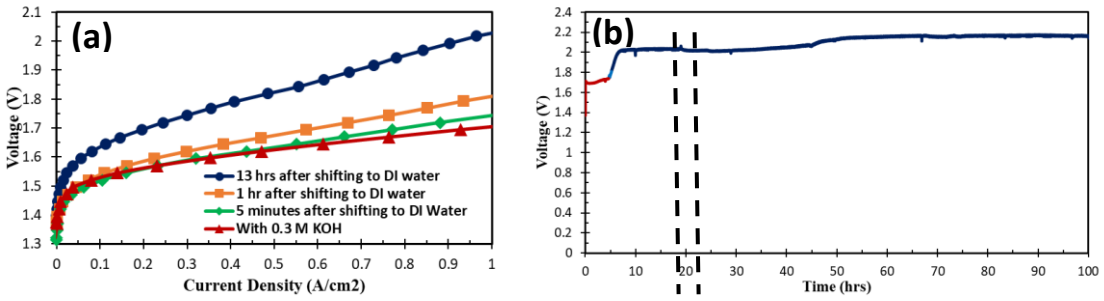

Figure 3.2: a). Polarization curves collected at start of the cell while break-in on 0.3 M KOH and then at different times while the cell was switched to DI water feed. b). Steady state voltage response of the cell break-in on 0.3 M KOH and the switched to DI water while operating at a constant current density of 1A/cm^2. AEM: GT-72-10 (30 µm), IrOx as OER electrocatalyst and PtNi as HER with no backpressure at cell temperature 60 ^{0}C.

Lastly, once the cell reached true DI water operation, it was allowed to run at steady state until 100 total hr was achieved (**Figure 3.2b**). During this time, the cell voltage increased to ~ 2.15 V at a degradation rate of around 1.3 mV/h. It is possible that this increased operating voltage is related to membrane, ionomer, or catalyst degradation initiated by the harsh initial alkaline environment in the AEMEL anode at the beginning of

testing – where both high pH and high potential are present. All of those components perform efficiently on alkaline feed, however, that feed can have a detrimental effect on long term durability.

To show the possible effects of the electrolyte concentration on durability, a cell was broken-in on KOH and set to operate at a constant current density of 1.0 A/cm^2 for four days. The result is shown in **Figure 3.3**. During polarization, **Figure 3.3a**, the cell voltage at 1.0 A/cm^2 was again 1.7 V, with low kinetic resistance. At the beginning of the durability test, the operating voltage exactly matched the polarization curve, but over the next 20 hr, the voltage increased to 1.8 V (5 mV/h degradation rate). After 20 hr, the cell voltage started to decrease again. Though this may be viewed as a positive sign, it is known that internal short-circuits from physical changes can also lead to this behavior **[172]**. Such a short would also result in a decrease in the H_2 production rate. Therefore, the hydrogen flowrate was measured at various intervals and it was found that the hydrogen flowrate was reduced by approximately 50% after 50 hr operation. This behavior was confirmed by running multiple cells. Therefore, it is likely that although a more concentrated alkaline environment is good for initial performance, it may be detrimental to long-term durability. Even breaking in the cell on alkaline feed and then switching to DI water may be detrimental and could initiate cell degradation, as shown in **Figure 3.2b**.

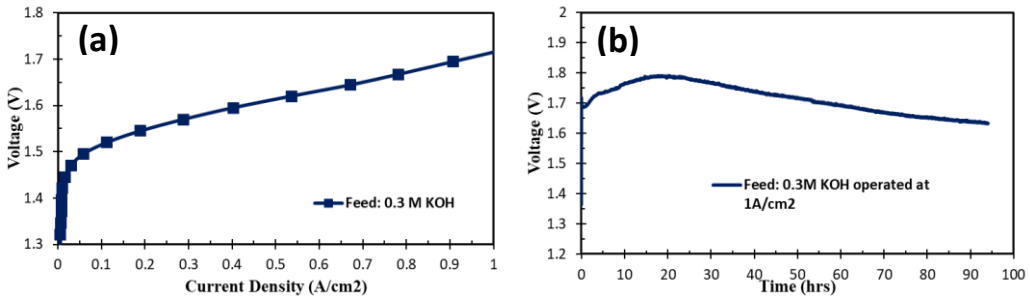

Figure 3.3: AEMEL (a) polarization curves and (b) durability test (at 1.0 A/cm^2) showing voltage response of a cell that was completely operated while feeding 0.3 M KOH electrolyte. AEM: GT-72-10 (30 µm). Anode catalyst: IrOx. Cathode catalyst: PtNi. Cell temperature: 60 ^{o}C.

3.2 Electrochemical Impedance Spectroscopy (EIS) measurements

EIS analysis was performed at three current densities, 100, 500 and 1000 mA/cm^2, for cells operated on both 0.3 M KOH and DI water. The resulting Nyquist plots are shown in **Figure 3.4**. Important parameters like Ohmic area-specific resistance (R_s), charge transfer resistance (R), and double layer capacitance (Q) were extracted. At 100 mA/cm^2, the Ohmic resistance of the cell while operating on 0.3 M KOH was 0.21 Ohm cm^2 which increased to 0.26 Ohm cm^2 when operating with DI water feed. At that same current, the charge transfer resistance was 0.44 Ohm cm^2 with 0.3 M KOH and 0.65 Ohm cm^2 with DI water feed. The double layer capacitance was 1.11 F (5 cm^2 area) in 0.3 M KOH which decreased to 0.17 F when cell was switched to DI water feed. At 500 mA/cm^2, the ohmic resistance increased from 0.20 Ohm cm^2 to 0.31 Ohm cm^2 when shifted from alkaline solution to DI water feed while the charge transfer resistance increased from 0.14 Ohm cm^2 to 0.26 Ohm cm^2. At 1000 mA/cm^2, the ohmic resistance increased from 0.22 Ohm cm^2 to 0.32 Ohm cm^2 when shifted from alkaline solution to DI water feed while the charge transfer resistance increased from 0.09 Ohm.cm^2 to 0.15 Ohm.cm^2.

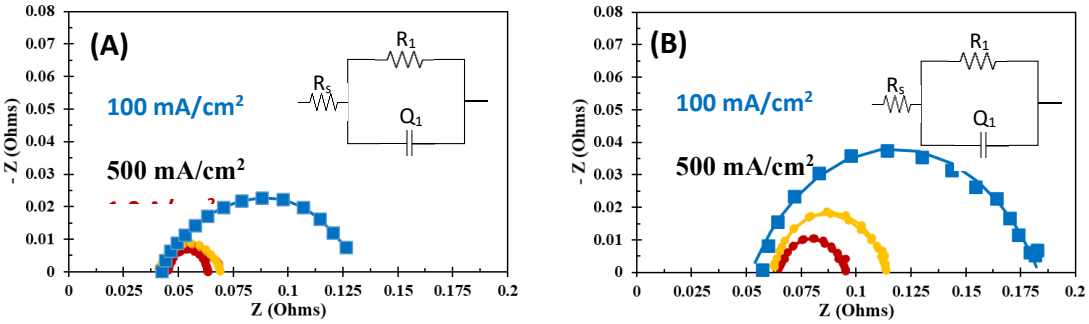

Figure 3.4: Nyquist plots and circuit analysis for an AEMEL operating at 100 mA/cm^2 (Blue curves), 500 mA/cm^2 (Yellow curves) and 1000 mA/cm^2 (Red curves) operated in (A) 0.3 M KOH; and (B) DI water.

Table 3.1 shows EIS data parameters obtained by fitting the data with an equivalent circuit at different current densities while operating on 0.3 M KOH and DI water. Both the Ohmic resistance and the charge transfer resistance increased when the operating electrolyte was changed from 0.3 M KOH to DI water feed. The average increase in the Ohmic resistance was 43%. This was driven by a reduction in the charge carrier concentration in when DI water is fed vs. KOH. AEMs are well-known to uptake liquid water during operation and DI water is not able to assist with ion transport within the electrode and membrane in the same way as a KOH solution can contribute. KOH feed also offers added benefits of osmotic deswelling, also noted elsewhere **[193]**. Additionally, the average increase in the charge transfer resistance was 45%. This increase in resistance could be attributed to reduction in additional ion-transport pathways and ion-transport in the ionomer resulting in a lower electrochemically active surface area when operating on

DI water versus KOH **[194]** these trends are in agreement with other prior work **[195], [196]**.

Table 3.1: EIS data parameters obtained by fitting the data with an equivalent circuit at different current densities while operating on (A) 0.3 M KOH and (B) DI water

Parameter	**0.3 M KOH**			**DI water**		
	100 mA/cm^2	**500 mA/cm^2**	**1000 mA/cm^2**	**100 mA/cm^2**	**500 mA/cm^2**	**1000 mA/cm^2**
Q_1 (s^a/Ω)	1.10661	0.509898	0.178236	0.170222	0.079326	0.153619
A	0.62144	0.708758	0.83654	0.67152	0.790077	0.756816
R_S (Ω)	0.042035	0.040652	0.045338	0.052312	0.0618	0.06441
R_1 (Ω)	0.087624	0.028482	0.018081	0.130921	0.052089	0.031112
X^2	0.011895	0.008204	0.003794	0.030734	0.011121	0.002551

3.3 Cell break-in and operation on DI Water Feed

To investigate if exposure to KOH accelerates AEMEL degradation, it is important to break-in and operate a cell that was never exposed to flowing KOH. That is not to say that DI water operation is completely safe from an AEMEL perspective. Operating an AEMEL on pure water can introduce ionomer swelling, dissolution and poisoning **[160]**. Cells were assembled with only DI water feed during break-in and operation. Representative data is shown in **Figure 3.5**, with a polarization curve shown in **3.5a**. For this cell, the operating voltage was around 2 V at 1.0 A/cm^2, which is consistent with the data in **Figure 3.2**. Operating at a steady current of 1.0 A/cm^2, the cells operated quite stably, with a low degradation rate of 93.5 μV/hr over 500 hr. It should also be noted that the DI water pH was monitored during the operational lifetime and was measured to be 7.6 at the end of operation. Lastly, the exiting hydrogen volumetric flowrate was measured

during operation, fluctuating at steady state from 39.4 to 40.1 mL/min, which corresponds to a faradaic efficiency between 98.8-99.8 %, even after 500 hours. This data strongly suggests that exposure of AEMELs to KOH at any point during operation is detrimental to their long-term stability. If the field is to transition to true DI water operation, there is a need to improve the performance, likely by increasing the electrochemical surface area of existing systems without the addition of KOH. Previous reports have investigated the use of carbonates as the supporting electrolyte for these systems, but that leads to other systems-level problems during operation such as carbonate accumulation and lower ion mobility resulting in increased cell resistance. This means that new strategies are needed for cell and component design, including the structure of the catalysts and electrodes as well as their integration into operating AEMELs.

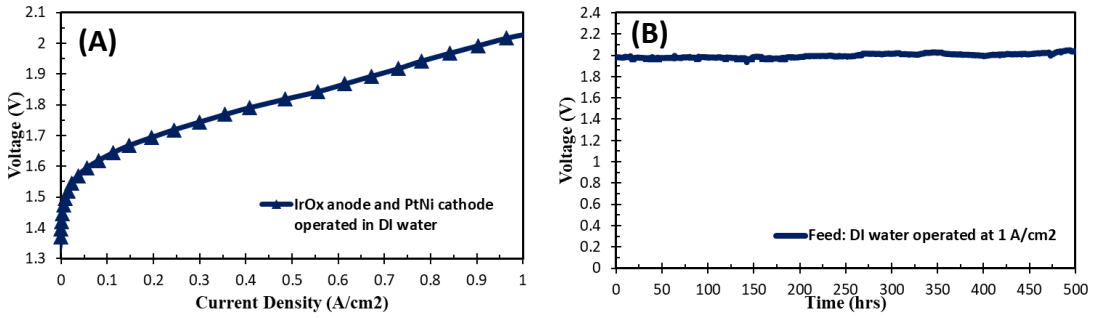

Figure 3.5: (A) Polarization curves and (B) durability test (at 1.0 A/cm^2) for an AEMEL only exposed to DI water during operation. AEM: GT-72-10 (30 µm); Anode: IrOx; Cathode: PtNi. Cell temperature: 60 ^{o}C.

4. Conclusions

Anion exchange membrane water electrolyzers (AEMELs) have the potential to lower the cost of hydrogen production. However, there is significant research and development that remains to make these cells and systems commercial-ready. In the AEMEL, the oxygen evolution reaction (OER) electrode dictates much of its performance

as it is critical in terms of facilitating water transport to the membrane, removing oxygen bubbles, and enabling anion and electron exchange while flooded in water. This study showed that the performance of the OER electrode is strongly affected by the concentration of supporting electrolyte. Because of this, it is likely that many of the studies in the literature begin their data collection before the AEMEL is fully purged of KOH, which can lead to under-prediction of the DI-water operating voltage in these systems. It was also shown that exposure to KOH can be detrimental to cell stability, meaning that there is a balance between performance and durability that needs to be found. A cell operation on DI water for its entire life was able to achieve 500 h life at a low degradation rate, but at a higher operating voltage than desired for commercial applications.

CHAPTER 4

EFFECT OF POROUS TRANSPORT LAYER PROPERTIES ON THE ANODE ELECTRODE IN ANION EXCHANGE MEMBRANE ELECTROLYZERS[3]

Abstract

Anion exchange membrane water electrolyzers (AEMELs) have recently received significant attention due to their potential advantages over existing commercial water electrolysis technologies. However, AEM electrolyzers have lower performance and durability than desired. One of the most important components in dictating AEMEL performance is the porous transport layer (PTL) which serves multiple purposes in the oxygen evolution reaction (OER) electrode, including: (i) water transport into the cell, (ii) electron transport from the bipolar plate to the catalyst layer, (iii) maintaining mechanical pressure for sealing, (iv) supporting and adhering the catalyst layer, and (v) oxygen bubble removal from the catalyst layer to the flow field. In this study, several PTLs were investigated, comprising a range of materials, fabrication methods, feature size and thickness. It was found that higher porosity helped to facilitate multiphase (O_2, H_2O, etc.)

---

[3]Hassan, N.U., Motyka, E., Kweder, J., Ganesan, P., Brechin, B., Zulevi, B., Mercado, H.R.C., Kohl, P.A. and Mustain, W.E., Effect of porous transport layer properties on the anode electrode in anion exchange membrane electrolyzers, *J. Power Sources*, (2022).

transport; however, catalyst layer adhesion decreased, contact resistance increased and the cell operating voltage increased. Nickel-based PTLs perform relatively better than stainless steel. It was possible to achieve low operating voltages with both fiber felts and sintered structures. Furthermore, an increase in thickness (from 0.30 to 0.65 mm) did not affect transient voltage response, however, it had negative effect on performance stability. The experimental findings presented here provide important insights for development of PTL materials and structures for efficient and low-cost water electrolysis.

1. Introduction

Renewable energy sources such as solar, wind, and tidal have seen a drastic reduction in cost in recent years **[197]**. However, due to their intermittent nature, energy storage solutions are needed that can reversibly store excess energy for later use. Batteries are one possible option. Lithium-ion-based systems have proven high energy efficiency, reliability and are widely available. However, their relatively high cost makes their deployment at the multi-GW scale economically unattractive. Another possibility is to store the excess electricity in chemical bonds. Hydrogen is one promising options that can be stored in large tanks, underground caverns **[198]** or fed into the existing natural gas grid. This hydrogen can be used later to produce electrical energy either in fuel cells or by powering gas turbines, or it can be used for industrial purposes.

Hydrogen can be produced by various methods including methane steam reforming, water electrolysis, etc. Unlike reforming, which requires high quality heat, electrochemically-driven water electrolysis using renewable energy can potentially enable truly zero-emission hydrogen production. In fact, commercial-scale electrolysis technologies have been in operation for the last 100 years. The most widespread and cost-

effective electrolysis system today is the alkaline electrolyzer (AEL), which feeds a highly concentrated KOH solution (20-40 wt%) to both sides of the cell, operates at low current density (typically 0.2-0.4 A/cm^2) **[199]**, and has relatively low discharge hydrogen pressure (1-30 bar). Such operating parameters make AEL systems large, somewhat risky in terms of safety, and cumbersome to maintain.

To address the limitations of the AEL, the proton exchange membrane water electrolyzer (PEMEL) emerged in the 1960s, first introduced by General Electric **[200], [201].** The membrane-based ionic separator allows for a compact design, high operating current density (1.0-5.0 A/cm^2), simplified balance-of-plant, easy maintenance, rapid response, operation on ultra-pure water and high hydrogen discharge pressure (up to 90bar) **[202], [203], [204], [205], [206]**. However, to achieve the best performance, PEMELs use carbon-supported platinum at the hydrogen evolution reaction (HER) cathode and IrO_2 at the oxygen evolution reaction (OER) anode as well as expensive Nafion membranes. Moreover, the PEMEL porous transport layers (PTLs) and bipolar plates are titanium-based and coated with a Pt layer to avoid corrosion. These metals are expensive, and iridium is scarcer than platinum and some have suggested that their scalable deployment for integration with renewables may not be feasible **[207]** with such a high reliance on these metals.

A relatively new and emerging technology is the anion exchange membrane water electrolyzer (AEMEL). The AEMEL has gained traction in recent years because it potentially can combine benefits from both traditional alkaline and PEM water electrolysis – leading to an economically viable and scalable solution **[208], [209], [210], [211]**. In an AEMEL, the electrode compartments are separated by a thin, dense, polymer membrane

similar to the PEMEL. This anion exchange membrane (AEM) moves hydroxide ions (OH^-) from the cathode to the anode during operation as in AELs, but the system is much more compact. The operating pH of the system reduces corrosion issues of the component materials, allowing the platinized titanium in the PTLs and bipolar plates to be replaced by stainless steel (SS) or nickel alloys. It is also possible for platinum group metal (PGM) catalysts to be substituted by cheap and abundant materials like nickel and iron etc. **[209],** though the exploration of catalysts that lower the PGM content is outside the focus of this work.

Of the cell components listed above, one of the most critical for membrane-based electrolyzers (both PEMELs and AEMELs) is the PTL in the OER anode. The anode PTL serves multiple purposes, including: (i) water transport into the cell, (ii) electron transport from the bipolar plate to the catalyst layer, (iii) maintaining mechanical pressure for sealing, (iv) supporting and adhering the catalyst layer, and (v) oxygen bubble removal from the catalyst layer to the flow field **[205], [212], [213], [214]**. These functions are illustrated in **Figure 4.1**.

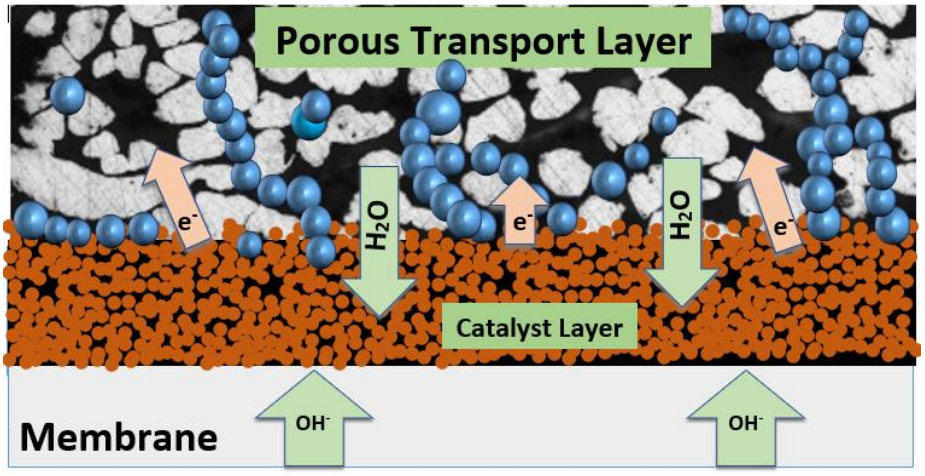

Figure 4.2: Schematic diagram of porous transport layer, depicting transport phenomena in the catalyst layer

Taking all of the above functions into consideration, it is no surprise that in PEMELs it has already been shown that the PTL material type and structure are very important. The material of construction can be a significant driver for the ohmic resistance while the PTL structural properties (i.e., porosity, pore diameter) primarily influence the mass transport resistance of liquid and gas species **[214]**. The PTL structure can be controlled by changing the particle or fiber type, shape, and size of the starting material during the manufacturing procedure. Generally, the starting material with larger particles/fibers results in a larger pore diameter and higher porosity. In PEMELs, it has been shown that the PTL with large porosity will boost gas removal but will also increase the ohmic resistance of the PTLs **[215]** . The optimum PTL pore diameter in PEMELs has been reported to be around 10 μm **[215], [216]** and the optimum PTL porosity is in the range of 30 – 50 % **[214], [217]**. PTL thickness has also been studied, but the findings have been more complex and difficult to generalize **[212], [217], [218], [219], [220]**. Another area where PTL material and structure may play a role is the interfacial contact between PTL and catalyst layer **[214]**. Suermann et al., **[221]** and Schuler et al., **[222]** found that the interface between PTL and catalyst layer not only effect mass transport but also the high frequency resistance.

Taking the discussion above into consideration, it is no surprise that recent work has found that in many configurations the PTL has the most statistically significant effect on AEMEL performance **[223]**. Just like the PTL in PEMELs, the PTL in AEMELs must have carefully engineered material and structural properties **[224]**. Though many of the properties from PEMELs are expected to translate to AEMELs, this has not been confirmed, which is important given the difference in operation and the water balance

between modern PEMELs and AEMELs. Despite these differences, it is particularly troublesome the low number of studies that are available in the literature for AEMEL PTLs to date. Recently, Zu et al., **[225]**, investigated a series of anodes with commercial SS PTLs having different pore and surface structures. They found that the PTL with the smallest fibers and the smoothest surface led to the best performance. They concluded that larger contact area, higher catalyst utilization, and decreased lateral catalyst-layer electrical resistance led to the improved performance. Park et al., **[226]** recently reported AEMEL performance studying the effect of pore structures in nickel-based porous transport layers by comparing with conventional Ti-felt and attributed this superior performance to the reduced mass transfer resistance due to interconnected pore structure. Xiao et al., **[227]** used a Ni foam PTL and suggested that such PTL materials may also offer catalytically active species throughout the pores of the PTL, which may increase activity. These early results show that the AEMEL anode PTL with engineered chemistry and porosity must be realized **[224]**.

Though the above studies on AEMELs have shown that the PTL has a significant effect on performance, and they have done a good job discussing available materials and physical properties, what these studies have not done is make definitive links between the PTL material, porosity, structure, and fabrication process and performance. Therefore, the purpose of this paper is to fill the gap in the literature and to make the needed definitive links by investigating a series of anode PTLs that cover a spectrum of materials, fabrication processes, physical structure, and electrical properties. In this work, 14 commercial and pre-commercial PTLs were used. These PTLs were purchased or created to cover a wide range of properties, including porosity, pore size, thickness, electrical conductivity,

manufacturing method and material. Each PTL was integrated into the anode of several operating AEMELs. The steady-state and transient performance of the AEMELs was investigated with each of the PTLs. Where possible, strong links were made between specific PTL properties and performance as well as operational stability.

2. Materials and Methods

2.1 PTL Selection and Custom Manufacturing

Fourteen PTLs were studied in this work. They were either purchased/donated from commercial sources or custom-made. Table 4.1 and Table 4.2 summarize the PTL physical and electrical properties. Figure 4.2 provides a flowchart showing the relationship between all of the PTL types.

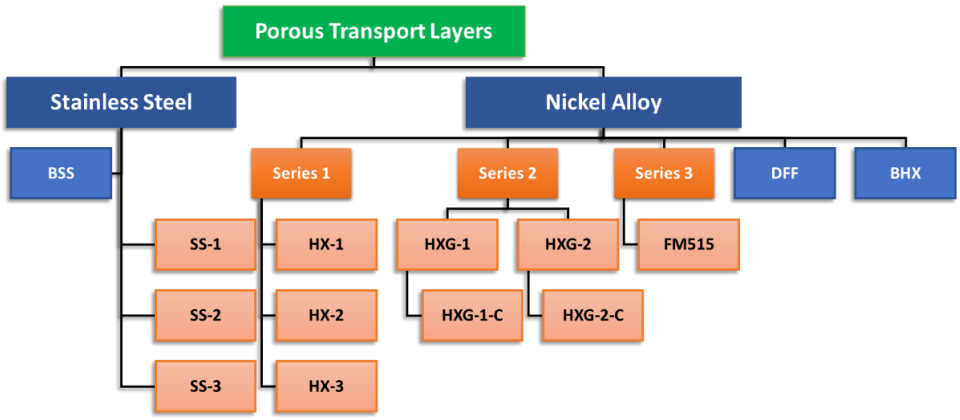

Figure 4.3: Flowchart showing the all the PTLs studied in this work.

Three commercial PTLs were used: Ni fiber paper (Dioxide Materials, denoted as DFF), stainless steel fiber paper (Bekaert 20FP3, denoted as BSS), and a sintered Ni felt (Bekaert, denoted as BHX). The other eleven PTLs were manufactured by Technetics Group. They were fabricated using a proprietary process that starts from elongated particles – either Ni-alloy (Hastelloy X, UNS N06002) or stainless steel (Type 347, UNS S34700) . Process steps to form the PTLs include particle preparation, deposition,

sintering, densification, and finishing. Particle preparation after formation includes cleaning, drying, and size classification. After particle synthesis, a blending process adds hexagonal boron nitride (h-BN) particles to the metal fibers. Additive manufacturing is used to deposit a solid layer onto a forming table. The deposition is a line-of-sight process using directed nozzles or gravity to build the sheet on the forming table to the prescribed thickness. At this stage, the sheet of fibers is essentially a "green compact" in powder metallurgy terms, which is an unsintered low-strength material. To achieve the required density and strength, the green compact sheets are batch sintered in vacuum furnaces using a partial pressure non-oxidizing atmosphere. The sintering processes are designed to bond the fibers without pore closure. The final process steps include mechanical compaction to achieve thickness uniformity then final sizing by traditional cutting operations.

Table 4.1: Material, manufacturer, fabrication method and abbreviation for the PTLs

Sr. #	**Description**	**Material**	**Manufacturer**	**Fabrication method**
1	HX-1	Ni alloy	Technetics Group	Sintered
2	HX-2	Ni alloy	Technetics Group	Sintered
3	HX-3	Ni alloy	Technetics Group	Sintered
4	SS-1	Stainless steel	Technetics Group	Sintered
5	SS-2	Stainless steel	Technetics Group	Sintered
6	SS-3	Stainless steel	Technetics Group	Sintered
7	DFF	Ni alloy	Dioxide Materials Inc.	Fiber felt paper
8	BSS	Stainless steel	BEKAERT	Fiber felt paper
9	BHX	Ni alloy	BEKAERT	Sintered

10	HXG-1	Ni alloy	Technetics Group (custom made)	Sintered gradient
11	HXG-1-C	Ni alloy	Technetics Group (custom made)	Sintered gradient
12	HXG-2	Ni alloy	Technetics Group (custom made)	Sintered gradient
13	HXG-2-C	Ni alloy	Technetics Group (custom made)	Sintered gradient
14	FM515-C	Ni alloy	Technetics Group (standard product, modified)	Sintered

Table 4.2: PTL characteristic properties, including thickness, porosity, pore size, feature size, contact resistance and electrical resistivity.

Desc.	**Thickness (mm)**	**Porosity (%)**	**Pore/hole size (µm)**	**Feature size; fiber diameter (µm)**	**Cont. Resis. @ 50 N/cm^2 (Ohms.cm^2)**	**Electrical resistivity (Ohm.cm)**
HX-1	~ 0.95	~ 80	> 15	~ 15	0.35	0.00266
HX-2	~ 0.5	~ 65	> 10	~ 15	-	-
HX-3	~ 0.27	~ 38	> 5	~ 15	0.20	0.00074
SS – 1	~ 0.82	~ 79	> 15	~ 20	1.20	0.00282
SS – 2	~ 0.5	~ 65	> 10	~ 20	-	-
SS – 3	~ 0.27	~ 32	> 4	~ 20	-	-
DFF	0.3	~ 68	> 10	~ 10	0.40	1.18
BHX	~ 0.65	~ 65	> 20	~ 20	0.15	0.12
BSS	0.30	~ 70	> 15	~ 12	0.60	0.83
HXG-1	1.04	~ 60	10 – 40	~30	0.10	1.26

HXG-1-C	0.60	~ 24	2 – 10	~30	0.09	-
HXG-2	~ 0.92	~ 88	20 – 40	~30	-	3.22
HXG-2-C	~ 0.18	~ 34	5 – 15	~30	0.19	0.68
FM515-C	~ 0.28	~ 38	10 – 30	~15	0.19	0.92

2.2 Catalysts, Ionomers and Membranes

Because this work is focused on the PTL, standard commercial materials from previous literature were used for the catalysts. This allows the effect of the PTL to be studied without also having to be concerned about the effects of the catalyst synthesis and batch-to-batch variability. For the cathode, the HER catalyst was a platinum nickel alloy (PtNi, Pajarito Powder). The cathode PTL was Toray-60 carbon paper with 5% wetproofing (Fuel Cell Store). For the anode, iridium/iridium oxide (IrOx, Nel Hydrogen) was used to facilitate the OER. The PTLs used at the anode were discussed in the previous section.

The AEM was a 40 μm thick functionalized and quaternized poly(norbornene) copolymer with 72% halogenated monomer and 10% crosslinker, sold as XION^{TM} Composite-72-10CL by Xergy Inc. The details regarding the synthesis of this polymer have been reported previously **[228]**, **[229], [230]**. The anode and cathode ionomers were poly(norbornene) copolymers with no added cross-linker. The synthesis and characterization of the ionomers, including their physical properties and ion-exchange capacity (IEC), was also previously reported **[231], [232], [233], [234]**. The cathode

ionomer was comprised of 73% halogenated monomer (GT73; IEC = 3.56) while the anode ionomer was comprised of 32% halogenated monomer (GT32; IEC = 1.88).

2.3 Electrode Fabrication

The anode and cathode electrodes were prepared by hand spraying a catalyst ink directly onto the PTLs. The ink preparation method was adapted from our previous work **[235], [236], [237], [238]**. At the anode, a typical process began by soaking 62.5 mg of GT73 in DI water (1-2 mL) for 30 mins. Then, the swollen ionomer was ground with a mortar and pestle for 10 minutes to allow it to break up into its fine particles. Next, 250 mg of the catalyst and 20 mg of PTFE powder (Ultraflon MP-25, Fuel Cell Store) were added, and the materials were further ground for 10 minutes, forming a uniform paste/slurry. Then, 9-10 mL of 2-Propanol (IPA) was added to convert this slurry into a uniformly dispersed ink. The ink was then transferred into a vial and sonicated in an ice bath for 60 – 90 mins. Finally, the catalyst ink was hand-sprayed using an Iwata spray gun onto 25 cm^2 PTLs, which were later cut into smaller electrodes for testing. An identical procedure was applied for preparing the cathode ink. The catalyst to ionomer ratio in the cathode was 4:1 while it was 3:1 in the anode. The cathode solids were typically comprised of 30 mg of GT32 ionomer, 150 mg of catalyst and 12 mg of PTFE powder.

2.4 AEM Electrolyzer Assembly and Testing

Prior to cell assembly, the AEMs and electrodes were ion exchanged in a 1.0 M KOH solution for a total of 60 min (refreshing the solution every 20 min). Excess surface KOH was removed from the electrodes and AEM by rinsing with DI water, followed by lightly dabbing with lint-free laboratory towels (Kimwipes). To assemble the cell, the AEM was placed between the two electrodes in customized 5 cm^2 Scriber cell hardware with no

prior hot pressing. Both the anode and cathode flow field had single serpentine channels. The anode flow field was made from 316 stainless steel while the cathode flow field was made from graphite. While assembling the cell, gaskets were placed outside of the active area but between the AEM and the hardware. The gaskets not only provided gas-sealing, but their thicknesses were selected to provide a compression of approximately 25%.

Once assembled, the lab-scale AEMELs were tested using a custom-built electrolysis test station powered by an Arbin Model BT-2000. All tests were performed at a cell temperature of 60 °C. All cells were fed with a 0.3 M KOH solution at a rate of ~ 2 mL/min using a BT100S Basic Variable Speed Peristaltic Pump with Pump Head YT25. The feed solution was preheated and maintained at 60 ^{o}C before being fed to the anode only. The cathode inlet was closed while the outlet was fed to a bubbler to visualize hydrogen evolution before being sent to the building exhaust. The cathode effluent was periodically fed to a Thermo Fisher Scientific GFM Pro Flowmeter to measure the volumetric flowrate of the evolved H_2 gas, which was then used to determine the faradaic efficiency of the operating cells.

To begin cell testing, each cell was equilibrated at the desired temperature for 30 to 60 min at zero current while flowing the feed solution to the anode only. The cell was conditioned by applying a small current (100 mA/cm^2) and allowing the voltage to reach steady state over a period of 30-60 mins. After the cells were broken-in, polarization curves were collected from 1.3 V to 2.4 V at a 20 mV/s scan rate. Then, the current density was set to 1.0 A/cm^2 and the steady-state voltage was monitored.

2.5 Physical Characterization

Interfacial contact resistance was measured in fuel cell hardware that was modified by covering the graphite current collectors with ELAT, LT-1200-W carbon cloths [(D.P. Davies, 2000)]. The bottom piece of carbon cloth was adhered to the edges of the graphite plate, while the top carbon cloth remained unattached. A 25 µm-thick PTFE film with a circular opening (9mm in diameter) was placed on the surface of the bottom carbon cloth. The purpose of the PTFE film was to control the exposed electrical contact area of the test sample. The PTL was placed on the 9mm opening of the PTFE film so that it would sit on the top of the carbon cloth and the second carbon cloth was placed on top of it. The other side of the fuel cell hardware was used to close the cell. The assembled cell was then placed in between the two platens of a hydraulic press. In between the top platen and the fuel cell hardware, a compression-only load button cell (model: LBC-750, Transducer Techniques) was used to measure the compression force. Once in place, a current of 100 mA (Biologic VSP) was applied and the voltage was measured as a function of applied compression. The contact resistance was calculated using the surface area of the 9 mm diameter window, while the compression on the PTL was calculated from the total area of the PTL. No corrections for carbon cloth resistance or hardware resistance were done. The measured area specific contact resistances at 50 N/cm^2 are provided in Table 4.2 and a plot of the resistance as a function of pressure will be given and discussed later in the paper.

The electrical resistivity was determined using a four-probe technique by applying a 200 mA current for five minutes to 5 × 0.5 cm PTL strips/specimens. Five minutes was selected to allow all of the samples to show a stable voltage. At the end of the five minutes, the final voltage was used to calculate the resistance. The thickness of the PTLs was

measured using a digital micrometer with a 0.001 mm resolution and a ratchet stop for measuring flexible samples. Current probes consisting of two alligator clips were attached lengthwise at the outer edges of the PTL strips. The corresponding potential leads (consisting of "hook clips") were used as potential probes separated at a distance of 1.27 cm. The resistivity was calculated using the formula $\rho = R\frac{w \cdot t}{L}$, where "*R*" is resistance calculated from the current (A) induced voltage drop across the distance of potential probes, "*w*" is the width of the sample, "*t*" is the thickness, and "*L"* is the distance between the potential probes. The measured electrical resistivities for all the PTLs are provided in Table 4.2.

To visualize and evaluate PTL pore structure and feature size, a ZEISS Gemini 500, 0.02–30 kV Ultraplus Thermal FESEM microscope equipped with an Inlens secondary electron detector was used. The SEM images were collected with a 5 kV electron beam. The thicknesses of the PTLs were measured using high precision screw gauge micrometer (Mitutoyo 293-340-30 Digimatic 0-1"/25.4MM). Cross-sections of samples were prepared using methods preferred for thermal spray coatings, specifically epoxy-infiltration cold mounting and polishing methods **[239]**. Optical microscopy and image analysis using Leica LAS phase analysis software were used to measure the area-% porosity. For SEM imaging, non-mounted materials were examined directly but the polished mounts were sputter-coated with gold prior to imaging.

3. Results and Discussion

3.1 Sintered Ni Alloys (Hastelloy)

SEM images for the three Hastelloy X (UNS N06002) PTLs, fabricated by Technetics from sintered particles, are shown in Figure 4.3A-C and their characteristic properties are listed in Table 4.2. HX-1 is the least dense (80 % void volume) and is 0.95 mm thick. This is confirmed in Figure 4.3A, which shows large, open pores as well as varied structural features on the surface. HX-2 and HX-3 were made from sections of the HX-1 sheet; they were rolled to further compress it, simultaneously lowering the thickness and reducing porosity. HX-2 had a porosity of 65% and thickness of 0.50 mm, while HX-3 had a porosity of 38% and thickness of 0.27 mm. As the sintered HX-1 sheet was compressed to form HX-2 and HX-3, the typical feature size was the same, but the pore size was decreased. The compression also made the surface of HX-2 smoother than HX-1 and the surface of HX-3 to be nearly flat. The increased density has the possible negative of constricting mass transport in/out of the PTL. On the positive side, higher density can lower the contact resistance with the cell hardware (to be quantified later in this article), lower the electrical resistance (to be quantified later in this article), lower the stress on the catalyst layer and the membrane under cell compression, provide enhanced area for catalyst deposition, and improve the contact between the catalyst layer and the membrane. The effect of the surface density on the deposited catalyst layer is shown in Figure 4.4D-F in the Supporting Information. For HX-1, some catalyst particles were deposited on top of the PTL, but many were also deposited inside of the large holes/pores, losing their direct contact with the membrane and likely not contributing significantly to the OER. This means that fewer active sites are available at the interface for the reaction to happen.

However, large pores offer the advantage of facile gas bubble removal. On the other extreme, HX-3 has better catalyst particle coverage and a smooth surface, offering more active sites for reaction to happen and better contact. However, the dense catalyst layer may block the pores into the PTL, hindering bubble removal and increasing operating voltage.

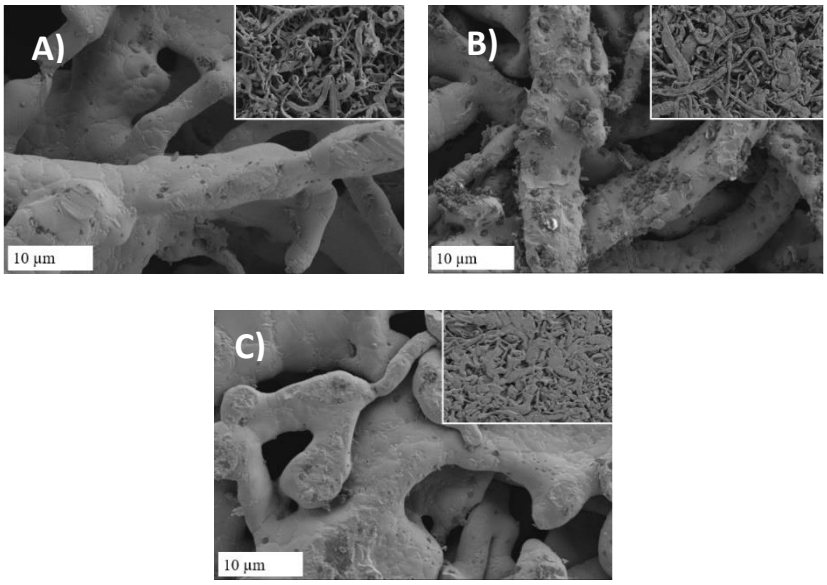

Figure 4.3: SEM images of the Ni alloy PTLs: (A). HX-1, (B). HX-2, (C). HX-3, showing the porous structure and surface features. Inset: Zoomed out images at 100 µm scale (1.35 kX magnification).

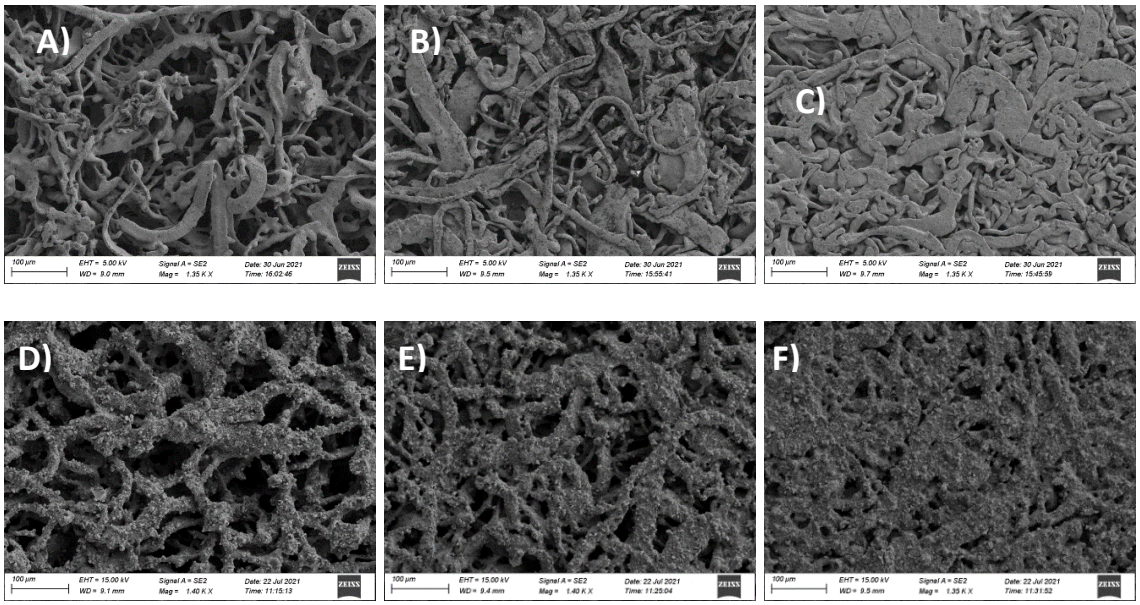

Figure 4.4: SEM images of Technetics Group Ni alloy PTLs and electrodes: (A). HX-1, (B). HX-2, (C). HX-3, showing plain porous structure and surface features, (D). catalyst layer deposited on HX-1, (E). catalyst layer deposited on HX-2, (F). catalyst deposited on HX-3.

Figure 4.5A shows the polarization behavior for AEMELs with the HX anode PTLs. In the low current density region, all three PTLs performed similarly. At higher current densities, where series resistances (ionic and electronic) contribute to the observed behavior, HX-1 and HX-2 showed slightly higher operating voltage than HX-3. One possible cause for this is the lower contact resistance for the thinner, higher density PTL as shown in Figure 4.6A where HX-3 has a much lower contact resistance than HX-1 over the entire range of applied pressure. Moreover, as shown in Figure 4.6B, the electrical resistivity for HX-1 was higher than HX-3, most likely driven by its increased thickness and large inter-feature spacing. It is also worth noting that no mass transport limitations were observed with any of the HX-X PTLs, even when the current density exceeded 3.5 A/cm^2. Mass transport and data/discussion on the effects of flowrate on performance is elaborated on in the Supporting Information file.

During steady-state operation at 1.0 A/cm^2, HX-3 also showed slightly lower operating voltage. Interestingly, for HX-2 and HX-3, the cell voltage increased over the first few hours of operation, while this did not occur for HX-1. The most likely explanation for this is that higher density PTLs, with their accompanying higher surface coverage and pore restriction near the catalyst layer, experience bubble accumulation over time, covering active sites, which results in a slightly drifting voltage. It is also possible that a denser PTL could also reduce water transport, developing a water gradient in the cell during operation. The last effect of lower density PTLs is that they have fewer contact points under compression, making the local stress higher for HX-1 vs. HX-2 and HX-3. This mechanical force can cause the extended PTL features and/or catalyst particles to penetrate into the swelled membrane and initiate membrane thinning and gas cross-over issues, which was observed with HX-1. In Figure 4.5B, starting at around 50 hours of operation the operating cell voltage started to lower. This was combined with a reduction in the exit hydrogen flowrate, clearly indicating that a short-circuit event had occurred. This was repeatable and occurred for many experiments with HX-1, thus what is shown here can be considered representative. The data in this section suggests that there are possible tradeoffs in behavior that are driven by the porosity/density of the PTL, each having a unique effect on AEMEL performance. All considered, it appears that a higher density, smooth surface is preferred, particularly in the context of supporting the catalyst, making contact with the hardware, and facilitating strong interaction of the catalyst layer and the AEM. Of course, there is an upper limit to the tolerable density, which will be discussed later.

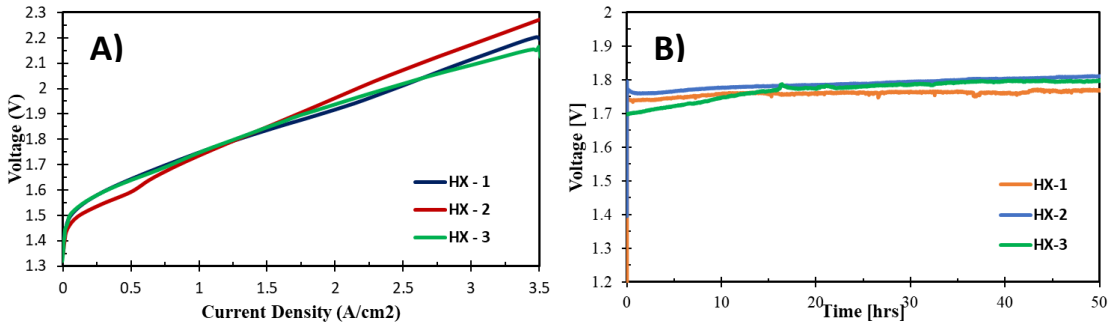

Figure 4.5: (A). Polarization curves and (B)steady-state response at 1.0 A/cm^2 for the three Ni-alloy PTLs. The AEM used was GT75-5 (40 um). IrOx anode and PtNi cathode. Cell temperature = 60 ^{o}C. Cells were operated with 0.3 M KOH fed to the anode only.

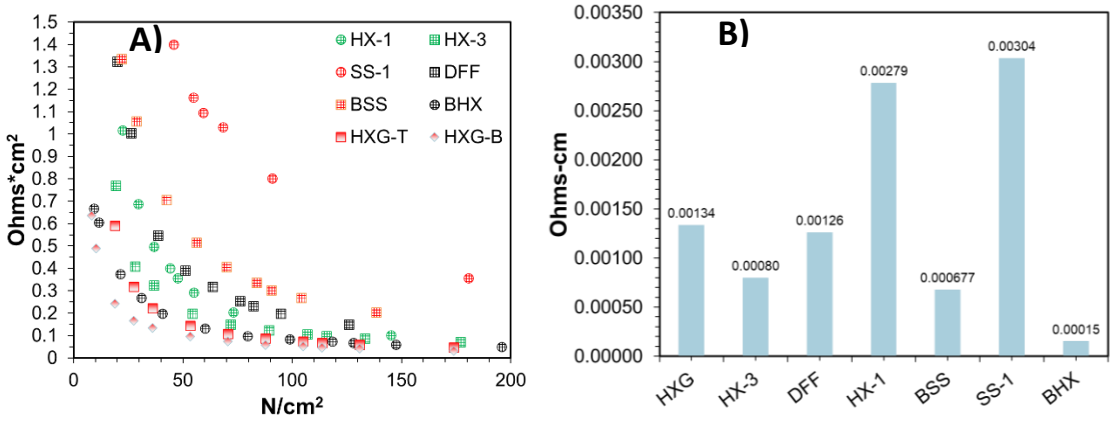

Figure 4.6: A) Contact resistance at various compression pressures and B) Electrical resistivity of the various Ni-alloy and SS PTLs investigated in this work

3.2 Sintered Stainless Steel

SEM images of the three sintered stainless steel (Type 347, UNS S34700) PTLs (SS-1, SS-2 and SS-3) are shown in Figure 4.7A-C. Physically, these PTLs had a slightly different structure than the sintered Hastelloy PTLs, with twisted, elongated, bar-like features, though their physical properties (i.e. porosity, feature size) were very similar. Again, a single large sheet, SS-1, was manufactured. It had a thickness of ~0.82 mm, porosity of 79% and a feature size ~ 20 um. Then, sections of the SS-1 sheet were rolled

to provide two additional PTLs with reduced thickness and porosity. As shown in Table 4.2, SS-2 had a thickness of 0.5 mm and a porosity of 65%; SS-3 had a thickness of 0.27mm and a porosity of 32%. Similar to the HX-1 PTLs, SS-1 had large pores and sharp features on the surface. The surface became smoother and less porous when rolled down in the case of SS-2 and SS-3. The SS-1 PTLs appeared to be softer that the HX-1 PTLs and hence experienced a little more flattening when rolled.

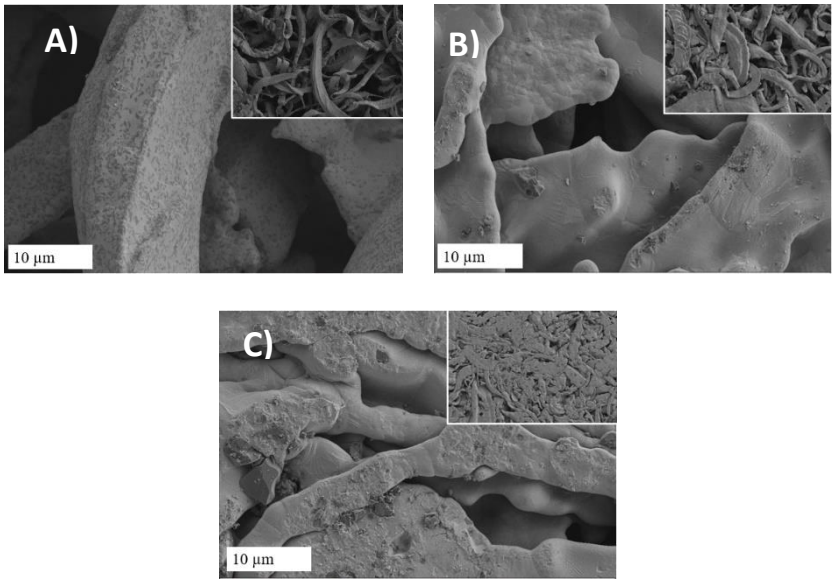

Figure 4.7: SEM images of the sintered stainless steel PTLs: (A). SS-1, (B). SS-2, (C). SS-3, showing the porous structure and surface features. Inset: Zoomed out images at 1.35 kX magnification.

Figure 4.8 shows polarization and steady state behavior of the SS-X anode PTLs when tested in an AEMEL. In the low current density region, all of the PTLs performed similarly. At higher current densities (in ohmic region), SS-1 and SS-2 show higher operating voltages, which mimics the trend observed with the three HX-X PTLs. Similar behavior to HX-X was also observed at steady state (1.0 A/cm^2), meaning that all of the

learning from the HX-X PTLs can be applied here and the same extensive discussion does not need to be repeated.

The similarity in structure and behavior of the HX-X and SS-X PTLs does allow for a very important comparison – the role of the manufactured material itself: Hastelloy versus stainless steel. In short, when the physical properties/structure of the PTL was similar, the SS-based PTLs always showed an operating voltage that was ~ 100 mV higher than the equivalent Hastelloy PTL. It is possible that this is due to the higher oxidative resistance for Hastelloy when compared to stainless steel. It is also possible that the PTL contributes to the cell performance as Ni oxidation products in alkaline media are comprised of a thin layer of hydroxides/oxy-hydroxides with known OER activity **[224], [240]**. However, one clear difference between the PTLs was their contact resistance. All of the SS PTLs showed higher contact resistance than their HX counterpart. Comparing the HX-1 and SS-1 PTLs at the highest tested pressure (180 N/cm^2, Figure 4.6A), SS-1 had its lowest contact resistance of 0.37 $\Omega\ cm^2$ while the HX-1 PTL showed a minimum contact resistance of 0.1 $\Omega\ cm^2$. This difference of 0.27 $\Omega\ cm^2$, would translate to a voltage drop of 270 mV at 1.0 A/cm^2. Of course, the results from the ex-situ test do not perfectly match the in-cell conditions, but it does show that the contact resistance of the material itself can play a key role in the measured AEMEL performance. Moreover, with similar thickness and pore structure, SS-1 had slightly higher electrical resistivity compared to HX-1 which also support electrochemical results.

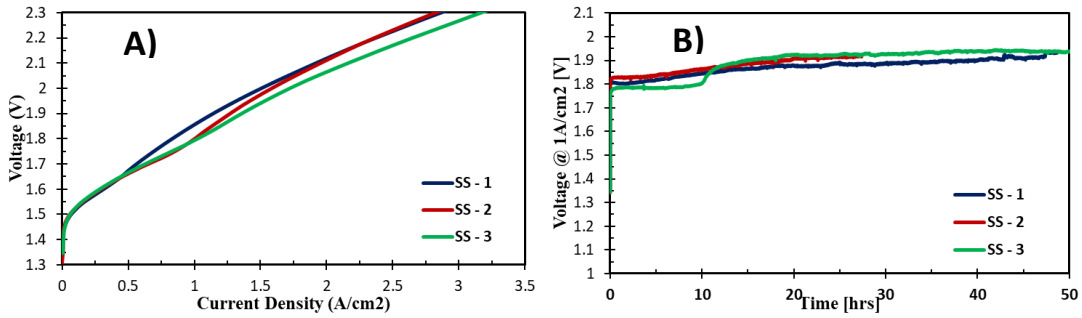

Figure 4.8: (A) Polarization curves and (B) steady-state response at 1.0 A/cm^2 for the three SS-X PTLs. The AEM used was GT75-5 (40 um). IrOx anode and PtNi cathode. Cell temperature = 60 ^{o}C. Cells were operated with 0.3 M KOH fed to the anode only.

3.3 Bekaert and Dioxide Materials Commercial PTLs

Next, the three commercial PTLs were investigated. The first was a Ni-based fiber felt from Dioxide Materials Inc (denoted as DFF). The second was a sintered Ni from Bekaert (denoted as BHX). The third was a Bekaert SS-based fiber felt (denoted as BSS). SEM images of these three PTLs are shown in **Figure 4.9** and their porosity, thickness, pore size and feature size are provided in **Table 4.2**. The DFF and BSS were both ~ 0.3 mm thick with bamboo like fibers and very similar porosity (~ 70%) and feature size (~ 10 um). The BHX PTL had more rectangular and larger features (~ 20 um), slightly lower porosity (65 %) and was approximately double in thickness (0.65 mm) than DFF and BSS. BHX had a similar porosity to HX-2 and SS-2, but larger features and larger pore size. It is also worth noting here that the two Ni-based DFF and BHX PTLs had very similar contact resistances that were much lower than BSS (Figure 4.6-A).

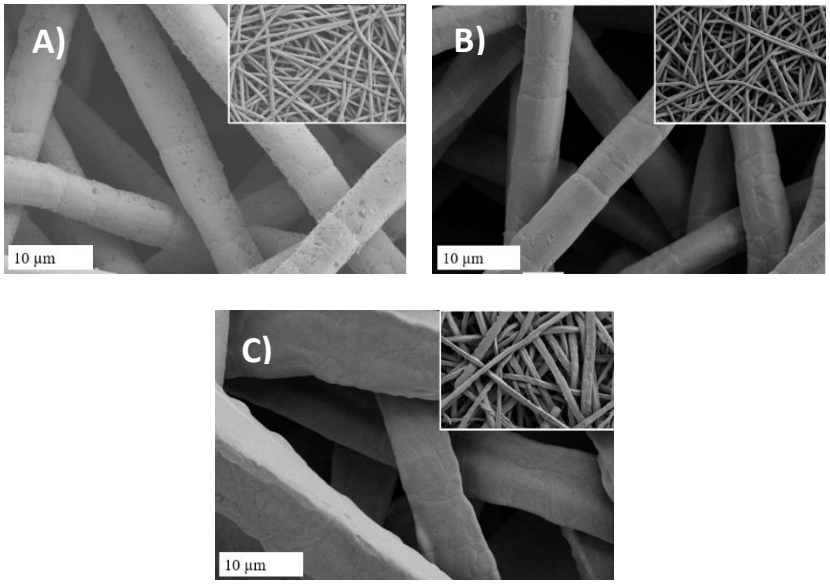

Figure 4.9: SEM images of the commercial PTLs in this study: (AI) Dioxide Materials Ni fiber felt; (B) Bekaert Stainless Steel fiber felt; (C) Bekaert sintered Ni. Insets: Zoomed out images at 1.35 kX magnification.

Figure 4.10 shows polarization and steady-state performance for these three PTLs during AEMEL operation. With similar properties, the Ni-based DFF performed better than the SS-based BSS – again by ~100 mV at 1.0 A/cm^2 – showing the same trend as HX-X vs. SS-X sintered PTLs. Comparing the Ni-based materials, HX-3, that was pressed to reduce thickness which also smoothed the surface, offered slightly lower contact resistance and had lower electrical resistivity compared to DFF. However, DFF performed better in electrochemical testing likely due to efficient bubble removal and water transport. A similar trend was observed comparing BSS with SS-3 – where they both had the same thickness, but the different features and porous structure allowed BSS to perform better. Lastly, in the polarization experiments (Figure 4.10A), BHX appeared to outperform all previous PTLs (Table 4.3), being superior to DFF by ~ 60 mV at 1.0 A/cm^2, despite being double twice in thickness (a false result discussed more below), which appeared to support

the conclusions from the HX-X section above that the PTL thickness is not critical for device operation. Performance seems to be driven more by feature size and surface PTL density.

Under steady-state operation (Figure 4.10-B), DFF and BSS showed stable voltage with similar voltage difference as observed in the polarization curves. However, the most significant difference was in the operational stability. Though the BHX showed the lowest operating voltage during polarization and at the start of constant-current operation, the operating voltage markedly increased within a few hours and then cell experienced a short circuit. In fact, every cell assembled with the BHX PTL in its raw form (> 10 cells) experienced a cell short, even with lower assembly torque. It is likely that its large rectangular features with sharp edges penetrate into the membrane (similar to the higher-stress features with HX-1 and SS-1). These sharp edges allowed the membrane to be initially compressed, likely artificially reducing the cell Ohmic resistance – making it appear that this PTL had the highest performance. To test this, the BHX PTL was chemically treated with 10 M KOH for 24 hours at 60 ^{o}C to round the edges (shown in Figure 4.15 in the Supporting Information File). After the chemical treatment, the PTL was tested in the cell its performance in the form of polarization scan and steady-state voltage response at 1.0 A/cm^2 is shown in Figure 4.9. The treated BHX PTL surface avoiding shorting issue and voltage was very stable (Figure 4.10-B), but the polarization performance was similar to DFF at all current densities, showing that the high performance was a false result caused by membrane penetration.

Table 4.3: Voltage at 1.0 A/cm^2 and achievable current densities at 1.80 V and 2.0 V

Type of PTL	**Voltage @ 1 A/cm2 (V)**	**Current density @ 1.80 V (A/cm2)**	**Current density @ 2.0 V (A/cm2)**
HX-1	1.75	1.22	2.51
HX-2	1.74	1.21	2.29
HX-3	1.75	1.24	2.39
SS-1	1.83	1.13	1.83
SS-2	1.88	1.08	1.67
SS-3	1.88	0.92	1.61
DFF	1.73	1.44	2.74
BHX	1.68	1.85	3.42
BHX**	1.74	1.50	2.97
BSS	1.78	1.18	2.16
HXG-1	1.73	1.43	2.58
HXG-1-C	2.02	0.99	0.52
HXG-2	1.79	1.34	2.26
HXG-2-C	1.65	1.93	3.45
FM515-C	1.64	1.93	3.47

** *BHX treated in 10 M KOH for 24 hours.*

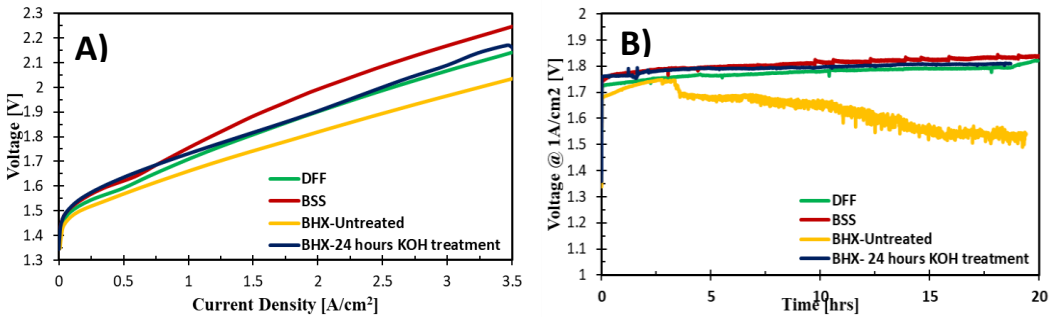

Figure 4.10: (A) Polarization curves and (B) steady-state response at 1.0 A/cm^2 for the three commercial PTLs. The AEM used was GT75-5 (40 um). IrOx catalyst in anode and PtNi in cathode. Cell temperature = 60 ^{o}C. Cells were operated with 0.3 M KOH fed to the anode only.

3.4 Gradient-structured Ni-based PTLs

From the results above, it is clear that physio-chemical differences in the anode PTLs lead to significant differences in performance, even when using the same catalyst materials coupled with the same cathode. Three of the most important variables identified above were the material of construction (Hastelloy > stainless steel), feature size and density. Related to the latter, high porosity is preferable for efficient bubble removal, but leads to increased contact resistance and sub-optimal catalyst deposition. On the other hand, lower porosity, and a smooth surface offer lower contact resistance, but at the expense of bubble accumulation. This suggests that multi-layer PTLs with varying porosity might be able to balance these two effects and increase performance. Therefore, two gradient Hastelloy PTLs were created, denoted as HXG-1 and HXG-2. Graded porosity PTLs have been studied in PEMELs and have been shown to be effective for water management and gas transport **[212]**. In such work in PEMELs, the graded porosity was reported to be most effective when porosity increased from the catalyst layer to the water flow channels **[241], [242], [243], [244]**.

HXG-1 was created in 7 layers and the cross-sectional view is presented in Figure 4.17. It was shown above that PTL thickness was not a significant factor increasing the operating voltage, making it possible to fabricate a structure where the contact area could be enhanced on one side (lower porosity) and bubble removal could be eased on the other side (higher porosity). The total thickness of the PTL was 0.041" (1.0414 mm). Porosity was controlled by changing the fiber size creating gradient porous structure. At its most dense side, the porosity was only ~48%. Its least dense side had a porosity of ~78 %. The average feature size, similar to the HX-X PTLs, was ~ 15 um. Figure 4.11A-B shows a birds-eye view of both the low density and high-density sides of the PTL (panels A and B, respectively). The less porous side was smoother, had more surface area for catalyst particles to deposit and make contact with the AEM, while the opposite side was more porous to help water transport to get in and gas bubbles be removed efficiently.

HXG-2 was created in two layers with an average fiber diameter of ~ 30 um. The material was initially sintered with total thickness of 0.036 in (0.914 mm). One side had an average porosity of 85 % while the other side had a porosity of 92%, as shown in Figure 4.12A-B showing the top and bottom views. The main differences between HXG-1 and HXG-2 were a gradual graded structure (7 layers) versus an abrupt bilayer as well as their thickness. Moreover, the more porous side of HXG-2 was much more porous thank HXG-1 with fragile surface features that could easily be compressed down and lose the contact within the cell assembly facing bipolar plate.

Because of the much lower density of the two graded PTLs compared to the most successful ones discussed above, they were also further compressed to densify and smooth the surface and are denoted as HXG-1-C and HXG-2-C respectively. HXG-1-C (the

compressed version of HXG-1) was reduced to a thickness ~ 600 um. Figures 10C-D show SEM images of HXG-1-C where the features were packed together, decreasing the overall porous structure to an average density of ~ 78%. This was the most dense PTL created in this work. HXG-2-C was created by rolling HXG-2 to a thickness of 175 um, increasing its density as shown in Figures 11C-D. In this structure, the overall density was ~ 66 % and the two layers had similar porosity, though it was clear from the SEM images in Figure 4.12 C-D that the top side was denser than the bottom side.

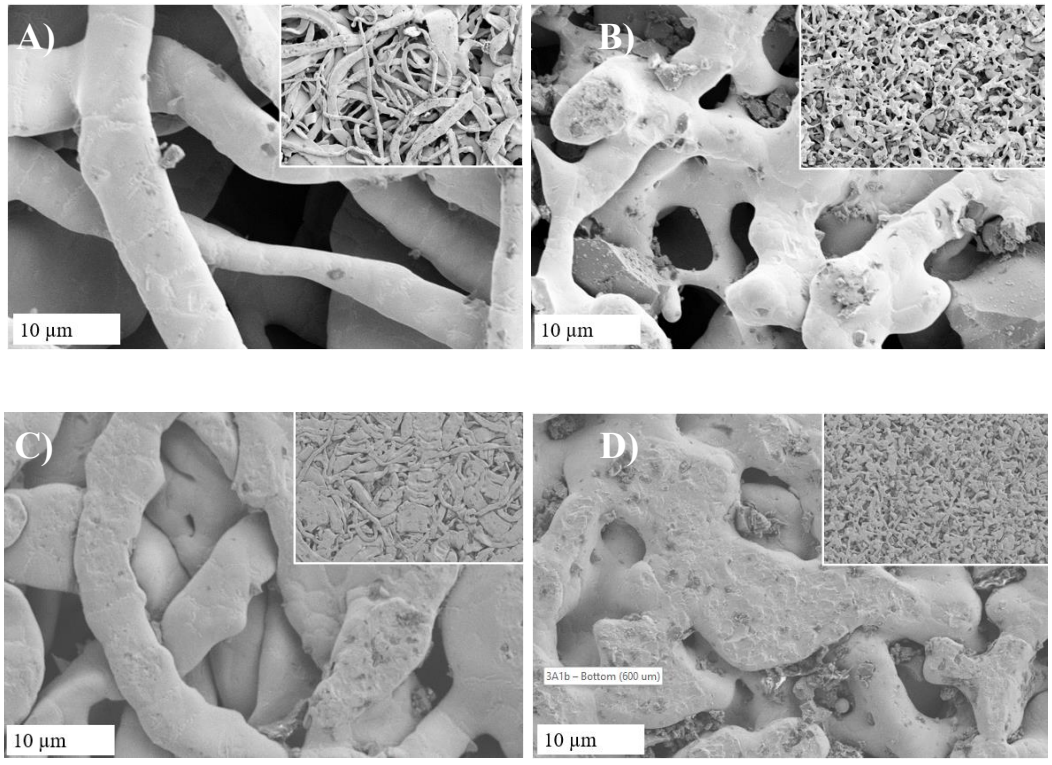

Figure 4.11: (A-B) HXG-1 PTL's SEM images: A). Top view (least dense side), B). Bottom view (most dense side), (C-D) HXG-1-C PTL's SEM images (a compressed version of HXG-1), C). Top view (least dense side), D). Bottom view (most dense side). Inset: Zoomed out images at 1.35 kX magnification.

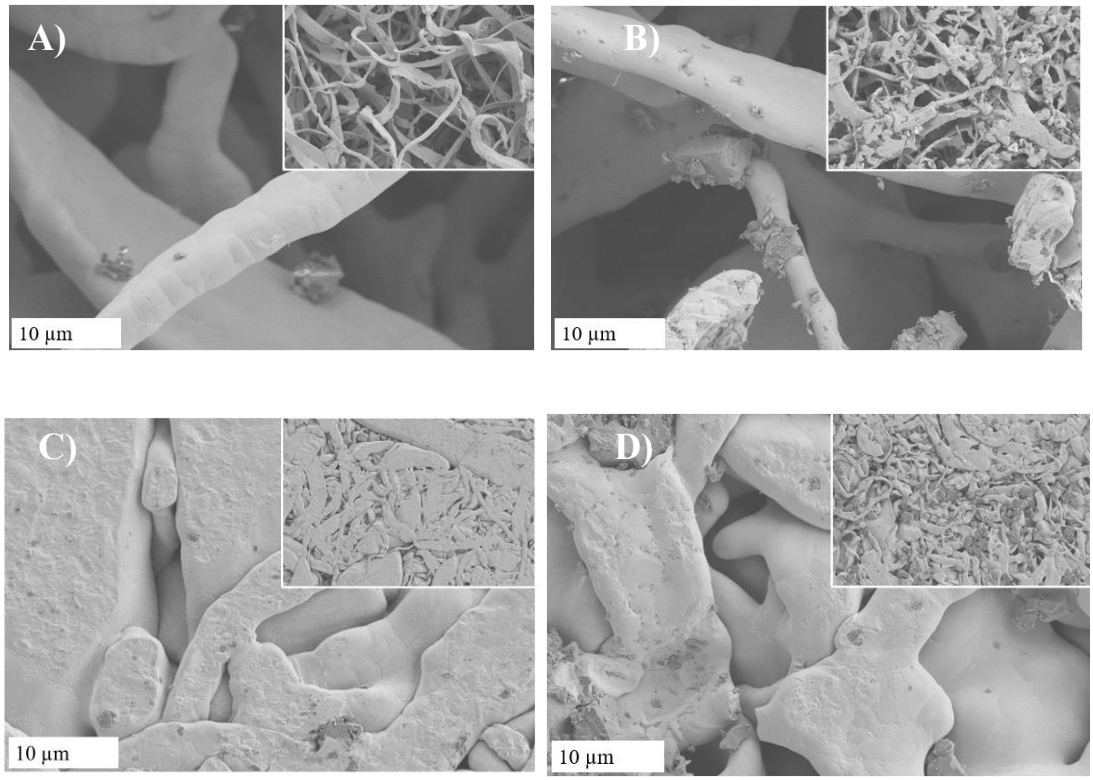

Figure 4.12: (A-B) HXG-2 PTL's SEM images: A). Top view (least dense side), B). Bottom view (most dense side), (C-D) HXG-2-C PTL's SEM images (a compressed version of HXG-2), C). Top view (least dense side), D). Bottom view (most dense side). Inset: Zoomed out images at 1.35 kX magnification.

Figure 4.13 shows the polarization and steady-state response for HXG-1, HXG 2 and their compressed versions. For HXG-1, the performance was tested with both the denser and the more porous side facing the catalyst layer. As expected, the performance was much better with the dense side of the PTL supporting the catalyst layer and the more porous side making contact with the cell hardware (Figure 4.16). Positively, the performance of HXG-1 was comparable to the best performing PTLs above (e.g. DFF), with an operating voltage ~ 1.70 V at 1.0 A/cm^2, which was slightly better than HX-3. HXG-2, with catalyst layer built on denser side of the PTL, showed slightly lower

performance, with an achieved operating voltage of 1.79 V at 1.0 A/cm^2. This was mainly due to higher contact resistance at the same compression. The operating voltage was also less stable and cells commonly experienced a short circuit, likely due to sharp features of the denser side of the PTL facing the membrane.

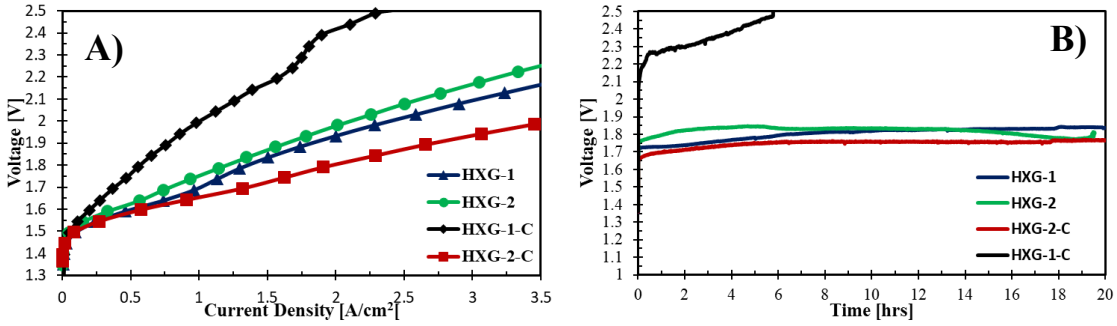

Figure 4.13: (A). Polarization curves, (B). Steady-state response at 1 A/cm^2, comparing HXG PTLs. The AEM used was GT75-5 (40 um). IrOx catalyst as anode and PtNi as cathode. Cell temperature 60 ^{o}C, operated in 0.3 M KOH fed to anode only.

Next, HXG-1-C and HXG-2-C were evaluated for their voltage response and durability. The aim was to smooth the surface of the PTL for decreased contact resistance and densify the structure. The polarization and steady state results are presented in Figure 4.13. HXG-1-C showed extremely high cell voltage, over 2.0 V at 1.0 A/cm^2 and even worse at higher currents. Moreover, poor durability showing an abrupt increase in voltage within a few hours of operation suggesting the significance of water and oxygen transport through pores. As the most dense PTL, it was clear that 80% density is too high for AEMEL operation.

HXG-2-C showed very good voltage response ~1.65 V at 1.0 A/cm^2 with no transport issues even at higher currents. The cell also showed also very good durability, though there was ~ 50 mV increase in voltage within a few hours of operation likely due

to gas bubble accumulation in the relatively dense structure. These results suggest that achieving the right PTL density is relatively more important than gradient pores for efficient water and gas transport which led us further for development of optimal PTL characteristics.

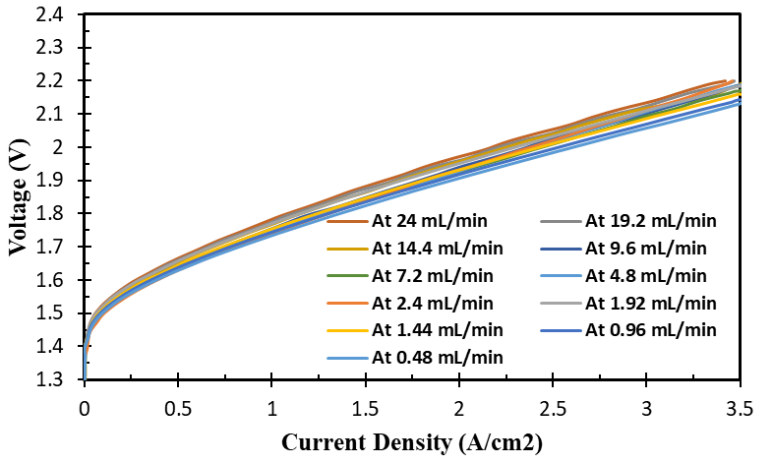

Figure 4.14: (A). Polarization curves comparing AEM electrolyzer operation with different feed electrolyte flowrates. AEM used was GT75-5 (40 um). IrOx catalyst deposited on DFF PTL as anode and PtNi on carbon paper as cathode. Cell temperature 60 ^{o}C, operated with 0.3 M KOH feed to anode only.

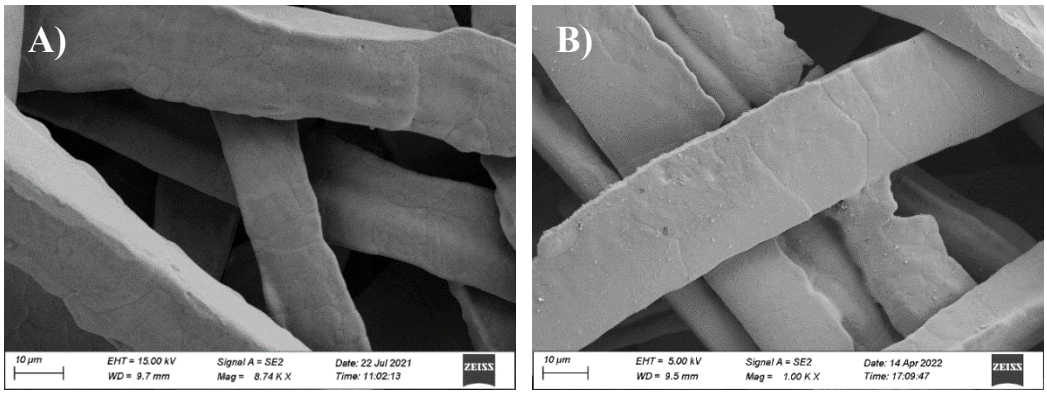

Figure 4.15: SEM images of (A). BHX-Untreated, B). BHX-24 hours treatment in 10 M KOH at 60 ^{o}C

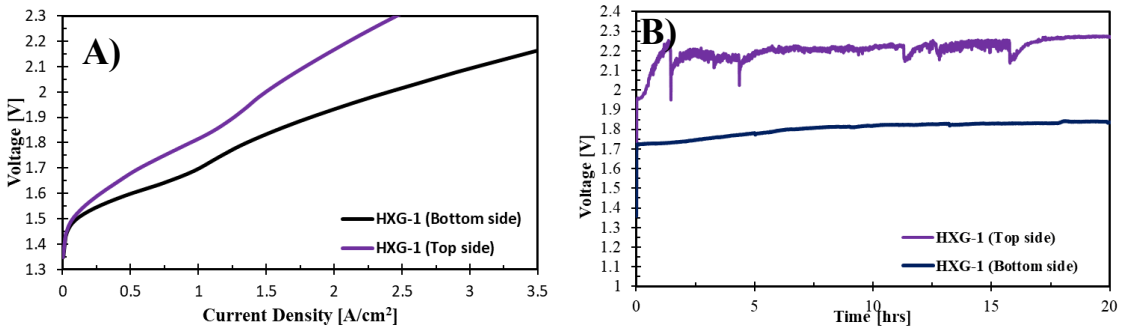

Figure 4.16: (A). Polarization curves, (B). Steady-state response at 1 A/cm^2, comparing HXG-1 PTL with catalyst deposited on bottom side (denser) and top side (less dense). The AEM used was GT75-5 (40 um). IrOx catalyst as anode and PtNi as cathode. Cell temperature 60 ^{o}C, operated in 0.3 M KOH fed to anode only.

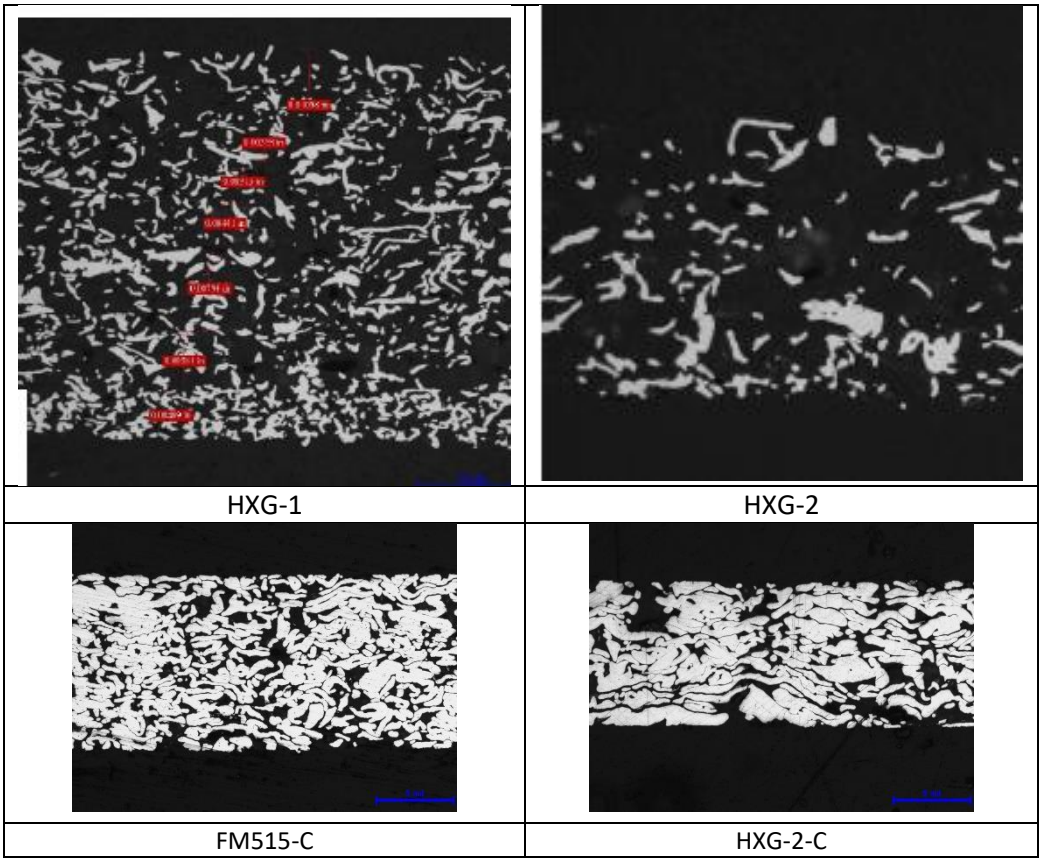

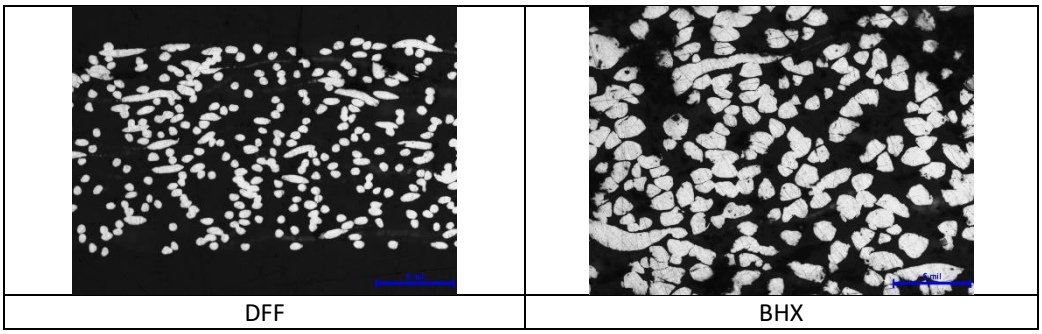

Figure 4.17: Cross-section images showing the porous structure of the PTLs

3.5 Optimized PTL

Creation of a PTL structure that not only leads to excellent performance, but is simple to manufacture is important. Therefore, it was sought to create a Hastelloy PTL with a thickness near 300 μm (to be comparable with other commercial PTLs) and a density in the 60-65% range. To do this, we began with an already commercialized product from Technetics, Feltmetal^{TM} FM515, which is a single-layer. The FM515 was rolled to a thickness of 280 μm, resulting in a density of ~ 62 %. This PTL will be denoted as FM515-C. As shown in Figure 4.18A, FM515-C had relatively large features to allow for efficient water and oxygen transport while also providing a robust surface for catalyst layer deposition.

Figures 4.18B and 4.18C show the polarization and steady-state behavior of FM515-C in an AEMEL. No mass transport limitation observed up to 3.5 A/cm^2 and voltage of ~ 1.64 V was achieved at 1.0 A/cm^2 with very good durability outperforming all the PTLs presented in this study. Looking at all the PTLs studied here, FM515-C and HXG-2-C outperformed all of the other PTLs, showing a minimal operating voltage ~ 1.65 V at 1.0 A/cm^2 with no transport limitations even at higher current densities. Figure 4.18D compares these two PTLs to the best performing commercial PTLs (DFF and BHX).

FM515-C and HXG-2-C offer a lower operating voltage by ~ 100 mV at 1.0 A/cm^2. They are both Hastelloy X, 180-280 µm in thickness, have a 62-65% density and a mean fiber diameter range of 10-30 microns. They also are low cost, easy to manufacture and are durable. Therefore, this work helps to take an important step in the commercialization of AEMELs.

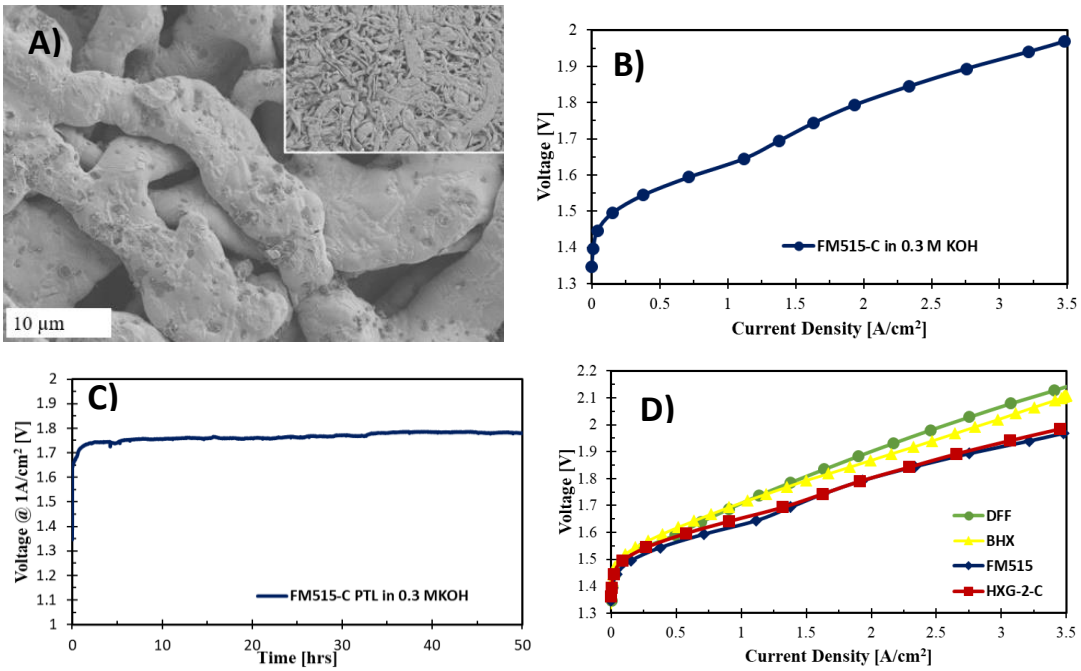

Figure 4.18: A) SEM images of FM515-C showing the porous structure and surface features. Inset: Zoomed out images at 100 µm scale (1.35 kX magnification). B). Polarization curves and (C) Steady-state response at 1.0 A/cm^2 of AEMELs with the FM515-C PTL, D). Polarization curves comparing the best performing commercial and Technetics synthesized PTLs. The AEM used was GT75-5 (40 um). IrOx catalyst anode and PtNi as cathode. Cell temperature = 60 ^{o}C. 0.3 M KOH fed to the anode only.

4. Conclusion

In this study, we studied 14 different PTL structures broadly categorizing into Nickel alloy and stainless steel. We custom developed three series of PTLs and compared them with state of the art commercially available PTLs. It was found that Ni based PTLs offer up to 100 mV lower voltage compared to SS-based PTLs, showing the same trend

among custom developed and commercial PTLs. It was observed that with similar porosity and fiber structures, thickness (0.2 – 1.2 mm) of the PTLs has no significant effect on electrolyzer performance. PTL porous structure is important for water and gas transport as well as catalyst layer development on the surface. Higher porosity is preferred for efficient water and gas transport while is a disadvantage for optimal catalyst layer development due to less available surface area. Therefore, a trade-off is essential for optimal PTL structure offering lower voltage loss in the electrolyzer. It was found that the porosity around 40 % may offer lower contact resistance with ease of water and gas transport resulting in optimal performance in the AEMELs. Moreover, PTL feature size and shape influence contact resistance as well as compatibility with AEM. Large features and irregular shape fibers may penetrate the AEM causing mechanical failure. Therefore, surface features modification by compression or other chemical treatment can help smooth the surface. It was concluded that the PTL with 10-20 µm fiber diameters with round shape or compressed to smooth the edges offer lower contact resistance and higher performance in the electrolyzer. The optimal PTL structure developed after systematic study, easy to manufacture FM515-C with around 15 µm fiber diameter, 0.3 mm thick, 62 % dense and compressed to smooth the surface sharp edges offered the best performance of over 3.5 A/cm2 under 2.0 V operating at 60 C.

CHAPTER 5

ACHIEVING HIGH PERFORMANCE AND 2000-HOUR STABILITY IN ANION EXCHANGE MEMBRANE FUEL CELLS BY MANIPULATING IONOMER PROPERTIES AND ELECTRODE OPTIMIZATION[4]

Abstract

The primary function of the ionomers that are incorporated into fuel cell electrode catalyst layers is to provide pathways for ion transport between the catalyst active sites and the electrolyte. High ion transport and chemical-mechanical stability is desired to enable high cell performance and operational stability. Ion transport within the ionomer is influenced by many variables, including the ion-exchange capacity, water uptake, and molecular weight. In anion exchange membrane fuel cells (AEMFCs), the degree of water uptake is particularly important because it can lead to ionomer swelling and/or flooding at the anode where a significant amount of water can be present during operation. Additionally, if too little water is taken-up by the ionomer, it can dry out, reducing anion transport and/or increasing chemical degradation, which are especially concerning at the AEMFC cathode. Therefore, controlling ionomer water uptake in each electrode is an

---

[4]Hassan, N.U., Mandal, M., Huang, G., Firouzjaie, H.A., Kohl, P.A. and Mustain, W.E., Achieving High-Performance and 2000 h Stability in Anion Exchange Membrane Fuel Cells by Manipulating Ionomer Properties and Electrode Optimization, *Adv. Energy. Matr.* **10,** 2001986 (2020).

important consideration when looking to maximize cell performance. In this study, three poly(norbornene) tetrablock copolymer ionomers with a range of physical properties were synthesized and incorporated into AEMFC anode and cathode electrodes. Independently controlling ionomer in the catalyst layers of each electrode allowed the peak power density to be increased by 75% (i.e., from 1.6 W/cm^2 to 2.8 W/cm^2) and the current density at 0.2 V to be increased by 42% (i.e., from 5.9 A/cm^2 to 8.4 A/cm^2). Additional electrode engineering, incorporating hydrophobic PTFE into the electrodes, allowed for very high peak power and current densities to be achieved, 3.2 W/cm^2 and 9.4 A/cm^2 (at 0.2 V), respectively. Moreover, the top-performing electrode configuration was tested in an operating AEMFC at the US Department of Energy defined current density of 600 mA/cm^2 for 2000 hrs, showing a record-low voltage decay rate of15.36 μV/hr with voltage loss of only 3.65% over 2000 hours. This work sets a new bar for AEMFCs, reporting the best combination of performance and durability of any AEMFC reported to date.

1. Introduction

Over the past few decades, fuel cells have emerged as a potential high-efficiency, clean energy source for a wide range of applications. Proton exchange membrane fuel cells (PEMFCs) have received significant attention due to their high energy density and well-established materials (e.g. Pt-based catalysts and Nafion membranes and ionomers) **[245], [246]** However, PEMFCs are commercially challenged due to the high cost of these materials and component manufacturing costs, which are driven by the fact that PEMFCs require specialized component materials due to the highly acidic operating environment. To alleviate these costs, anion exchange membrane fuel cells (AEMFCs) have recently emerged as an alternative to PEMFCs. The higher pH operating environment offers several

advantages such as lower material and manufacturing costs. For example, AEMFCs can use platinum group metal (PGM) free cathodes, have more facile oxygen reduction kinetics **[247], [248]** and may enable a wider range of fuels (e.g. methanol, hydrazine).

However, early AEMFC developments suffered from very low overall performance and durability **[249], [250].** From a durability perspective, cells were mostly believed to be limited by chemical degradation of the anion exchange membrane (AEM) and ionomer at high pH. Because of this, there has been a significant amount of investment targeting the design and manufacturing of stable anion exchange membranes (AEMs) and ionomers. As a result, several AEMs have been shown to be stable both at elevated temperature (≥ 80^{o}C) and pH for hundreds or even thousands of hours during ex-situ testing **[251], [252], [253], [254], [277].**

Another issue that has started to be addressed in the AEMFC literature is water management. Water is formed at the AEMFC hydrogen anode and consumed at the oxygen cathode. As water is produced at the anode, it must be removed to avoid flooding – either through the anode gas stream or, preferably, through the AEM to the cathode (via back-diffusion) where it is needed to react **[259].** If too little water is supplied to the cathode by water-diffusion it can dry out; if more water arrives to the cathode than can be reacted, it is also possible for the cathode to flood. Therefore, there is a need for both the anode and cathode catalyst layers to be able to passively transport water. The ability of the ionomer in the catalyst layer to facilitate such ion transport is related to the overall hydrophilicity of the monomers used in the polymer membranes and ionomer. One example where ionomer water uptake has been limiting is the well-known ethylene-tetrafluoroethylene copolymer (ETFE) based powder ionomer **[260].** Though the ion exchange capacity (IEC)

of that material is modest (only 1.24 meq/g), recent work has found that its water uptake was very large, and the high-water content of the AEMFC anode resulted in excessive electrode swelling, **[284]** which blocked the catalyst sites and hindered gas transport, resulting to lower cell performance in fully humidified cells **[276].** One of the ways that the amount of water in the electrodes can be reduced and avoid swelling is to lower the relative humidity of the feed gases during AEMFC operation and rely on convective evaporation to remove excess anode water **[256], [281].** Another method to mitigate electrode swelling is to reconfigure the electrode composition and architecture. For example, Yang et al. **[261]** showed that ionomer content plays a significant role in activation, ohmic and mass transport losses within the cell. Later, Omasta et al. **[255]** optimized the ionomer:carbon:catalyst ratio of an AEMFC anode catalyst layer, finding that having increased void space in the catalyst layer can improve performance and operational stability, likely by being able to accommodate swelling. Recently, Truong et al. **[280]** and Peng et al. **[284]** have shown that adding a hydrophobic agent (PTFE) into the catalyst layers can improve both performance and stability.

Another method that can be used to control the water transport properties of the electrodes is to modify the anion exchange ionomers in the catalyst layer. For example, Sun et al. **[262]** prepared pendant quaternary ammonium-based ionomers and demonstrated low Ohmic and charge transfer resistances resulting from balanced conductivity-hydrophobicity and dimensional stability. Unlu et al. **[263]** devised an ionomer impregnation method and achieved higher performance by balancing the ionomer distribution within the catalyst layer. Zhou et al. **[264]** demonstrated significantly reduced ionomer water uptake by employing hydrophobic octafluoro-biphenyl groups in the

backbone and prepared a series of partially fluorinated copoly(arylene ether) alkaline ionomers followed by amination with trimethylamine.

Others studies have provided insight into how AEMFC ionomers might be designed somewhat differently than the AEM itself. For instance, Ahlfield et al. **[265]** pointed out that when operating as an AEM, the polymer needs to act as a low gas permeability separator while facilitating bulk ion transport. As an ionomer, higher gas solubility is preferred, and transport occurs at short lengths, not through the bulk. This suggests that the ionomers in the catalyst layer may require different properties than the polymers for AEMs, even if they come from the same chemical family. Also, Li et al. **[266]** suggested that the use of ionomers with high IEC or high water uptake properties may lead to limited gas transport to the catalyst due to unwanted cation-hydroxide-water co-adsorption. Moreover, such ionomers can facilitate swelling and anode flooding as discussed above. It is also likely that the AEMFC cathode, where water is consumed, would benefit from higher water retention in the catalyst layer. Therefore, ionomers with differing IEC and/or water uptake than the AEM might be expected to lead to higher performance. It is also likely that the optimum ionomers for the anode and cathode are not the same.

Studies of varied ionomer properties, such as the ones discussed above, are possible with a number of polymer chemistries. However, an effective approach might be to fine-tune the properties of already high-performing materials. One family of materials that has shown excellent performance in AEMFCs and is highly tunable is poly(norbornene) tetrablock copolymers. Recently, Mandal et al., reported highly conductive cross-linked poly(norbonene) membranes (198 mS/cm) that showed no significant ionic conductivity loss over 1000 hours in 1 M KOH at 80 ^{o}C **[251].** Huang et al., used similar materials in

AEMFCs, enabling very high peak power density to be achieved (3.4 W/cm^2) under H_2/O_2 reacting gases, **[267]** which was recently improved to 3.5 W/cm^2 by using thinner membranes **[268].**

In this study, three poly(norbornene) tetrablock copolymer ionomers with different IEC, molecular weight, dispersity, and water uptake were synthesized and fully characterized for their physical and electrochemical properties. The ionomers were integrated into operating AEMFCs with symmetric (same ionomer in both catalyst layers) and asymmetric (different ionomers in the anode and cathode catalyst layers) electrode configurations. After finding an appropriate balance of water uptake properties for the anode and cathode ionomers, additional electrode engineering was performed to increase their hydrophobicity. These final, highest performing, electrodes were operated at various conditions, including long-term testing (2000 h) with excellent results. Overall, this work highlights the balance between ionic conductivity, hydrophobicity and morphology (molecular weight) of ionomers which are essential for high-performance and long-term stability in AEMFCs.

2. Experimental

2.1 Tetrablock Copolymer Ionomer Preparation

Three tetrablock copolymers, denoted as GTXX, were synthesized following a previously reported procedure using bromobutyl norbornene (BBNB) and bromopropyl norbornene (BPNB) **[251], [269].** In their designation, the XX is an indicator of the percentage of the monomer that is halogenated. Hence, GT32, GT64, and GT78 describe polymers that contain 32 mol%, 64mol%, and 78 mol%, respectively. In essence, the

number designation is an indicator of the ion exchange capacity, which impacts other variables such as hydrophilicity and water uptake.

After synthesis, the polymers were analyzed by ^{1}H NMR using a Bruker Avance 400 MHz NMR instrument using $CDCl_3$ as the solvent. The number average molecular weight (M_n) and dispersity (Đ) of GT32, GT64, and GT78 were determined by gel permeation chromatography (GPC) (Shimadzu) equipped with an LC-20 AD HPLC pump and a refractive index detector (RID-20A, 120 V). GPC measurements were performed in Tetrahydrofuran (THF) with the eluent flow rate of 1.0 mL/min at 30°C and calibrated against a polystyrene standard.

2.2 Measurement of ionomer Properties

The IEC of the precursor polymers was determined by ^{1}H NMR. The detailed procedure for calculating IEC by this method has already been reported **[269].** Mohr's titration method was used to measure the IEC of the membranes after cross-linking and quaternization to confirm the accuracy of the NMR results **[279]**. In a typical procedure, the polymer in Br^- form was converted to Cl^- form by soaking in 0.1 M NaCl solution for 24 h. The film was removed from the NaCl solution, thoroughly washed with DI water and dried in vacuum for >24 h. The dry film weight was recorded. Next, the membranes were immersed in a fixed volume of 0.05 M $NaNO_3$ for 24 h. Finally, the released Cl^- was titrated with an aqueous $AgNO_3$ solution using K_2CrO_4 (10 wt%) as the indicator. Measurements were performed in triplicate to ensure repeatability. The IEC was calculated using Equation 1.

$$\mathrm{IEC} = \frac{C_{AgNO_3} \times V_{AgNO_3}}{M_d} \qquad (1)$$

In Eq. 1, V_{AgNO_3} (mL) is the volume of $AgNO_3$ solution needed to fully precipitate the choride, C_{AgNO_3} is the concentration of the $AgNO_3$ (0.05 mol·L^{-1}) solution, and M_d (g) is the weight of the dried sample.

To determine the water uptake (WU), dry mass (M_d) of the film was measured by drying the films in vacuum oven **[270]**. Next, the films were immersed in 18.2 MΩ deionized water (DI) for 24 hours. After removing the film from the DI water, the excess surface water was wiped from the surface and the wet mass (M_w) was measured. For both M_d and M_w, measurements were made on multiple films and an average value is reported here. Then, the water uptake was calculated using Equation 2

$$\mathrm{WU}(\%) = \frac{M_w - M_d}{M_d} \times 100 \qquad (2)$$

It is pertinent to mention that water uptake measurements for GT64 and GT78 were made after adding 5% cross-linker (*N,N,N′,N′*-Tetramethyl-1,6-hexanediamine) while for GT32, no cross-linker was added. The cross-linker was added to avoid gel formation due to more hydrophilic properties of the GT64 and GT78 ionomers and reliable water uptake measurements were not possible without adding the cross-linker. Then, the percent swelling for each ionomer was calculated by Equation 3, where V_d is dry volume of the membrane and V_w is the volume of the fully hydrated membrane after removing excess surface water. The volumes were calculated by multiplying length, width, and thickness in dry and hydrated states.

$$\text{Swelling } (\%) = \frac{V_w - V_d}{V_d} \times 100 \qquad (3)$$

Ionic Area Specific Resistance (ASR) was calculated using Equation 4:

$$\text{ASR } (\Omega\text{-cm}^2) = L/\sigma \qquad (4)$$

where L = film thickness in cm; σ = ion conductivity in S/cm (at 80 °C). The in-plane hydroxide conductivity of the membrane samples were measured by four probe electrochemical impedance spectroscopy (EIS) using a PAR 2273 potentiostat/galvanostat (Princeton Applied Research) for frequencies from 1 Hz to 2 MHz **[251], [286]**.

Finally, The storage modulus of the GT64-15 AEM was measured by dynamic mechanical analysis (DMA) using a TA Instruments Q800 under a 1 Hz single-frequency strain mode in air at 30°C. A fully hydrated, rectangular sample was loaded into the DMA with tension clamps after removing surface water. Experiential parameters for the DMA were set to 0.1% strain and a preload force of 0.01 N with a force track of 125% **[267]**.

2.3 Electrode Fabrication Using GTXX Ionomers

Gas diffusion electrodes (GDEs) were fabricated using a previously developed method **[255], [256]** where a catalyst ink was made from the GTXX ionomers, DI H_2O/isopropyl alcohol solvent and Pt-based electrocatalysts. The ink was sprayed onto Toray 60 gas diffusion layers (GDLs) with 5% wet proofing. 40% Pt/C (Alfa Aesar HiSPEC 4000, Pt nominally 40 wt%, supported on Vulcan XC-72R carbon) was used at the cathode and 60% Pt-Ru/C (Alfa Aesar HiSPEC 10000, Pt nominally 40 wt%, and Ru, nominally 20 wt%, supported on Vulcan XC-72R carbon) was used at the anode. Two different types of electrode inks were made and deposited onto the GDLs to make the GDEs. The GDEs are designated "Type 1" and "Type 2" throughout this manuscript. Type 1 GDEs were formed following our standard composition **[255]** where Vulcan carbon was added to the ink such that the final anode ionomer:carbon:PtRu mass ratio in the electrode was 1:2.5:1.5 and the cathode ionomer:carbon:Pt mass ratio was 1:2.5:1.5. Type 2 GDEs were formed with the same standard composition as Type 1 except that 8 wt% (of catalyst mass) PTFE was added

to the inks for both electrodes. For all electrodes, inks were sprayed onto 25 cm^2 area GDLs, which were then cut into 4 electrodes each with an active area of 5 cm^2. The noble metal loadings at the anode and cathode electrode were 0.7±0.05 mg/cm^2 and 0.6±0.05 mg/cm^2 respectively.

2.4 MEA Fabrication

For in-situ evaluation of the ionomer performance, the GDEs were formed into membrane electrode assemblies (MEAs), and loaded into 5 cm^2 Scribner fuel cell hardware with a single-serpentine flow field. All of the MEAs in this work used a GT64-15 (the number after hyphen indicates the mol% cross-linker concentration) AEM, the synthesis of which was reported previously **[267]**. The GT64-15 AEM has a high IEC (3.28 meq/g), as well as high storage modulus (175 MPa), low water uptake (29 wt%), low dimensional swelling (14%) and low area specific resistance (ASR, 0.020 Ω cm^2). The first step in the MEA fabrication was to pretreat the AEM and the GDEs to convert them to the OH^- form. This was done by soaking the membrane and electrodes in a 1 M KOH solution in separate containers for one hour, replacing the solution every 20 minutes. Excess KOH was completely removed from the surface of membrane and electrodes before assembly. Following pretreatment, the GT64-15 AEM was sandwiched between the anode and cathode GDEs (without any hot pressing) and the cell was torqued to 45 in.lb. 6 mil (150 μm thick) PTFE sheets were used as the gasket material at both the anode and cathode.

2.5 AEMFC Testing

All of the operating AEMFCs in this work were controlled using a Scribner 850e fuel cell test station. At cell startup, N_2 was flowed through the anode and cathode at 0.4 L/min and 100% relative humidity until a cell temperature of 60°C was reached. Then, the N_2

feeds were switched to pure H_2 and O_2 and a constant voltage of 0.5 V was applied to initiate the cell break-in procedure. After a stable current density was established, the dew points of the anode and cathode reacting gases were systematically optimized as previously described **[255], [256], [271]**. The cell temperature was gradually increased to 80°C in 5°C increments, with the anode/cathode dew points being simultaneously optimized with the cell temperature to avoid membrane dry out. After the cell temperature reached 80°C, the degree of back-pressurization was also set. After the cell equilibrated at the desired conditions for around 30 min, a polarization curve was collected by slowly sweeping the voltage from the open circuit voltage to 0.1 V at a 10 mV/s scan rate. The top-performing electrode configuration was further subjected to the DOE long-term AEMFC durability protocol where the cell was held at a constant current density of 600 mA/cm^2 for 2000 hr. During this long-term test, the cell temperature was set at 75°C while the dew points of the reacting gases were initially set to 72°C at the anode and 74°C at the cathode. The dew points were adjusted occasionally (± 1°C) to ensure adequate membrane hydration. Also, the cell high frequency resistance (HFR) was monitored (at a frequency of 7 kHz) by the fuel cell test station throughout the test.

3. Results and Discussion

3.1 Ionomer Properties

Table 5.1 shows the characteristic properties of the three ionomers investigated in this study. Of the synthesized ionomers, GT78 had the highest IEC (3.74 meq/g) because of the highest mole fraction of quaternary ammonium group (i.e., 78 mol%). GT32 had the lowest IEC of 1.88 meq/g, whereas the IEC of GT64 (3.37 meq/g) lies in between GT78 and GT32. The molecular weights (M_n) of the three ionomers, GT78, GT64, and GT32,

were 103.6 kg/mol, 50.96 kg/mol, and 114.9 kg/mol, respectively. The M_n of GT32 and GT78 were nearly twice that of GT64. Higher molecular weights enable greater chain entanglement and the formation of more efficient channels for to transport hydroxide and water. This is clearly shown when comparing the hydroxide mobility (the quotient of the hydroxyl ionic conductivity, σ, and the IEC) of GT64 and GT32. For GT32, σ/IEC (at 80 °C) was 65.2, whereas for GT64, σ/IEC (at 80 °C) was 54.2 **[268], [269]**.

Table 5.1: Characteristic properties of the GTXX ionomers investigated in this study

Sample	M_n[b] **(kg/mol)**	**Dispersity (Đ)**	**IEC**[c] **(meq/g)**	**Water Uptake (%)**	**Ionic ASR (Ohm-cm^2)**
GT32[d]	114.9	1.42	1.88	63	0.08
GT64[e]	50.96	2.02	3.37	90	0.05
GT78[a,e]	103.6	1.30	3.74	163	0.06

Note: [a]Block copolymers using bromobutyl norbornene (BBNB) as the halogenated block. [b]Measured by gel permeation chromatography at RT in THF relative to polystyrene standards. [c]IEC (Ion Exchange Capacity) was determined by ^{1}H NMR. [d]From ref. **[269]** [e]From ref. **[268]**

The WU of the GT32, GT64 and GT78 polymers was measured by first casting a film as described in the Experimental section. The WU for the GT78, GT64 and GT32 ionomers at room temperature were 163%, 90 % and 63%, respectively. The increasing trend in WU of a polymer with IEC is due to a higher concentration of ion pairs and their hydration **[268], [272], [278]**. Also, increased IEC typically translates to a polymer with increased hydrophilicity. Hence, it is expected that in an operating cell, the higher IEC ionomers will take-up more water and swell to a greater extent while the lower IEC ionomer (relatively more hydrophobic character) will uptake less water and may even allow the electrodes to

more effectively reject water. Both extremes could create flooding or dry out conditions if improperly implemented, which would have a negative effect on cell performance.

3.2 Single Cell Performance

AEMFC performance with the GTXX ionomers was compared by collecting polarization and power density curves with H_2/O_2 feed gases entering the cell at a volumetric flowrate of 1 L/min. As discussed in the Experimental section, prior to recording any data, the dew point of the anode and cathode reacting gases was optimized and the cell temperature was set at 80°C. In the discussion below, the dew points are displayed in an anode/cathode format; i.e., 71/73°C would refer to a dew point of 71°C at the anode and 73°C at the cathode. **Figure 5.4** compares the polarization and power curves for AEMFCs with a symmetric ionomer configuration, meaning that one of the GT32, GT64 or GT78 ionomers was used both in the anode and cathode. When GT32 was used as the ionomer in both electrodes (blue curves), the optimized reacting gas dew points were 79/80 °C. The same procedure was used to find the optimized dew points for cells employing GT64 (green curves) and GT78 (red curves) ionomers at both electrodes, which were 76/78 °C and 74/77 °C, respectively. The trend in the dew points follows an inverse relationship to the IEC and WU, where the lowest WU ionomers require the highest dew point for operation. The high dew point values for cells symmetrically employing the GT32 ionomers operate with a narrow balance between hydration and dry out. In terms of the peak power density and current density at 0.2V, there was not a clear trend with the ionomer WU, however, the mass transfer limited current density was higher with GT78 most likely due to its higher WU and resulting water transport. The GT32 electrodes and GT78 electrodes showed very similar peak power density, 2.2 W/cm^2. Cells with GT64

ionomer in both electrodes showed low performance relative to the other two (1.6 W/cm^2) and an early transition to mass transport limited behavior.

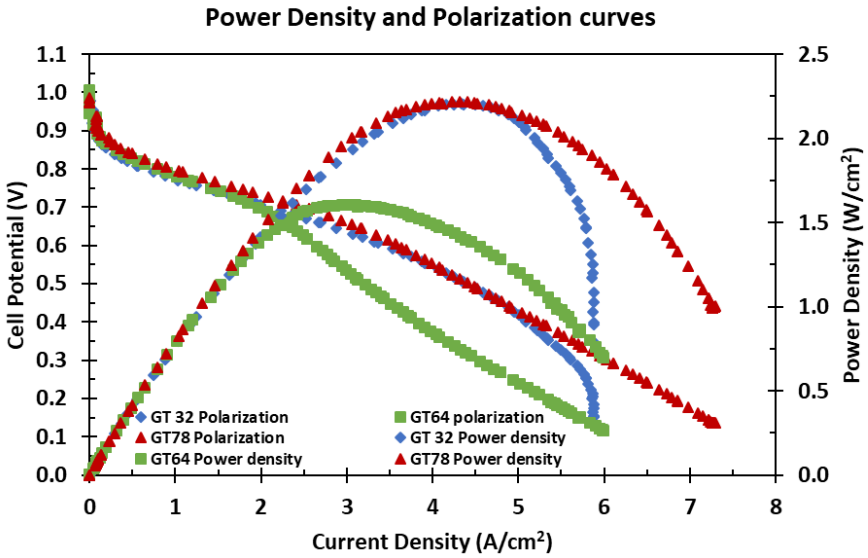

Figure 5.1: Polarization and power curves for operating H_2/O_2 AEMFCs with symmetric deployment of GT32, GT64 and GT78 ionomers in Type 1 GDEs at optimized dew points. Cell temperature = 80 °C; flowrates = 1 L/min; GT64-15 AEM; no backpressure.

With GT32 ionomer in both electrodes, the sudden transition of the cell at 5 A/cm2 to transport limited behavior suggests that near 5 A/cm^2 there is either excess water in the anode or a deficiency of water in the cathode. During the experiment, the average HFR with GT32 ionomer in both electrodes was higher (6.2 mOhm, ASR=31 mΩ·cm^2) than the electrodes with GT64 (5.6 mOhm, ASR=28 mΩ·cm^2) and GT78 (5.4 mOhm or ASR 27 mΩ·cm^2) ionomers, despite the fact that the dew points were the highest for GT32. High dew points suppress convective evaporation, and hence typically keep the membrane well-hydrated. The higher HFR suggests that there is likely a deficiency in liquid water in the cathode, due to the low water uptake of the polymer there. For the electrodes with GT78 in both electrodes, the polymer has the highest water uptake and the lowest optimized dew points. This likely allows the cell to balance the generation and transport of the water fairly

well, though the performance-limiting process here is most likely water removal and anode flooding. This explains the gradual decay in the cell voltage at higher current density instead of the sudden mass transport observed drop in current with GT32. Finally, the cells using GT64 ionomer in both electrodes did not perform well. One explanation for this could be directly linked to the WU of GT64, which fell between GT32 and GT78. Another possible contributor to the observed performance is the hydroxide mobility (σ/IEC), which is also an indicator for water transport rate. GT64 had the lowest σ/IEC, which suggests that the rate that water can be taken up by the polymer is the lowest. It also requires the dew points of the reacting gases to be higher than GT78, suppressing convective evaporation. Fujimoto et al., linked mechanical properties with polymer molecular weight. [41] The authors found that less than 20% increase in polymer molecular weight increased 300% elongation and discussed the sensitivity of mechanical properties in lower molecular weight region. With similar IEC and WU, the higher the molecular weight, the better mechanical properties are. Due to low M_w of GT64 ionomer, it showed poor mechanical properties compared to GT32 and GT78 ionomers which are critical especially at higher current densities. Therefore, another appealing explanation could also be that it was unable to provide an optimal electrochemical interface. Hence, GT64 may represent an undesirable combination of properties for AEMFC electrodes, despite performing very well as an AEM. Based on these results, GT32 and GT78 were down-selected for further investigation.

Because the anode and cathode in the AEMFC operate very differently – the latter produces water and the former consumes it – it is possible that their ionomer requirements are different. In other words, one electrode may benefit from increased water uptake, either

providing a buffer for water at the anode or holding in reacting water at the cathode. The ionomer hydrophobic/hydrophilic effect on cell performance was investigated by making asymmetric electrodes with different ionomers in each electrode. **Figure 5.2a** shows polarization curves and power curves for the asymmetric deployment of the GT32 and GT78 ionomers. In one embodiment, GT32 was used in the anode electrode and GT78 was used in the cathode. In the other embodiment, GT78 was used in the anode electrode and GT32 was used in the cathode. For the former (blue color), the optimized dew points were 79/80 °C. In the latter case, the optimized dew points were much lower, 70/75 °C. From a performance perspective, the better configuration was GT78 at the anode and GT32 at the cathode. The peak power density was only slightly higher than the data in **Figure 5.1**, 2.3 W/cm^2, though the achievable current at 0.2 V was much higher (8.2 vs. 7.4 A/cm^2)

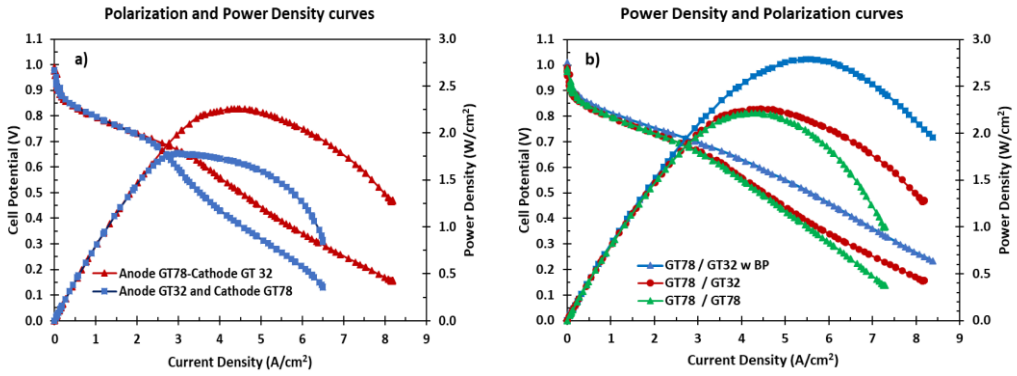

Figure 5.2: Behavior of asymmetric deployment of the GTXX ionomers. a) Polarization and power curves at optimized dew points comparing the asymmetric deployment of GT32 and GT78 ionomers in Type 1 GDEs, no backpressure; b) Polarization and power curves at optimized dew points comparing Type 1 GDEs, GT78 ionomer both sides, GT78/GT32 configuration without and with 200 kPa backpressure applied to the cathode side only. For all experiments, the cell with temperature was 80 °C, H_2/O_2 flowrates were 1 L/min; and AEM was GT64-15.

The combination of GT32 at the anode and GT78 at the cathode suffered from ohmic losses and mass transport losses, which can be seen by observing the broad peak of the power density curve, transitioning to sudden and severe mass transport limitations. This is

supported by looking at the average HFR recorded during testing. The average HFR with the GT32/GT78 in the anode/cathode was around 5.6 mOhm (ASR=28 $m\Omega \cdot cm^2$) compared to 5.1 mOhm (ASR=25.5 $m\Omega \cdot cm^2$) for GT78/GT32. This is despite the fact that the optimized dew points for the GT32/GT78 configuration were much higher than the GT78/GT32 configuration. The fact that GT78 on the anode side and GT32 on the cathode side, with lower optimized reacting gas dew points, leads to higher performance suggests that the higher water uptake and IEC of GT78 helps the anode electrode discharge water more quickly to the membrane (for back-diffusion to the cathode) and to the anode gas. At the cathode, the main difference between having GT32 and GT78 ionomer (**Figure 5.2b**) is that there is slight increase in the cell performance at higher current densities, > $4A/cm^2$. However, the overall shape of both polarization curves suggests that there is an underlying mass transport issue limiting both cells that could be remedied. One possible explanation for such behavior is low water content at the cathode – where the GT78 ionomer distributes the water too quickly, moving it from the AEM through the cathode to the GDL and flowfield instead of retaining it to either react or keep the cathode hydrated. If this were true, the high current density cell performance would be improved by adding backpressure to the cathode side of the cell. Adding backpressure would suppress convective evaporation, essentially allowing additional water to be taken up by the cathode ionomer. The application and significance of backpressure in AEMFCs has been studied by several researchers **[256], [274], [275]**. In this case, the result of adding backpressure to the cathode side was a clear increase in performance. Not only was the high current density performance increased (**Figure 5.2b**), but the kinetics were also slightly enhanced as well. This resulted in an increase in the peak power density to 2.7 W/cm^2 with optimized reacting

gas dew points of 68 °C/73 °C. The lower reacting gas dewpoints with the back pressurization were lower than the case without backpressure, most likely to balance the amount of water taken up by the polymer and limited swelling. In contrast, application of back pressure on the anode side had a negative effect due to flooding, supporting the conclusion above that evaporation at the anode is critical. Moreover, application of backpressure was not effective when added to either of the electrodes when anode/cathode ionomer configuration was GT32/GT78.

Based on the results in **Figure 5.2**, it appears that the anode prefers more conductive and hydrophilic ionomers than the cathode to increase performance as long as electrode flooding does not occur. This might explain why our results – where the anode prefers the high IEC ionomer and the cathode prefers the low IEC ionomer – differ from Leonard and coworkers **[284]**. As evidenced by the lower mass transport limiting current in their study and lower cell performance at higher humidity conditions, their hexyltrimethyl ammonium-functionalized poly(phenylene) AEM and poly(fluorene) ionomer like have lower water transport properties than the poly(norbornene) materials in this work. This led to the observation that their anode preferred the low IEC ionomer and cathode preferred the high IEC ionomer.

In addition to the preferred asymmetric electrode configuration for high IEC and higher water transport materials, the data above also showed that the application of back pressure was effective in terms of enhancing performance by allowing for additional water into the cathode. Therefore, to allow for high water content while imbibing the electrodes with an increased ability to reject excessive liquid water, Type 2 GDEs were investigated where PTFE was incorporated into both catalyst layers. At the cathode, it is also possible that

adding PTFE in the electrode makes it even more hydrophobic than the AEM, effectively holding water at the AEM/cathode interface where water is needed for the reaction, without having extensive water throughout the catalyst layer which may lead to flooding. In all Type 2 GDEs configurations, the peak power and current density increased compared to the results in **Figure 5.2** without the added hydrophobic agent. The results for all of the Type 2 electrodes are shown in **Figure 5.3** and the best combination is presented and discussed below.

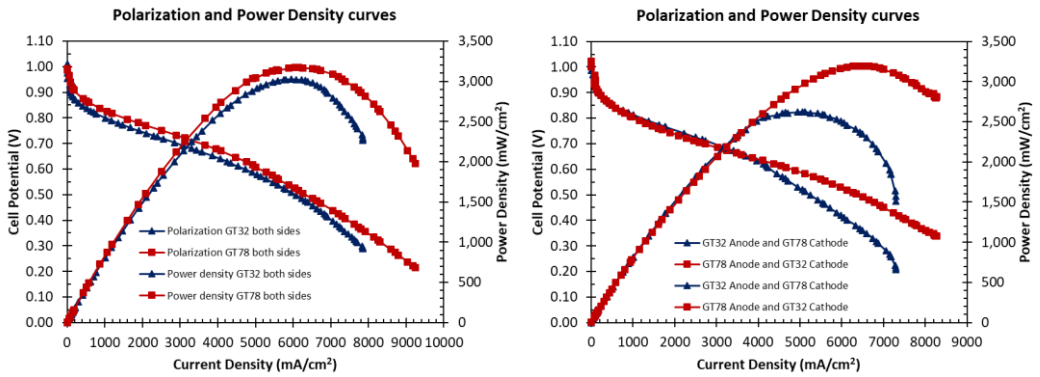

Figure 5.3: A). Polarization and power curves comparing GT78 Ionomer in both electrodes to GT32 Ionomer in both electrodes, (B). Polarization and power curves comparing the asymmetric deployment of GT32 and GT78 ionomers. Type 2 GDEs with cell temperature 80 °C and individually optimized dew points, volumetric flowrate 1 Liter/min on both sides with no backpressure

Of particular note is the performance of the cells that were constructed with Type 2 GT78 ionomer GDEs at the anode and Type 2 GT32 ionomer GDEs at the cathode, **Figure 5.4**. In this configuration, the cell peak power density and maximum achievable current density were the highest of any investigated configuration. A peak power density of around 3.2 W/cm^2 was obtained with H_2/O_2 while a peak power density of around 1.75 W/cm^2 was recorded with H_2/Air (CO_2-free) reacting gases. As can be seen from the H_2/Air polarization curve, mass transport issues become noticeable at higher current density, but not in H_2/O_2 cells, which suggests that the mass transport-limiting process in these high

performing cells is oxygen, not water, transport. These two facts (water transport from the anode to the cathode and oxygen is the limiting reagent in air-cathode cells) implies that the critical active cathode area is at the cathode/membrane interface. Operating on H_2/O_2, it is noteworthy that these cells could operate at currents exceeding 9.0 A/cm^2 at 0.2 V.

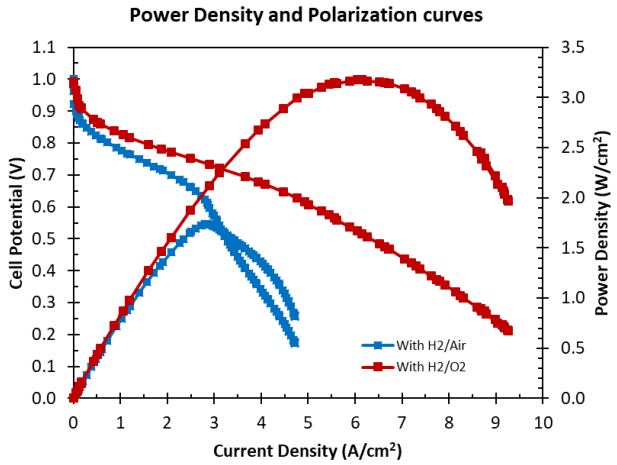

Figure 5.4: Polarization and power curves for AEMFCs with a Type 2 GT78 GDE in the anode and Type 2 GT32 GDE in the cathode operating on both H_2/O_2 and H_2/ CO_2-free air feeds. Cell conditions: temperature = 80 °C; Optimized dew points: 72/74 °C with H_2/O_2 and 68/72 °C with H_2/ CO_2-free Air; Flowrates: 1 L/min; GT64-15 AEM

3.3 Long-Term Durability

It has been well-documented that the durability of prior AEMFCs has been mostly poor **Error! Reference source not found.**, and durability has remained one of the critical issues l imiting the expansion of AEMFC deployment and commercial consideration. To some extent, the previous poor durability is troubling because many modern membranes and ionomers have shown acceptable ex-situ stability for several hundred hours. This suggests that operational stability may be a function of more than chemical stability, and that other variables exacerbate the stability problem, such as the balance and transport of water. Because water likely plays an important role in the operational stability, and the results above show that the physical properties of the ionomer play an important role in AEMFC operation, the ionomer properties might also influence AEMFC durability.

Figure 5.6 shows the results of a 2000 hr durability test for an AEMFC operating at 600 mA/cm^2 with Type 2 electrodes with the GT78 ionomer at the anode and the GT32 ionomer at the cathode. For this cell, the reacting gas flowrates were both 0.3 L/min and no backpressure was applied. The initial anode/cathode reacting gas dew points were 72/74 ^{o}C, though the dew points were slightly adjusted occasionally to ensure that the cell had adequate humidification. The results presented here show the lowest reported voltage decay rate for any AEMFC reported to date: only 15 μV/hr. Additionally, the HFR only increased by around 3.6 mΩ (area-specific resistance, ASR, increase of 18 mΩ·cm^2). It is noted that increase in ASR of of 18 mΩ·cm^2 corresponds to a 11 mV increase in resistive loss over the life of the cell compared to the 15 μV/hr for 2000 hr total loss of 30 mV over the 2000 hr period. Hence, a significant fraction of the voltage loss during the experiment was caused by the slow increase in the ASR. This was further confirmed by the negligible change in the polarization curves over the 2000 hr test (**Figure 5.5** in the Supporting information file, collected in the region of operational interest). It should be noted that the durability experiment was performed at different conditions than the polarization experiments, resulting in lower performance for the polarization curves in **Figure 5.5** compared to the polarization curve in **Figure 5.4**. First, a lower flowrate was used (0.3 vs. 1.0 L/min). Second, the operating temperature was slightly lower (75 vs. 80 ^{o}C). Third the relative humidity of both the anode and cathode reacting gases were higher. All of these were done to increase the amount of liquid water that was present in the cell, increasing the degree of hydration during steady-state operation. These can make water management more challenging at higher currents during transient performance (e.g. while taking polarization curves). However, high currents were not the objective here. The objective

was to stabilize operation at 600 mA/cm^2. It has been shown that if a different operating point were desired, different dew points could be set to re-balance the cell water to maximize performance under those conditions **[284]**.

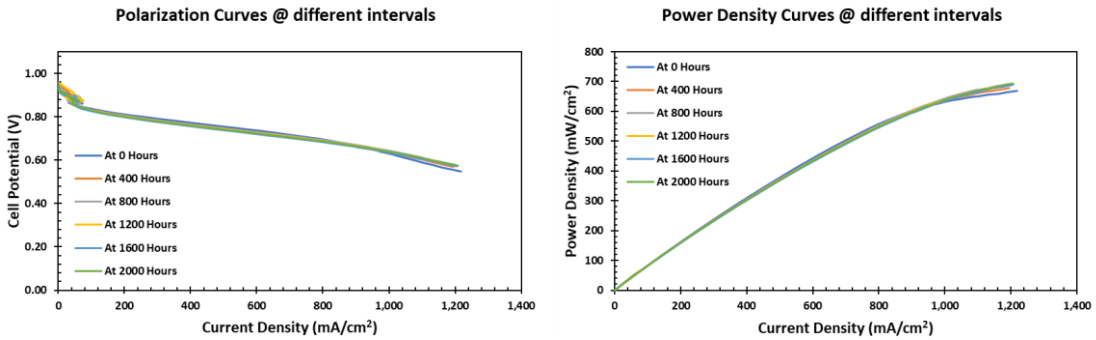

Figure 5.5: A). Polarization curves, **(B).** Power density curves with GT78 in anode and GT32 in cathode in Type 2 GDEs composition, cell temperature 75 °C and 72 °C / 74 °C dew points, volumetric flowrate 0.3 Liter/min on both sides with no backpressure

The results in **Figure 5.6** are significantly better than what was observed for Type 1 GDEs using GT78 ionomer in both electrodes in the Supporting Information) where the degradation rate was 289.46 µV/hr (only operated for 150 hours). Therefore, the results of this work represent an attractive combination of high performance and record setting durability for AEMFCs. The improvements here were enabled by a combination of high performing AEMs, new ionomers and electrode engineering to create highly effective GDEs – and the results presented here can be used by the field as a guide and benchmark for future work.

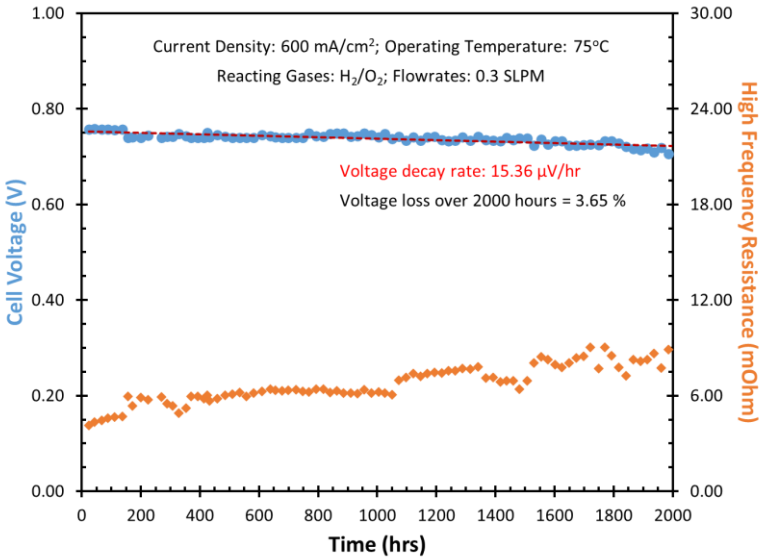

Figure 5.6: Cell Voltage and HFR during a long-term durability test with Type 2 GDEs (GT78 ionomer anode and GT32 ionomer cathode), cell temperature 75 °C and dew points 72/74 °C operating at 600 mA/cm^2, volumetric flowrate: 0.3 Liter/min on both sides.

4. Conclusions

In this work, three tetrablock poly(norbornene) copolymers – GT32, GT64 and GT78 – were synthesized and incorporated into the anode and cathode of operating AEMFCs. These ionomers demonstrated excellent dimensional stability without significantly sacrificing the ionic conductivity. IEC, water uptake and molecular weight were evaluated for each polymer and tied to AEMFCs performance and durability. It was demonstrated that a combination of hydrophilic (GT78) ionomer in the anode electrode and more hydrophobic (GT32) ionomer in the cathode electrode resulted in the best behavior. This was explained based on the fact that the anode and cathode have different water requirements, hydrophobic/hydrophilic properties, and conductivity. This best-performing electrode combination was able to achieve very high peak power density, 3.2 W/cm^2, and very high current density. The top-performing electrodes were also tested for their longevity in AEMFCs. Record-setting AEMFC durability was observed over 2000 hours

while operating at a DOE-prescribed current density of 600 mA/cm^2, with an ultra-low decay rate of 15.36 μV/hr, which resulted in only a 3.65% voltage loss over the 2000 hr experiment. In future, instead of adding additional hydrophobic content (PTFE) in GDEs, it would be interesting to explore the ionomers performance by fine-tuning the hydrophilic/hydrophobic properties through the polymer chemistry itself.

CHAPTER 6

UNDERSTANDING RECOVERABLE VS. UNRECOVERABLE VOLTAGE LOSSES AND LONG-TERM DEGRADATION MECHANISMS IN ANION EXCHANGE MEMBRANE FUEL CELLS[5]

Abstract

Anion exchange membrane fuel cells (AEMFCs) have recently shown excellent progress in terms of their performance – e.g., achievable power and current density. However, very few AEMFCs have been demonstrated with the ability to operate for a long duration (>1000 hr). In addition, it is unknown whether performance losses observed during operation are reversible, irreversible, or a combination of the two. In this study, a high-performance AEMFC operated continuously at 600 mA/cm^2 for 3600 hours (150 days) at 80^{o}C with H_2/O_2 reacting gases was demonstrated. Throughout testing, the electrochemical properties of the AEMFC were probed to provide information about performance degradation pathways and their degree of reversibility. It was found that a portion of the performance loss that occurs during AEMFC operation was due to sub-optimal reaction conditions and can be recovered. At the end of the experiment, the cell

---

[5]Hassan, N.U., Zachman, M.J., Mandal, M., Firouzjaie, H.A., Kohl, P.A., Cullen, D.A., and Mustain, W.E., Understanding Recoverable vs Unrecoverable Voltage Losses and Long-Term Degradation Mechanisms in Anion Exchange Membrane Fuel Cells, *ACS Catal.*, **12,** 8116-8126 (2022).

was disassembled, and its structure and composition were evaluated at the nanoscale by aberration-corrected scanning transmission electron microscopy and energy-dispersive X-ray spectroscopy. The structure and composition of the electrode were compared to cells at the beginning of their operational life. It was found that the primary mechanism for long-term AEMFC performance loss was catalyst agglomeration. In fact, during the operational time there was no evidence of significant polymer degradation, which was possible due to the high hydration state of the cell. By documenting the long-term changes in high-performing AEMFCs, this work provides important information for the systematic design of cell components and demonstrates the importance of controlling cell operation, which can aid in the commercialization and widespread deployment of low-cost, long-life AEMFCs.

1. Introduction

Though anion exchange membrane fuel cells (AEMFCs) have historically suffered from low performance and durability **[287]**, **[288], [289]**, they have seen a surge in performance over the past few years, with several research groups advancing their achievable peak power density, current density, and longevity **[290], [291], [292], [293]**. State-of-the-art AEMFCs are now able to achieve peak power densities of 3.5 W cm^{-2} operating on H_2/O_2 and 1.75 W cm^{-2} operating on H_2/air (CO_2-free) **[290], [291], [294], [295]**. These advances have been possible because of new reactor engineering that carefully manages the quantity and distribution of cell water **[295], [296], [297], [298], [299]**, as well as the emergence of high-performance anion exchange membranes (AEMs) **[300], [301], [302]**, anionomers (AEIs) **[295], [296]**, and efficient electrocatalysts **[303], [304], [305], [306]**.

Despite advances in the performance, the durability of AEMFCs has generally remained poor **[287], [289]**. In fact, only two cells have been documented in the literature with good stability over 1000 hours of operation **[291], [292], [293], [294], [295]**. However, neither of these long-duration studies reported extensive post-operational physical and electrochemical characterization, leaving a void in the understanding of the dominant degradation mechanisms in operating cells **[289]**. To some extent, poor durability is troubling because many modern membranes and ionomers have shown acceptable *ex-situ* stability over hundreds or thousands of hours. This suggests that operational stability may be a function of more than simply the chemical stability of the individual components, with other variables such as water balance and transport potentially exacerbating the stability problem. In addition, it is unknown the extent to which the decline of AEMFC operating voltage is recoverable versus unrecoverable and what the dominant mechanisms are for each type of loss under normal operating conditions.

One possible source of degradation is the AEM, where polar moieties can undergo oxidation or nucleophilic attack **[287], [307], [308], [309], [310], [311], [312], [313]**. Another possible source for degradation is the *in-situ* aging of the anode and cathode catalysts. It has been stated that the alkaline environment in the AEMFC might provide a less corrosive environment for electrocatalysts than the acidic environment in proton-exchange membrane fuel cells (PEMFCs), which may make it possible to avoid the catalyst agglomeration that has been well-documented in PEMFCs **[314], [315], [316]**. However, some recent studies with AEMFCs have shown evidence for both carbon corrosion and catalyst agglomeration, making changes in catalyst structure important to study in long-life cells **[317], [318]**. In addition to these suggested degradation mechanisms, new

performance loss mechanisms may be present in AEMFCs that are not yet documented or understood. To move AEMFC technology forward, it is important to identify the relevant degradation mechanisms and understand the extent to which the corresponding performance losses are reversible (e.g., driven by sub-optimal operating conditions) or irreversible (e.g., from material or interface degradation). Such information may enable appropriate methods for minimizing their effects to be developed.

In this work, a high-performing, durable AEMFC was operated continuously at a constant current density of 600 mA cm^{-2} for 3600 hours (150 days), which is a seminal achievement for AEMFCs. During this time, there were periods of extremely high operational stability, particularly over the first 2000 hours. That 2000-hour dataset was previously reported by our team to emphasize the achievable peak power density and to show that it is possible to operate AEMFCs with a low voltage decay rate. However, just after the first 2000 hours of operation, and the submission of our previous publication, the rate of voltage decay increased along with the high frequency resistance (HFR). Therefore, this publication focuses on understanding the operational the phenomena that contributed to the increased voltage decay and detailing how the cell performance was recovered. It is shown that some of the voltage loss was attributable to the operating conditions and was recoverable, while some was due to chemical and physical changes in the cell and was unrecoverable. The chemical and physical changes experienced by the cell components that drove the irrecoverable losses were quantified by disassembling the cell at the end of the 3600 hours of operation, which involved an extensive array of high-resolution aberration-corrected scanning transmission electron microscopy (STEM) and spectroscopy. It should be noted that the cell teardown was purposely carried out while

the cell was still in a stable operating condition, not after a catastrophic failure. The result of this effort is the first comprehensive study of the degradation mechanisms that occur during AEMFC operation.

2. Experimental

2.1 Electrode Preparation

Both the anode and cathode electrodes were prepared using the procedure described in previous publications **[291], [295], [296], [319].** In summary, ionomer and PTFE (Ultraflon MP-25, Fuel Cell Store) were first introduced into a mortar and ground with a pestle for 10 min. Following the initial grind, catalyst and additional carbon black (Vulcan XC-72R) were added to the mortar and the mixture was ground for 10 min. Next, a small amount of 18.2 MΩ deionized water (DI) was added to the mortar, forming a paste by further agitation with the pestle. The paste was transferred to a Teflon vortex tube and 2-propanol (IPA) was added such that the IPA:DI ratio was 9:1. Finally, the mixture was sonicated to create an ink dispersion that was sprayed onto a 25 cm^2 Toray-060 gas diffusion layer (GDL) with 5% PTFE wetproofing to create a gas-diffusion electrodes (GDE).

For all the experiments in this work, the anode catalyst was PtRu/C (Alfa Aesar HiSPEC® 10000, Pt nominally 40%wt., and Ru, nominally 20%wt., supported on Vulcan XC-72R carbon) and the cathode catalyst was Pt/C (Alfa Aesar HiSPEC 4000, Pt nominally 40%wt., supported on Vulcan XC-72R carbon). The AEIs used for ionic conduction in the anode and cathode were poly(norbornene)-based copolymers whose synthesis has been described elsewhere. The anode AEI was a GT-78 ionomer (where 78% of the monomer groups are quaternized, IEC= 3.74 meq/g). The cathode AEI was a GT-32 ionomer (where 32% of

the monomer groups are quaternized, IEC=1.88 meq/g). In a typical anode ink preparation, the mass of ionomer, PTFE, PtRu/C, and added Vulcan XC-72R were 45 mg, 12 mg, 150 mg, and 60 mg, respectively, and the volume of DI and IPA were 1 mL and 9 mL, respectively. In a typical cathode ink preparation, the mass of ionomer, PTFE, and Pt/C were 25 mg, 8 mg, and 100 mg, respectively (with no additional Vulcan), and the volume of DI and IPA were 1 mL and 9 mL, respectively. Following the preparation above, individual 5 cm^2 electrodes were cut from the larger electrodes for cell testing.

2.2 AEMFC Assembly and Testing

After being cut to the appropriate size, the anode GDE, cathode GDE, and membrane were hydrated in DI water for 20 min and then soaked three times (20 min each) in 1.0 M KOH to remove impurities and ion exchange the quaternary ammonium groups before cell assembly. After the excess KOH was removed from the components and the electrode thickness was measured, the membrane was sandwiched between the two electrodes in 5 cm^2 active area Scribner and Associates Fuel Cell Hardware with a single-channel serpentine flow field. During cell sealing, the thicknesses of the Teflon gaskets were selected to enable ca. 25% compression. After cell assembly, N_2 was flowed through the anode and cathode at 0.4 L/min and 100% relative humidity until a cell temperature of 60°C was reached. Then, the N_2 feeds were switched to ultra-high purity H_2 and O_2 and a constant voltage of 0.5 V was applied to initiate the cell break-in procedure. After a stable current density was established, the dew point of the anode and cathode reacting gases were systematically optimized as previously reported **[320]**. The cell temperature was gradually increased to 80°C in 5°C increments, with the anode/cathode dew points being simultaneously optimized with the cell temperature to avoid membrane dry-out. After the

cell temperature reached 80°C, the degree of back-pressurization was also set. After the cell equilibrated at the desired conditions for around 30 min, a polarization curve was collected by slowly sweeping the voltage from the open circuit voltage to 0.1 V at a 10 mV/s scan rate.

After cell break-in and collecting of the initial polarization curve, multiple cells were exposed to limited testing, where the current density was held for 24 hours at 600 mA/cm^2. This type of operation allowed for the baseline cell performance to be measured and the membrane electrode assembly (MEA) to be bonded (strong adhesion between the electrodes and membrane). This condition will be considered in this work to represent the beginning-of-life (BOL). One cell was subjected to long-term testing where a U.S. Department of Energy-recommended current density of 600 mA/cm^2 **[321],** was maintained for 3600 hr (150 days). Though this cell never experienced catastrophic failure, it was decommissioned in order to study the underlying degradation mechanisms that govern "normal" operation. The results following the 3600 hr test will be referred to as the end-of-life (EOL). During the long-term test, the cell temperature was set at 75°C and the dew points of the reacting gases were initially set to 72°C at the anode and 74°C at the cathode. The dew points were adjusted occasionally (typically ± 1°C) to ensure adequate membrane hydration. Also, the cell high frequency resistance (HFR) was monitored (at a frequency of 7 kHz) by the Scribner 850e fuel cell test station throughout the test.

2.3 Electrochemical Characterization

In addition to the galvanostatic experiments and polarization curves described above, it was also important for the hydrogen crossover to be determined. It is well-known that hydrogen from the anode electrode may permeate through the AEM and degrade cell

performance by reducing the OCV and by decreasing fuel efficiency. The extent to which the fuel crossover affects the cell is often dominated by the physical state of the membrane and can be used as a measurement of the mechanical integrity of the membrane over time. The hydrogen crossover was measured at BOL and EOL by feeding N_2 to the cathode (1.0 L/min at 100 % relative humidity) and hydrogen to the anode (1.0 L/min at 100 % relative humidity) at a cell temperature of 75^{o}C. The cell voltage was swept linearly at a rate of 1 mV/s from the open circuit voltage (~ 0.1 V) to 0.8 V **[322]**. In a typical experiment, the current response initially increased, but leveled off at a constant value that is dictated by the rate of H_2 diffusion through the AEM, which can be converted by Faraday's law into the H_2 flux.

The behavior of the BOL and EOL cells were also investigated by electrochemical impedance spectroscopy (EIS). EIS is a very common experimental technique where a small alternating current (AC) current or voltage signal is imposed on an electrochemical device and the amplitude and phase of the response are monitored. EIS experiments were carried out from 0.1 Hz to 10 kHz with an amplitude of 5% of the applied current. Important properties of the cell including Ohmic (bulk ion transport) resistance, charge transfer resistance, double layer capacitance, and diffusion behavior were extracted from the raw data.

2.4 Cell dismantling, STEM and EDS analysis

Both BOL and EOL cells were dismantled and subjected to microscopic analysis by analytical STEM. Sample preparation was performed by embedding small portions of the BOL and EOL MEAs in epoxy (Araldite 6005, dodecenylsuccinic anhydride (DDSA), and 2,4,6-tris(dimethylaminomethyl)phenol (DMP-30)), allowing the embedded samples

to cure, and generating thin cross-sectional samples from them by ultramicrotome. The sections were cut nominally 150 nm thick, which increased structural integrity of the assembly during preparation compared to thinner slices. Aberration-corrected STEM imaging and energy dispersive X-ray spectroscopy (EDS) were performed to analyze the MEA structure, catalyst particle morphology, and elemental composition of all structures present. A JEOL NEOARM instrument in the Center for Nanophase Materials Sciences at Oak Ridge National Laboratory was used to collect the STEM data. The instrument was operated at 200 kV with a semiconvergence angle of 28 mrad and a probe current of ~0.3 nA. EDS was performed using dual JEOL SDDs, which provided a large total solid angle for collection. EDS maps were generally acquired with dwell times of 5-10 µs/pixel at a resolution of 512×512 pixels, summing multiple drift-corrected frames for a total acquisition time of around six minutes, giving a total applied dose of <100 $e^-/Å^2$. Data was background subtracted in Python using a linear fit beneath each EDS peak, and appropriate k factors were applied to convert integrated intensities to compositional information.

3. Results and Discussion

3.1 BOL to EOL Morphological Changes: STEM and EDS Analysis

During long-term operation, it is expected that the components of any device will undergo a number of physical changes. Often, these physical changes drive the behavior of the cell and are accompanied by performance degradation. This makes it important to quantify the physical changes that occur in well-performing cells, which allows researchers to understand underlying mechanisms that can be managed or eliminated in later device generations. To do this for AEMFCs for the first time, both BOL and EOL MEAs were dismantled following their break-in and designated operation. First, the MEAs were

visually inspected for any signs of damage or corrosion, and no signs of any physical damages were found. Additionally, the MEAs were all very well laminated. Following this inspection, the BOL and EOL MEAs were sectioned for STEM and EDS analysis as described in the Experimental section.

Some of the most common degradation mechanisms in PEMFCs are catalyst sintering, growth, and agglomeration. To study the extent to which catalyst agglomeration occurred during long-term AEMFC operation, aberration-corrected high-angle annular dark-field (HAADF) STEM was used to image catalyst particles in the BOL and EOL MEA cross sections. **Figure 6.1** shows representative HAADF-STEM images of the cathode and anode catalyst particles at the BOL and EOL (additional images with measured particle/feature sizes are provided in **Figure 6.2** and **Figure 6.3**). At the BOL, the Pt cathode catalyst particles had a range of diameters from approximately 1 nm to 10 nm, as shown in **Figure 6.1a**, with an average size of ca. 2.5 nm (**Figure 6.5a**). By the EOL, the cathode particles significantly enlarged, with few particles under ~6 nm remaining (**Figure 6.2** and **Figure 6.5a**). Increasing the cathode catalyst particle size can lead to many effects including a smaller surface area, which would increase the local current density for the constant current operation used here, and an increase in charge transfer resistance due to lower surface catalytic activity (i.e., chemical change in the surface during rearrangement). This can also lead to an increase in local hydroxide and water turnover frequency at each site due to higher local current density, driving increased mass transport resistance as well.

In contrast to the Pt cathode particles, the PtRu anode catalyst particles did not change in size or morphology as significantly over the life of the cell. The BOL anode consisted mainly of particles in approximately the 2-5 nm range, which were agglomerated

into larger structures. At the EOL, the particle size had increased somewhat, with agglomerated super-structures similar to the BOL (**Figure 6.3** and **Figure 6.5a**). Hence, agglomeration at the oxygen cathode was more extensive than the hydrogen anode and much of the increase in kinetic resistance that occurred during operation may be attributable to the cathode. That is not to say that the anode catalyst did not change at all during operation, but to a lesser extent than the cathode catalyst. STEM-EDS showed that the local atomic ratio of Pt:Ru in the anode varied between ~2:1 and ~3:1 at the EOL, compared to 1:1 at the BOL. STEM-EDS also revealed that some of the Ru lost from the PtRu particles agglomerated into Ru-rich nanoparticles at the anode-AEM interface (**Figure 6.4**). This compositional change can act to increase the charge transfer resistance of the anode over time **[323]**.

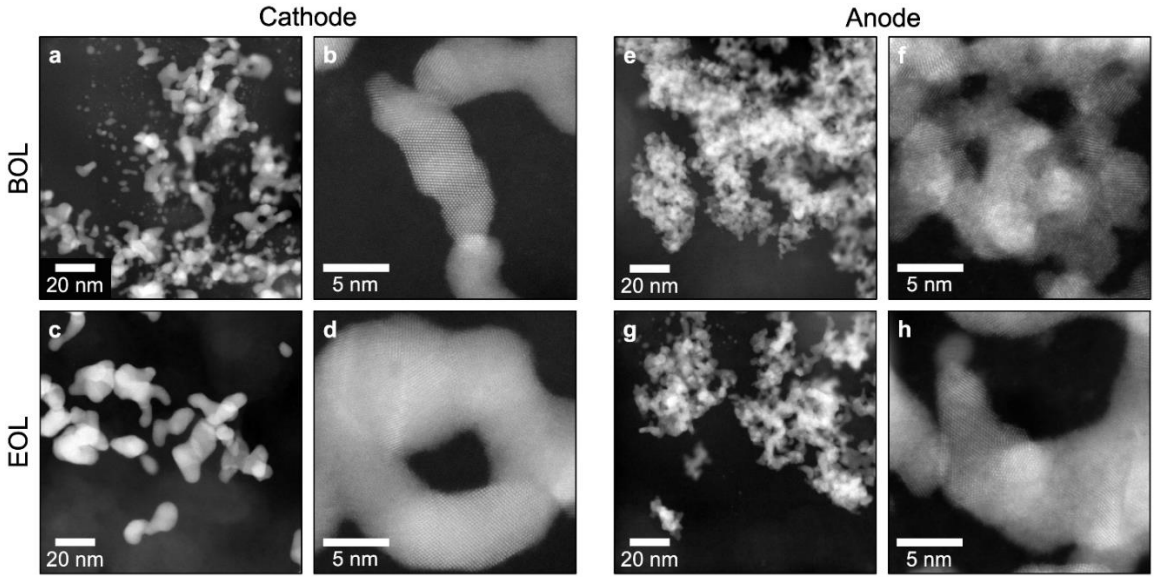

Figure 6.5: Representative HAADF-STEM images of cathode and anode particles at BOL and EOL. (a) A range of Pt cathode particles with sizes from ~1 nm to ~10 nm across were present at BOL. (b) The particles consistent of crystal grains spanning the full width of the particles. (c) The cathode particles enlarged significantly by EOL, with particles typically >10 nm across. (d) The grain size correspondingly enlarged, generally still spanning the width of the particles. (e) PtRu anode particles were individually a few nm across but tended to be present in large agglomerations. (f) As with the cathode particles, the constituent crystal grains spanned the width of the anode particles. (d) Little change was observed in the agglomerate structure of the anode particles by EOL. (h) The individual particle and grain sizes increased to ~5 nm, however.

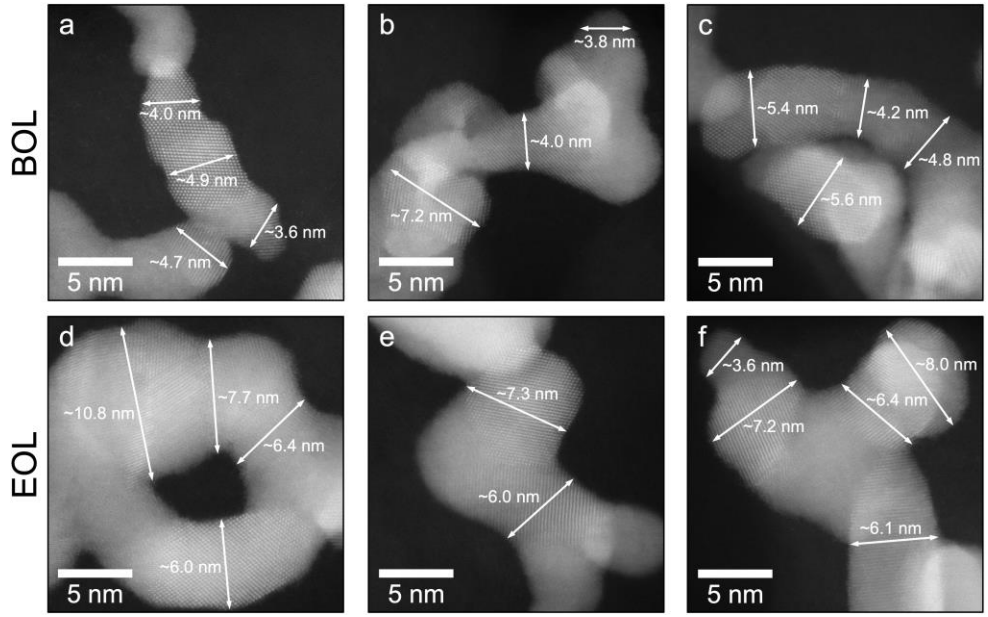

Figure 6.2: Representative HAADF-STEM images of BOL and EOL cathode nanoparticles (excluding smallest BOL particles) with measurements of individual crystal grains that span an agglomerate shown.

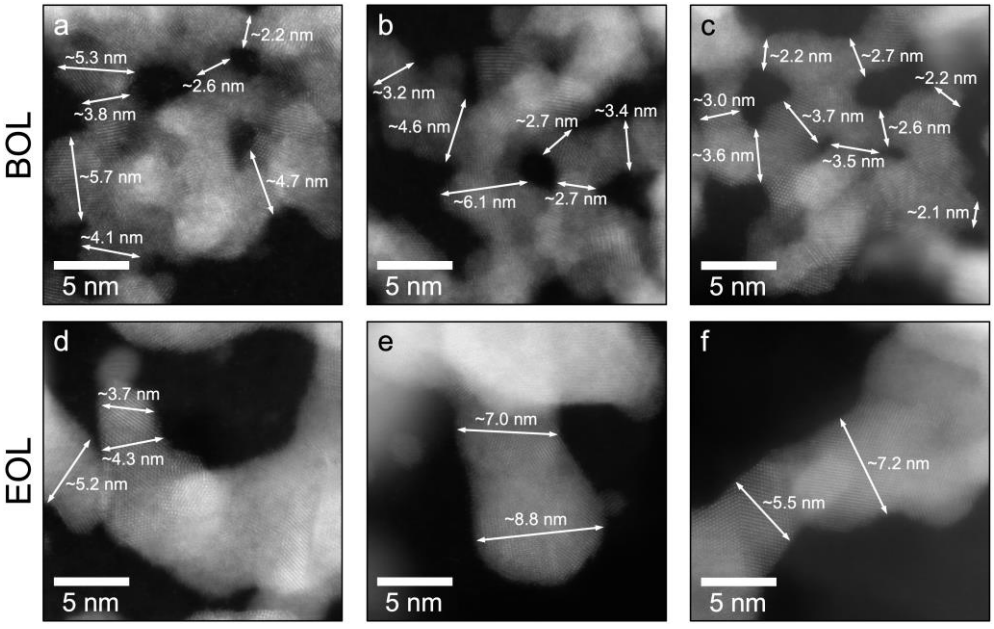

Figure 6.3: Representative HAADF-STEM images of BOL and EOL anode nanoparticles with measurements of single crystal grains that span an agglomerate shown.

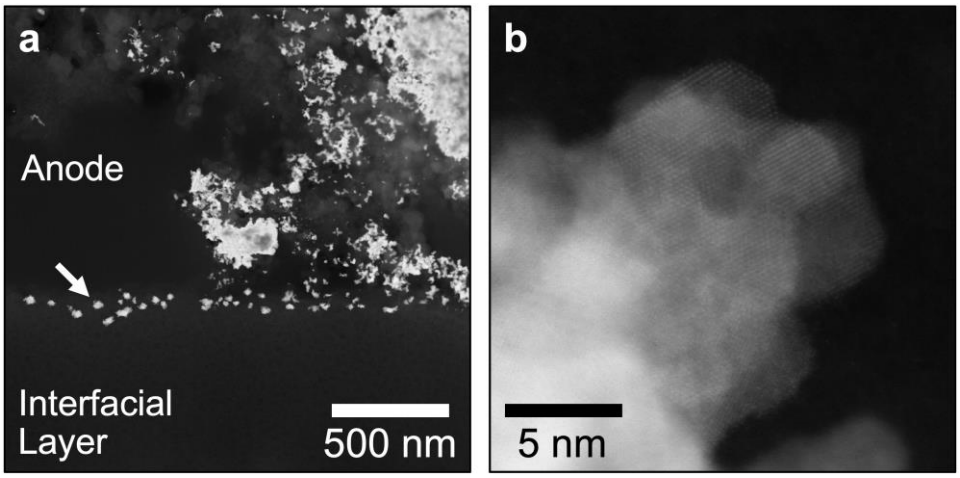

Figure 6.4: HAADF-STEM images of the occasionally Ru-rich nanoparticles embedded just inside of the interfacial layer, at its interface with the anode.

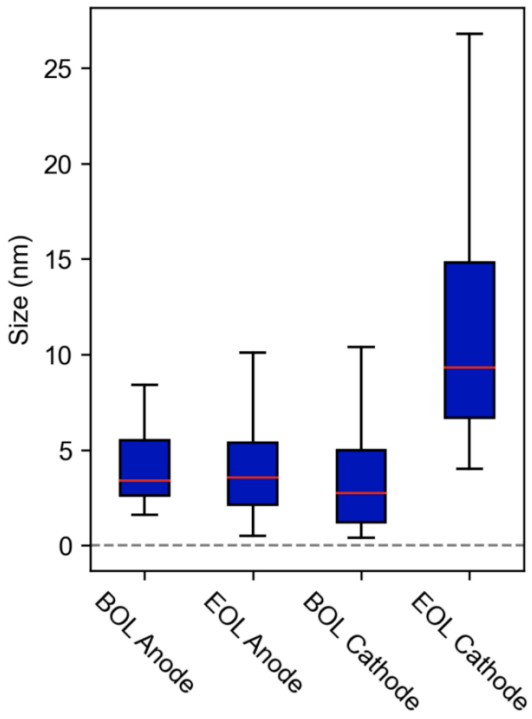

Figure 6.5a: Catalyst size measurements from HAADF-STEM images. Particle feature sizes were measured from the lower magnification HAADF-STEM images in Fig. 4 (main manuscript). For approximately spherical particles, the size was defined as the diameter of the particle. For non-spherical particles, a measurement was made across both the short and long axis to capture the range of lengths present. For highly agglomerated particles, measurements were performed either where widths of isolated sections of the particles could be discerned or where surface features protruded from the agglomerate, in a similar manner to the single crystal grain size measurements The results demonstrate that the feature sizes of the BOL anode, EOL anode, and BOL cathode catalysts are similar, while those of the EOL cathode are significantly larger. In the plot, the red line indicates the median size, while the boxes and whiskers indicate the upper/lower quartiles and most extreme (non-outlier) values, respectively. The numbers of measurements were 71, 134, 420, and 52 for the BOL anode, EOL anode, BOL cathode, and EOL cathode, respectively.

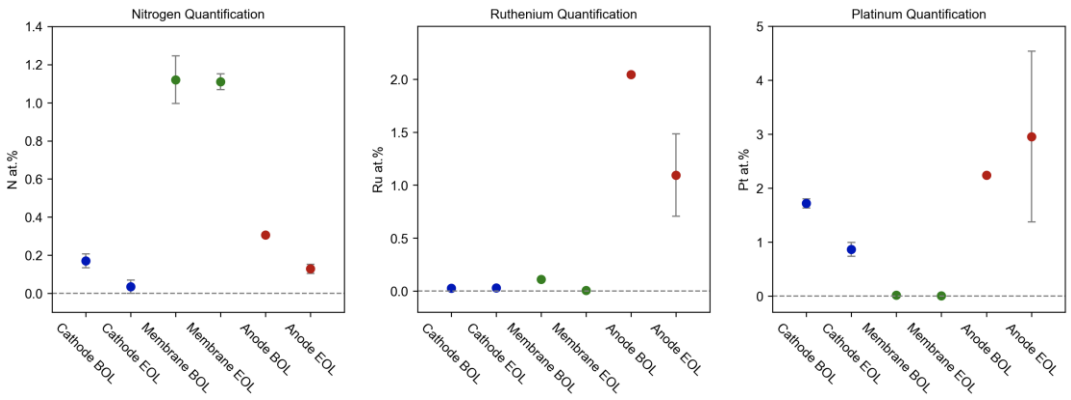

Figure 6.5b: Quantification of nitrogen, ruthenium, and platinum in the cathode, membrane, and anode at BOL and EOL by STEM-EDS. Each data point represents multiple measurements from separate regions, with error bars show the standard deviation of the measurements, which includes compositional variations and fluctuations due to noise. The proportion of N in the electrodes is slightly lower in the EOL samples than the BOL, while it was unchanged in the membrane. The proportion of Ru in the anode markedly drops from BOL to EOL, while Pt drops in the cathode and increases in the anode (due to the decrease in Ru). Note that the nonzero Ru content in the BOL membrane is due to the presence of a small quantity of Cl and the overlap of Cl-K and Ru-L peaks.

STEM-EDS elemental mapping of BOL and EOL MEA thin sections was also performed to identify degradation processes involving nanoscale compositional and morphological changes to the other cell components. **Figure 6.6** shows the results for the EOL MEA, including a HAADF image, compositional maps (atomic percentages extracted from background subtracted data, with elements separately normalized for display purposes), and compositional profiles from spectra averaged parallel to the AEM-catalyst layer interface, all acquired across the membrane from the cathode to the anode. In addition to the greater agglomeration of anode particles than cathode particles (though the average individual particle size was larger in the cathode, as noted above, and the change from BOL to EOL was more significant in the cathode), the HAADF image in **Figure 6.6a** also showed the presence of two structures hundreds of nanometers across present at the

electrode-membrane interface. From this image, it appears that the material within these interfacial layers was homogeneous, though micrometer-sized pores were present. The compositional maps in **Figure 6.6b** show that these layers contain nitrogen (from the quaternary ammonium groups) while being free of fluorine (from the PTFE membrane support), as confirmed by the line profiles in **Figure 6.6c**, derived from spectroscopic data parallel to the electrode surface in this region. To investigate when and where these layers were present, imaging was done on several BOL samples and the EOL sample, both inside and outside of the active area. In short, these interfacial layers were found across most samples and the thickness of these layers could not be correlated with the cell age. Their thickness did appear to be correlated with overall membrane thickness, however. Taken together, these data suggest that the interfacial layers were comprised from excess polymer on the membrane reinforcement and are therefore an artifact of the membrane casting process. It was noted, however, that the BOL samples with the thickest interfacial layers appeared to have the best adhesion, though this was not quantified. The presence of these layers likely explains why the MEAs were well-bonded despite the lack of a hot-pressing step prior to cell assembly.

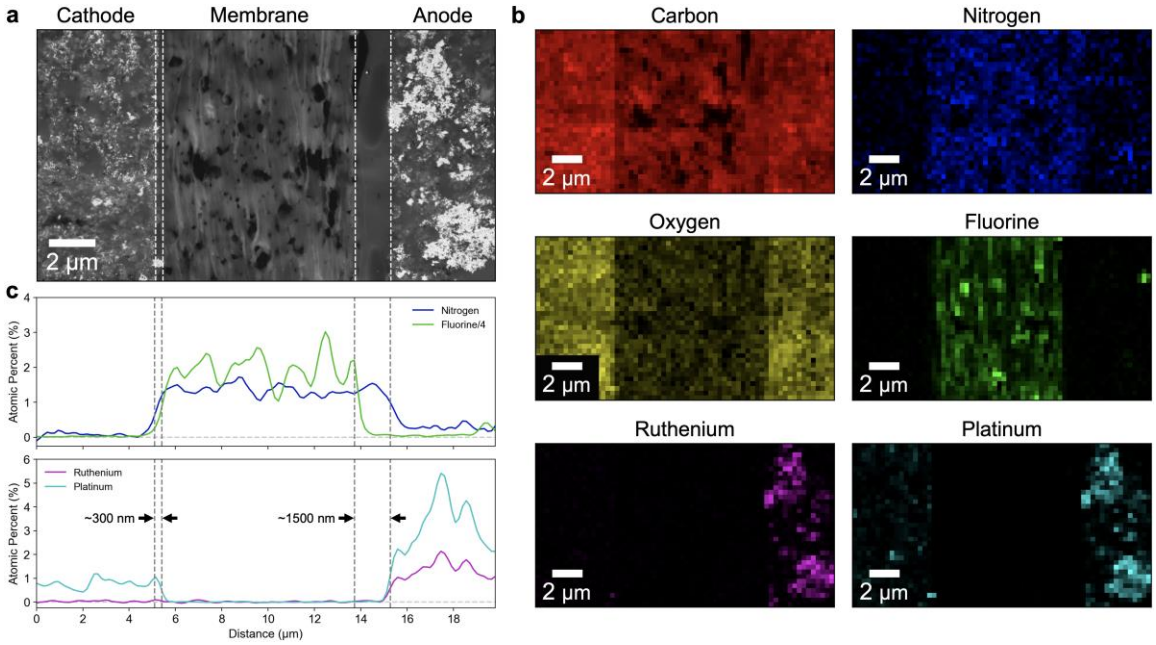

Figure 6.6: EOL compositional maps and profiles across the cathode, membrane, and anode. (a) Two regions with a different morphology than either the membrane or electrodes was observed by HAADF at the membrane-electrode interfaces. This interfacial layer was thicker on the anode side of the membrane. (b) Compositional maps show that nitrogen extends from the membrane into interfacial layer, while fluorine from the polytetrafluoroethylene (PTFE) membrane support does not. These maps show atomic percentages, with each separately normalized for display purposes. (c) Compositional profiles from average EDS across the region shown in (a) further reveal that these interfacial layers have a similar nitrogen content like the membrane but lack its significant fluorine content. In addition, the cathode has nearly zero nitrogen content while the anode does have a small amount of nitrogen.

A broader view of the electrode-level changes away from the cathode-membrane and anode-membrane interfaces are shown in **Figure 6.7** and **Figure 6.8**, respectively. **Figure 6.7** shows a clear difference in the cathode catalyst size and distribution from the BOL to the EOL. The heterogeneity of the interfacial layer can be seen as well. In the BOL MEA shown here, there was no obvious discrete interfacial layer, with proportions of both nitrogen and fluorine both decreasing at similar locations near the edge of the membrane. In contrast, the EOL sample had a small, discrete interfacial layer ~400 nm

across at the cathode-membrane interface, where the fluorine content dropped more rapidly than nitrogen with distance from the membrane.

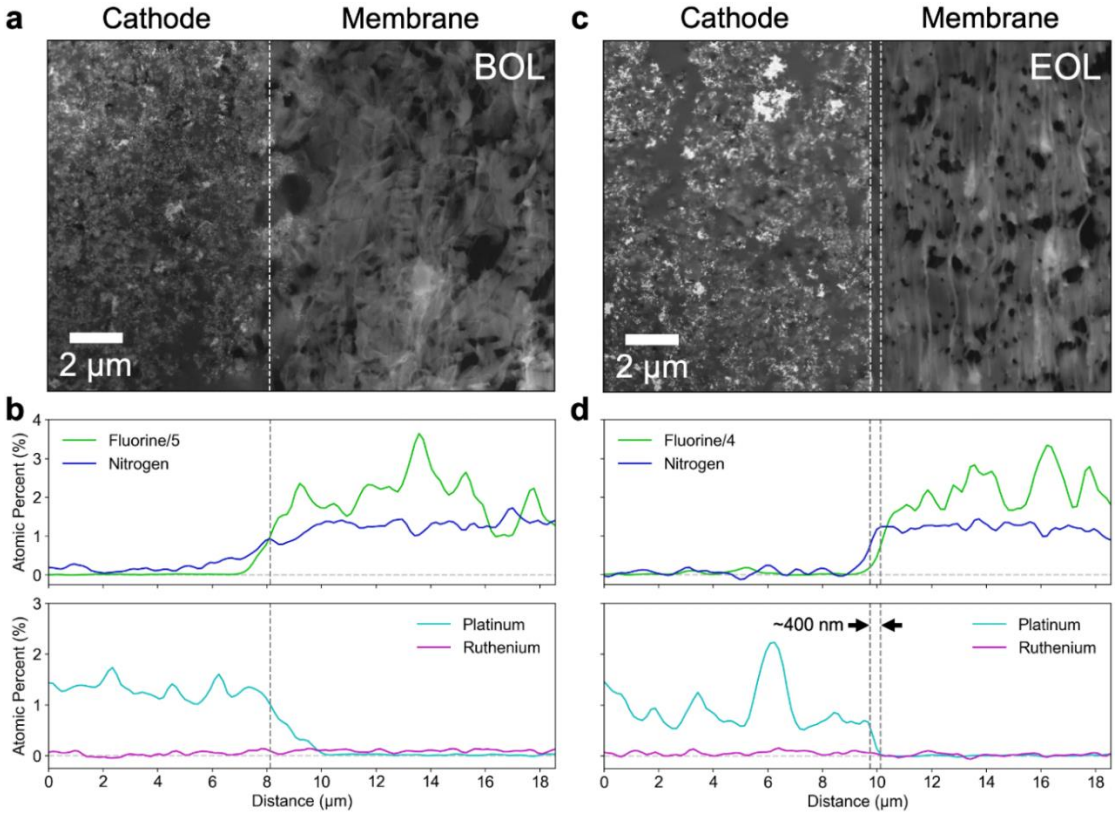

Figure 6.7: Comparison of compositional profiles across the cathode-membrane interface at BOL and EOL. (a) At BOL, very few large catalyst particles are observable. The BOL sample also happened to have no discernable interfacial layer in the HAADF imaged region. (b) Average EDS profiles from the region in (a) showing the chemical composition change from the AEM to the cathode catalyst layer. (c) At the EOL there is much more catalyst agglomeration. Also, this sample did have a thin interfacial layer that was ~400 nm wide as detected by HAADF. (d) Compositional profiles from average EDS across the region in (c).

The anode-AEM interface was similarly investigated and is shown in **Figure 6.8**. Consistent with the STEM imaging above, **Figure 6.8a** shows that there were already many more large catalyst agglomerates in the BOL anode than the cathode. Also, both samples in this case had interfacial layers (~750 nm in the BOL and ~1750 nm in the EOL). Combined with **Figure 6.7**, this shows the typical range of the interfacial layers that were observed.

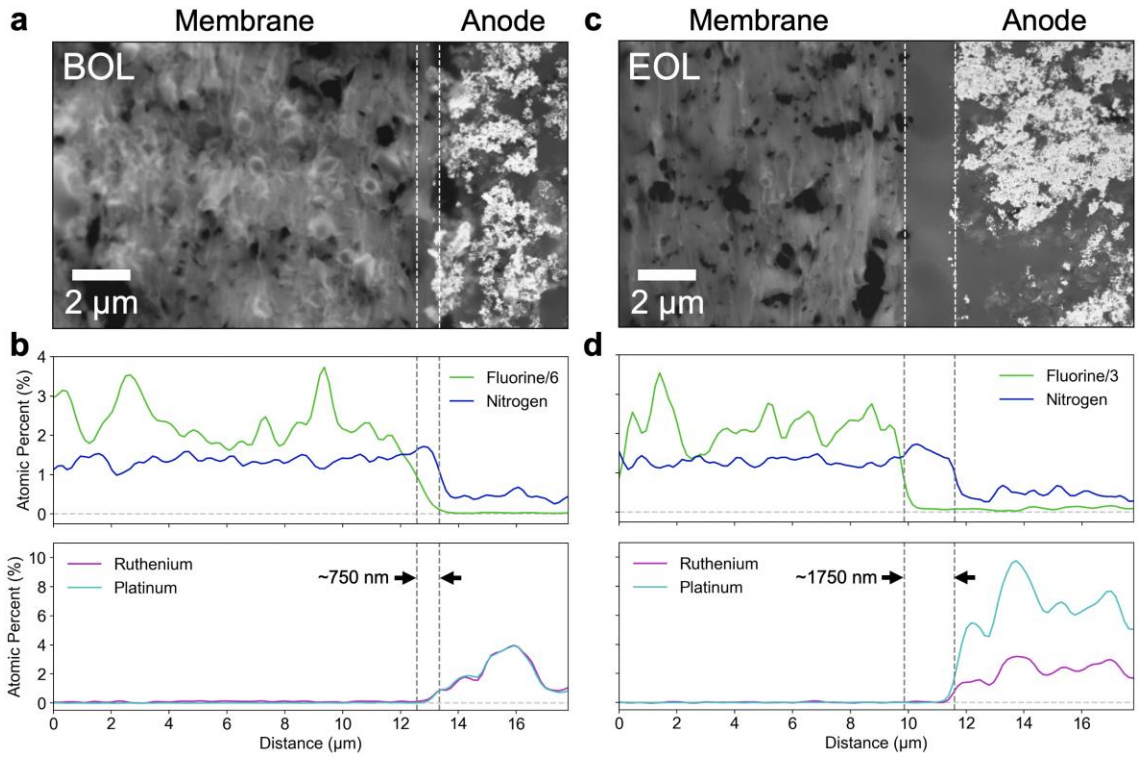

Figure 6.8: Comparison of compositional profiles across the anode-membrane interface at BOL and EOL. (a) At BOL, agglomerated PtRu catalyst and a narrow interfacial layer ~750 nm wide can be observed by HAADF. (b) Average EDS compositional profiles from the region in (a). (c) At EOL, there is some additional catalyst agglomeration and a lower Ru:Pt ratio than the BOL. Catalyst particles can be see embedded at the outer surface of this layer. (d) Compositional profiles from average EDS across the region in (c).

It should also be noted that there was no evidence of membrane degradation, supported by four observations. First, the compositional line scans for N in **Figure 6.7b** and **6.7d** as well as **Figure 6.8b** and **4d** are approximately flat throughout the AEM. Quantification of the N content in the AEM, **Figure 6.5b**, showed that indeed no change was observed from the BOL to the EOL (see **Figure 6.9** and **Figure 6.10** for information about quantification procedure and dose-sensitivity of the N, respectively). Second, H_2 crossover tests (**Figure 6.13a**) showed no differences from the BOL to EOL, which suggests that the AEM's mechanical properties were not compromised. Third, in the electrodes, it is also notable that the line profiles at the BOL and EOL show similar N

content, though this is not surprising because of the sp^3 nature of the poly(norbornene) AEMs and ionomers used here **[324]**, which should rule out any degradation mechanisms that involve N loss such as Hofmann elimination. Lastly, the HFR was not significantly increased during operation (discussed later in section 3.3).

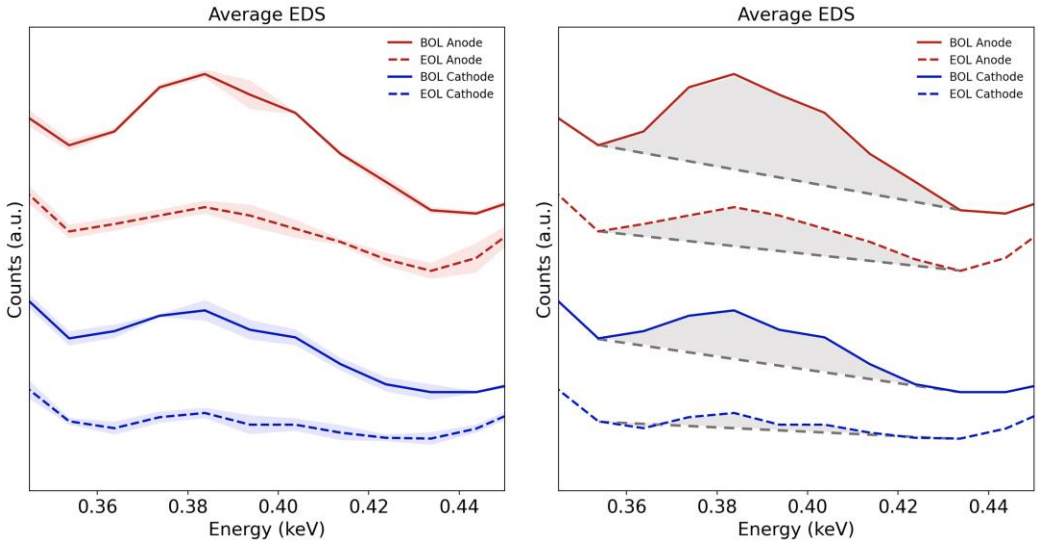

Figure 6.9: Average N-K EDS peaks showing (left) the standard deviation of all measurements made, and (right) a schematic of the method of background subtraction and integration used to produce the measurements. Background subtracted and integrated signals were then converted to at.% by application of appropriate factors, as discussed in the Experimental section of the main text.

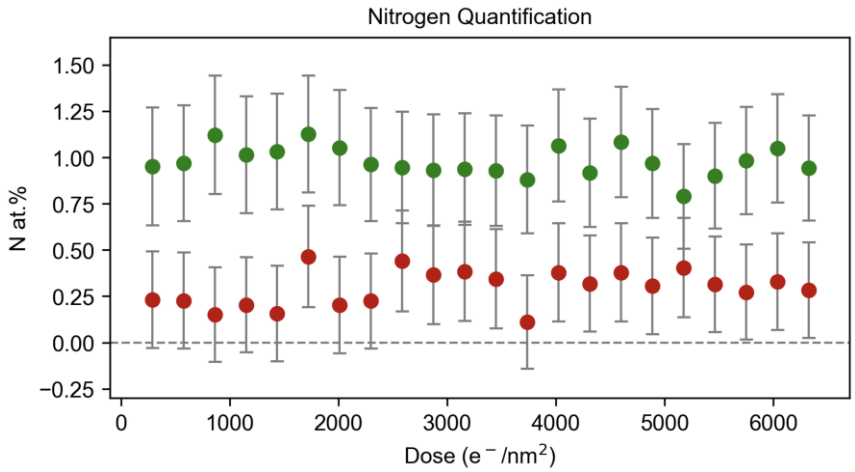

Figure 6.10: Measurement of N concentration at a single location in the BOL anode (red) and membrane (green) for increasing electron doses, up to approximately the total dose used to acquire all data. In this case, error bars represent uncertainty due to shot noise.

3.2 BOL vs. EOL Electrochemical Behavior

In response to the physical and compositional changes over the 3600-hour operation, the AEMFCs also experienced changes in performance. **Figure 6.11** shows typical polarization and power density curves (green circles) for an AEMFC operating on H_2 and O_2 reacting gases that has been broken-in, set to operate at 80°C and its dew points optimized. As in previous publications with this set of materials **[290], [291], [295]** the peak power density was well over 3.0 W/cm^2 and the mass transport limited current density was greater than 9.0 A/cm^2. The high mass transport limited current was expected here since the cell was operating on pure O_2. This makes the mass transport-limiting process the diffusion of water through the AEM, which is quite fast given the water uptake and thinness of the AEMs.

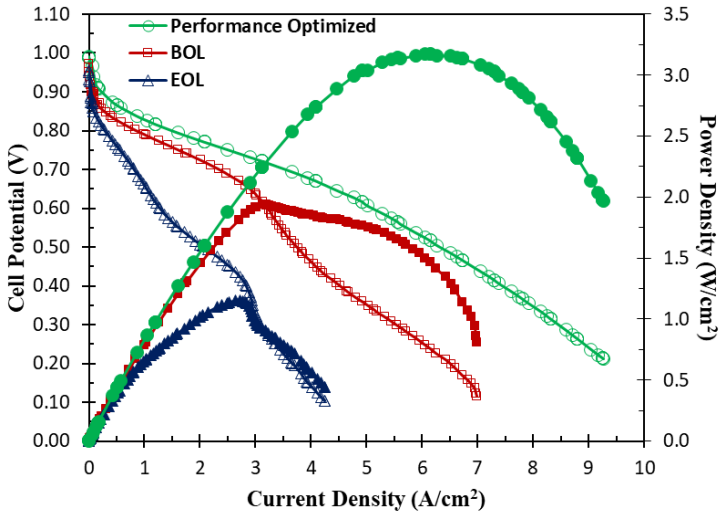

Figure 6.11: Polarization and power curves for AEMFCs operating at: i) 80 ºC and reacting gas flowrates of 1.0 L/min with anode/cathode dew points that optimize power density (71/73 ºC) with no back pressurization (green circles); ii) BOL conditions – 75 ºC with a reacting gas flowrate of 0.3 L/min and anode/cathode dew points of 73/74 ºC with no back pressurization (Red squares), iii) EOL conditions – 75 ºC with a reacting gas flowrate of 0.3 L/min and anode/cathode dew points of 72/74 ºC with no back pressurization (Blue triangles)

However, as seen in previous studies **[291], [295]** the conditions where AEMFCs achieve their highest performance (peak power density or current density) are not necessarily the same as those where they operate with maximum stability (minimum voltage variation at a constant current). The conditions for peak power are typically set to maximize water removal from the anode using lower anode and cathode dew points; this allows for both facile convective evaporation of water from the anode catalyst layer as well as high water flux through the AEM. For long-term stability, however, it is important to consider that stationary cations in the polymers that comprise the AEM and ionomer can degrade more rapidly at low hydration than at full hydration **[310], [325], [326]**. This suggests that it is important to avoid dry-out conditions in the cell, especially in the cathode where water is consumed and the electrode potential is high. To ensure that sufficient liquid water was in the cell, three changes were made to the operating conditions for the long-duration test. First, the cell operating temperature was reduced from 80ºC to 75ºC.

Second, the dew points of the anode and cathode feed gases were increased. The combination of lower operating temperature and higher dew points resulted in more liquid water being present in the cell and higher relative humidity. Such a high hydration state of the cell was only recently made possible by the inclusion of PTFE wet-proofing into the catalyst layers **[295]**, which allows the anode to reject water more easily. Third, the flowrate of the feed gases at the two electrodes was lowered from 1.0 L/min to 0.3 L/min. This was done to reduce the amount of convective water evaporation from the cell, which can contribute to cell dry-out. The polarization curve for the cell after these changes is shown by red squares in **Figure 6.11**. Clearly, the lower temperature and higher hydration state influenced the cell performance, as seen by the lower achieved current and peak power. The kinetics were slightly depressed (i.e., current at the highest voltages) and there was an earlier transition to mass transport control (i.e., current at low voltage) as liquid water removal from the anode becomes performance-limiting.

The cell was then operated at a constant current density of 600 mA/cm^2 for 3600 hours (150 days) until it was decommissioned in its EOL state. At the EOL, four experiments were performed on the cell before it was dismantled for the STEM experiments discussed earlier. The first was acquisition of an EOL polarization curve (blue triangles in **Figure 6.11**) at identical conditions to the BOL (red squares in **Figure 6.11**). At the EOL, it was clear that there were losses in the kinetic, Ohmic, and mass transport regimes. To quantify those changes, EIS analysis was performed at two current densities, 200 and 600 mA/cm^2, for both the BOL and EOL cells. The resulting Nyquist plots are shown in **Figure 6.12**. The EIS data was fit using an equivalent circuit model in the AfterMath program, developed by Pine Research Instrumentation. The qualities of the

fittings are shown in **Figure 6.12A** for the 200 mA/cm^2 experiments and **Figure 6.12B** for the 600 mA/cm^2 experiments. From the fittings, important parameters like Ohmic resistance (R_s), charge transfer resistance (R_1, R_2), and double layer capacitance (Q_1, Q_2) were extracted. These parameters are presented in the supporting information as **Table 6.1 (panels a and b)**.

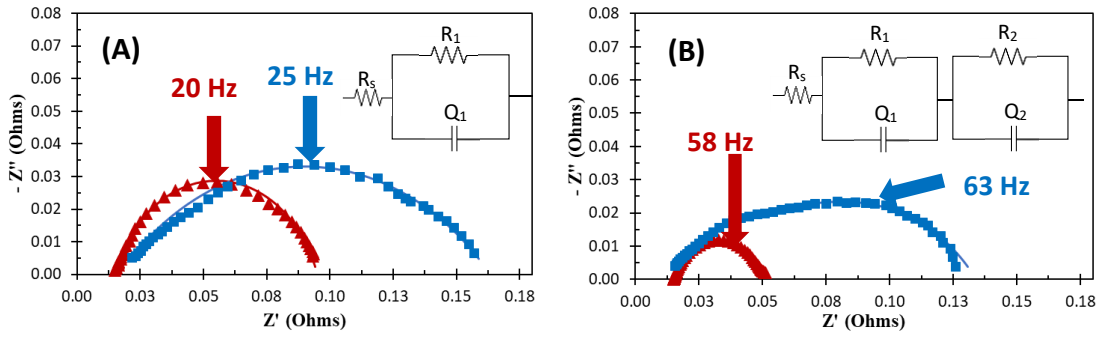

Figure 6.12: Impedance spectra with circuit fits comparison BOL cell (red triangles) vs. EOL cell (blue squares) at a current densities of (A) 200 mA/cm^2; and (B) 600 mA/cm^2.

Table 6.3a: EIS data parameters obtained by fitting the data with an equivalent circuit at 200 mA/cm^2

BOL Cell			
Element	Parameter	Value	Unit
Q1	Q	0.32	s^a/Ω
	A	0.79	
Rs	R	0.015	Ω
R1	R	0.080	Ω
EOL Cell			
Element	Parameter	Value	Unit
Q1	Q	0.34	s^a/Ω
	A	0.59	
Rs	R	0.020	Ω
R1	R	0.141	Ω

Table 6.1b: EIS data parameters obtained by fitting the data with an equivalent circuit at 600 mA/cm^2

BOL Cell			
Element	Parameter	Value	Unit
Q1	Q	0.37	s^{α}/Ω
	A	0.92	
Q2	Q	1	s^{α}/Ω
	A	0.67	
Rs	Rs	0.015	Ω
R1	R1	0.026	Ω
R2	R2	0.010	Ω
EOL Cell			
Element	Parameter	Value	Unit
Q1	Q	1	s^{α}/Ω
	A	0.69	
Q2	Q	0.75	s^{α}/Ω
	A	0.53	
Rs	Rs	0.018	Ω
R1	R1	0.077	Ω
R2	R2	0.035	Ω

At 200 mA/cm^2, the equivalent circuit (shown in **Figure 6.12A**) used for data fitting consisted of a resistive element (representing the high frequency resistance) in series with an element containing the charge transfer resistance and a constant phase element in parallel. At lower current densities, this simple circuit is appropriate as the ORR dominates the kinetic behavior, hence explaining why only a single arc was observed at the BOL. The x-intercept of this single kinetic arc at high frequency gives the total uncompensated cell resistance (R_s), which is essentially a sum of the contributions from contact and ohmic resistances of cell components such as the membrane, catalyst layer, backing, and end plate, and their interfacial resistances **[327]**. The second intercept is the sum of R_s and the cathode charge transfer resistance (R_1). Here, the BOL R_s was around 15 mΩ and R_1 was around 80 mΩ.

At the EOL, a second apparent semicircle was observed; however, it was not ascribable to any new circuit element. As the EIS frequency is lowered in cells operating at a given current (not at open circuit), the Nyquist curve approaches the x-axis at a value higher than the charge transfer resistance (in fact, it will exactly meet the charge transfer resistance as the frequency approaches zero) because an operating cell has a real impedance (the sum of kinetics, Ohmic, mass transport, etc., resistances) that can be measured on an i-V curve, which is captured as the frequency approaches zero. Hence, the low frequency impedance also carries information about the diffusion layer inside the MEA. As the cell ages, and the mass transport conditions change, a double semicircle can emerge **[328]**. At the BOL, the cell was operating with low mass transfer resistance, which led to the single-apparent arc. However, at the EOL, catalyst agglomeration and changes in electrode morphology over long-term operation (seen in STEM/EDS) contribute to the appearance of a transport barrier in the cell, which allows the mass transfer resistance to become more evident. At the EOL, R_s was 20 mΩ and R_1 was 141 mΩ – both significantly higher than the BOL cell. The higher charge transfer resistance could be an indication of reduced catalyst active area in the cathode.

At 600 mA/cm^2, two parallel (resistor + constant phase) elements (**Figure 6.12B**) were used to fit the impedance data. This was done to accommodate a small second semicircle that appeared at the BOL. The second semicircle, R_2, was caused by the HOR kinetics in the anode as the HOR in alkaline media is not as facile as it is in acid media **[329]**. At the BOL, R_s was 15 mΩ, R_1 was 26 mΩ and R_2 was 10 mΩ. Again, at the EOL, new mass transfer effects were observed. It was also observed that all of the cell resistances increased: R_s was 18 mΩ, R_1 was 77 mΩ, and R_2 was 35 mΩ. The increase in the Ohmic,

kinetic, and mass transport resistances support the findings in **Figure 6.11**. Changes in electrode catalyst layer morphology and structure were also observed during the microscopic STEM analysis of the EOL samples, as discussed above, and can explain the increase in charge transfer resistance and mass transfer resistance.

The third experiment performed on the EOL MEA was measurement of the steady-state open circuit voltage (OCV). At the EOL, the OCV was 1.006 V, a 72 mV (7.4%) decrease from the BOL (**Figure 6.13b**). There are many possible causes for a lower OCV, including an increase in gas permeation through the AEM. Therefore, the final experiment was a measurement of the H_2 crossover. Importantly, as shown in **Figure 6.13a**, there was no increase in the fuel crossover during the 3600-hour experiment and the amount of fuel crossover was quite low, equivalent to ca. 2 mA/cm^2. Moreover, after the cell was taken apart, there were no signs of physical damage to the AEM. These results show that the reduction in OCV is not due to bulk membrane degradation, which is also supported by the STEM imaging and EDS analysis. The change in the OCV is tied to the differences in the catalysts and double layer effects.

3.3 Long-Term Steady State Operation: Stability and Reversible vs. Irreversible Losses

Figure 6.11 shows the BOL vs. EOL polarization performance of the long-term AEMFC. However, it does not show a time lag for the evolution in the cell behavior or give a sense for the steady-state operation of the cell under relevant conditions, such as the DOE-suggested operating current of 600 mA/cm^2. **Figure 6.15a** shows the voltage response and the high frequency resistance (HFR) while operating the long-term cell at 600 mA/cm^2 for 3600 hours. For the first 2000 hours of operation, the voltage stability was excellent, with an average degradation rate of only 15 μV/hr. It should be noted that during

the test, the anode/cathode reacting gas dew points were occasionally adjusted a small amount to ensure that the cell was able to maintain adequate humidification, as shown in **Figure 6.15b**. However, the average degradation rate does not tell the whole story. After a few hundred hours of constant current operation, both the voltage and the HFR plateaued. Starting at around 1050 hours, the HFR started to increase linearly with time. From 1050 hours to 2000 hours, the HFR increased from 6 mΩ to 9 mΩ (~3 μΩ/hr), which translated to a voltage decay rate of 9.5 μV/hr – meaning that up to 2000 hours the rising HFR was able to account for an overwhelming majority of the voltage loss.

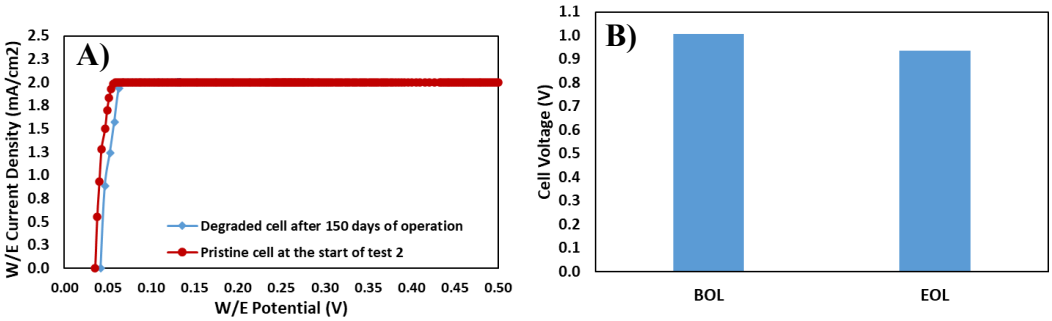

Figure 6.13: A). Hydrogen cross over comparison. B) OCV comparison initial and after 150 days of operation.

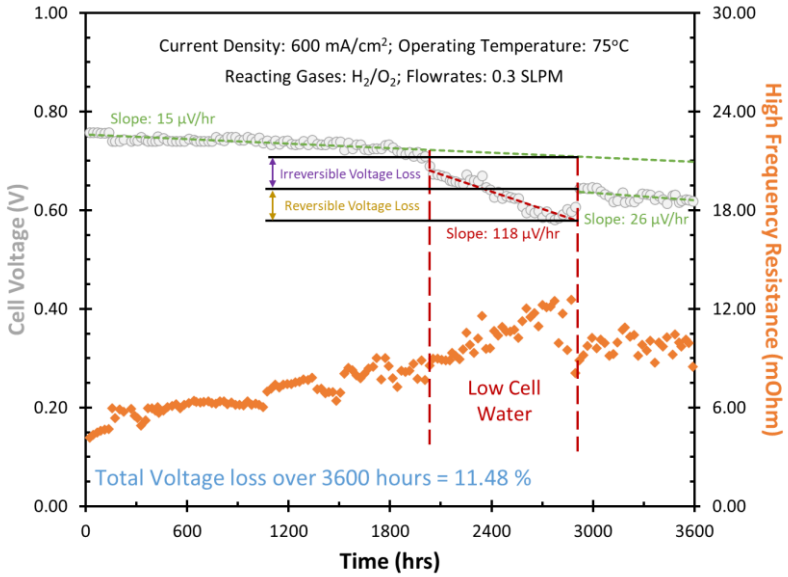

Figure 6.14: Reversible vs irreversible voltage loss

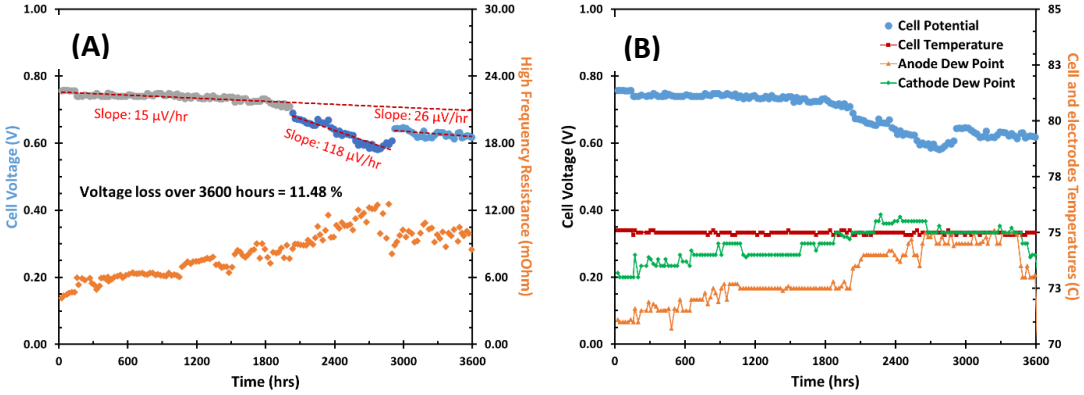

Figure 6.15: (A) Cell Voltage and HFR during a long-term durability test with GT78 ionomer anode and GT32 ionomer in cathode, cell temperature 75 °C and dew points 72/74 °C operating at 600 mA/cm2, volumetric flowrate: 0.3 L/min on both sides, no backpressure, (B) Cell Voltage variation over time with cell temperature and feed gas dew points.

After 2000 hours, the degradation rate of the cell sharply increased to 118 µV/hr, paired with a surge in the HFR at a rate of 4.6 µΩ/hr. Despite the increased HFR, HFR-driven voltage loss during this time accounts for only 13.8 µV/hr, or 12% of the observed loss. This suggests that complicated cell dynamics are involved in the rate of voltage decay in operating AEMFCs. One of the most likely drivers for the non-linearity between the

increasing HFR and voltage loss is a dry cathode. If the cathode becomes dry, three effects manifest: i) increased HFR; ii) reduced reaction kinetics at the cathode; and iii) increased mass transfer resistance. This type of loss is expected to be reversible when adequate water is again available. Thus, if a water imbalance results in cell performance degradation, rebalancing the cell water may allow for a significant portion of the lost cell operating voltage to be recovered, which is particularly important since the operating voltage decreased significantly from 0.71 V at 2000 hours to 0.59 V at 2700 hours. Another likely driver for non-linear voltage loss is component degradation. This type of loss is expected to be irreversible and that portion of the operating voltage will not be recovered once adequate water is again available.

One of the most straightforward ways to adjust the cell water balance is to manipulate the reacting gas dew points. Though this was occasionally done over the first 2000 hours (as shown in **Figure 6.15b**), it was done more frequently after 2000 hours in order to adjust the distribution of cell water, with the goal of increasing the amount of water in the cathode. The first approach to rebalancing the water was to increase the cathode dew point. However, such an increase (at around 2200 hours) led to no discernable change in the degradation rate. This is most likely due to the fact that the PTFE-containing electrodes are quite hydrophobic, which does not allow them to uptake excess water from the gas phase within the GDL. Later, at around 2630 hours, the dew point of the anode reacting gas was slightly increased, coinciding with a significant decrease in the degradation rate and increase in the cell operating voltage. Increasing the anode dew point resulted in these changes due to suppressed convective evaporation at that electrode. Since the operating current was held constant, the rate of water production was also constant.

The suppressed convective evaporation therefore resulted in excess water at the anode. To avoid flooding, this water was forced to back-diffuse through the AEM from the anode to the cathode. As the cathode received water from the anode, the degree of membrane hydration increased (as indicated by the lowering of the HFR in **Figure 6.15a**), the mass transfer and kinetic resistances were reduced, and the cell voltage recovered significantly. Additionally, the voltage degradation rate was drastically lowered to 26 μV/hr. Operating under these modified conditions, the cell was stable until it was purposely decommissioned after 3600 hours of operation.

By solving the water balance issue, approximately half of the cell voltage that was lost in the time period from 2000-2600h was recovered. **Figure 6.14** shows an annotated version of Figure 6.6a, with the regions of high vs. low cathode water and reversible vs. irreversible voltage loss labeled. This does show that it is possible that a significant fraction of cell voltage loss during testing can be from sub-optimal operating conditions and it something that should be considered in the research community when performing constant-current cell measurements. Combined with the other data presented here, **Figure 6.14** also supports the idea that the irreversible losses caused by component-level degradation occurred when the cathode was experiencing dry-out, meaning that the cathode catalyst agglomeration was likely accelerated by the absence of sufficient water. This also shows that the cell operating conditions can play a huge role in driving irreversible performances losses as well. Finally, the data shown here does show that although great strides have been made in AEMFC longevity, their they do remain at least somewhat more sensitive to the balance of cell water during operation than their PEMFC counterparts. Identifying approaches to alleviate this sensitivity is an important area for research.

The work here presents four unique and important findings. First, it is possible to create stable, high-performing AEMFCs. The next phase will be to accomplish this on H_2/air – initially CO_2-free air, and later with CO_2-containing air. Second, the AEM appears to be extremely stable during operation. Third, during periods of performance decline, a significant portion of that loss can be driven by the operational variables – meaning that performance loss can be recovered. Lastly, the cathode is likely responsible for a large portion of the unrecoverable performance loss of the cell over its lifetime, since a larger proportion of catalyst degradation was observed there compared to the anode. Further studies are needed in this area to identify the exact mechanism for catalyst growth. For example, it has been noted that carbon may not be intrinsically more stable in alkaline media than acid media **[330]**, which can lead to catalyst detachment and subsequent sintering and agglomeration. In summary, this work demonstrated a new state-of-the-art AEMFC durability, and the knowledge gained here about the remaining degradation mechanisms will accelerate the rapidly approaching viability of these devices as a low-cost alternative to PEMFCs.

4. Conclusions

In this work, a high-performing, durable AEMFC was successfully operated at 600 mA/cm^2 for 3600 hours (150 days) without failure, after which the cell was characterized to allow the dominant degradation mechanisms during operation to be clearly delineated for the first time. During the 3600 hours of operation, only 11.5 % of the cell voltage was lost. It was found that some of the performance loss was recoverable by rebalancing cell-level water level, while some of the loss was unrecoverable. It was revealed that a large fraction of the unrecoverable performance decay occurred over a relatively brief operating

time (~600 h) and was mostly caused by degradation at the cathode. Specifically, the cathode experienced increased particle growth compared to the anode. The anode also experiences mild degradation, with Ru leaching from the PtRu catalyst and a portion of it being deposited as nanoparticles at the interface between the AEM and the anode. The AEM itself does not appear to undergo degradation during operation, as evidenced by its unchanged composition and no measurable increase in H_2 crossover.

The long-term performance of the cell demonstrated here shows that AEMFCs are rapidly becoming a viable alternative to PEMFCs, and the observations of the remaining degradation mechanisms made here will help the AEMFC community design the next generation of increasingly durable cell components, further accelerating the commercialization of this promising technology.

CHAPTER 7

STABLE, HIGH-PERFORMING BIFUNCTIONAL ELECTRODES FOR ANION EXCHANGE MEMBRANE-BASED UNITIZED REGENERATIVE FUEL CELLS[6]

Abstract

Anion exchange membrane unitized regenerative fuel cells (AEM-URFCs) are a promising technology for energy storage and electricity production; however, their efficiency is limited by the kinetics of the bifunctional oxygen electrode (BOE) where the oxygen evolution reaction (OER) and oxygen reduction reaction (ORR) occur. A particular concern when designing the BOE is that the OER and ORR have differing catalytic requirements, which make it challenging to develop effective bifunctional electrocatalysts with single active sites. In this study, we focus on advancing the BOE performance using Pt-IrO_x and Pt-$NiCoO_x$ electrocatalysts. Single-layer and dual-layer Pt-IrO_x BOEs were made, with the dual-layer electrode leading to improved performance due to efficient catalyst utilization in both modes. Using the dual-layer oxygen electrode paired with a

---

[6]Hassan, N.U., Ganesan, P., Lando, A.A., Mustain, W.E. and Colon-Mercado, H.R., Stable, high-performing bifunctional electrodes for anion exchange membrane-based unitized regenerative fuel cells, *J. Power Sources,* **541,** 231599 (2022).

PtRu/C hydrogen electrode, a round trip efficiency (RTE) as high as 50% (62 $\%_{iR\text{-}free}$) was achieved at 500 mA/cm^2 and operation for more than 24 hours, which included five one-hour-long H_2 generation and consumption cycles followed by one eight-hours-long cycle. To the best of our knowledge, this is the highest performance for AEM-URFCs reported to date. Lastly, the approach is extended to electrodes with a Pt loading of 0.5 mg/cm^2 and the IrO_x substituted by $NiCoO_x$.

1. Introduction

A unitized regenerative fuel cell (URFC) is a single device that can reversibly operate as both a fuel cell and an electrolyzer. A URFC can serve as an energy storage device (via water electrolysis) to store excess electricity in the form of hydrogen during peak production times. This is particularly attractive from intermittent renewable energy resources like solar, wind, tidal, etc. **[331]**, **[332], [333], [334]**, where a large amount of storage may be needed and traditional batteries would require a very large footprint. URFCs can also function as an energy conversion device (fuel cell mode) that generates electricity from the stored hydrogen and oxygen (either co-stored from electrolysis or from air). URFCs can be a high energy storage capacity, low cost, simple, compact, and environmentally friendly technology with advantages over conventional energy storage technologies **[335], [336], [337], [338], [339], [340]**. Because of this, URFCs have received an increased amount of research attention in recent years.

Among existing URFC technologies, proton exchange membrane (PEM)-based systems have benefitted from the highest level of investment. As such, they are more mature and have shown the best round-trip efficiencies **(RTE=$\frac{E_{FC}}{E_{EC}}x100$)** to date – up to 60 % RTE **[341]** – as well as relatively good durability. Lim and Lee et al. **[342]** recently

reported 51 % RTE using a Pt-Ir bifunctional electrocatalyst while operating at 400 mA/cm^2. Kus et al. **[343]** showed an RTE of 47 % at 400 mA/cm^2 and 31.8 % at 1.0 A/cm^2 utilizing a sandwich-like Pt-Ir bifunctional anode electrocatalyst. Similarly, Regmi et al., **[344]** reported 57 % and 60 % RTE at 1.0 A/cm^2 operating with air and O_2, respectively, at 80^o C. Peng et al., **[345]** demonstrated 53% RTE at 1.0 A/cm^2 with constant gas mode and continuously operated the system for 500 hrs with negligible performance degradation. Unfortunately, PEM-URFCs are expensive due to their acidic environment requiring the use of specialized component materials (e.g. perfluorinated membranes) and platinum group metal (PGM)-based electrocatalysts.

Alternately, AEM-based technologies are emerging due to their less corrosive operating environment and possible use of low-cost membranes, inexpensive component materials, and PGM-free electrocatalysts while offering competitive performance.

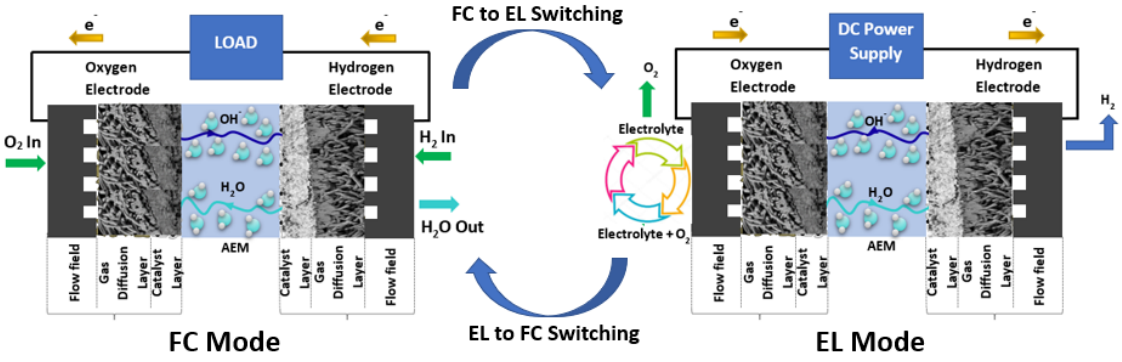

Figure 7.1: AEM-URFC schematic

The operation of AEM-URFCs (as shown in Figure 7.1) is driven by the reactions at the hydrogen (Equation 1) and oxygen (Equation 2) electrodes, and the overall reaction (Equation 3).

$$4H_2O + 4e^- \leftrightarrow 2H_2 + 4OH^- \qquad E^o = -0.828V \qquad (1)$$

$$O_2 + 2H_2O + 4e^- \leftrightarrow 4OH^- \qquad E^o = 0.401V \qquad (2)$$

$$2H_2 + O_2 \leftrightarrow 2H_2O \qquad (3)$$

From a catalytic perspective, the lower potential required of the oxygen electrode in the AEM versus the PEM system decreases the number of oxygenated adlayers on the catalyst surface, lowering the catalyst-oxygen bond formation energy and thus reducing the overpotential of the ORR in alkaline compared to acid electrolyte **[346], [347]** and making that electrode more active in alkaline than in acid **[348], [349].** Additionally, the less corrosive alkaline environment allows for low-cost stack components (membranes, bipolar plates, air loop, cooling, etc.) to be used **[350].** Fortunately, significant progress has been made recently in the development of oxygen electrocatalysts as well as stable and highly conductive AEMs and ionomers. These advances have led to increased device operational life in discrete fuel cells **[351], [352], [353], [354], [355], [356]** and discrete electrolyzers **[357], [358], [359], [360], [361],** which has revived researchers' interest in AEM-URFCs.

Several AEM-URFC prototypes have been reported in literature **[362], [363], [364], [365], [366], [367], [368]**; however, their performances and round-trip efficiencies are still lower than those of PEM-based URFCs. For instance, Ng et al., **[364]** reported

RTEs of 42-45% at 20 mA/cm^2 operating at 55^o C. Bretthaur et al., **[369]** reported 52 % RTE at a very low current density of 0.1 mA/cm^2 using lanthanum based electrocatalyst materials. Such very low current densities are not suitable for any practical application. Gayan and Ramani et al., **[370]** recently touted an AEM-URFC using a Pt-pyrochlore bifunctional oxygen electrocatalyst that achieved a RTE of 75% at 100 mA/cm^2, but the RTE was only ~36% at a more commercially-realistic operating current of 500 mA/cm^2. The best performing AEM-URFC in the literature to date was recently reported by Yan and co-workers **[371]** where the RTE at 500 mA/cm^2 was 48%. They were also able to show one-hour cycling durability with ~ 10 mins each cycle.

From the above literature data, it is clear that AEM-URFCs have shown lower operating current densities and higher degradation rates than PEM-URFCs. This is true in the case of PGM-based catalysts that have been carried over from PEM-URFCs. At the oxygen electrode, the ORR and OER require different active sites since their rate determining steps (RDS) and the electrocatalyst surfaces are completely different under ORR and OER conditions **[372], [373].** In PEM-URFCs, this has been mostly accommodated by mixing Pt and Ir, the most stable and mature catalysts for ORR and OER, together in one electrode. This allows them to be operated as a mixture of their base metals (in FC mode) and oxides (in electrolyzer mode) in traditional URFCs **[375], [376], [377], [378], [379].** These bimetallic composites of Pt-Ir have been shown to efficiently enable both OER and ORR on the same electrode **[342], [343], [344]** in PEM-URFCs.

The mixing of Pt and Ir in the PEM-URFC electrode has been accomplished in a number of ways. Various combinations of Pt and Ir or its oxides have been investigated where their elemental ratio, catalyst preparation method, microstructure, etc. have been

manipulated. From a catalyst perspective, there does not seem to be a consensus in the literature for the optimal ratio between Pt and Ir. In typical studies, the proportion of Ir (or IrO_2) can range from 1 wt% to 50 wt%. This variability in results might be due to the different catalyst / electrode preparation methods and structures across the different studies. In general, it is believed that the proportion of Pt should be more than half of the total metal loading, due to the incapability of Ir towards ORR. For instance, Jung et al., **[397]** investigated various ratios of Pt:Ir and found that 85:15 Pt:Ir (wt:wt) was the best, achieving a RTE of 49 % at 500 mA/cm^2. At the electrode level, the most commonly employed method of combining Pt and Ir is mechanical mixing as it is an easy and direct method for the preparation of a composite BOE. However, it has been found that agglomeration tends to occur quickly after mixing, which hinders fine dispersion of different catalyst components. To solve this problem, different synthesis methods have been developed instead of direct mixing, including Pt supported on IrO_x, IrO_x deposited onto Pt, or the use of multi-layer electrodes where catalysts are separately deposited in discrete layers. In general, better particle dispersion and less agglomeration has been achieved in multi-layer structures **[398].** Unfortunately, the effects of electrode structure and the integration of OER and ORR catalysts in AEM-URFCs has not been studied well. It is important to find the right balance and configuration of these materials thus increasing the dispersion of active sites, which can be done through catalyst and/or electrode design and optimization. Also desirable in AEM-URFCs is to transition away from PGM-containing catalysts in order to reduce the cost compared to PEM-URFCs.

Therefore, in this work, two approaches were taken. The initial approach was to create a Pt-IrO_x composite catalyst layers with multiple structures. Pt and IrO_x were chosen

first to understand how composite electrodes behave in AEM-URFC systems and investigate whether the learnings from PEM-URFCs can be directly translated to AEM-URFCs. The first electrode structure was comprised of a single-layer electrode. The second electrode structure was comprised of two layers where an IrO_x base layer was first deposited onto the porous transport later (PTL) followed by a Pt top layer, which was in direct contact with the AEM in the membrane electrode assembly (MEA). The idea behind the layered electrode configuration was to enhance the access to the active sites in each mode and boost the cell performance while maintaining the OER catalyst at a distance from the AEM. The performance and durability of these two electrode types are compared. Additionally, the ionomer content of the oxygen electrode was optimized and the inclusion of Nafion™ as a binder in the OER electrode was studied. The second approach extended the dual-layer electrode concept to a low-PGM electrode where the IrO_x was substituted by $NiCoO_x$. The performance and cyclability of this configuration are demonstrated and discussed.

2. Materials and Methods

2.1 Materials

Three catalysts, 75 wt% PtRu on high surface area advanced carbon support (Alfa Aesar 47371; Platinum, nominally 50%, Ruthenium nominally 25%), Pt black (HiSPEC™ 1000), and IrO_x (Premion®, 99.99% metal basis and Ir 84.5% min) were purchased from Alfa Aesar. 2-Propanol (ACS reagent >99.5%) and potassium hydroxide (BioXtra, >85% KOH basis) were purchased from Sigma-Aldrich®. Vulcan® XC-72R carbon black was obtained from Cabot Corporation. Nickel cobalt oxide (99% trace metal analysis basis, <150 nm particles) was obtained from Sigma-Aldrich®. Low molecular weight anion

exchange resin (TM1 Durion™ from Orion Polymer), 5 wt% wet proofed Toray carbon paper (TGP-H-060), Pention™ Membranes (30 µm Pention-AEM-72-30-15% and 5 µm Pention-AEM-72-5-15%, both 15% crosslinked), and D520 Nafion™ dispersion ionomer (alcohol based 1000 EW at 5wt%) were purchased from the Fuel Cell Store. All materials were used as received.

2.2 Ink preparation

URFC oxygen electrodes were prepared by spray coating carbon paper PTLs with Pt-IrO_x for the oxygen electrode and PtRu/C for the hydrogen electrode. Two electrode designs were considered for the oxygen electrode – a single-layer and a dual-layer configuration. The ink for the single-layer oxygen electrodes was prepared by mixing the appropriate amounts of TM1 resin with 2.4 mL of deionized water and 3.3 mL of 2-propanol and mixing the components ultrasonically for 90 minutes at 40 ºC. Once all of the resin was dispersed, if used, an appropriate amount of Nafion™ dispersion was added into the solution and vortex mixed. After the solution cooled to room temperature, 125 mg of IrO_x and 62.5 mg of Pt black were added under a blanket of inert atmosphere. Once the catalyst was well incorporated, 20.7 mL of 2-propanol was added. The resulting slurry was then ultrasonically mixed for an additional 90 minutes in an ice bath. Specific amounts of anion exchange resin (TM1), Nafion™ (D520) and the ionomer to catalyst ratio (I/C) are listed in Table 7.1. Similar catalyst ink preparation method was used for PGM-free/low-PGM catalysts.

Table 7.1: Electrode ink composition mixed with 125 mg of IrO_x and 62.5 mg Pt black in 2.4 mL of H_2O and 24 mL of 2-propanol. Note-I/C includes both TM1 and D520.

TM1/D520 Dry wt%	**I/C**	**TM1 (mg)**	**D520 (µL)**
15/0	0.178	33.0	0
15/2	0.206	34.0	100
15/4	0.234	34.7	200
20/0	0.251	47.0	0
20/2	0.283	48.2	105
20/4	0.321	50.0	220
25/0	0.336	63.0	0
25/2	0.370	64.0	115
25/4	0.407	66.0	225
35/2	0.589	104.5	129
35/4	0.640	107.6	267

To prepare the dual-layer oxygen electrodes, two inks were prepared, one containing IrO_x and the other containing Pt black. Similar solvent composition and polymer amounts were used as in the single-layer electrode. In the first ink, 43.5 mg of TM1 resin was mixed with 2.4 mL of deionized water and 3.3 mL of 2-propanol followed by ultrasonic mixing for 90 min. at 40 ºC. Once all of the resin was dispersed and after the solution was cooled to room temperature, 130.4 mg of IrO_x was added in an inert atmosphere followed by 20.7 mL of 2-propanol. The mixture was then sonicated for an additional 90 min. in an ice bath. In the second ink, the same recipe and procedure was

employed except that 65.4 mg of Pt black and 21.8 mg of TM1 were used. The optimized I/C ratio was used to prepare low-PGM single- and dual-layer oxygen electrodes. The procedures and solvent mixtures previously described were followed, however $NiCoO_x$ was used instead of IrO_x as the OER catalyst.

The ink for the hydrogen electrodes was prepared by ultrasonically mixing 91 mg of TM1 resin with 3 mL of deionized water and 6 mL of 2-propanol for 90 minutes at 40 ºC. Once all of the resin was dispersed, 150 µL of Nafion™ D520 dispersion was added, and vortex mixed. After cooling to room temperature, 240 mg of PtRu/C and 120 mg of Vulcan® XC-72 were added under an inert atmosphere. Once all the catalyst was fully incorporated into the slurry, 18 mL of 2-propanol was added to the mixture and ultrasonically mixed for an additional 90 min. in an ice bath.

2.3 Electrode Fabrication

While carbon is avoided for high voltage operation, commercially available wet proofed carbon paper PTLs are considered a low-cost and easily accessible alternative for short-term testing as opposed to metal based PTL that will require wet proofing optimization **[388]**. Additionally, during electrolysis, the operating potentials and current density were maintained below 2 V and 1 A/cm^2 respectively, to minimize the negative impacts of carbon corrosion on the overall cell performance **[389]**. All electrodes were fabricated using an automated ultrasonic sprayer (Prism-400BT, Ultrasonic Systems, Inc.). Initially, the ink was loaded into the system and mechanically mixed for an additional 30 minutes before spraying. Carbon paper PTLs (Toray 60 with 5% wetproofing) having 25 cm^2 area were placed on a heated vacuum plate (at 60 ºC) and coated with the desired catalyst loadings. The ink was sprayed at a flowrate of 500 µL/minute, a nozzle speed of

60 mm/s, and a nozzle height of 50 mm. The hydrogen electrode metal loading (Pt+Ru) was maintained at 1.25 ± 0.05 mg_{metal}/cm^2 and the total oxygen electrode loading ($Pt+IrO_x$) was kept at 2.6 ± 0.05 mg/cm^2 for single- and dual- layer electrodes. Dual-layer oxygen electrodes were prepared by first spraying the IrO_x ink (~1.6 mg_{IrOx}/cm^2) followed by the Pt black ink (~1.0 mg_{Pt}/cm^2). Low PGM single- and dual-layer oxygen electrodes were prepared following the procedures previously described. However, the electrodes were made with $NiCoO_x$ (1.10 or 2.00 mg/cm^2) and Pt black (0.50 mg/cm^2).

2.4 Cell assembly

Prior to the cell assembly, 5 cm^2 electrodes were cut from the larger 25 cm^2 electrodes. The cut electrodes and the membrane were then immersed in 1 M KOH solution. The solution was changed every twenty minutes three times to ensure full ion exchange and to minimize any carbonates. Immediately afterwards, the components were loaded into electrolyzer hardware (Scribner Associates, Inc.) with triple serpentine flow-fields. Glass reinforced silicone gaskets (165 μm) were used to control the degree of compression, resulting in a pinch of around 25%. Once the MEA was assembled, the bolts holding the cell hardware together were tightened with a torque of 3.4 N-m each.

2.5 URFC Testing

Short-term testing was performed using an Arbin Instruments fuel cell test station. During cell start up, humidified nitrogen was purged at a rate of 750 sccm to the anode and cathode until the cell reached the operating temperature of 60 ºC. The humidifiers were set to 58 ºC and 56 ºC for the oxygen and for the hydrogen side, respectively. Once all of the set temperatures were stable, the nitrogen flow was stopped and switched to oxygen (cathode) and hydrogen (anode) to operate the cell in fuel cell mode. To break the cell in,

the cell was polarized to 0.5 V to activate the MEA for 5 minutes. Then, polarization curves were recorded from the open circuit voltage (OCV) to 0.1 V every five minutes until stable performance was obtained. Once steady polarization behavior was achieved, two fuel cell polarization curves were recorded and a reductive current density of 500 mA/cm^2 was applied for a desired duration. After the constant current run, the cell was allowed to rest back to the OCV, and the gases were switched to humidified nitrogen. To initiate the electrolyzer mode, a 0.1 M KOH was fed to the oxygen electrode at a rate of 0.3 mL/min. The cell was allowed to equilibrate for 10 minutes prior to collecting a polarization curve from OCV to 2.0 V or 1.0 A/cm^2. After the polarization, an oxidative current of 0.5 A/cm^2 was applied for a desired time. To switch back to fuel cell mode, the liquid feed was stopped, and the gases were switched back to oxygen and hydrogen at 750 sccm. After keeping the cell at OCV for one minute, two fuel cell polarization curves were collected, and the cycle was repeated. After the second cycle, the high frequency resistance (ca. 10 kHz) was measured under open circuit conditions (10 mV amplitude) and 0.1 M KOH flow by means of potentiostatic electrochemical impedance spectroscopy using a potentiostat (HCP-803, Biologic).

Longer term cycling was performed using two separate test stations; a Scribner 850E was used for fuel cell testing while an Arbin BT2000 was used for electrolyzer testing. A similar procedure was applied for longer term cycling. First, in FC mode, nitrogen gas with full humidification was fed to both electrodes and the cell temperature was set to 60^o C. When the cell temperature was stabilized, hydrogen and oxygen were fed to respective electrodes and a break-in procedure was applied where the cell was gradually polarized from OCV to 0.1 V. Next, the hydrogen and oxygen reacting gas dew

points were optimized, and polarization curves were collected. The cell was then operated at 0.5 A/cm^2 for the desired time. To switch to electrolyzer mode, nitrogen was fed to both sides of the cell, replacing hydrogen and oxygen. The cell was then disconnected from the Scribner test station and connected to the Arbin. Then, dilute KOH (0.1 M, 1.6 mL/min) solution was constantly circulated to the oxygen electrode only while the cell temperature was maintained at 60 ^{o}C. Next, polarization curves were collected, scanning from 0.0 – 1.0 A/cm^2. After polarization, a constant current of 0.5 A/cm^2 was applied for a desired duration. To switch back to fuel cell mode, the 0.1M KOH flow was stopped and connected with the fuel cell test station while not allowing the cell temperature to drop. Cell temperature and gas humidification temperatures were set to desired levels and the cell was operated again at a constant current density of 0.5 A/cm^2 after the temperatures were equilibrated.

3. Results and discussion

URFCs with single-layer oxygen electrodes were assembled and tested to better understand how two electrode-level variables influence cell performance, reversibility, and durability. The first variable was the inclusion of the Nafion^{TM} D520 binder. Nafion^{TM} has been widely used in the literature as a binder in AEM-URFCs **[357], [380], [381], [382]** to reduce catalyst detachment despite the fact that it does not contribute to the ionic conductivity of the electrode. In fact, Nafion^{TM} ionomers and the AEM polymer resin could be incompatible and differences in the thermal and hydrated expansion of the interface between the Nafion^{TM} ionic binder and catalyst could result in performance loss **[382]**. Moreover, it is possible that there is some charge neutralization at the AEM:PEM interface, which can reduce water mobility and OH^- transport. Figure 7.2 shows

polarization and steady-state voltage response data for an electrode with only the TM1 anionomer and an electrode with both TM1 and Nafion^{TM} D520. In Figure 7.2a, the electrode employing only TM1 (I/C=0.336) showed very good performance in both fuel cell and electrolyzer modes. At the target operating current density of 500 mA/cm^2, the TM1 electrode was able to operate at a cell voltage of 1.49 V as an electrolyzer and 0.77 V as a fuel cell, resulting in a round-trip-efficiency of 52 %. At 1.0 A/cm^2, this configuration also performed well, with the ability to achieve an electrolyzer voltage of 1.57 V, fuel cell operating voltage of 0.69 V and round-trip efficiency of 44 %. Increased amounts of TM1 and Nafion^{TM} D520 markedly reduced the performance and the cell voltages in both modes were negatively impacted. At 500 mA/cm^2, the electrolyzer operating voltage increased to 1.62 V, while the fuel cell voltage was reduced to 0.69 V, which resulted in a compromised RTE of 43 %. Additionally, the polarization curves in both modes showed a lower achievable current, and a clear transition to mass-transport controlled conditions, most likely due to reduced water and anion transport. The negative effect of Nafion^{TM} D520 and excess TM1 addition was confirmed at steady-state as well, Figure 7.2b, where the operating voltages were worsened once Nafion^{TM} was added, and the voltage stability was reduced. These results show that although adding Nafion^{TM} ionomer can help catalyst adhesion, it reduces the overall URFC performance suggesting that other strategies are needed to improve catalyst adhesion while employing anion-conducting materials in AEM-URFCs.

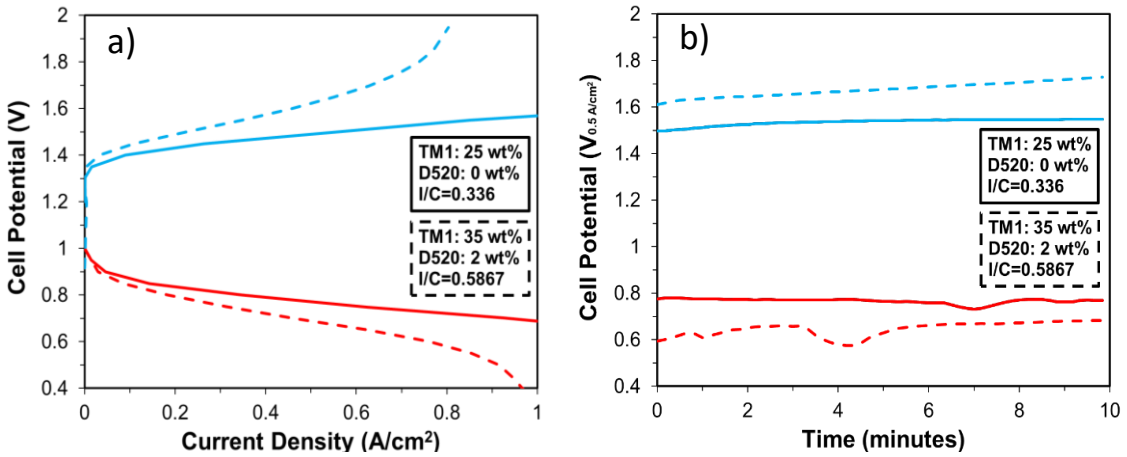

Figure 7.2: URFC performance for electrodes prepared with 25 wt% TM1 (I/C-0.336, solid lines) and with 35 wt% TM1 + 2 wt% D520 (I/C=0.587, dashed lines). a) URFC polarization curve and b) potential response as a function of time under a current hold of 0.5 A/cm^2. Hydrogen electrode: 1.27 mg/cm^2 PtRu/C, 750 sccm H_2 or N_2, 1 bara; Oxygen electrode: 2.6 mg/cm^2 Pt+IrO_x, 750 sccm O_2 or 0.3 mL/min 0.1 M KOH; Membrane: Pention-AEM-72-30-15%; Cell size: 5 cm^2.

The second variable that was investigated in the single-layer electrodes was the ionomer/catalyst (I/C) ratio. Oxygen electrodes with several I/C ratios listed in Table 7.1 were prepared and tested. Both polarization and steady-state measurements were made. The results of 10 minute cycle (2nd cycle, iR-free) steady-state voltage measurements at 500 mA/cm^2 are shown in Figure 7.3. The results show a mostly flat fuel cell response, though the electrolyzer performance shows a gradual decrease in electrolysis potential and a corresponding improvement in RTE up to an increase in the I/C ratio of 0.3-0.4. Beyond this ratio, a decrease in both cell voltage and RTE was observed. The data suggests that an I/C ratio in the range of 0.3-0.4 was optimal. At I/C=0.336, an RTE as high as 50% (62% based on iR-free cell voltage at 500 mA/cm^2) was obtained which is one of the highest ever reported efficiency values in the literature for PEM or AEM URFCs. The optimum I/C ratio of 0.3-0.4 yields an approximate ionomer content of 25 wt% (I/C=0.336), which was used for the rest of the electrodes tested in this study.

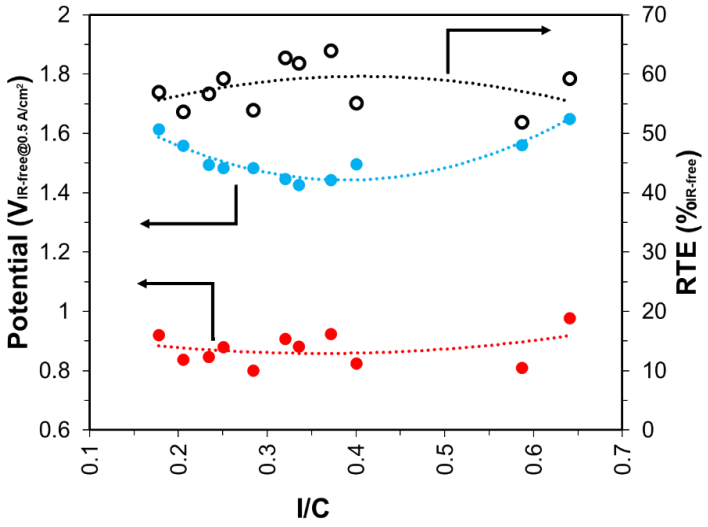

Figure 7.3: iR-free potential response at 0.5 A/cm^2 for the second cycle of electrodes evaluated for fuel cell (red line) and electrolysis (blue line) performance. Secondary y-axis shows the iR-free second cycle RTE (black line). Hydrogen electrode: 1.27 mg/cm^2 PtRu/C, 750 sccm H_2 or N_2, 1 bara; Oxygen electrode: ~2.6 mg/cm^2 Pt+IrO_x, 750 sccm O_2 or 0.3 mL/min 0.1 M KOH; Membrane: Pention-AEM-72-30-15%; Cell size: 5 cm^2.

Next, the cycling durability of an AEM-URFC with the optimized I/C ratio was investigated. Figure 7.4a shows polarization curves for optimized single-layer electrodes at the beginning of life (BOL). After collecting the BOL data, the cell durability was evaluated and is reported in Figure 7.4b. During the durability experiment, the cell was tested cyclically in electrolyzer and fuel cell modes for one hour duration at each mode, while operating at a constant current density of 500 mA/cm^2. In electrolysis mode, the cell voltage was 1.58 V in the first cycle and increased to 1.62 V and 1.77 V at the end of 2nd and 3rd cycles, respectively. While operating in FC mode, the cell potential was 0.804 V during the first cycle and decreased to 0.774 V and 0.723 V at the end of 2nd and 3rd cycles, respectively. The corresponding RTE during cycling of the cell was ~ 50 % during the first cycle which then decreased to ~ 48% and ~ 46% for the 2nd and 3rd cycles, respectively. One of the reasons for the reduced performance with cycling was a gradual increase in area specific resistance (ASR) in just three cycles, where the measured ASR was 33 mΩ cm^2 at

the beginning of the first cycle and increased to 67 mΩ cm^2 at the end of 3rd cycle. This accounts for ~ 17 mV degradation at 500 mA/cm^2, which was only a small fraction of the overall voltage change. Additional performance degradation during URFC operation can be due to catalyst detachment, though this was not observed in the present study. Another possible cause for reduced cell performance is reactant limitations at higher current densities due to change in the wetting properties of the catalyst layer. Having both reactions occurring in a single-Pt-IrO_x catalyst layer can lead to degradation due to exposure of the ORR catalyst and ionomer to the OER reaction products and operating conditions, especially at high potentials, and vice versa. This can lead to diffusional limitations such as bubble trapping and electrode attrition due to gas evolution.

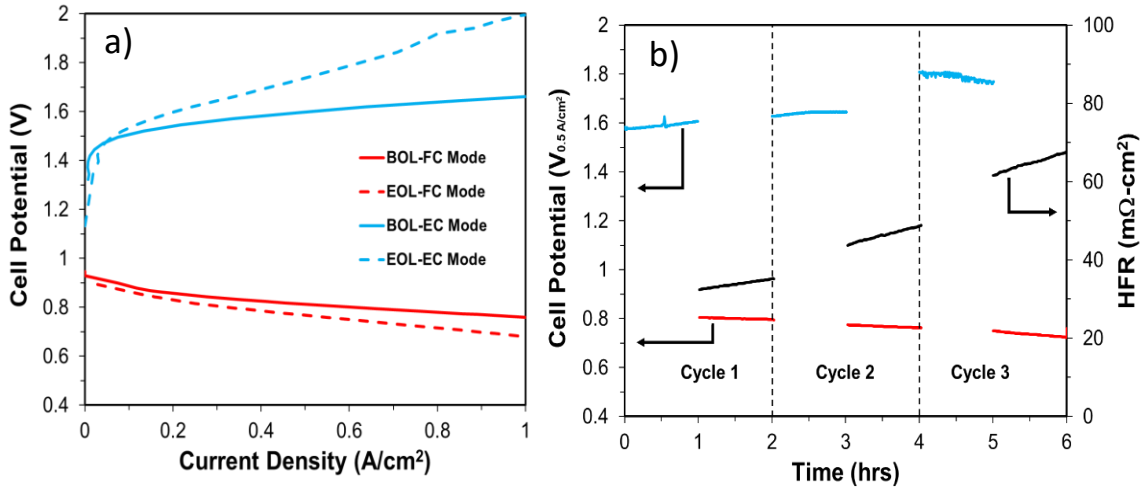

Figure 7.4: Single-layer electrode results: a) URFC polarization curve, the electrodes prepared with 25 wt% TM1 (I/C-0.336) BOL – solid lines and EOL – dashed lines. Hydrogen electrode: 1.27 mg/cm^2 PtRu/C, 1000 sccm H_2 or N_2, 1 bara; Oxygen electrode: 2.6 mg/cm^2 Pt+IrO_x, 1000 sccm O_2 or 1.6 mL/min 0.1 M KOH; Membrane: Pention-AEM-72-5-15%; Cell size: 5 cm^2. b) Potential response as a function of time under a current hold of 0.5 A/cm^2 – FC-red and EC-blue solid lines and HFR over time – black solid lines.

Therefore, an electrode design was conceived that would allow for each catalyst in the oxygen electrode to operate independently by creating a dual-layer oxygen electrode. In this configuration, an IrO_x layer was first deposited onto the PTL and then a Pt black

layer was deposited on top of that as described in Materials and Methods section. The Pt layer is in intimate contact with the AEM, which is desired in FC mode where ionic mobility is only facilitated by the solid electrolyte. In electrolysis mode, an alkaline electrolyte, 0.1 M KOH, is fed, which allows for ion transport in the liquid and solid phases from the outer layer to the AEM. In electrolysis mode, water and evolved oxygen are not required to rapidly penetrate the entire thickness of the catalyst layer as only the outer layer is electroactive.

The BOL and EOL polarization curves and cyclic durability of a dual layer MEA in an AEM-URFC are shown in Figure 7.5. As shown in Figure 7.5a, the BOL and EOL polarization curves were very similar. In fact, at the EOL, there was no change in overpotentials in the electrolysis mode while a slight decrease in voltage is recorded in FC mode due to an increase in the ASR at the EOL. The cycling durability of the dual-layer electrode was also superior to the single-layer electrode, as shown in Figure 7.5b.

Starting with electrolysis mode, the cell voltage was 1.60 V during first cycle which remained unchanged after 5 cycles. In FC mode, the cell potential was 0.788 V (slightly lower than the single layer) during the first cycle and decreased to 0.754 V at the end of the 5^{th} cycle, which is an improvement of ~ 30 mV over the 3^{rd} cycle of the single-layer electrode. There was no significant increase in the ASR (increased from 51.5 $m\Omega.cm^2$ to 57 $m\Omega.cm^2$) during the first 5 cycles. The RTE was ~ 49.4 % at the start of cycle 1 and declined to ~ 48% at the end of 5^{th} cycle. For the 6^{th} cycle, the cell was exposed to one long-duration cycle of ~ 8 hrs in each mode, yielding a total continuous operating time of 26 hours. To the best of our knowledge, the present work shows the highest combination of RTE and cyclic durability at 500 mA/cm^2 for an AEM-URFC. However, improvements

are still needed, and our future work will focus on further improving the performance and durability. The slight increase in ASR suggests that there is still a water deficiency when operating the URFC in fuel cell mode that needs to be addressed. It is also possible that some of the voltage decay can be related to the oxidation of carbon PTL in the oxygen electrode while operating at higher potentials for extended duration **[383]**.

Similar two-layer configurations have been studied in the literature for PEM-URFCs. For example, Chen et al., **[399]** deposited a Pt layer directly onto the GDL and the Ir layer onto the membrane in a PEM-URFC. They concluded that the dual-layer approach showed a more homogeneous and porous surface than a single-layer electrode, which prevented water flooding at high current density in fuel cell mode. The current work shows a different configuration where the OER catalyst was first deposited onto the PTL followed by the ORR catalyst in such a way that the Pt black is in close contact with the AEM. Though slightly different in conformation, the results indicate that the dual-layer electrodes are effective in AEM-URFCs, which, to the best of our knowledge, has not been reported previously.

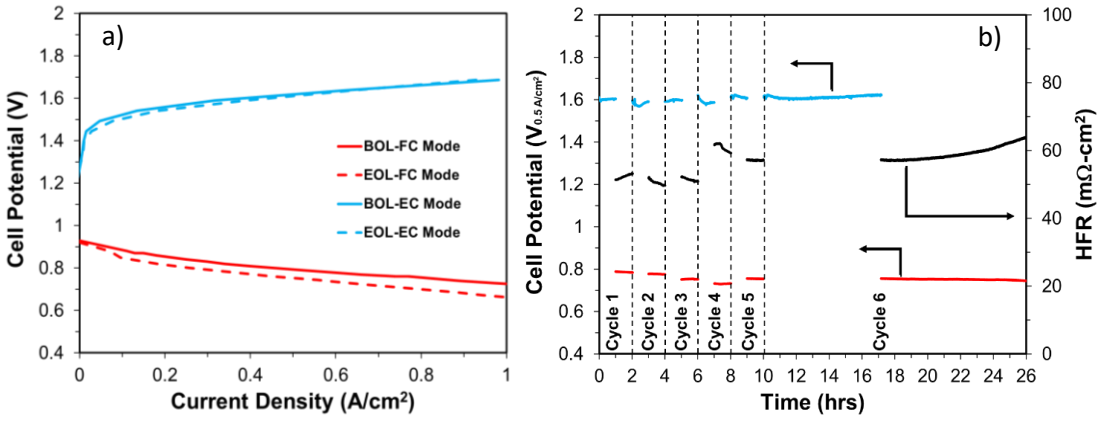

Figure 7.5: Dual-layer electrode results: a) URFC polarization curve, the electrodes prepared with 25 wt% TM1 (I/C-0.336) BOL – solid lines and EOL – dashed lines. Hydrogen electrode: 1.27 mg/cm^2 PtRu/C, 1000 sccm H_2 or N_2, 1 bara; Oxygen electrode: 2.6 mg/cm^2 Pt+IrO_x, 1000 sccm O_2 or 1.6 mL/min 0.1 M KOH; Membrane: Pention-AEM-72-5-15%; Cell size: 5 cm^2. b) Potential response as a function of time under a current hold

Another important focus for future work is the replacement of PGM-based catalysts with low-cost PGM-free metal catalysts. The use of low-cost cell construction materials and PGM-free electrocatalysts is one of the most often cited advantages of alkaline electrochemical systems and most of the studies in the literature continue to focus solely on PGM-containing materials. An important fact is that the stability of both ORR and OER catalysts at the entire potential window of operation (0.6-1.8 V) must be considered while designing a URFC BOE. Moreover, transition metal oxide PGM-free OER catalysts have been the focus of many recent studies **[390], [391], [392], [393], [394],** showing relatively good performance and stability. The best-performing PGM-free ORR catalysts are mostly based on Fe-N-C type and despite their good ORR catalytic activity, these catalysts do not show good stability **[395], [396].** Because of this, we made low PGM-loading oxygen electrodes that use Pt black as the ORR catalyst and commercial $NiCoO_x$ as the OER catalysts to replace the expensive IrO_x. Also, the loading of Pt black was reduced to 0.5 mg/cm^2 resulting in PGM loading reduction from 2.6 mg/cm^2 to 0.5 mg/cm^2 or an 80% PGM catalyst reduction at the oxygen electrode. Figure 7.6 compares the effect of dual-layer and single-layer electrodes containing PGM-free OER catalyst. As observed in high PGM loading dual-layer electrodes, the low PGM loading dual-layer electrode showed superior performance compared to the single-layer electrode. These results support the notion that electrode structure and optimization can yield improvements in AEM-URFC performance and can be used to offset the lower performance normally observed with PGM-free catalysts.

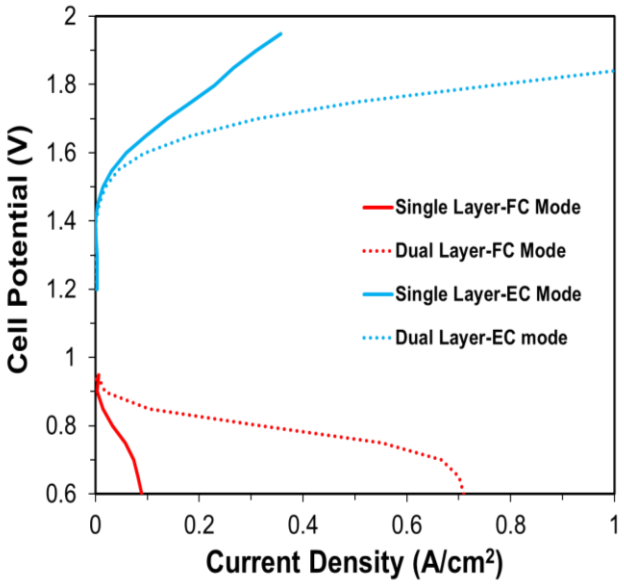

Figure 7.6: URFC polarization curves for low PGM single layer and dual layer bifunctional electrodes prepared with $NiCoO_x$ OER catalyst and low loading Pt black ORR catalyst at the oxygen electrode. Oxygen electrodes prepared with 25 wt% TM1 (I/C-0.336); Single layer – solid lines and Dual layer – dotted lines, FC-red and EC-blue solid lines. Hydrogen electrode: 1.27 mg/cm^2 PtRu/C, 750 sccm H_2 or N_2, 1 bara; Oxygen electrode: 1.1 mg/cm^2 $NiCoO_x$ and 0.5 mg/cm^2 Pt black, 750 sccm O_2 or 0.3 mL/min 0.1 M KOH; Membrane: Pention-AEM-72-5-15%; Cell size: 5 cm^2.

Next, the dual layer Pt-$NiCoO_x$ oxygen electrode was tested for its cycling durability. The BOL and EOL polarization curves and cyclic durability of a dual-layer MEA in AEM-URFC are shown in Figure 7.7. It is important to note that while the Pt loading is kept the same at 0.5 mg/cm^2, the $NiCoO_x$ loading was increased from 1.1 mg/cm^2 to 2.0 mg/cm^2. The increase in the OER catalyst resulted in an increased electrolysis performance while improving the fuel cell performance. The increase in fuel cell performance can be explained as follows: the $NiCoO_x$ catalyst forms a microporous layer-like surface which facilitates uniform Pt deposition and increases Pt utilization for the ORR. With the increase in FC performance, the low PGM loading electrode performed as good as the single-layer or dual-layer high PGM-loading electrode.s. As shown in Figure 7.7a, performance degradation is observed from BOL to EOL polarizations in both EC and the FC modes. For the EC mode, the electrode went through an initial catalyst deactivation

period during the first 45 minutes of electrolysis operation (Figure 7.7b). After this deactivation region, the OER performance was stable during the test showing minimal degradation after 3 cycles (or 6 hrs of testing). On the other hand, no drastic voltage loss is observed in the FC mode; however, it did undergo a slow linear decay throughout the test.

Starting with operation in FC mode, the cell voltage was 0.789 V which is almost identical to that of the high PGM loading electrodes discussed in Figure 7.5. By the end of the third fuel cell cycle, the voltage decreased to 0.735 V (loss of 54 mV). This decrease was much higher than that observed in Figure 7.5 after 26 hrs of operation; however, the degradation was lower than the 80 mV of degradation observed after three cycles for the high PGM loading single layer electrode shown in Figure 7.4. In EC mode, the initial potential was 1.648 V at 0.5 A/cm^2 and after the initial deactivation in the first cycle, the voltage was 1.782 V. At the end of the third EC cycle, the voltage was 1.798 V. Disregarding the initial degradation step, only a 16 mV loss is observed for the PGM-free OER electrode which is significantly lower than the degradation by 192 mV observed in Figure 7.4 for the high PGM loading single-layer electrode. The RTE was 48 % prior to initial degradation. After the initial degradation, a RTE of 44% was obtained. At the end of the third cycle the final RTE was 41%. Apart from the previously discussed possible degradation mechanisms, it is possible that the PGM-free OER catalyst degradation is affecting the ORR, though this is an area that is not well understood and is outside the scope of the present work. Certainly, this work shows complete replacement of the OER catalyst with a low-cost PGM-free material that is still able to operate at commercially-relevant current densities (500 mA/cm^2) while achieving high RTE for an AEM-URFC.

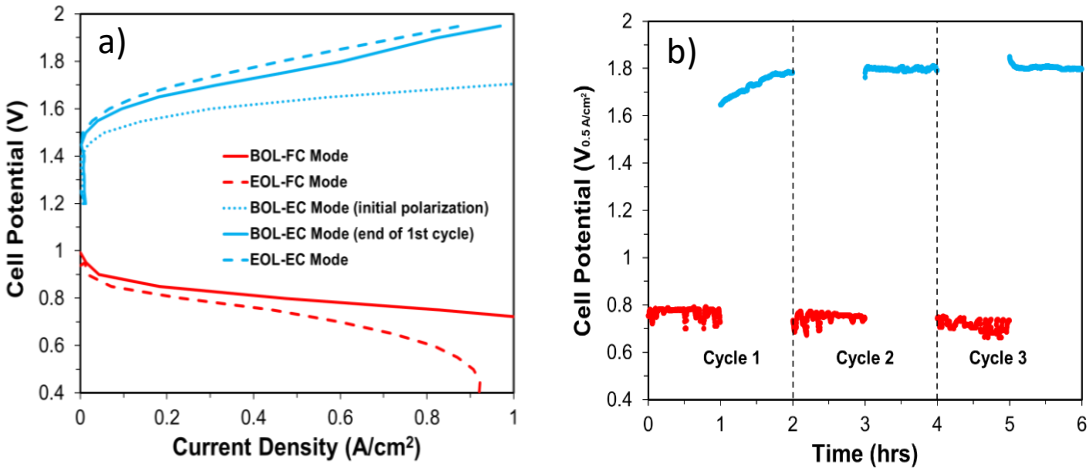

Figure 7.7: Dual-layer electrode results for a low PGM bifunctional oxygen electrode: a) URFC polarization curve, the electrodes prepared with 25 wt% TM1 (I/C-0.336) BOL – solid lines and EOL – dashed lines. Hydrogen electrode: 1.27 mg/cm^2 PtRu/C, 750 sccm H_2 or N_2, 1 bara; Oxygen electrode: 2.0 mg/cm^2 $NiCoO_x$ + 0.5 mg/cm^2 Pt black, 750 sccm O_2 or 0.3 mL/min 0.1 M KOH; Membrane: Pention-AEM-72-5-15%; Cell size: 5 cm^2. b) Potential response as a function of time under a current hold of 500 mA/cm^2 – FC-red and EC-blue solid lines.

4. Conclusions

In this study, the oxygen electrode for an AEM-URFC was studied with several configurations and catalyst layer composition. The addition of Nafion^{TM} as a binder was evaluated as part of the electrode design to increase catalyst layer adhesion, however, it has a negative effect on performance and durability due to an increase in Ohmic resistance. An ionomer to catalyst ratio of 0.336 was found optimal with a round-trip efficiency of 50% (62% when the data was iR-corrected). Single-layer and dual-layer Pt-IrO_x BOE structures were prepared and tested in AEM-URFC. It was found that the dual-layer electrode structure resulted in an improved URFC performance due to efficient catalyst utilization in both modes. The dual-layer electrode configuration, with an IrO_x layer deposited directly onto the PTL and a Pt layer deposited on the surface facing the AEM, resulted in higher URFC performance than a single-layer electrode. This structure also allowed for a significant improvement in long-term operation and electrode durability. Lastly, the dual-

layer electrode structure was extended to low PGM loading BOE electrodes having 0.5 mg/cm^2 Pt for the ORR and up to 2.0 mg/cm^2 $NiCoO_x$ for the OER. The low PGM loading BOE showed comparable overall URFC performance to that of high PGM loading single- or dual-layer BOE. The low PGM loading BOE employing inexpensive $NiCoO_x$ exhibited an initial RTE of 48% and 7% reduction after a short-term durability cycling. These promising results obtained using dual-layer low PGM loading BOE opens new avenues for further optimization of inexpensive PGM-free electrocatalysts for AEM-URFC application.

CHAPTER 8

RESEARCH SUMMARY AND RECOMMENDATIONS FOR FUTURE WORK

1. Summary of Enclosed Work

The main objective of this PhD study was to understand electrochemical science and engineering fundamentals and apply those principles to enhance the performance and durability of AEMELs, AEMFCs and AEM-URFCs devices. Starting with AEMELs, MEAs were studied in depth at the component level. A design of experiments (DoE) factorial design approach was used to optimize four parameters in the OER electrode: catalyst loading, catalyst material selection, additive catalyst support and PTL type. The operating voltage at 1.0 A/cm^2 was used as the output design variable in the experiment matrix. The key finding was that the PTL type was statistically the most influential factor contributing OER electrode performance within the experimental matrix. It was also found that higher catalyst loadings lower the voltage up to 3 mg/cm^2 after which increasing the catalyst loading had a negative effect. Additionally, introduction of additive carbon into the anode electrode had positive effect on voltage response up to 30 % addition after which it had negative impact. The outcome of this comprehensive study was a well-performing electrolyzer device that was able to run stably over 720 hr (30 days) without significant degradation.

The second study included in this thesis was related to the water feed. The key finding was that the performance of the OER electrode is strongly affected by the

concentration of supporting electrolyte. In fact, even small amounts of salt in the water feed can significantly improve the device performance. This finding alone called into questions many literature reports of "DI water" operation where they had either poor flushing protocols or no protocols at all. In addition, it was shown that exposure to KOH during cell break-in can be detrimental to cell stability. This finding led to a change in how cells were operated where now all cells are broken in on DI water. Moreover, an ionomer-rich OER electrode was designed that offered enhanced anion conductivity and hence performance and durability. The result was a cell operation on DI water for its entire life while achieving 500 h longevity, with an operating voltage near 2.0 V at 1.0 A/cm^2.

Building from the DoE experiments, the next study explored the development of commercially viable and cost effective PTLs. 14 different PTLs, broadly categorized into Nickel alloy and stainless steel were investigated. Those PTLs included both custom developed PTLs and state-of-the-art commercially available PTLs. It was found that Ni based PTLs offer up to 100 mV lower voltage compared to SS-based PTLs. It was observed that with similar porosity and fiber structures, PTL thickness (0.2 – 1.2 mm) has no significant effect on electrolyzer performance. PTL porous structure is important for water and gas transport as well as catalyst layer development on the surface. Higher porosity is preferred for efficient water and gas transport while it is a disadvantage for catalyst layer development due to less available surface area and poorer adhesion. It was found that the porosity around 40 % may offer lower contact resistance with ease of water and gas transport resulting in optimal performance in the AEMELs. Moreover, PTL feature size and shape influence contact resistance as well as compatibility with the AEM. Large features and irregular shape fibers may penetrate the AEM causing mechanical failure.

Therefore, surface features modification by compression or other chemical treatment can help smooth the surface. It was concluded that the PTL with 10-20 µm fiber diameters with round shape or compressed/smoothed edges offer lower contact resistance and higher performance. The key outcome of this study was the optimal PTL structure, which was easy to manufacture: ~15 µm in fiber diameter, 0.3 mm thick, 60-65% dense and a compressed/smoothed surface. This enabled an operating voltage with 0.3 M KOH feed of 1.64 V at 1.0 A/cm^2 and the under 2.0 V at 3.5 A/cm^2 at 60 ^{o}C.

On the AEMFC side, three tetrablock poly(norbornene) copolymers were synthesized and incorporated into the anode and cathode of operating AEMFCs. These ionomers demonstrated excellent dimensional stability without significantly sacrificing the ionic conductivity. IEC, water uptake and molecular weight were evaluated for each polymer and tied to AEMFCs performance and durability. It was demonstrated that a combination of hydrophilic ionomer in the anode electrode and more hydrophobic ionomer in the cathode electrode resulted in the best performance. This was explained based on the fact that the anode and cathode have different water requirements, hydrophobic/hydrophilic properties, and conductivity. This best-performing electrode combination was able to achieve very high peak power density, 3.2 W/cm^2, and very high current density. The top-performing electrodes were also tested for their longevity in AEMFCs. Record-setting AEMFC durability was observed over 2000 hours while operating at a U.S. Department of energy prescribed current density of 600 mA/cm^2, with an ultra-low decay rate of 15.36 µV/hr, which resulted in only a 3.65% voltage loss over the 2000 hr experiment.

The same AEMFC device was operated at 600 mA/cm^2 for 3600 hours (150 days) without failure, after which the cell was characterized to allow the dominant degradation

mechanisms during operation to be clearly delineated for the first time. During the 3600 hours of operation, only 11.5 % of the cell voltage was lost. It was found that some of the performance loss was recoverable by rebalancing cell-level water level, while some of the loss was unrecoverable. It was revealed that a large fraction of the unrecoverable performance decay occurred over a relatively brief operating time (~600 h) and was mostly caused by degradation at the cathode. Specifically, the cathode experienced increased catalyst agglomeration compared to the anode. The anode also experienced mild degradation, with Ru leaching from the PtRu catalyst and a portion of it being deposited as nanoparticles at the interface between the AEM and the anode. The AEM itself does not appear to undergo degradation during operation, as evidenced by its unchanged composition and no measurable increase in H_2 crossover. The long-term performance of the cell showed that AEMFCs were rapidly becoming a viable alternative to PEMFCs, and the observations of the remaining degradation mechanisms made in that study can help the AEMFC community design the next generation of increasingly durable cell components, further accelerating the commercialization of this promising technology.

With a thorough understanding developed through discrete fuel cell and water electrolyzer systems, AEM-URFC were tackled, with the idea of combining the functionalities of the fuel cell and electrolyzer into a single device. This study focused on the oxygen electrode with several configurations and catalyst layer compositions. The addition of Nafion^{TM} as a binder was evaluated as part of the electrode design to increase catalyst layer adhesion; however, it has a negative effect on performance and durability due to an increase in Ohmic resistance. An ionomer to catalyst ratio of 0.336 was found optimal with a round-trip efficiency of 50% (62% when the data was iR-corrected). Single-

layer and dual-layer Pt-IrO_x structures were prepared and tested in AEM-URFC. It was found that the dual-layer electrode structure resulted in an improved URFC performance due to efficient catalyst utilization in both modes. The dual-layer electrode configuration, with an IrO_x layer deposited directly onto the PTL and a Pt layer deposited on the surface facing the AEM, resulted in higher URFC performance than a single-layer electrode. This structure also allowed for a significant improvement in long-term operation and electrode durability. Lastly, the dual-layer electrode structure was extended to lower PGM loading electrodes (having 0.5 mg/cm^2 Pt for the ORR and 2.0 mg/cm^2 $NiCoO_x$ for the OER.) The low PGM loading showed comparable overall URFC performance to that of high PGM loading single- or dual-layer BOE. The low PGM loading electrode employing inexpensive $NiCoO_x$ exhibited an initial RTE of 48% and 7% reduction after a short-term durability cycling. These promising results obtained using dual-layer low PGM loading electrodes opens new avenues for further optimization of inexpensive PGM-free electrocatalysts for AEM-URFC application

2. Recommendations for Future Work

Despite important understandings and new knowledge gained during the execution of this thesis, there is still a lot to explore to take AEMELs, AEMFCs and AEM-URFCs to the next level. The rest of this section presents some ideas for future research needs and exploration. The suggested research directions are divided into three sections based on the individual devices.

2.1 AEM Water Electrolyzers:

- In one of the PTL investigations, it was found that AEM electrolyzers prefer more dense structures (55-60%) for enhanced contact and catalyst utilization. However,

an initial voltage loss during steady-state operation was also observed that was associated with bubble accumulation in the anode PTL and catalyst layer. To further investigate this phenomenon, x-ray computed tomography studies are recommended to observe gas bubble evolution, bubble size and/or extent of bubble accumulation. This may help electrode design for efficient bubble removal, leading to enhanced voltage efficiency and durability. This technique has been used to visualize PEMWE electrodes, however, it has not been applied to AEMELs to date Figure 8.1 shows an interface schematic of the catalyst coated membrane (CCM) and porous transport electrode (PTE) assemblies for PEM electrolyzer focusing the water transport and oxygen resident in pores of the PTL / interface **[401]**.

- It is generally believed that hydrophilic PTLs in the AEMEL anode allow for better water transport. However, hydrophilic PTLs may cause larger gas bubbles to be retained in the pores, resulting in inefficient gas evolution. Further investigation towards some degrees of wet proofing of anode PTLs (usually Ni alloys or SS based) is recommended, which might reduce gas bubbles size for efficient removal, resulting in higher efficiency and durability.

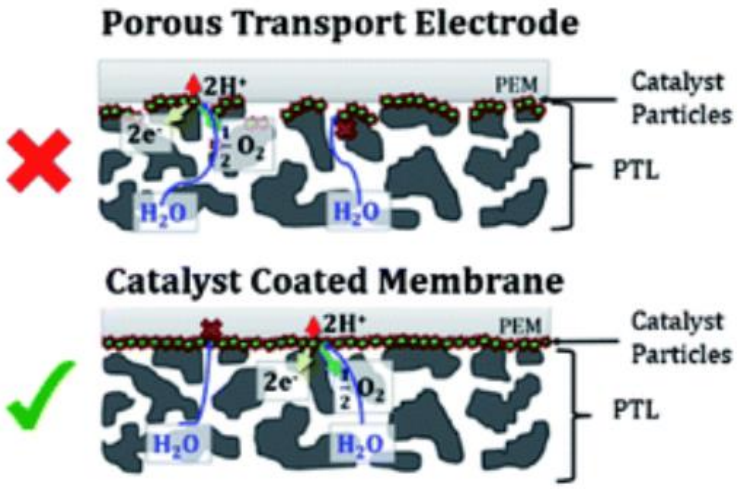

Figure 8.1: Schematic showing catalyst coated membrane and porous transport electrode assemblies **[401]**

- The true promise of AEM based water electrolysis is to deploy PGM-free catalyst materials while achieving high voltage efficiency and durability. Most of the AEM electrolyzers reported in literature employ PGM based catalysts (Ir-based for anode and Pt-based for cathode) and still suffer lower voltage efficiency and durability. Very limited reports have been found showing reasonable activity PGM-free catalysts especially for HER. There is huge voltage penalty (over 400 mV) when switching from PGM to PGM-free HER catalysts and poor durability. It is recommended that further focused investigations on HER catalysis be done to explore PGM-free materials offering enhanced activity and durability, especially in MEA based working environment. Nickel-based materials might be a way forward, combined with other earth abundant metals.

2.2 AEM Fuel Cells

U.S. department of energy (DOE) has set MEA milestones for AEMFCs. These targets provide pathways and opportunity to better understand the underlying fundamentals

of this technology. Table 8.1 shows those milestones. The true promise of AEM fuel cells is to make use of PGM free electrocatalysts with enhanced activity and durability. Moreover, AEMs, ionomers and flow field plates are critical components to be focused to make this technology commercially viable.

Table 8.1: U.S. DOE AEMFC MEA milestones, reproduced from **[400]**

Year	Description
2021	Initial performance: 100 mW cm^{-2} at 0.8 V with ⩽0.2 mgPGM cm−2; H_2/air; T ⩾ 80 °C; P ⩽ 250 kPa
2022	Initial performance: 0.65 V at 1000 mA cm^{-2} on H_2/O_2; T ⩾ 80 °C; P ⩽ 150 kPa; total PGM loading ⩽0.2 mg cm^{-2} Durability: ⩽10% voltage degradation over 1,000 h; T ⩾ 80 °C; P ⩽ 150 kPa; total PGM loading ⩽0.2 mg cm^{-2}
2024	Durability: H_2/air (CO_2-free) after AST ⩽40% loss after 10,000 square-wave cycles 0.6–0.95 V (per8)a), ⩽ 0.125 mg cm^{-2} Durability (membrane): H2 crossover ⩽15 mA cm^{-2} during 1,000 h OCV hold at 70% RH and ⩾80 °C, H_2/N_2
2025	Initial performance:1,000 mW cm^{-2} at 0.65 V; H_2/air (CO_2-free) total PGM loading ⩽ 0.125 mg cm^{-2}, T⩾ 80 °C,Pressure ⩽250 kPa
2030	Initial performance: ⩾600 mW cm^{-2} under H_2/air (maximum pressure of 1.5 atm) in PGM-free MEA
Ultimate	Initial performance: ⩾1,000 mW cm^{-2} at rated power; PGM-free; H_2/air; T ⩾ 80 °C, P ⩽ 250 kPa

To achieve, these milestones, the following pathways are suggested:

- Over the past few years, peak power density and durability of AEM fuel cells have been tremendously improved as could be seen in literature reports. However, a majority of these reports utilize PGM based materials in both anode and cathode electrodes. Several reports have shown good activity of PGM-free cathodes such as NiMo, Fe-N-C etc., however, these systems still show poor durability in actual

working environments. Moreover, there is almost no reasonable PGM-free catalyst options reported for the anode so far. So, lowering the PGM content in the anode coupled with PGM-free cathodes would be realistic way to move forward. Besides their activity, durability should be a main focus. I recommend targeting DOE 2024 target first, achieving durability on H_2/air (CO_2-free) AEM system after accelerated stress testing (AST), demonstrating ⩽40% loss after 10,000 square-wave cycles 0.6–0.95 V. This would allow quick evaluation of low-PGM catalysts materials to advance this technology.

- Thin AEMs have been reported to offer improved performance due to better water management and lower HFR. However, their mechanical properties are not up to the mark, which leads to higher gas crossovers and mechanical failures. Mechanically robust and improved anionic conductivity AEMs need to be developed for better water management, leading to higher performance and durability. Moreover, catalyst coated substrate (CCS) have been shown to be more effective compared to catalyst coated membranes (CCM) at lab scale. But CCMs are more commercially attractive and are the common way to produce PEMFC MEAs at scale. Further studies are needed to assess the effectiveness and improved methodology of CCMs for AEMFCs.

2.3 AEM Unitized Regenerative Fuel Cells

- Fuel cell mode requires hydrophobic PTL properties for efficient water management while electrolyzer mode requires more hydrophilic properties due to liquid water transport into the cell. The use of metallic PTLs – such as Ni alloys or

stainless steel – make it even more challenging to find a balance between desired porosity, pore size distribution and hydrophobic/hydrophilic behavior in each mode. There, teflonization (PTFE treatment) to control wet proofing of the PTLs may be interesting to investigate and improve efficiency/durability of URFC systems.

- Presently, most AEM- URFCs reported in literature employ PGM catalyst materials and still show low round-trip-efficiency and cyclic durability compared to PEM-URFCs. In this work, it was possible to achieve comparable AEM-URFC efficiency as PEM-URFCs with good short-term durability using PGM based materials. However, efficiency and durability were much lower when low-PGM or PGM-free catalysts were deployed. Further investigation is need to understand the degradation pathways in reversible modes with extended cycles using PGM-free catalyst materials.
- Another important area is to delve deeper into the flowfield patterns suitable in both reversible operating modes and bipolar plate materials. Carbon based bipolar plate materials are generally used in fuel cells but are not stable at higher potentials in oxygen electrode in electrolyzer side. Stainless steel or other transition metal BPs may experience passivation during long-term operation, increasing Ohmic resistance. Flow field plates with protective coatings or highly stable materials in alkaline operating media showing good thermal & electrical conductivity need to be explored

REFERENCES

[1]. Momete, D. C., Analysis of the potential of clean energy deployment in the European Union, IEEE Access, 2018, 6, 54811-54822.

[2]. Xu, Q; Lan, P; Zhang, B; Ren, Z. and Yan, Y., Energy Sources, 2013, 35, 848-858.

[3]. Trop, P. and Goricanec, D., Energy, 2015, 108, 155-161.

[4]. Fornara, F; Pattitoni, P; Mura, M; Strazzera, E., J. Environ. Psychol., 2016, 45, 1-10.

[5]. Borovik, M. R. and Albers, J.D., Electr. J., 2018, 31, 33-39.

[6]. EIA, Installed electricity capacity, 2020, (Accessed: August 2022).

[7]. Lazard, Lazard's levelized cost of energy analysis, version 15.0, 2021 (accessed: August 2022).

[8]. Marques, A. C; Fuinhas, J.A; Pereira, D.S., Economic Analysis and Policy, 2019, 63, 188–206.

[9]. Agency, I. E., The power of transformation: Wind, sun and the economics of flexible power systems, IEA (2014).

[10]. Hirth, L. and Muller, S., Energy Economics, 2016, 56, 51–63.

[11]. Al-Shetwi, A. Q; Hannan, M.A; Jern, K.P; Mansur, M. and Mahlia, T.M.I., Journal of Cleaner production, 2020, 253, 119831.

[12]. Das, P; Mathuria, P; Bhakar, R; Mathur, J; Kanudia, A. and Singh, A., Energy Strategy Reviews, 2020, 29, 100482.

[13]. Erdiwansyah, M.; Husin, H.; Nasaruddin, Z. M. and Muhibbuddin, Protection and Control of Modern Power Systems, 2021, 6, 181-3.

[14]. Hadjilambrinos, C., Understanding technology choice in electricity industries: A comparative study of France and Denmark, Energy Policy, 2000, 28, 1111–1126.

[15]. Islam, M. R; Lu, H; Hossain, M.J. and Li, L., Journal of Cleaner production, 2019, 239, 117932.

[16]. Bird, L; Milligan, M.; Lew, D., Integrating variable renewable energy Challenges and solutions, National Renewable Energy lab (NREL), 2013, 6A20-60451.

[17]. Kharrazi, A; Sreeram, V. and Mishra, Y., Renewable and Sustainable Energy Reviews, 2020, 120, 109643.

[18]. Abbasi, R; Setzler, B. P; Lin, S; Wang, J; Zhao, Y; Hu, H; Pivovar, B; Tian, B; Chen, X; Wu, G. and Yan, Y., Adv. Mater., 2019, 31, 1805876.

[19]. M. Momirlan, T. V., Int J Hydrog Energy, 2005, 30, 795-802.

[20]. J. L. Gillette, R. L., Argonne National Lab. (ANL), Argonne, 2008, IL, USA.

[21]. A. Lord, P. K., Int. J. Hydrogen Energy, 2014, 39, 15570.

[22]. B. Pivovar, N. R., Electrochem. Soc. Interface, 2018, 27, 47.

[23]. NREL Renewable Electrolysis, National Renewable Energy Laboratory, 2022.

[24]. D. Parra, G. W., Sustain Cities Soc, 2014, 1-10.

[25]. A. Sgobbi, W. N., Int J Hydrog Energy, 2016, 41, 19-35.

[26]. M. Bodner, A. H., Wiley Interdiscip. Rev.: Energy Environ, 2015, 4, 365.

[27]. M. Felgenhauer, T. H., Int. J. Hydrogen Energy, 2015, 40, 2084.

[28]. LeRoy, R., Int. J. Hydrogen Energy, 1983, 8, 401.

[29]. Willy, Hydrogen Production by Electrolysis (Ed: A. Godula-Jopek), 2015, New York: John WIlly & Sons.

[30]. K. E. Ayers, C. C., ECS Trans., 2012, 41, 15.

[31]. K. E. Ayers, E. B., ECS Trans, 2010, 33, 3.

[32]. M. Götz, J. L., Renewable Energy, 2016, 85, 1371.

[33]. K. E. Ayers, E. B.-Y., ECS Trans, 2013, 45, 121.

[34]. L. Xiao, S. Z., Energy Environ. Sci., 2012, 5, 7869.

[35]. Cho, M. K., Lim, A., Lee, S., Kim, H., Yoo, S., Sung, Y., & Park, H. A., J. Electrochem. Sci. Technol., 2017, 8, 183–196.

[36]. Leng, Y., Chen, G., Mendoza, A., Tighe, T., & Hickner, M. A., J. Am. Chem. Soc., 2012, 134, 9054–9057.

[37]. Miller, H., Bouzek, K., Hnat, J., Loos, S., Bernacker, C., WeiBgarber, T., & Rontzsch, L. A., Sustainable Energy & Fuels, 2020, 4, 2114-2133.

[38]. Vincent, I. A., Renew, Sustain. Energy Rev., 2018, 81, 1690–1704.

[39]. J. Liu Z. Kang, D. L., J. Electrochem. Soc., 2021, 168, 054522.

[40]. B. Motealleh, Z. L., Int J. of Hydrogen Energy, 2020, 46, 3379.

[41]. G. Huang, M. Mandal., J. Electrochem. Soc., 2020, 168, 024503.

[42]. G. Huang, M. Mandal, J. Electrochem. Soc., 2021, 167, 164514.

[43]. P. Chen, X. H., Adv. Energy Mat., 2020, 10, 2002285.

[44]. M. S. Cha, J. E., Energy Environ. Sci., 202, 13, 3633.

[45]. A. Carbone, S. C., International Journal of hydrogen energy, 2020, 45, 9285.

[46]. P. Ganesan, A. S., ACS Appl. Mater. Interfaces, 2017, 9, 12416.

[47]. C. Li, J. B., Nano Energy, 2021, 87, 106162.

[48]. Q. Zu, S. Z., ACS Energy Lett., 2021, 6, 305.

[49]. R. Bock, H. K., Int. J.Hydrogen energy, 2020, 45, 1236.

[50]. J. E. Park, S. Y., Electrochimica Acta, 2019, 295, 99.

[51]. K. Thangavel, M. H., Energy Environ. Sci., 2020, 13, 3447.

[52]. Y. Leng, G. C., J. Am. Chem. Soc., 2012, 134, 9054.

[53]. D. Li, J. P., Nat. Energ., 2020, 5, 378.

[54]. J. Xiao, A. O., ACS Catal., 2021, 11, 264.

[55]. Q. Feng, X. Z., J. Power Sources, 2017, 366, 33.

[56]. L. Xiao, S. Z., Energy Environ. Sci., 2012, 5, 7869.

[57]. N.U. Hassan, M. Mandal, Electrochim. Acta, 2021, 409, 140001.

[58]. P. Lettenmeier, S. K., Energy Environ. Sci.,2017, 10, 2521.

[59]. M. C. O. Monteiro, A. G., ACS Catal., 2021, 11, 14328.

[60]. J. A. D. Rosario, G. L., Applied Catalysis B: Environmental, 2021, 288, 119981.

[61]. R. Soni, S. M., ACS Appl. Energy Mater., 2020, 4, 1053.

[62]. A. Lim, H. K., J. Ind. Eng. Chem., 2019, 76, 410.

[63]. G. A. Lindquist, S. Z., ACS Appl. Mater. Interfaces, 2021, 13, 51917.

[64]. J. Weber, K. D., Adv. Mater, 2008, 20, 2595.

[65]. M. P. Nieh, M. D., Macromolecules, 2008, 41, 6176.

[66]. J. R. Varcoe, R. C., Fuel Cells, 2005, 5, 187.

[67]. B. Y. S. Lin, D. W., J. Power Sources, 2006, 161, 474.

[68]. J. R. Varcoe, P. A., Energy Environ. Sci., 2014, 7, 3135.

[69]. D. R. Dekel, Power Sources, 2018, 375, 158.

[70]. M. Mandal, G. H., ACS Appl. Energy Mater., 2019, 2, 2447.

[71]. J. Wang, Y. Z. C., Nat. Energy, 2019, 4, 392.

[72]. C. Wang, B. M., J. Memb. Sci., 2018, 556, 118.

[73]. M. R. Gerhardt, L. M., J. Electrochem. Soc., 2019, 166, F3180.

[74]. S. D. Poynton, R. C. C., J. Mater. Chem. A, 2014, 2, 5124.

[75]. X. Peng, D. K., Nat. Commun., 2020, 11, 3561.

[76]. M. Ünlü, J. Z., Fuel Cells, 2010, 10, 54.

[77]. T. J. Omasta, L. W., J. Power Sources, 2018, 375, 205.

[78]. D. Yang, H. Y., J. Power Sources, 2014, 267, 39.

[79]. T. J. Omasta, A. M., Energy Environ. Sci., 2018, 11, 551.

[80]. V. Truong, C. W., J. Power Sources, 2018, 402, 301.

[81]. Thompson S. T., P. D., J. Electrochem. Soc., 2020, 167, 084514.

[82]. Regmi, Y., Peng, X., Fornaciari, J., Wei, M., Myers, D., Weber, A., and Danilovic, N., Energy Environ. Sci., 2020,13, 2096-2105.

[83]. Zhao, S., Yan, L., Luo, H., Mustain, W., & Xu, H., Nano Energy, 2018, 47, 172–198.

[84]. Bard, A. J., & Fox, M., Acc. Chem. Res., 1995, 28, 141–145.

[85]. Wang, Y., Leung, D., Xuan, J., & Wang, H., Sustain. Energy Rev., 2017, 75, 775–795.

[86]. Sadhasivam, T., Dhanabalan, K., Roh, S., Kim, T., Park, K., & Jung, S., Int. J. Hydrogen Energy, , 2017, 42, 4415–4433.

[87]. Chen, G., Bare, S., & Mallouk, T., J. Electrochem. Soc., 2002, 149, A1092–A1099.

[88]. Ge, X., Sumboja, A., Wuu, D., An, T., Li, B., & Goh, F., ACS Catal., 2015, 5, 4643–4667.

[89]. Yang, F., Green, Z., Strasser, D., Shi, W., Rojas-Carbonell, S., Yan, Y., & Xu, H., ECS Meeting Abstr. MA, 2020, 02 2439.

[90]. Chen, G., Delafuente, D., Sarangapani, S., & Mallouk, T., Catal. Today, 2001, 67, 341–355.

[91]. Rivas, S., Arriaga, L., Morales, L., & Fernandez, A., Int. J. Electrochem. Sci., 2012, 7, 3601–3609.

[92]. Zhigang S, Baolian Y, and Ming H., J Power Sources, 1999, 79, 82–5.

[93]. Ioroi T, Kitazawa N, Yasuda K, Yamamoto Y, Takenaka H., J Electrochem Soc., 2000, 147, 2018–22.

[94]. Ioroi T, Kitazawa N, Yasuda K, Yamamoto Y, Takenaka H., J Appl Electrochem., 2001, 31, 1179–83.

[95]. Ioroi T, Yasuda K, Siroma Z, Fujiwara N, Miyazaki Y., J Power Sources, 2002, 112, 583–7.

[96]. Yim S. D, Lee W. Y, Yoon Y. G, Sohn Y. J, Park G. G, Yang T. H., Electrochim Acta, 2004, 50, 713–8.

[97]. Yim S, Park G, Sohn Y, Lee W, Yoon Y, Yang T., Int. J Hydrog Energy, 2005, 30, 1345–50.

[98]. Cruz J. C, Baglio V, Siracusano S, Ornelas R, Arriaga L. G, Antonucci V., Int J Hydrog Energy, 2012, 37, 5508–17.

[99]. Chen G, Zhang H, Cheng J, Ma Y, Zhong H., ElectrochemCommun, 2008, 10, 1373–6.

[100]. Chen G, Zhang H, Ma H, Zhong H., Electrochim Acta, 2009, 54, 5454–62.

[101]. Pettersson J, Ramsey B, Harrison D J., Electron Lett., 2006, 42, 1444–6.

[102]. Ioroi T, Oku T, Yasuda K, Kumagai N, Miyazaki Y., J Power Sources, 2003, 124, 385–9.

[103]. Jung H., S. Park and B. N. Popov, J. Power Sources, 2009, 191, 357–361.

[104]. Peng, X; Taie, Z; Liu, L; Zhang, Y; Peng, X; Regmi, Y. N. Fornaciari, J. C; Capuano, C; Binny, D; Kariuki, N. N; Myers, D. J; Scott, M. C; Weber, A. Z; Danilovic, N., Energy Environ. Sci. 2020, 13, 4872-4881

[105]. Wu, X; Scott, K., J Power Sources, 2012, 206, 14–9.

[106]. Wu, X; Scott, K; Xie, F; Alford, N., J Power Sources, 2014, 246, 225–31.

[107]. Ng, J.W; Gorlin, Y; Hatsukade, T; Jaramillo, T.F., Adv Energy Mater 2013, 3, 1545–50.

[108]. Ng, J. W. D; Tang, M; Jaramillo, T. F., Energy Environ Sci. 2014, 7, 2017–24.

[109]. Takeguchi, T; Yamanaka, T; Takahashi, H; Watanabe, H; Kuroki, T; Nakanishi, H., J Am Chem Soc. 2013, 135, 11125–30.

[110]. Bretthauer, C; Müller, C; Reinecke, H., J Power Sources, 2011, 196, 4729–34.

[111]. L. Wang, M. Bellini, H. A. Miller, J. R. Varcoe, J. Mater. Chem. A, 2018, 6, 15404–15412.

[112]. L. Wang, X. Peng, W. E. Mustain, J. R. Varcoe, Energy Environ. Sci. 2019, 12, 1575–1579.

[113]. M. S. Cha, J. E. Park, S. Kim, S.-H. Han, S.-H. Shin, S. H. Yang, T.-H. Kim, D. M. Yu, S. So, Y. T. Hong, S. J. Yoon, S.-G. Oh, S. Y. Kang, O.-H. Kim, H. S. Park, B. Bae, Y.-E. Sung, Y.-H. Cho, J. Y. Lee, Energy Environ. Sci. 2020, 13, 3633–3645.

[114]. Y. Yang, PEM fuel cell system manufacturing cost analysis for automotive applications, Austin Power Engineering LLC, Wellesley (2015).

[115]. W. Cole, T. Mai, J. Richards, P. Das, P. Donohoo-Vallett, 2017 Standard Scenarios Report: A U.S. Electricity Sector Outlook, National Renewable Energy Lab. (NREL), Golden, CO, USA (2017).

[116]. A. Lord, P. H. Kobos, D. J. Borns, Int. J. Hydrogen Energy, 2014, 39, 15570.

[117]. J. L. Gillette, R. L. Kolpa, Overview of Interstate Hydrogen Pipeline Systems, Argonne National Lab. (ANL), 2008, Argonne, IL, USA.

[118]. B. Pivovar, N. Rustagi, S. Satyapal, Electrochem. Soc. Interface, 2018, 27, 47.

[119]. R. Ramachandran, R. K. Menon, Int. J.Hydrogen Energy, 1998, 23, 593.

[120]. Lazard's Levelized Cost of Energy and Levelized Cost of Storage, 2020.

[121]. K. E. Ayers, E. B. Anderson, C. B. Capuano, M. Niedzwiecki, M. A. Hickner, C.-Y. Wang, Y. Leng, W. Zhao, ECS Trans. 2013, 45, 121.

[122]. M. Felgenhauer, T. Hamacher, Int. J. Hydrogen Energy, 2015, 40, 2084.

[123]. J. Liu Z. Kang, D. Li, M. Pak, S. M. Alia, C. Fujimoto, G. Bender, Y. S. Kim, A. Z. Weber, J. Electrochem. Soc. 2021, 168, 054522.

[124]. B. Motealleh, Z. Liu, R. I Masel, J. P. Sculley, Z. R. Ni, L. Meroueh, Int J. of Hydrogen Energy, 2020, 46, 3379.

[125]. Y. Leng, G. Chen, A.J. Mendoza, T.B. Tighe, M.A. Hickner, C.Y. Wang, J. Am. Chem. Soc. 134 (22) (2012) 9054.

[126]. W.E. Mustain, Current Opinion in Electrochemistry, 2018, 12, 233.

[127]. L. Xiao, S. Zhang, J. Pan, C. Yang, M. He, L. Zhuang, J. Lu, Energy Environ. Sci., 2012, 5, 7869.

[128]. D. Li, E. J. Park, W. Zhu, Q. Shi, Y. Zhou, H. Tian, Y. Lin, A. Serov, B. Zulevi, E. D. Baca, C. Fujimoto, H. T. Chung, Y. S. Kim, Nat Energy, 2020, 5, 378.

[129]. J. Xiao, A. M. Oliveira, L. Wang, Y. Zhao, T. Wang, J. Wang, B. P. Setzler, Y. Yan, ACS Catal., 2021, 11,, 264.

[130]. J. E. Park, S. Y. Kang, S. H. Oh, J. K. Kim, M. S. L. C. Y. Ahn, Y. H. Cho, Y.E. Sung, Electrochimica Acta, 2019, 295, 99.

[131]. Q. Zu, S. Z. Oener, G. Lindquist, H. Jiang, C. Li, S. W. Boettcher, ACS Energy Lett. 2021, 6, 305.

[132]. R. Bock, H. Karoliussen, F. Seland, B. G. Pollet, M. S. Thomassen, S. Holdcroft, O. S. Burheim, Int. J.Hydrogen energy, 2020, 45, 1236.

[133]. P. Chen, X. Hu, Adv. Energy Mat. 2020, 10.

[134]. M. S. Cha, J. E. Park, S. Kim, S. H. Han, S. H. Shin, S. H. Yang, T. H. Kim, D. M. Yu, S. So, Y. T. Hong, S. J. Yoon, S. G. Oh, S. Y. Kang, O. H. Kim. H. S. Park, B. Bae, Y. E. Sung, Y. H. Cho, J. Y. Lee, Energy Environ. Sci., 2020, 13, 3633.

[135]. A. Carbone, S. Campagna Zignani, I. Gatto, S. Trocino, A.S. Aric, Int. J.hydrog. energy, 2020, 45, 9285.

[136]. P. Ganesan, A. Sivanantham, S. Shanmugam, ACS Appl. Mater. Interfaces, 2017, 9, 12416.

[137]. C. Li, J. B. Baek, Nano Energy, 2021, 87, 106162.

[138]. K. Thangavel, M. Ha, S. Kumaraguru, A. Meena, A. N. Singh, A. M. Harzandia, K. S. Kim, Energy Environ. Sci., 2020, 13, 3447.

[139]. J E. Park, M. J. Kim, M. S. Lim, S. Y. Kang, J. K. Kim, S. H. Oh, M. Her, Y. H. Cho, Y. E. Sunga, Applied Catalysis B: Environmental, 2018, 237, 140.

[140]. G. Huang, M. Mandal, N. H. Hassan, K. Groenhout, A. Dobbs, W.E. Mustain, P.A. Kohl, J. Electrochem. Soc. 2021, 167, 164514.

[141]. G. Huang, M. Mandal, N. H. Hassan, K. Groenhout, A. Dobbs, W.E. Mustain, P.A. Kohl, J. Electrochem. Soc. 2020, 168, 024503.

[142]. M. Mandal, G. Huang, P. A. Kohl, Journal of Membrane Science, 2019, 570, 394.

[143]. N. U. Hassan, M. Mandal, G. Huang, H. A. Firouzjaie, P. A. Kohl, W. E. Mustain, Advanced Energy Materials, 2020, 10, 2001986.

[144]. M. Mandal, G. Huang, N.U. Hassan, X. Peng, T. Gu, A.H. Brooks-Starks, B. Bahar, W.E. Mustain, P.A. Kohl, J. Electrochem. Soc. 2020, 167, 054501.

[145]. M. Mandal, G. Huang, N. U. Hassan, W. E. Mustain, P.A. Kohl, J. Mater. Chem. A, 2020, 8, 17568.

[146]. Nair, V. N., Pregibon, D., Technometrics. 1988, 30, 247.

[147]. G. E. P. Box, W. G. Hunter, J. S. Hunter, Statistics for Experimenters. An Introduction to Design, Data Analysis, and Model Building, John Wiley & Sons, New York, 1978.

[148]. Lenth, R. V., Technometrics. 1989, 31, 469.

[149]. F. Arbabi, A. Kalantarian, R. Abouatallah, R. Wang, J. S. Wallace, A. Bazylak, Journal of Power Sources, 22014, 58, 142.

[150]. J. G. Navarro, M. Schulze, K. A. Friedrich, ACS Sustainable Chem. Eng., 2019, 7, 1600−1610.

[151]. J. Parrondo, M. George, C. Capuano, K.E. Ayers, V. Ramani, J. Mater. Chem. A, 2015, 3, 10819.

[152]. J. Prakash, D.A. Tryk, E. B. Yeager, J. Electrochem. Soc. 1999, 146, 4145.

[153]. D.W. Shoesmith, J. J. Noël, Corrosion, 2010, 3, 2042.

[154]. D. Prando, A. Brenna, M. V. Diamanti, S. Beretta, F. Bolzoni, M. Ormellese, M. P. Pedeferri, J Appl Biomater. Funct. Mater, 2017, 15, 291.

[155]. Lazard's Levelized Cost of Energy and Levelized Cost of Storage, 2021.

[156]. a) W. Cole, T. Mai, J. Richards, P. Das and P. D. Vallett, National Renewable Energy Lab. (NREL), USDOE Office of Energy Efficiency and Renewable Energy (EERE), Golden, CO, USA (2017). b) W. Cole, B. Frew, P. Gagnon, A.

Reimers, J. Zuboy, R. Margolis, Energy, 2018, 155, 690; c) F. Creutzig, P. Agoston, J. Goldschmidt, G. Luderer, G. Nemet, R. Pietzcker, Nat. Energy, 2017, 2, 17140; d) D. Heide, L. von Bremen, M. Greiner, C. Hoffmann, M. Speckmann, S. Bofinger, Renewable Energy, 2010, 35, 2483; e) J. Apt, J. Power Sources, 2007, 169, 369.

[157]. B. Pivovar, N. Rustagi and S. Satyapal, Electrochem. Soc. Interface, 2018, 27, 47.

[158]. B. Decourt, B. Lajoie, R. Debarre, O. Soupa, The Hydrogen-Based Energy Conversion FactBook, The SBC Energy Institute, Houston, TX, USA, 2014.

[159]. R. L. LeRoy, Int. J. Hydrogen Energy, 1983, 8, 401.

[160]. D. Li, A. R. Motz, C. Bae, C. Fujimoto, G. Yang, F. Zhang, K. E. Ayers and Y. S. Kim, Energy Environ. Sci., 2021, 14, 3393.

[161]. C. Li and J. B. Baek, Nano Energy, 2021, 87, 106162.

[162]. R. Abbasi, B. P. Setzler, S. Lin, J. Wang, Y. Zhao, H. Xu, B. Pivovar, B. Tian, X. Chen, G. Wu and Y. Yan, Advanced materials, 2019, 31, 1805876.

[163]. Hydrogen Production by Electrolysis (Ed: A. Godula-Jopek), John Wiley & Sons, New York, 2015.

[164]. M. Bodner, A. Hofer, V. Hacker, Wiley Interdiscip. Rev.: Energy Environ., 2015, 4, 365.

[165]. a) K. E. Ayers, E. B. Anderson, C. Capuano, B. Carter, L. Dalton, G. Hanlon, J. Manco, M. Niedzwiecki, ECS Trans., 2010, 33, 3; b) K. E. Ayers, E. B. Anderson, C. B. Capuano, M. Niedzwiecki, M. A. Hickner, C.-Y. Wang, Y. Leng, W. Zhao, ECS Trans., 2013, 45, 121; c) K. E. Ayers, C. Capuano, E. B. Anderson, ECS Trans., 2012, 41, 15.

[166]. E. Anderson, presented at 2nd Int. Workshop on Durability and Degradation Issues in PEM Electrolysis Cells and its Components, Freiburg, Germany, 2016.

[167]. M. Götz, J. Lefebvre, F. Mörs, A. McDaniel Koch, F. Graf, S. Bajohr, R. Reimert, T. Kolb, Renewable Energy, 2016, 85, 1371.

[168]. a) K. Zeng, D. k. Zhang, Prog. Energy Combust. Sci. 2010, 36, 307; b) EU's Funding Programme for Research and Innovation, Horizon 2020, Fuel Cells and Hydrogen Joint Undertaking (FCH JU). Multi-Annual Work Plan 2014−2020, 2016.

[169]. A. Lim, M. K. Cho, S. Y. Lee, H.-J. Kim, S. J. Yoo, Y.-E. Sung, J. H. Jang, H. S. Park, J. Electrochem. Sci. Technol., 2017, 8, 265.

[170]. O. Schmidt, A. Gambhir, I. Staffell, A. Hawkes, J. Nelson, S. Few, Int. J. Hydrogen Energy, 2017, 42, 30470.

[171]. Y. Leng, G. Chen, A.J. Mendoza, T.B. Tighe, M.A. Hickner and C.Y. Wang, J. Am. Chem. Soc., 2012, 134, 9054.

[172]. D. Li, J. Park Eun, W. Zhu, Q. Shi, Y. Zhou, H. Tian, Y. Lin, A. Serov, B. Zulevi, D.B. Ehren, C. Fujimoto, T. C. Hoon and S.K. Yu, Nat. Energ., 2020, 5, 378.

[173]. J. Xiao, A.M. Oliveira, L. Wang, Y. Zhao, T. Wang, J. Wang, B.P. Setzler and Y. Yan, ACS Catal., 2021, 11, 264.

[174]. Q. Feng, X. Z. Yuan, G. Liu, B. Wei, Z. Zhang, H. Li, H. Wang, J. Power Sources, 2017, 366, 33.

[175]. L. Xiao, S. Zhang, J. Pan, C. Yang, M. He, L. Zhuang and J. Lu, Energy Environ. Sci., 2012, 5, 7869.

[176]. Q. Xu, S. Z. Oener, G. Lindquist, H. Jiang, C. Li, and S. W. Boettcher, ACS Energy Lett., 2021, 6, 305.

[177]. N.U. Hassan, M. Mandal, B. Zulevi, P. A. Kohl and W. E. Mustain, Electrochim. Acta, 2021, 409, 140001.

[178]. P. Lettenmeier, S. Kolb, N. Sata, A. Fallisch, L. Zielke, S. Thiele, A.S. Gago and K.A. Friedrich, Energy Environ. Sci., 2017, 10, 2521.

[179]. T. Schuler, J.M. Ciccone, B. Krentscher, F. Marone, C. Peter, T.J. Schmidt and F.N. Büchi, Adv. Energy Mater., 2020, 10, 1903216.

[180]. J. Liu, Z. Kang, D. Li, M. Pak, S. M. Alia, C. Fujimoto, G. Bender, Y. S. Kim and A. Z. Weber, J. Electrochem. Soc., 2021, 168, 054522.

[181]. M. C. O. Monteiro, A. Goyal, P. Moerland, and M. T. M. Koper, ACS Catal., 2021, 11, 14328.

[182]. J. A. D. Rosario, G. Li, M. F. M. Labata, J. D. Ocon, P. A. Chuang, Applied Catalysis B: Environmental, 2021, 288, 119981.

[183]. R. Soni, S. Miyanishi, H. Kuroki and T. Yamaguchi, ACS Appl. Energy Mater., 2020, 4, 1053.

[184]. J. Xiao, A.M. Oliveira, L. Wang, Y. Zhao, T. Wang, J. Wang, B.P. Setzler and Y. Yan, ACS Catal., 2021, 11, 264.

[185]. A. Lim, H.J. Kim, D. Henkensmeier, S.J Yoo, J.Y. Kim, S.Y. Lee, Y.E. Sung, J.H. Jang and H.S. Park, J. Ind. Eng. Chem., 2019, 76, 410.

[186]. G. A. Lindquist, S. Z. Oener, R. Krivina, A. R. Motz, A. Keane, C. Capuano, K. E. Ayers, and S. W. Boettcher, ACS Appl. Mater. Interfaces, 2021, 13, 51917.

[187]. M. Mandal, G. Huang and P. A. Kohl, Journal of Membrane Science, 2019, 570, 394.

[188]. N. U. Hassan, M. Mandal, G. Huang, H. A. Firouzjaie, P. A. Kohl and W. E. Mustain, Advanced Energy Materials, 2020, 10, 2001986.

[189]. M. Mandal, G. Huang, N.U. Hassan, X. Peng, T. Gu, A.H. Brooks-Starks, B. Bahar, W.E. Mustain and P.A. Kohl, J. Electrochem. Soc., 2020, 167, 054501.

[190]. M. Mandal, G. Huang, N. U. Hassan, W. E. Mustain and P.A. Kohl, J. Mater. Chem. A, 2020, 8, 17568.

[191]. G. Huang, M. Mandal, N.H. Hassan, K. Groenhout, A. Dobbs, W.E. Mustain and P.A. Kohl, J. Electrochem. Soc., 2021, 167, 164514.

[192]. G. Huang, M. Mandal, N.H. Hassan, K. Groenhout, A. Dobbs, W.E. Mustain and P.A. Kohl, J. Electrochem. Soc., 2020, 168, 024503.

[193]. I. Vincent, A. Kruger, and D. Bessarabov, Int. J. of Hydrogen Energy, 2017, 42, 10752.

[194]. J. Liu, Z. Kang, D. Li, M. Pak, S. M. Alia, C. Fujimoto, G. Bender, Y. S. Kim and A. Z. Weber, J. Electrochem. Soc., 2021, 168, 054522.

[195]. A. Baricci, A. Bisello, A. Serov, M. Odgaard, P. Atanssov and A. Casalegno, Sustainable Energy & Fuels, 2019, 12, 3375.

[196]. I. Vincent, E. C. Lee, and H. M Kim, Scientific reports, 2021, 11, 293.

[197]. LAZARD'S levelized cost of energy analysis – version 15.0, New York, USA, 2021.

[198]. Caglayan, D. G; Weber, N; Heinrichs, H.U; LinBen, J; Robinius, M; Kukla, P.A and Stolten, D, Int. J. Hydrog. Energy, 2020, 45, 6793–6805.

[199]. Carmo, M.; Fritz, D.L; Mergel, J; Stolten, D, Int. J. Hydr. Energy, 2013, 38, 4901–4934.

[200]. Maximilian Schalenbach, M; Zeradjanin, A.R;, Kasian, O; Cherevko, S and Mayrhofer, K.J.J., Int. J. Electrochem. Sci., 2018, 13, 1173 – 1226.

[201]. Nuttall, L.J.; Fickett, A.P. and Titterington, W.A., Hydrogen Generation by Solid Polymer Electrolyte Water Electrolysis, Hydrogen Energy, Springer, Boston, MA, 1975.

[202]. Ayers, K. E.; Anderson, E.B.; Capuano, C; Carter, B; Dalton, L; Hanlon, G; Manco, J and Niedzweicki, ECS Trans, 2010, 33, 3-15.

[203]. Ayers, K. E; Capuano, C. and Anderson, E.B., ECS Trans, 2012, 41, 15–22.

[204]. Barbir, F., Sol. Energy, 2005, 78, 661–669.

[205]. Barbir, F. Main Cell Components, Material Properties, and Processes, PEM fuel cells (chapter 4), Cambridge Academic Press., 2013, 73-117.

[206]. Stiber, S; Balzer, H; Wierhake, A; Wirkert, F.J; Roth, J; Rost, U; Brodmann, M; Lee, J.K; Bazylak, A; Waiblinger, W; Gago, A.S. and Friedrich, A. K., Adv. Energy Materials, 2021, 11, 2100630.

[207]. Metalary, Iridium price: Accessed August 2022,

[208]. Cho, M. K; Lim, A; Lee, S.Y; Kim, H.J; Yoo, S.J; Sung, Y.E; Park, H.S and Jang, J.H, J. Electrochem. Sci. Technol., 2017, 8, 183–196.

[209]. Miller, H.A; Bouzek, K; Hnat, J; Loos, S; Bernacker, C.I; WeiBgarber, T; Rontzsch, L and Haack, J.M, Sustainable Energy & Fuels, 2020, 4, 2114-2133.

[210]. Leng, Y; Chen, G; Mendoza, A.J; Tighe, T.B; Hickner, M.A and Wang, C.Y, J. Am. Chem. Soc, 2012, 134, 9054–9057.

[211]. Vincent, I. and Bessarabov, D., Renew, Sustain. Energy Rev, 2018, 81, 1690–1704.

[212]. Omrani, R and Shabani, B., Int J Hydrog Energy, 2017, 42, 28515-28536.

[213]. Park, J; Oh, H; Ha, T; Lee, Y.I and Min, K., Appl Energy, 2015, 55, 866-880.

[214]. Doan, T. L; Lee, H.E; Shah, S.S.H; Kim, M; Kim, C.H; Cho, H.S. and Kim, T., Int. J Energy Research, 2021, 45, 14207–14220.

[215]. Grigoriev S.A; Millet, P; Volobuev, S. and Fateev, V.N., Int. J. Hydrog. Energy, 2009, 11, 4968-4973.

[216]. Ito, H; Maeda, T; Nakano, A; Hwang, C.M; Ishida, M; Kato, A and Yoshinda, T, Int J Hydrog Energy, 2012, 37, 7418-7428.

[217]. Li, H; Fujigaya, T; Nakajima, H; Inada, A and Ito, K, J. Power Sources, 2016, 332, 16-23.

[218]. Omrani, R and Shabani, B., Int J Hydrog Energy, 2019, 44, 3834-3860.

[219]. Siracusano, S; Blasi, A.D; Baglio, V; Brunaccini, G; Briguglio, N; Stassi, A; Ornelas, R; Trifoni, E; Antonucci, V and Arico, A.S., Int J. Hydrogen Energy, 2011, 36, 333-3339.

[220]. Hussain, N; Steen, E.V; Tanaka, S and Levecque, P, J Power Sources, 2017, 337, 18-24.

[221]. Suermann, M; Takanohashi, K; Lamibrac, A; Schmidt, T.J. and Buchi, F.N, J. Electrochem. Soc. 2017, 164 F973

[222]. Schuler, T; Bruycker R.D; Schmidt, T.J and Buchi, F.N, J. Electrochem. Soc., 2019, 166 F270.

[223]. Hassan, N.U; Mandal, M; Zulevi, B; Kohl, P.A and Mustain, W.E, Electrochimica Acta, 2022, 409, 140001.

[224]. Santoro, C; Lavachhi, A; Mustarelli, P; Noto, V.D; Elbaz, L; Dekel, D.R and Jaouen, F, ChemSusChem, 2022, 8.

[225]. Zu, Q; Oener, S.Z; Lindquist, G; Jiang, H; Li, C. and Boettcher, S.W., ACS Energy Lett., 2021, 6, 305-312.

[226]. Park, J.E; Choi, H.J; Kang, S.Y; Jang, G.Y; Kim, O.H; Karuppannan, M; Sung, Y.E; Kwon, O.J and Cho, Y.H., International Journal of Energy Research, 2022, 8331.

[227]. Xiao, J; Oliveira, A.M; Wang, L; Zhao, Y; Wang, T; Wang, J; Setzler, B.P and Yan, Y, ACS Catalysis, 2021, 11, 264–270.

[228]. Huang, G; Mandal, M; Hassan, N. H; Groenhout, K; Dobbs, A; Mustain, W.E; Kohl, P.A., J. Electrochem. Soc. 2021, 167, 164514.

[229]. Huang, G; Mandal, M; Hassan, N. H; Groenhout, K; Dobbs, A; Mustain, W.E; Kohl, P.A., J. Electrochem. Soc. 2020, 168, 024503.

[230]. Mandal, M; Huang, G and Kohl, P.A., M. Mandal, G. Huang, P. A. Kohl, Journal of membrane sciences, 2019, 570, 394-402.

[231]. Mandal, M; Huang, G; Hassan, N,U; Mustain, W.E and Kohl, P.A., J Material Chem A, 2020, 8, 17568-17578.

[232]. Mandal, M; Huang, G; Hassan, N.U; Peng, X; Gu, T; Brooks-Starks, A.H; Bahar, B; Mustain, W.E; Kohl, P.A. J. Electrochem. Soc. 2020, 167 054501.

[233]. Hassan, N. U; Mandal, M; Huang, G; Firouzjaie, H. A; Kohl, P. A; Mustain, W. E., Adv. Energy Mater. 2020, 10, 2001986.

[234]. Mandal, M; Huang, G; Hassan, N,U; Mustain, W.E and Kohl, P.A., J Material Chem A, 2020, 8, 17568-17578.

[235]. Huang, G; Mandal, M; Hassan, N. H; Groenhout, K; Dobbs, A; Mustain, W.E; Kohl, P.A. J. Electrochem. Soc. 2021, 167, 164514.

[236]. Huang, G; Mandal, M; Hassan, N. H; Groenhout, K; Dobbs, A; Mustain, W.E; Kohl, P.A., J. Electrochem. Soc. 2020, 168, 024503.

[237]. Hassan, N.U; Zheng, Y; Kohl, P.A and Mustain, W.E., J. Electrochem. Soc. 2022, 169, 044526.

[238]. Hassan, N.U; Ganesan, P; Lando, A.A; Mustain, W.E and Mercado, H.R.C, J. Power Sources, 2022, 541, 231599.

[239]. Accepted Practice for Metallographic Preparation of Thermal Spray Coating Samples, ASM Thermal Spray Society, 2022.

[240]. Cook, W.G. and Olive, R.P., Corrosion Science, 2012, 58, 284-290.

[241]. Lee, J.K; Lee, C.H and Bazylak, A, J. Power Sources, 2019, 437, 226910.

[242]. Zhan, Z; Xiao, J; Zhang, Y; Pan, M. and Yuan, R., Int J Hydrog Energy, 2007, 32, 4443-4451.

[243]. Zhang, Y; Verma, A. and Pitchumani, R., Int J Hydrog Energy, 2016, 41, 8412-8426.

[244]. Huang, Y.X; Cheng, C.H; Wang, X.D and Jang, J.Y., Energy, 2010, 35, 4786-4794.

[245]. J. Weber, K. D. Kreuer, J. Maier, A. Thomas, Adv. Mater. 2008, 20, 2595.

[246]. M. P. Nieh, M. D. Guiver, D. S. Kim, J. Ding, T. Norsten, Macromolecules 2008, 41, 6176.

[247]. J. R. Varcoe, R. C. T. Slade, Fuel Cells 2005, 5, 187.

[248]. B. Y. S. Lin, D. W. Kirk, S. J. Thorpe, J. Power Sources 2006, 161, 474.

[249]. D. R. Dekel, J. Power Sources 2018, 375, 158.

[250]. J. R. Varcoe, P. Atanassov, D. R. Dekel, A. M. Herring, M. A. Hickner, P. A. Kohl, A. R. Kucernak, W. E. Mustain, K. Nijmeijer, K. Scott, T. Xu, L. Zhuang, Energy Environ. Sci. 2014, 7, 3135.

[251]. M. Mandal, G. Huang, P. A. Kohl, ACS Appl. Energy Mater. 2019, 2, 2447.

[252]. L. Wang, X. Peng, W. E. Mustain, J. R. Varcoe, Energy Environ. Sci. 2019, 12, 1575.

[253]. J. Wang, Y. Zhao, B. P. Setzler, S. Rojas-Carbonell, C. Ben Yehuda, A. Amel, M. Page, L. Wang, K. Hu, L. Shi, S. Gottesfeld, B. Xu, Y. Yan, Nat. Energy 2019, 4, 392.

[254]. A. Wright, S. Holdcroft, ACS Macro Lett. 2014, 3, 444.

[255]. T. J. Omasta, A. M. Park, J. M. Lamanna, Y. Zhang, X. Peng, L. Wang, D. L. Jacobson, J. R. Varcoe, D. S. Hussey, B. S. Pivovar, W. E. Mustain, Energy Environ. Sci. 2018, 11, 551.

[256]. T. J. Omasta, L. Wang, X. Peng, C. A. Lewis, J. R. Varcoe, W. E. Mustain, J. Power Sources 2018, 375, 205.

[257]. W. E. Mustain, Curr. Opin. Electrochem. 2018, 12, 233.

[258]. Z. F. Pan, L. An, T. S. Zhao, Z. K. Tang, Prog. Energy Combust. Sci. 2018, 66, 141.

[259]. M. R. Gerhardt, L. M. Pant, A. Z. Weber, J. Electrochem. Soc. 2019, 166, 7.

[260]. S. D. Poynton, R. C. T. Slade, T. J. Omasta, W. E. Mustain, R. Escudero-Cid, P. Ocón, J. R. Varcoe, J. Mater. Chem. A 2014, 2, 5124.

[261]. D. Yang, H. Yu, G. Li, Y. Zhao, Y. Liu, C. Zhang, W. Song, Z. Shao, J. Power Sources 2014, 267, 39.

[262]. L. Sun, J. Guo, J. Zhou, Q. Xu, D. Chu, R. Chen, J. Power Sources 2012, 202, 70.

[263]. M. Ünlü, J. Zhou, I. Anestis-Richard, H. Kim, P. A. Kohl, Electrochim. Acta 2011, 56, 4439.

[264]. J. Zhou, M. Ünlü, I. Anestis-Richard, H. Kim, P. A. Kohl, J. Power Sources 2011, 196, 7924.

[265]. J. Ahlfield, G. Huang, L. Liu, Y. Kaburagi, Y. Kim, P. A. Kohl, J. Electrochem. Soc. 2017, 164, 12.

[266]. D. Li, E. J. Park, W. Zhu, Q. Shi, Y. Zhou, H. Tian, Y. Lin, A. Serov, B. Zulevi, E. D. Baca, C. Fujimoto, H. T. Chung, Y. S. Kim, Nat. Energy 2020, 5, 378.

[267]. G. Huang, M. Mandal, X. Peng, A. C. Yang-Neyerlin, B. S. Pivovar, W. E. Mustain, P. A. Kohl, J. Electrochem. Soc. 2019, 166, 10.

[268]. M. Mandal, G. Huang, N. U. Hassan, X. Peng, T. Gu, A. H. Brooks-Starks, B. Bahar, W. E. Mustain, P. A. Kohl, J. Electrochem. Soc. 2020, 167, 5.

[269]. M. Mandal, G. Huang, P. A. Kohl, J. Memb. Sci. 2019, 570, 394.

[270]. J. Zhou, M. Ünlü, I. Anestis-Richard, H. Kim, P. A. Kohl, J. Power Sources 2011, 196, 7924.

[271]. T. Omasta, Y. Zhang, A. M. Park, X. Peng, B. Pivovar, J. R. Varcoe, W. E. Mustain, J. Electrochem. Soc. 2018, 165, 9.

[272]. C. Chen, Y. L. S. Tse, G. E. Lindberg, C. Knight, G. A. Voth, J. Am. Chem. Soc. 2016, 138, 991.

[273]. Y. Oshiba, J. Hiura, Y. Suzuki, T. Yamaguchi, J. Power Sources 2017, 345, 221.

[274]. S. Gottesfeld, D. R. Dekel, M. Page, C. Bae, Y. Yan, P. Zelenay, Y. S. Kim, J. Power Sources 2018, 375, 170.

[275]. C. E. Diesendruck, D. R. Dekel, Curr. Opin. Electrochem. 2018, 9, 173.

[276]. M. Ünlü, J. Zhou, P. A. Kohl, in Fuel Cells, 2010, 10, 54.

[277]. C. Wang, B. Mo, Z. He, Q. Shao, D. Pan, E. Wujick, J. Guo, X. Xie, X. Xie, Z. Guo, J. Memb. Sci. 2018, 556, 118.

[278]. W. Chen, M. Mandal, G. Huang, X. Wu, G. He, P. A. Kohl, ACS Appl. Energy Mater. 2019, 2, 2458.

[279]. C. Wang, B. Mo, Z. He, Q. Shao, D. Pan, E. Wujick, J. Guo, X. Xie, X. Xie, Z. Guo, J. Memb. Sci. 2018, 556, 118.

[280]. V. Truong, C. Wang, M. Yang, H. Yang, J. Power Sources. 2018, 402, 301.

[281]. D. R. Dekel, I. G. Rasin, M. Page, S. Brandon, J. Power Sources 2018, 375, 191.

[282]. K. Fukuta, Electrolyte Materials for AMFCs and AMFC Performance, 2011.

[283]. Z. Wang, M. Mandal, S. Sankarasubramanian, G. Huang, P.A. Kohl, V.K. Ramani, ACS Appl. Energy Mater. 2020, 3, 4449.

[284]. X. Peng, D. Kulkarni, Y. Huang, T. J. Omasta, B. Ng, Y. Zheng, L. Wang, J. M. LaManna, D. S. Hussey, J. R. Varcoe, I. V. Zenyuk, W. E. Mustain, Nat. Commun. 2020, 11, 3561.

[285]. C. Fujimoto, D. S. Kim, M. Hibbs, D. Wrobleski, Y. S. Kim, J. Memb. Sci. 2012, 423, 438.

[286]. N. Robertson, H. Kostalik, T. Clark, P. Mutolo, H. Abruna, G. Coates, J. Am. Chem. Soc. 2010, 132, 3400.

[287]. Dekel D. R., J. Power Sources, 2018, 375, 158-169.

[288]. Varcoe J. R., Atanassov P., Dekel D.R., Herring A.M., Hickner M.A., Kohl P.A., Kucernak A.R., Mustain W.E., Nijmeijer K., Scott K., Xu T. and Zhuang L., Energy Environ. Sci., 2014, 7, 3135-3191.

[289]. Mustain W. E., Chatenet M., Page M. and Kim Y. S., Energy Environ. Sci., 2020, 13, 2805 - 2838.

[290]. Huang G., Mandal M., Peng X., Yang-Neyerlin A.C., Pivovar B. S., Mustain W.E. and Kohl P.A., J. Electrochem. Soc., 2019, 166 F637.

[291]. Hassan N. U., Mandal M., Huang G., Firouzjaie H. A., Kohl P. A., and Mustain W. E., Adv. Energy Mater., 2020, 10, 2001986.

[292]. Chen N., Hu C., Wang H. H., Kim S. P., Kim H. M., Lee W. H., Bae J. Y., Park J. H. and Lee Y.M., Angew. Chemie Int., 2021, 133, 7789-7797.

[293]. Maurya S., Noh S., Matanovic I., Park E. J., Villarrubia C. N., Martinez U., Han J., Bae C., and Kim Y. S., Energy Environ. Sci., 2018, 11, 3283-3291.

[294]. Mandal M., Huang G., Hassan N.U., Peng X., Gu T., Brooks-Starks A.H., Bahar B., Mustain W.E., Kohl P.A., J. Electrochem. Soc., 2020, 167, 054501.

[295]. Peng X., Kulkarni D., Huang Y., Omasta T. J., Ng B., Zheng Y., Wang L., LaManna J. M., Hussey D. S., Varcoe J. R., Zenyuk I. V. and Mustain W. E., Nat. Commun., 2020, 11, 3561.

[296]. Omasta T. J., Park A. M., Lamanna J. M., Zhang Y., Peng X., Wang L., Jacobson D. L., Varcoe J. R., Hussey D. S., Pivovar B. S. and Mustain W. E., Energy Environ. Sci., 2018, 11, 551 – 558.

[297]. Omasta T. J., Zhang Y., Park A. M., Peng X., Pivovar B., Varcoe J. R. and Mustain W. E., J. Electrochem. Soc., 2018, 165, F710.

[298]. Deng H., Wang D. W., Xie X., Zhou Y. B., Yin Y., Du Q. and Jiao K., Renewable Energy, 2016, 91, 166–177.

[299]. Deng H., Wang D. W., Wang R. F., Xie X., Yin Y., Du Q. and Jiao K., Appl. Energy, 2016, 183, 1272–1278.

[300]. Noh S., Jeon J. Y., Adhikari S., Kim Y. S. and Bae C., Acc. Chem. Res., 2019, 52, 2745–2755.

[301]. You W., Noonan K. J. T. and Coates G. W., Prog. Polym. Sci., 2020, 100, 101177.

[302]. Zheng Y., Colón L. N. I., Hassan N. U., Williams E. R., Stefik M., LaManna J. M., Hussey D. S., and Mustain W. E., 2021, 2, 102.

[303]. Jin C., Lu F. L., Cao X. C., Yang Z. R. and Yang R. Z., J. Mater. Chem. A, 2013, 1, 12170–12177.

[304]. Kreider M. E., Gallo A., Back S., Liu Y. Z., Siahrostami S., Nordlund D., Sinclair R., Norskov J. K., King L. A. and Jaramillo T. F., ACS Appl. Mater. Interfaces, 2019, 11, 26863–26871.

[305]. Adabi H., Shakouri A., Hassan N.U., Varcoe J. R., Zulevi B., Serov A., Regalbuto J. R., and Mustain W.E., Nature Energy, 2021, 8, 834-843.

[306]. Adabi H., Santori P. G., Shakouri A., Peng X., Yassin K., Rasin I. G., Brandon S., Dekel D. R., Hassan N.U., Sougrati M. T., Zitolo A., Varcoe J. R., Regalbuto J. R, Jaouen F., and Mustain W. E., Mat. Today Adv., 2021, 12, 100179.

[307]. Maurya S., Lee A. S., Li D. G., Park E. J., Leonard D. P., Noh S., Bae C. and Kim Y. S., J. Power Sources, 2019, 436, 226866.

[308]. Li D., Matanovic I., Lee A. S., Park E. J., Fujimoto C., Chung H. T. and Kim Y. S., ACS Appl. Mater. Interfaces, 2019, 11, 9696–9701.

[309]. Diesendruck C. E. and Dekel D. R., Curr. Opin. Electrochem., 2018, 9, 173–178.

[310]. Dekel D. R., Arnar M., Willdorf S., Kosa M., Dhara S. and Diesendruck C. E., Chem. Mater., 2017, 29, 4425–4431.

[311]. Gerhardt M. R., Pant L. M. and Weber A. Z., J. Electrochem. Soc., 2019, 166, F3180–F3192.

[312]. Wang L. Q., Magliocca E., Cunningham E. L., Mustain W. E., Poynton S. D., Escudero-Cid R., Nasef M. M., Ponce-Gonzalez J., Bance-Souahli R., Slade R. C. T., Whelligan D. K. and Varcoe J. R., Green Chem., 2017, 19, 831–843.

[313]. Thomas A., Maranzana G., Didierjean S., Dillet J. and Lottin O., J. Electrochem. Soc., 2013, 160, F191–F204.

[314]. Das P. K., Li X. and Liu Z. S., J. Power Sources, 2008, 179, 186 - 199.

[315]. Wang Q., Eikerling M., Song D. and Liu Z., J. Electroanal. Chem., 2004, 573, 61-69.

[316]. Chen L., Kang Q., and Tao W., Electrochimica Acta, 2019, 306, 454-465.

[317]. Wang R., Li D., Maurya S., Kim Y. S., Wu Y., Liu Y., Strmcnik D., Markovic N.M. and Stamenkovic V. R., Nanoscale Horiz., 2020, 5, 316-324.

[318]. Lafforgue C., Maillard F., Martin V., Dubau L. and Chatenet M., ACS Catal. 2019, 9, 5613–5622.

[319]. Omasta T. J., Wang L., Peng X., Lewis C. A., Varcoe J. R. and Mustain W. E., J. Power Sources, 2018, 375, 205–213.

[320]. Mustain W. E., Curr. Opin. Electrochem., 2018, 12, 233–239.

[321]. Thompson S. T., Peterson D., Ho, D. and Papageorgopoulos D., J. Electrochem. Soc., 2020, 167, 084514.

[322]. Cooper K. R., In Situ PEMFC Fuel Crossover & Electrical Short Circuit Measurement, Fuel Cell Magazine, Scribner Associates, Inc. 2008.

[323]. Wang G., Li W., Wu N., Huang B., Xiao L., Lu J., and Zhuang L., J Power Sources, 2019, 412, 282-286.

[324]. Mandal M., Huang G., Kohl P. A., J. Membr. Sci., 2019, 570, 394-402.

[325]. Chempath S., Boncella J. M., Pratt L. R., Henson N., and Pivovar B. S., J. Phys. Chem. C 2010, 114, 11977–11983.

[326]. Chempath S., Einsla B. R., Pratt L. R., Macomber C. S., Boncella J. M., Rau J. A. and Pivovar B. S., J. Phys. Chem. C, 2008, 112, 3179–3182.

[327]. Liu F., Yi B., Xing D., Yu J., Hou Z. and Fu Y., J. Power Sources, 2003, 124, 81 - 89.

[328]. Yuan X. Z., Song C., Wang H. and Zhang J., PEM Fuel Cells and their Related Electrochemical Fundamentals, Springer London, 2010.

[329]. Sheng W., Gasteiger H. A. and Horn Y. S., J. Electrochem. Soc., 2010, 157 B1529.

[330]. Yi Y., Weinberg G., Prenzel M., Greiner M., Heumann S., Becker S. and Schlogl R., Catalysis Today, 2017, 295, 32-40.

[331]. Bard, A. J; Fox, M.A., Acc. Chem. Res. 1995, 28, 141–145.

[332]. Nocera, D.G; Nash, M.P., Proceedings of the National Academy of Sciences of the United States of America, 2006, 103, 15729-15735.

[333]. Nocera, D.G., Inorg. Chem, 2009, 48, 10001–10017.

[334]. Zhao, S; Yan, L; Luo, H; Mustain, W; Xu, H., Nano Energy, 2018, 47, 172–198.

[335]. Wang, Y; Leung, D.Y.C; Xuan, J; Wang, H., Renew. Sustain. Energy Rev. 2017, 75, 775–795.

[336]. Gabbasa, M; Sopian, K; Fudholi, A; Asim, N., Int. J. Hydrogen Energy. 2014, 39, 17765–17778.

[337]. Sadhasivam, T; Dhanabalan, K; Roh, S.H; Kim, T.H; Park, K.W; Jung, S., Int. J. Hydrogen Energy, 2017, 42, 4415–4433.

[338]. Kanan, M.W; Nocera, D.G., Science, 2008, 321, 1072–1075.

[339]. Gorlin, Y; Jaramillo, T.F., J. Am. Chem. Soc. 2010, 132, 13612–13614.

[340]. Chen, G; Bare, S.R; Mallouk, T.E., J. Electrochem. Soc. 2002, 149, A1092–A1099.

[341]. Wang, Y; Leung, D. Y.C; Xuan J; Wang, H., Renew. Sustain. Energy Rev., 2016, 65, 961-977.

[342]. Lim, A; Lee, J. S; Lee, S; Lee, S.Y; Kim, H. J; Yoo, S. J; Jang, J. H; Sung, Y. E; Park, H. S., Applied Catalysis B: Environmental, 2021, 297, 120458.

[343]. Kúš, P; Ostroverkh, A; Khalakhan, I; Fiala, R; Kosto, Y; Šmíd, B; Lobko, Y; Yakovlev, Y; Nováková, J; Matolínová, I., Int. J. Hydrogen Energy, 2019, 44, 16087-16098.

[344]. Regmi, Y.N; Peng, X; Fornaciari, J.C; Wei, M; Myers, D.J; Weber, A.Z; Danilovic, N., Energy Environ. Sci., 2020, 13, 2096-2105.

[345]. Peng, X; Taie, Z; Liu, L; Zhang, Y; Peng, X; Regmi, Y. N. Fornaciari, J. C; Capuano, C; Binny, D; Kariuki, N. N; Myers, D. J; Scott, M. C; Weber, A. Z; Danilovic, N., Energy Environ. Sci. 2020, 13, 4872-4881.

[346]. Ota, K; Mitsushima, S., Hand. Fuel Cells, 2010.

[347]. Blizanac, B.B; Ross, P.N; Markovic, N.M., Electrochim. Acta 2007, 52 2264–2271.

[348]. Bockris, J.M; Penner, S.S; Selman, J.R; Shores, D; Yeager, E.B; Appleby, J. Members and ex officio members of the DOE advanced fuel cell working group (AFCWG), S.S. Penner (Ed.), Assessment of Research Needs for Advanced Fuel Cells, Pergamon, 1986, pp. vii–viii.

[349]. Appleby A.J. Electrocatalysis. In: Conway B.E., Bockris J.O., Yeager E., Khan S.U.M., White R.E. (eds) Comprehensive Treatise of Electrochemistry, 1983, Springer, Boston, MA.

[350]. Setzler, B.P; Zhuang, Z; Wittkop, J.A. Yan, Nat. Nanotechnol. 2016, 11, 1020–1025.

[351]. Mustain, W.E; Chatenet, M; Page, M; Kim, Y.S., Energy Environ. Sci. 2020, 13, 2805 – 2838.

[352]. Huang, G; Mandal, M; Peng, X; Yang-Neyerlin, A.C; Pivovar, B. S; Mustain, W.E; Kohl, P.A. J. Electrochem. Soc. 2019, 166 F637.

[353]. Hassan, N. U; Mandal, M; Huang, G; Firouzjaie, H. A; Kohl, P. A; Mustain, W. E. Adv. Energy Mater. 2020, 10, 2001986.

[354]. Mandal, M; Huang, G; Hassan, N.U; Peng, X; Gu, T; Brooks-Starks, A.H; Bahar, B; Mustain, W.E; Kohl, P.A. J. Electrochem. Soc. 2020, 167 054501.

[355]. Peng, X; Kulkarni, D; Huang, Y; Omasta, T. J; Ng, B; Zheng, Y; Wang, L; LaManna, J. M; Hussey, D. S; Varcoe, J. R; Zenyuk, I. V; Mustain, W. E. Nat. Commun. 2020, 11, 3561.

[356]. Mandal, M; Huang, G; Hassan, N. U; Mustain, W. E; Kohl, P.A., J. Mater. Chem. A, 2020, 34, 17568.

[357]. Li, D; Park, E. J; Zhu, W; Shi, Q; Zhou, Y; Tian, H; Lin, Y; Serov, A; Zulevi, B; Baca, E. D; Fujimoto, C; Chung, H. T; Kim, Y. S., Nat. Energy 2020, 5, 378.

[358]. Xiao, J; Oliveira, A. M; Wang, L; Zhao, Y; Wang, T; Wang, J; Setzler, B. P; Yan, Y., ACS Catal. 2021, 11, 264.

[359]. Zu, Q; Oener, S. Z; Lindquist, G; Jiang, H; Li, C; Boettcher, S. W., ACS Energy Lett. 2021, 6, 305.

[360]. Huang, G; Mandal, M; Hassan, N. H; Groenhout, K; Dobbs, A; Mustain, W.E; Kohl, P.A., J. Electrochem. Soc. 2021, 167, 164514.

[361]. Huang, G; Mandal, M; Hassan, N. H; Groenhout, K; Dobbs, A; Mustain, W.E; Kohl, P.A., J. Electrochem. Soc. 2020, 168, 024503.

[362]. Wu, X; Scott, K., J Power Sources, 2012, 206, 14–9.

[363]. Takeguchi, T; Yamanaka, T; Takahashi, H; Watanabe, H; Kuroki, T; Nakanishi, H., J Am Chem Soc. 2013, 135, 11125–30.

[364]. Ng, J. W. D; Tang, M; Jaramillo, T. F., Energy Environ Sci. 2014, 7, 2017–24.

[365]. Wu, X; Scott, K; Xie, F; Alford, N., J Power Sources, 2014, 246, 225–31.

[366]. Maiyalagan, T; Jarvis, K.A; Therese, S; Ferreira, P.J; Manthiram, A., Nat Commun 2014, 5.

[367]. Menezes, P.W; Indra, A; Sahraie, N.R; Bergmann, A; Strasser, P; Driess, M., ChemSusChem 2015, 8, 164–71.

[368]. Menezes, P.W; Indra, A; González-Flores, D; Sahraie, N.R; Zaharieva, I; Schwarze, M., ACS Catal. 2015, 5, 2017–27.

[369]. Bretthauer, C; Müller, C; Reinecke, H., J Power Sources, 2011, 196, 4729–34.

[370]. Gayan, P; Saha, S; Liu, X; Sharma, K; Ramani, V. K., Proceedings of the National Academy of Sciences of the United States of America, 2021, 118, 2107205118.

[371]. Yang, F; Green, Z; Strasser, D; Shi, W; Rojas-Carbonell, S; Yan, Y; Xu, H., ECS Meeting Abstr. MA, 2020-02 2439.

[372]. Takasu, Y; Yoshinaga, N; Sugimoto, W., Electrochem. Commun. 2008, 10, 668–672.

[373]. Ge, X; Sumboja, A; Wuu, D; An, T; Li, B; Goh, F.W.T., ACS Catal. 2015, 5, 4643–4667.

[374]. Yang, F; Green, Z; Strasser, D; Shi, W; Rojas-Carbonell, S; Yan, Y; Xu, H., ECS Meeting Abstr. MA, 2020-02 2439.

[375]. Chen, G; Delafuente, D.A; Sarangapani, S; Mallouk, T.E., Catal. Today, 2001, 67, 341–355.

[376]. Yim, S.D; Park, G. G; Sohn, Y. J; Lee, W. Y; Yoon, Y. G; Yang, T. H., Int. J. Hydrogen Energy, 2005, 30, 1345–1350.

[377]. Yim, S. D; Lee, W. Y; Yoon, Y. G; Sohn, Y. J; Park, G. G; Yang, T. H., Electrochim. Acta. 2004, 50, 713–718.

[378]. Rivas, S; Arriaga, L.G; Morales, L; Fernandez, A.M., Int. J. Electrochem. Sci. 2012. 7, 3601–3609.

[379]. Takasu, Y; Yoshinaga, N; Sugimoto, W., Electrochem. Commun. 2008, 10, 668–672.

[380]. Koshikawa, H; Murase, H; Hayashi, T; Nakajima, K; Mashiko, H; Shiraishi, S; Tsuji, Y., ACS Catal. 2020, 10, 1886–1893.

[381]. Grigoriev, S.A; Pushkarev, A.S; Pushkareva, I.V; Millet, P; Belov, A.S; Novikov, V. V; Belaya, I.G; Voloshin, Y.Z., Int. J. Hydrog. Energy, 2017, 42, 27845–27850.

[382]. Li, C; Baek, J. B., Nano Energy, 2021, 87, 106162.

[383]. Mçller, S; Barwe, S; Masa, J; Wintrich, D; Seisel, S; Baltruschat, H; Schuhmann, W., Angew. Chem. Int. Ed. 2020, 59, 1585 –1589.

[384]. Ng, J.W; Gorlin, Y; Hatsukade, T; Jaramillo, T.F., Adv Energy Mater 2013, 3, 1545–50.

[385]. Kormányos, A.; Speck, F. D.; Mayrhofer, K. J. J.; Cherevko, S., ACS Catal. 2020, 10, 10858–10870.

[386]. Hersbach, T. J. P.; Garcia, A. C.; Kroll, T.; Sokaras, D.; Koper, M. T. M.; Garcia-Esparza, A. T., ACS Catal. 2021, 11, 9904–9915.

[387]. Lafforgue, C.; Zadick, A.; Dubau, L.; Maillard, F.; Chatenet, M., Fuel Cells 2018, 18, 229–238.

[388]. Bender G; Carmo M; Smolinka T; Gago A; Danilovic N; Mueller M; Ganci F; Fallisch A; Lettenmeier P; Friedrich KA; Ayers K, Int. J. Hydrog. energy. 2019, 44, 9174-87.

[389]. Young, J.L.; Kang, Z.; Ganci, F.; Madachy, S. and Bender, G., Electrochemistry Communications, 2021, 124, 106941.

[390]. Hongsen W.; Yao Y.; Francis J. D. and Héctor D. Abruña, ACS Catal., 2020,10, 4608–4616.

[391]. Victor S.; Melina Z.; Meital S.; David Z. and Marian C., ACS Appl. Energy Mater. 2020, 3, 9, 8858–8870.

[392]. Lihua Z.; Qun F.; Kai L.; Sheng Z. and Xinbin Ma, Sustainable Energy & Fuels, 2020, 4, 5417-5432.

[393]. Mengjie C.; Lei W.; Haipeng Y.; Shuai Z.; Hui X. and Gang W., J. Power Sources, 2018, 375, 277-290.

[394]. Shiva G.; William K.;,Hui X.; Xien L.; Jaephil C. and Gang W., Chem. Asian J. 2016,11,10–21.

[395]. Adabi H, Shakouri A., Hassan N. U., Varcoe J.R., Zulevi B., Serov A., Regalbuto J.R., and Mustain W.E., Nature Energy, 2021, 6, 834-843.

[396]. Adabi H., Santori P.G., Shakouri A., Peng X., Yassin K., Rasin I.G., Brandon S., Dekel D.R., Hassan N. U., Sougrati M. T, Zitolo A., Varcoe J.R., Regalbuto J.R., Jaouen F. and Mustain W.E., Materials Today Advances, 2021, 12, 100179.

[397]. Jung H., Park S. and Popov B. N., J. Power Sources, 2009, 191, 357–361.

[398]. Wang Y, Dennis Y. C. L., Xuan J., Wang H, Renew. and Sust. Energy Rev., 2016, 65, 961–977.

[399]. Chen G, Zhang H, Ma H, Zhong H, Electrochim Acta, 2009, 54, 5454–62.

[400]. Thompson, S.T; Peterson, D; Ho, D. and Papageorgopoulos, D., J. Electrochem. Soc., 2020, 167, 084514.

[401]. Leonard, E; Shum, A.D; Danilovic, N; Capuano, C; Ayers, K.E; Pant, L.M; Weber, A.Z; Xiao, X; Parkinson, D.Y and Zenyuk, I.V., Sustainable Energy Fuels, 2020, 4, 921-931.